Numerical Simulation of Particle Collision and Agglomeration in Turbulent Channel Flows

Tosanbami Ogholaja

Submitted in accordance with the requirements for the degree of
Doctor of Philosophy

UNIVERSITY OF LEEDS

The University of Leeds
School of Chemical and Process Engineering

April, 2018

The candidate confirms that the work submitted is his/her own and that appropriate credit has been given where reference has been made to the work of others.

This copy has been supplied on the understanding that it is copyright material and that no quotation from the thesis may be published without proper acknowledgement.

Acknowledgement

Abstract

The study described in this thesis concerns the simulation of dispersed and dense particle-laden turbulent channel flows. The research primarily investigates the role of gravity; in terms of its contribution to particle collision, agglomeration and re-distribution. Large eddy simulation is employed to predict the fluid-phase, with solutions coupled with a Lagrangian particle tracking routine to model the particle-phase. In order to establish the validity of the preferred numerical method, results generated from the single-phase and the dilute particle-phase predictions were compared with those based on DNS, with good agreements found.

Results obtained for horizontal zero gravity channel flows, show effects of particle size, particle concentration and turbulence on colliding and agglomerating particles. All variables were shown to strongly impact on collision and agglomeration, with the number of events reaching maximum towards the channel walls due to increased particle concentrations and turbulence levels in these regions. The collision and agglomeration is, however, shown to enhance exponentially with the inclusion of gravity and accentuated on the lower wall of the channel. An extension of the investigation into vertical channels of upward and downward flow configurations, also demonstrated the significance of the gravity force on particle collision and agglomeration. The effect of the particles on the flow is small, owing to the low mass-loading. Agglomeration is found to be most favourable for flows of low turbulence; and unlike collisions, dominantly forms in the channel centre.

The investigation presented is a novel contribution to literature that provides a fundamental improvement on the understanding of turbulent fluid-particle flows. Particularly, it extends the existing knowledge on cohesive particle behaviours in turbulent flows by examining the effect of gravity on such flows. The contribution finds relevance in many engineering and industrial flow processes and should aide the design of better flow processes.

Table of Contents

List of Figures

List of Tables

Nomenclature

Roman Letters

A_p	Particle surface area
C	Sub-grid scale model parameter
C_D	Drag coefficient
C_0	Model constant
d_p	Particle diameter
e_n	Coefficient of restitution
F	Force
f_D	Drag factor
F_{SL}	Saffman lift force
g	Gravity
G	Filter function in LES
h	Channel half-height
H	Hamaker constant
i'^+_{rms}	Velocity fluctuation in i direction
k	Turbulence kinetic energy
k_{sgs}	Unresolved kinetic energy of the continuous phase
l	Length scale
N_a	Number of particle agglomerates
N_{agg}	Number of particle agglomeration
N_{col}	Number of particle collisions
N_p	Number of particle
N_{pp}	No of primary particle
p	particle
Re_τ	Shear Reynolds number

Re_p	Particle Reynolds number
Re	Reynolds number of the shear flow
St	Stokes number
T	Test filter level SGS stress tensor
t^+	Dimensionless Time
u, v, w	Velocities in x, y, z directions
u_b	Bulk velocity
u_f	Fluid velocity
u_p	Fluid velocity
u_τ	Shear velocity
$u'^+ w'^+$	Component of the shear Reynolds stress
$\boldsymbol{u}_{p,r}$	Relative velocity between colliding particles
v	Kinematic viscosity
V	Volume
V_i	Particle volume
V_p	Particle Volume
v_{sgs}	Sub-grid scale viscosity
v_1, v_2, v_3	Velocities of the colliding particles
x_1, x_2, x_3	Positions of the colliding particles
x, y, z	Cartesian coordinates
$\boldsymbol{x}_r$	Relative distance between colliding particles
X_{sgs}	Sub-grid velocity fluctuations on particle motion
$\Delta_x \Delta_y \Delta_z$	Grid resolution in x, y, z directions
Δx_{cell}	Minimum distance across the cell.

Greek Letters

τ_w	Mean shear stress at the wall
ϕ	Volume fraction

ξ_p	Component of the particle domain in x direction
n_p	Component of the particle domain in y direction
ζ_p	Component of the particle domain in z direction
$\overline{\sigma}$	Mean yield stress
δ_{ij}	Cartesian components of unit tensor (Kronecker symbol)
δ_0	Minimum contact distance
μ	Fluid dynamic viscosity
τ_t	Sub-grid time scale
ρ_p	Particle density
τ_p	Particle relaxation time
τ_f	Fluid relaxation time
Δ	Filter width
τ_{ij}	Sub-grid scale stress tensor
ω	Fluid rotation
ε	Turbulence energy dissipation rate
ξ_i	Random variable

Acronyms

CFD	Computational Fluid Dynamics
DEM	Discrete Element Method
DES	Detached Eddy Simulation
DNS	Direct Numerical Simulation
DVLO Overbeek	Agglomeration Theorem by Derjaguin and Landau and Verwey and
EIM	Eddy Interaction model (EIM)
EOR	Enhanced Oil Recovery
HPIV	Holographic Particle Image Velocimetry
HWA	Hot-wire Anemometry

$k - \varepsilon$	epsilon model
K-/	one-equation model
LDA	Laser Doppler Anemometry
LDV	Laser Doppler Velocimetry
LES	Large Eddy Simulation
LPT	Lagrangian Particle Tracking
PDA	Phase Doppler Anemometry
PDF	Probability Density Function
PIV	Particle Image Velocimetry
RANS	Reynolds Averaged Navier Stokes
RMS	Root mean square
SGS	Sub-Grid Scale

$k - \varepsilon$ epsilon model

K-/   one-equation model

1 Introduction

1.1 Background Studies on Multiphase Flows

The term multiphase flow refers to any fluid flow that consists of more than one component or phase. It is frequently encountered in a wide range of industries and more importantly, finds application in pharmaceutical, nuclear, petroleum and petrochemical, agricultural and the food processing industries. These flows are well known to occur in both laminar and in the turbulent flow regimes, of which the later remains one of the most complicated subject areas in fluid mechanics till date (Balachandar and Eaton, 2010). In many of these industrial processes, the need to transport fluid from one location to another is unavoidable. In most cases, this transport process results in complex interactions within the flow, between fluid, particles (or bubbles) and the wall regions of the transporting medium. Therefore, in such systems, an understanding on the physical conditions promoting these interactions and the consequent re-distribution, collision and agglomeration of the dispersed phase is fundamental in improving fluid flow assurance. The understanding will also play a primordial role in optimising the design of fluid processing facilities. For example, in crude oil exploration where sand levels per unit volume of crude oil has risen significantly due to depletion of ageing oil reservoirs, it is therefore necessary to understand particle-wall collision and subsequent corrosion mechanisms. This is crucial in preventing the erosion-corrosion synergy which occurs as a result of continuous bombardment of the particles on the pipe walls. With this understanding, the designers and operators of such facilities are well placed to make informed decisions on how to mitigate the effect of the particle impact by administering various mechanical and chemical treatments. Typical measures could range from optimising materials resistivity to mechanical stresses to implementing corrosion control measures like pigging and using inhibitors.

Multiphase flow is also a common feature in everyday occurrences. For example, the rain, fog, avalanches, snow, debris flow, sediment transport mudslides and other natural phenomena in some way contains a two or more phase system and occurs

at different levels of turbulence intensities. It generally consists of a continuous (carrier) phase and a dispersed phase within the continuous phase. In the industries, it is extensively relied upon as a means for moving a large amount of materials like slurries or aerosols over long distances through wall-bounded geometries (pipelines, ducts and channels) to processing or storage sites within a plant. One major reason for this is due to the fact that it has proven to be a more cost-effective approach when compared to other forms of material transport. For instance, in coal-operated power plants, coal is pulverized in a coal mill and then is transported pneumatically to the burners. Another important use is in spray forming or spray casting. In this process, molten metals are atomized into very fine droplets, transported by a carrier gas and then deposited on a given substrate. Biological and medical fluid flows are also classed as multiphase, from semen to blood flow to laser surgery cavitation and so on.

The degree of complexity of a turbulent multiphase flow system is generally dependent on factors including the shape and wall roughness of the flow geometry, fluid-particle density ratio, fluid velocity, particle size, mass loading (ratio of solids to gas in pneumatic flows or the ratio of solids to liquid in slurry flows), the forces acting on the fluid and the number of phases contained (phase coupling). In practice, these factors can result in a system with multi-flow regimes. However, this study will be restricted to the investigation of turbulent two-phase flows and will, therefore, be discussed further. This is necessary to reduce the complexities that arise from turbulent multiphase flows and attempt to provide a clear understanding of the effect of dispersed phase on the fluid flow. Of specific interest is the study concerning inter-particle collision and agglomeration as these become fundamental in dictating the dynamics of a turbulent two-phase flow at sufficiently high particle concentrations. Many attempts have been made over the years by researchers to understand these concepts in turbulent two-phase flows using experimental measurements like particle image velocimetry (Adrian, 1991), hot wire anemometry and laser Doppler velocimetry. However, the use of experimental techniques to measure these flows is known to have significant limitations due to the high financial cost involved in running such experiments. In recent times, the use of numerical procedures (computational fluid dynamics, CFD) have been adopted as an alternative and employed extensively in creating better understanding on these flows and in the optimisation of flow systems. This is due to its relatively low cost of running and the ability to give accurate predictions even at such low computational costs. The most common turbulent models employed to study turbulent fluid flows in the order of accuracy, includes the

direct numerical simulation (DNS), large eddy simulation (LES), and Reynolds-averaged Navier-Stokes (RANS).

1.2 Industrial Relevance of Study

It is evident from the instances cited that there is indeed a wide range of application of multiphase flows. However, the section aims to discuss the relevance of this work as it relates to current challenges in two main industrial processes where particle transport in turbulent flow is applied.

1.2.1 Oil and Gas Industry

The oil and gas industry is one of the largest and most complex industries across the globe. Its products among other energy sources remain the most popular resource in use today, (EIA, 2010) with huge economic and political significance. Its high popularity could be attributed to the ease of transportation across long distances by using production and transmission pipelines. Hence, in places like Russia and Alaska, hundreds of kilometre long carbon steel pipelines have been erected for the transportation of hydrocarbons from remote areas to marketing locations (Attanasi and Freeman, 2014).

However, across the upstream and downstream sectors of the oil and gas industry, the process of oil extraction, production and recovery faces challenges resulting from sand erosion, organic (asphaltenes, waxes, gas hydrates) and inorganic scales (sulphides, carbonates, iron), bio fouling and corrosion (Demadis et al., 2007). Scale formation is one of the major challenges encountered in the oil and gas industry. It is formed as a result of abrupt changes in temperature and pressure conditions when incompatible sea water is injected and mixes with formation water in production sites. This then results in the precipitation, deposition and adhesion of sparingly soluble salts on the surface of pipe walls under supersaturated conditions.
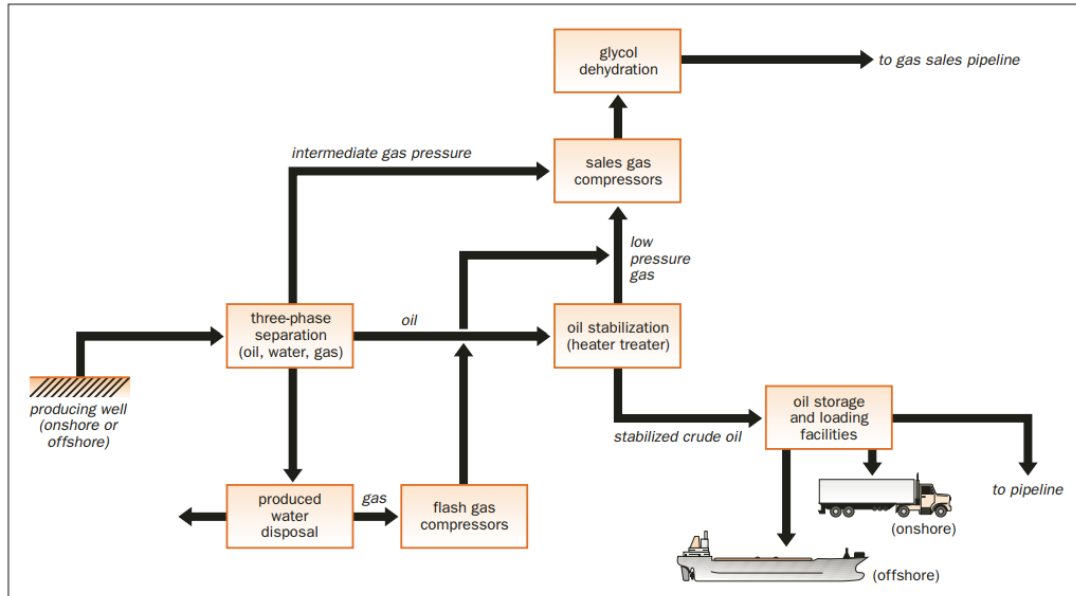
Figure 1.1: Crude oil processing flow diagram showing possible inorganic scale formation sites during enhanced oil recovery (EOR) (Technical, 1997)

The flow diagram in Figure 1.1 shows that scale formation can arise anywhere from the production well areas to the surface facilities. When not effectively managed, the deleterious precipitation of scaling materials could build up over time and cause severe flow restriction problems in pipes or valves and can also result in fouling in tanks and pumps (Crabtree et al., 1999). Removing the scale has proven to be a very difficult process (Sommerdijk and With, 2008) and sometimes may lead to a complete replacement of the affected material. In such instances, the lack of adequate technique to predict and monitor the fluid characteristics in terms of the scale formation rate and location as well as the resulting deposition and adhesion has ensured industries spend millions of pounds in prevention and removal of the scales. The use of CFD in this work serves as a useful tool in addressing these challenges on a fundamental level but can be tailored by introducing appropriate chemical reaction models to better understand the rheology of such flows.

1.2.2 Nuclear Industry

Of particular relevance of this work to the nuclear industry is in the treatment of nuclear legacy waste. More specifically, it concerns the treatment and management of highly active UK nuclear wastes stored over the past 50 years at the nuclear site managed by Sellafield Ltd. Sellafield Ltd is responsible for processing and disposing of nuclear wastes emanating from decaying fuel rods and used nuclear reactor parts, buried in highly radioactive waters of cooling ponds. The dissolution of metals in the

cooling ponds over time has accumulated into a dense sludge that emits radiation at very dangerous and potentially fatal levels (Deegan et al., 2013).

In order to adequately process the nuclear waste, there is need to mobilise and transport the sludge through pipes to processing units. This has proven to be very challenging due to problems arising from factors which promote settling of insoluble solids; like particle sizes, surface chemistry, flow regime changes and the instability in hydrodynamic forces acting on the fluid (Hyatt et al., 2009). When not adequately managed, small particles under these chemical and physical influences, agglomerate to form larger sized particles and deposit to form beds on pipe walls, which eventually leads to pipe blockages and possible leakages from localised corrosion-related activities. In this instance, the affected pipelines become extremely hazardous, very difficult to repair and therefore are most often abandoned. In order to prevent or minimise such occurrences, it becomes imperative to improve the understanding of the physical behaviours of the fluid in terms of the events promoting particle collision and agglomeration during transportation. An effective way of doing this is through the use of CFD to predict these behaviours as traditional experimental investigation methods may not be suitable due to the highly toxic nature of the legacy waste.

1.3 Study Objectives

In this research project, a study on the transport processes occurring in turbulent wall-bounded two-phase flows will be carried out using numerical techniques. The work aims to address fundamentally, the issue as related to the collision and agglomeration of solid particles and provide basic understandings on the physics that underpins their behaviour in industrial flow processes. This crucially is necessary to optimise the performance and enhance the design of engineering flow processes. The use of CFD in this thesis, therefore, serves as a useful alternative to the traditional experimental method due to the ease of obtaining results when compared to the former. The CFD method is also a more robust approach; and as such can handle more variablities than the experimental approach.

Specifically, the objectives of the project is as follows:

- Perform in-depth CFD studies on turbulent flows using the LES method across flows of three different Reynolds numbers; and validating the model

accuracy for both single and particle phase, by comparing LES generated results against results obtained from DNS studies.

- Integrate the LES model with a Lagrangian particle tracker (LPT) to predict particle dispersion across a range of different particle sizes; accounting for the effect of size variation on particle distribution as well as their impact on the fluid phase.

- Conduct analyses of the hydrodynamic forces acting on the particle and the resulting influence on particle distribution.

- Compare and contrast flows with- and without the presence of gravity in order to investigate the influence of gravitational force on the fluid flows.

- Investigate the effect of Reynolds number and particle concentration on particle dispersion, collision and agglomeration of flows under the influence of gravity.

- Determine the consistency of the findings on horizontal channel flows by altering the channel flow direction (vertical channel).

1.4 Thesis Layout

The rest of the thesis is structured according to the following arrangement:

Chapter 2: reviews some of the published research studies on the application of experimental and modelling techniques in investigating single and multiphase flows in channel, pipe and duct geometries.

Chapter 3: presents the physical equations governing the fluid flow and also discuss the numerical models employed in predicting both the particle and fluid phases.

Chapter 4: explains the channel flow geometry and provides results on the validation of the single and particle phases flows. It also includes analyses on particle dispersion and agglomeration and discusses the effect of concentration and hydrodynamic forces on the flow characteristics.

Chapter 5: extends the study of the channel flow in the previous chapter by investigating the effect of gravity on particle dispersion and agglomeration and the resulting influence on turbulence. It further discusses the influence of particle sizes, concentration and Reynolds number on the fluid flow.

Chapter 6: is an extension of the studies concerning turbulent horizontal channel flows. The flow direction is altered and made to travel in both upward and downward directions and compared with the horizontal flow.

Chapter 7: presents a conclusion on the findings in this thesis and provides recommendations on possible areas to be addressed in future.

2 Literature Review

2.1 Background Studies on Multiphase Flows

In this chapter, a review on some of the previous investigations carried out on turbulent two-phase flows in channel, pipe and duct geometries are performed. Firstly, the study discusses the concept of two-phase flows and further presents an outline of some of the fundamental parameters necessary in the classification of turbulent two-phase flows. In an attempt to improve the understanding of these flows, the available experimental and numerical techniques employed by researchers in predicting two-phase flows, as well as the resulting conclusions drawn from such investigations are reviewed. The review is then concluded by describing the relevance of the current work to previous studies.

2.2 Introduction to Two-Phase Flows

The research work is aimed at understanding two-phase flows in which the liquid is the continuous phase and solid particle the dispersed phase. The fluid considered is one where the flow is in a turbulent state and in continuous motion. The behaviour of such flows is generally dependent on the flow conditions, which is known to have significant influence on the characteristics of the fluid (Balachandar and Eaton, 2010; Li et al, 2001; Pang et al, 2011; Soldati and Marchioli, 2009; Tsuji et al., 1994). The nature of both the continuous phase turbulence and the random particle phase distribution increases the complexity of turbulent two-phase flows when compared with its single-phase counterpart (Balachandar and Eaton, 2010), which then makes experimental and numerical investigations far more complicated. Depending on the coupling between the carrier and dispersed phases, the presence of solid particles can result in the formation of wakes and vortex shedding which enhances the production of turbulence energy and further modifies the turbulence in the flow system (Elghobashi, 1994). This phenomenon is referred to as "turbulence modulation". The presence of particles can also result in the dissipation of turbulence in the flow. Turbulence modulation is one of the most important aspects of turbulent two-phase flow research (Sato and Hishida, 1996). In the context of this work, it is

described as the particles inertial effect on turbulence for a two-phase system when compared to the single phase. In other words, turbulence is modulated by the presence of solid particles in sufficiently large concentrations (Patro and Dash, 2014; Squires and Eaton, 1990a).

The transfer of kinetic energy from the carrier phase to the particle, the formation of vortex shedding and wakes behind the particles and the enhanced dissipation caused by particle presence in the fluid, are all mechanisms which contribute to turbulence modulation (Balachandar and Eaton 2010). Squires and Eaton (1990a) in agreement suggests that two major problems associated with turbulent two-phase flows are the dispersion of the particles by turbulence and the resulting modification of the turbulence properties by particles. The modification is to a large extent dependent on the category of the fluid-particle coupling. Rogers and Eaton (1991) discussed the complexity of particle-laden two-phase flows and concluded that the addition of the particulate phase to a single phase system, adds new parameters that modify the structure of the flow. These parameters are significant in defining fluid flow regimes in wall-bounded flows and ultimately shapes the characteristics of the particle phase, in terms of their collision, agglomeration, deposition and resuspension behaviours.

For a homogenous two-phase system where fluid flow exceeds the critical velocity, one would expect that particle segregation will be impossible based on the understanding that the critical velocity represents the minimum velocity required to maintain the turbulence at levels high enough to keep particles in suspension during flow. However, due to the complex nature of these flows, it is difficult to reach this conclusion as the flow behaviour is constantly being influenced by the flow parameters. In order words, it is safe to say that in reality no flow is completely homogenous. Crowe (2005) therefore, suggested that the flow could be classed as homogenous if only the decrease in particle concentration across a wall-bounded flow is less than 20%. The homogeneity is significantly dependent on the particle Stokes number, St (Kulick et al., 1994), which is an indication of the particle response to the perturbations arising from the turbulence field. A large particle, having a larger response time, therefore is more likely to deposit in the wall regions of a turbulent flow field. While the smaller sized particles tends to follow the fluid flow. The density ratio of the solid phase to the fluid also directly influences the flow homogeneity, as a large difference in densities will require a large critical velocity to keep the solid phase in suspension. The parameters which may directly impact on the fluid flow

includes, particle Reynolds number, hydrodynamic and gravitational forces, particle mass loading, particle size and shape, particle distribution, velocity gradient and particle-fluid density ratio. Others include the orientation of the flow geometry, wall roughness, particle interactions with the fluid phase and walls. The rate of interaction is dependent on the concentration of the particle in the fluid, measured in terms of the fluid volume fraction; and becomes fundamental in categorizing fluid flow regimes and the corresponding behaviours of the flow. In order to adequately predict such flows, it becomes necessary to classify two-phase flows according to the degree of contact between particles and their environment as well as gaining a thorough understanding on the factors which influences their rheological behaviours.

2.2.1 Classification of Two-Phase Flow Regimes

The study of two-phase flows over the years has been shown to be extremely significant in understanding and predicting turbulent flow behaviours in industrial production processes (Pang et al, 2011) and has, therefore, led to investigations by many researchers, both experimentally and numerically. In two-phase flow systems, there is always a certain degree of interaction between the carrier and the dispersed phase due to exchange in momentum and mass transfer. This is said to complicate modelling and analysis (Kleinstreuer 2003). Squires and Eaton (1990a) suggest that two major problems associated with turbulent two-phase flows are the dispersion of the particles by turbulence and the resulting modification of the turbulence properties by particles. In agreement with this, Elghobashi (1994) in his study on gas-particle flows, categorised particle-laden turbulent flow into three distinct flow regimes (one-way, two-way and four-way coupling) based on the particle volume fraction, ϕ_p

$$\phi_p = NV_p/V \qquad\qquad 2.1$$

where N is the number of particles; V_p is the volume of a single particle and V the volume occupied by the particles and fluid.

Their work described the flow regime classification by using the illustration in Figure 2.1 below.
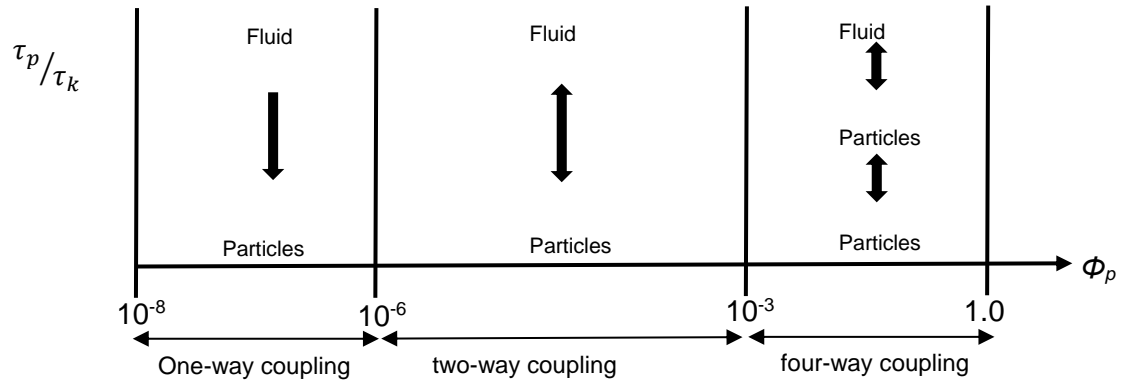
Figure 2.1. Map of flow regimes between turbulence and particle interactions (Elghobashi 1994)

Here, the vertical coordinate (τ_p/τ_k) is a function representing the particle response time, τ_p, to the Kolmogorov time scale, $\tau_k = (v/\varepsilon)^{1/2}$. v is the kinematic viscosity and ε the dissipation rate of the turbulence kinetic energy.

According to the chart, at very low volume fraction $(\phi_p \leq 10^{-6})$, particle-particle interactions becomes minimal and provides negligible contributions to the flow field structure. In such systems, the flow regime is described to be one-way coupled or dilute (collision free). In this instance, the dynamics of the particle is solely dictated by the fluid phase and has no significant impact on the turbulent flow due to negligible particle concentration. In one-way coupling flows, particles stay far apart such that there are no particle-particle collisions and fluid flow behaves as though no particle is present.

For a flow regime where the particle volume fraction is of the range $10^{-6} < \phi_p < 10^{-3}$ the flow is considered a dilute two-way coupled flow. the entire fluid flow field is influenced by the particles as the momentum transfer from the particle cloud becomes large enough to modify the structure of the fluid velocity field. Similar considerations apply to other transport processes, such as heat and mass transfer, when applicable. The structure of the fluid turbulence is also modified in this regime.

The third flow regime described as four-way coupling is a dense suspension flow which occurs at volume fraction, $\phi_p \geq 10^{-3}$. Due to the high particle concentration in these flows, particle-particle interactions and particle-turbulence interactions (two-

way coupling) are experienced; hence, particle collision and agglomeration becomes important and cannot be ignored (Elghobashi and Abou-Arab, 1984). The motion of the particle is dependent to a large extent on these interactions. The fluid turbulence under this flow regime is modified by the particle presence, which becomes increasingly visible with an increase in time. The turbulence could either be augmented or attenuated, depending on a number of factors, including particle size, shape, fluid-particle relative density and the motion of the particles in the fluid (Gore and Crowe, 1989; Lee and Durst, 1982; Rogers and Eaton, 1989; Squires and Eaton, 1990a; Tsuji and Morikawa, 1982). Crowe (2000); Gore and Crowe (1989) also identified that the fluid is influenced by the particles through the generation of wakes, stream line distortion due to particle presence, modification of the fluid velocity gradients and turbulence generation or damping due to the effect of drag forces on the particles.

Hetsroni (1989) showed that the modification can also be dependent on the Reynolds number of the particle to that of the fluid, which meant that high Reynolds number will increase turbulence and low Reynolds number will suppress turbulence. This can have significant impact on industrial processes in terms of flow rates, efficiency, energy conversion etc.; therefore leading to the increase research interest in the subject of dispersed phase turbulence and evident from the work of various researchers including; Tsuji, Morikawa et al. (1984); Sato and Hishida (1996) and so on. Sato and Hishida (1996) investigated particle-turbulence interactions in a solid-liquid channel flow both numerically and experimentally. Results generated shows that for particle size greater than the Kolmogorov length scale, the turbulence energy in the streamwise direction was augmented. Squires and Eaton (1990a) showed that for a one-way coupled turbulence field, light particles will collect preferentially in regions of high strain rate and low vorticity and will attenuate the turbulence when mass loading is increased sufficiently. The mass loading, M_p, is defined as $M_p = \alpha_p \rho_p / \alpha_f \rho_f$. Here ρ is density, α is volume fraction and the subscripts p and f denote the particle and fluid phases respectively. The experimental and numerical studies regarding two-phase flows will be explored in detail as the work progresses.

Finally, as the volume fraction approaches unity ($\phi_p = 1$) in the extreme limit of very high particle concentration, a granular flow in which no fluid is present is encountered. In this flow regime, the effect of the interstitial fluid becomes less significant as the inter-particle collision becomes the dominant mechanism. However, analysis on this

flow regime is beyond the scope of this work. In this study, the flow regime is considered four-way coupled since the particle volume fraction (10^{-3}) ensures that the average distance between particles is close enough to result in collision and agglomeration. It also worthy of note that, as water is used as the carrier phase in this study, the classification by Elghobashi regarding two-way coupling does not apply, as the dispersed-to-continuous phase density ratio is of order unity, so at volume fractions of order 10^{-3} the mass loading is too low for two-way coupling effects to be significant.

2.3 Experimental Methods for Measuring Two-phase Flows

In this section, a general description of available experimental techniques employed over the years for the investigation of turbulent two-phase flows is reported. Among several techniques, measuring approaches based on the photographic method have gained significant popularity in the experimental two-phase flow measurement. Some of these include; Laser Doppler Anemometry, LDA (also known as Laser Doppler-Velocimetry, LDV), Phase Doppler Anemometry, PDA, Ultrasonic Doppler Velocity Profiling, UDVP, Particle Image Velocimetry, PIV and Holographic Particle Image Velocimetry, HPIV technique. However, the photographic method is mainly suitable for the measurement of the particle velocity and concentration distribution but lacks accuracy due to the difficulty experienced when measuring the fluid phase. The fluid phase measurement is generally known to be more challenging due to constant interference arising from the particle phase.

The LDA is a laser-based technique for measuring two-phase flows. In this method, fluid velocities are obtained through the introduction of fine tracer particles into the flow field. Tracer particles due to their fine size tend to follow the fluid motion and therefore adopts the velocity of the fluid. Bearing this in mind, it becomes easier to obtain the fluid velocity using this principle by first calculating the velocity of tracer particles. This is done by detecting reflection signals from luminous particles using light scattering procedures. The light is set at a known frequency, which enables light scattering to be detected and collected through the use of a photomultiplier tube. As particles flow through, incident and scattered light reflections are picked up by a photo-detector sensor from which the Doppler shift between the scattered and incident light is calculated. In the LDA technique, Doppler shift between scattered and incident light is dependent on the size of the particles as larger particles will

scatter more light and yield a stronger signal reflection. Therefore, calculating the particle phase becomes straightforward as the Doppler shift produced by the larger and tracer particles becomes distinctively clear. When compared to other photographic technique the LDA is relatively expensive but has grown in popularity due to the fact that it does not intrude during fluid flow (Tsuji and Morikawa, 1982). However, the LDA measurements is obtained at a single point, meaning it is unable to sufficiently capture the spatial structure of a flow field, which becomes a major limitation.

Some of the studies where this technique has been extensively employed include Melling et al. (1976) Tsuji et al. (1984) who measured air-solid two-phase flows in vertical pipe; Kulick et al. (1994) where the interaction of small dense particles with fluid turbulence was studied for downward channel flow. Vassallo and Kumar (1999) who measured simultaneously the liquid and gas velocity in an air-water two-phase flow in a vertical duct; Yang and Kuan (2006) who used LDA in the investigation of two-phase flows in a 90° bend. The reader is referred to the work of Durst and Zaré (1976); Melling et al. (1976) for more information on LDA.

The PDA is an extension of the LDA technique for measuring two-phase flows. This single point measuring system functions by observing the Doppler shift in phase between signals of light detected from the LDA, which makes it possible to measure the size, concentration and velocity of spherical particles and droplets suspended in two-phase flow systems. Some of the experiments where this method has been applied include the study of Van de Wall and Soo (1997) who measured the properties of gas-solid suspensions using the PDA. Brenn et al. (2002) also performed investigations on water-bubble two-phase flow using this technique. More information on PDA is found in Bauckhage (1988).

The UDVP is another technique employed for two-phase flow measurement. In this method, the instantaneous fluid velocity profile is calculated by detecting the Doppler shift frequency in the echo of ultrasounds as a function of time. It works by transmitting an ultrasonic pulse which interferes with seeding particles. The frequency of the echoed signal then experiences a Doppler shift, from which the received signal is filtered to eliminate unwanted noise and then compared to the initial frequency transmission. The fluid velocity profile along the measurement axis can

then be obtained by measuring along a specified distance and angle. Early studies using this method include those performed by Takeda (1986, 1987). More recent studies where this method has been successfully applied include those performed by Ouriev and Windhab (2002); Yamanaka et al. (2002).

The PIV is a more recent technique and has largely superseded the use of LDA for measuring two-phase flows. It is an optical method employed for the visualisation of fluid properties such as the instantaneous fluid velocity. In PIV, the fluid dynamics is made visible through the seeding of small tracer particles in the flow. For sufficiently small tracer particles, the fluid profile is inferred from the particle motions since tracer particles will completely follow the fluid motion. In order for the particles to be visualised, a double-pulsed light sheet of high intensity is used to illuminate a plane in the flow field which makes it possible to measure the particle position and velocity. Due to the short duration of each pulse in PIV, the motion of the particle is frozen so a double exposure photograph of the particle can be obtained. Between time intervals of the particle displacement measurement and the pulses, two components of the instantaneous velocity vector are measured. The images of the tracer particles incident to the light sheet is recorded by video (or photographically). The PIV technique according to researchers has proven to be more efficient in terms of particle measurements in two-phase flows when compared to others. This is due to its ability to measure simultaneously over an imaged area the velocity of both phases. Experimental studies involving PIV includes Adrian (1984, 1991); Liu et al. (1991) and, more recently, Li et al., (2016) and Jain (2017). Further information concerning the PIV method is found in Westerweel (1997).

The HPIV is an extension to the classic two-dimensional PIV technique, which is known for the recording of double exposure images of small tracer particles in a flow field. In this method, the local velocities are obtained by measuring the displacement of the particles and recording over an entire volume sample the instantaneous three-dimensional velocity distribution. More details on experimental investigations using the HPIV technique can be found in Zhang et al. (1997).

Finally, to conclude on this section it is worthy of note that other experimental techniques for measuring single- and two-phase flows exists, although only a few have been discussed herein. Experimental investigations have been very useful in

providing relevant data for validating numerical models employed in fluid dynamics, except that they are less efficient for carrier phase measurement due to challenges arising from particle interference. For instance, laser-based methods struggle with differentiating between tracer particles and the dispersed particle phase. They also have reduced application because of the optimal operational conditions required for obtaining accurate measurements and the precise nature of the instrument set-up. The challenges encountered in these experimental investigations meant that a more accurate approach for characterising the behaviour of these flows was necessary for improving the general understanding. Combining experimental and numerical approach over the years by researchers has provided clarity on some of the complex areas of fluid dynamics and therefore a useful approach to improve understanding of these flows.

2.4 Numerical Methods for Predicting the Two-phase Flows

This section provides a review of the available computational methods for modelling and resolving the fluid phase of turbulent fluid flows, which can also be extended for two-phase flow predictions. The most preferred techniques for predicting the fluid phase are known for their implementation and integration of the full time-dependent Navier-Stokes equations of motion. Bird et al. (1960) provides more information on the Navier-Stokes equations of motion, including their derivation and applications. For the fluid phase prediction, in an order of decreasing accuracy and computational cost, the three main techniques (direct numerical Simulation, DNS; large eddy simulation, LES; and Reynolds-averaged Navier-Stokes, RANS techniques) applied in predicting the continuous phase are discussed and then followed by other available fluid modelling techniques. It is important to note that amongst other techniques for computing multiphase flows, the DNS, LES and RANS techniques hold specific relevance to this work because they solve for the full time-dependent Navier-Stokes equation during computation.

2.4.1 Direct Numerical Simulation Method

The DNS method is the most accurate model of turbulence available, with the ability to resolve turbulent length and time scales without any ad hoc modelling. Among other methods, it gives the most promising capability in terms of reproducing turbulent features even to the smallest Kolmogorov scale (Tian and Ahmadi, 2007). The DNS

at any point in the flow predicts turbulent fluctuations with precise accuracy since all turbulent parameters and their transport budget are accounted for during computation. For this reason, Moin and Mahesh (1998) describe it as a tool in turbulence research since it complements experiment based researches and provides instantaneous results that may otherwise not be measurable through experimental methodology or by any other technique. This is because it solves completely the instantaneous three-dimensional Navier-Stokes equations of motion for turbulent fluid flows. Results obtained from this technique provide detailed time-dependent, three-dimensional information due to the high resolution of the solution meshes. However, the high resolution required by the DNS makes it very computationally expensive to run and time-consuming. Based on this, the DNS is often restricted to simple geometry flows of relatively low Reynolds numbers and therefore not attractive for most engineering and industrial flow simulation processes (Mallouppas et al., 2013; McLaughlin, 1989a). However, technological advancement over time in the development of more efficient algorithms has enabled the DNS to be applied in the prediction of flows at much higher Reynolds numbers than previously known. This is believed to even get better with future computational advancement. The reader is referred to the study by Moin and Mahesh (1998) for more information on the DNS.

The DNS has also been implemented by numerous researchers to perform investigations on turbulent two-phase flows. Some notable examples which will be explored in a later section of this study include those of Squires and Eaton (1990), Elghobashi and Truesdell (1993), Truesdell and Elghobashi (1994) and more recently Balachandar and Eaton (2010), Borrell et al., 2013, El Khoury et al., 2013; Graham et al., 2013), Chin et al. (2014), Lee and Moser (2015), Zhang et al. (2015) and Marchioli (2017).

2.4.2 Large Eddy Simulation Method

Large eddy simulation is a computational fluid dynamics tool which combines fluid resolution procedures with numerical modelling approaches to provide a compromise between computational accuracy and simulation run-time cost. In this modelling method, the large energetic turbulent eddies are computed by solving directly the filtered time-dependent Navier-Stokes equations during the flow simulation; whilst smaller and less energetic eddies are assumed homogeneous and modelled. The LES employs a filtering operation to decompose and separate less turbulent eddies

from the larger and more energetic ones. With the use of a specified cut-off width and filtering function, the LES is able to resolve the most energetic length scales which would normally be greater than the cut-off width and resort to modelling the smaller eddies below the cut-off width (sub-grid scale, SGS). This way, the LES provides a less computationally expensive approach to turbulent flow modelling when compared to the DNS, as the fine resolution mesh required to completely capture and resolve the much smaller eddies is no longer required. With the use of a coarser mesh, it becomes possible for the LES to be applied in flows with much higher Reynolds numbers.

One major consideration of the LES is in the ability to effectively model the small-scale turbulence also referred to as the sub-grid scale, SGS in turbulent flows. Different SGS modelling approach exists for this but the eddy viscosity model as proposed by Smagorinsky (1963) and modified by Lilly (1967) remains one of the most commonly used SGS models. It functions by incorporating an eddy viscosity which models three-dimensional turbulence through the use of a relatively accurate Kolmogorov $k^{-5/3}$ cascade in the sub-grid scales. Through the study carried out by Deardorff (1970), the technique was made applicable to industrial related flows. The Smagorinsky model is however limited since is can be very dissipative in areas close to the wall, which makes it less accurate in predicting boundary layer transitions on a flat plate for flows initially laminar (Lesieur and Metais, 1996). However, this model remains a valid tool for SGS modelling and has been improved over years through the studies performed by various researchers. Schumann (1975) proposed a kinetic energy model which uses an additional scalar transport equation for the SGS kinetic energy calculation. In the study by Kraichnan (1976) a model which adequately describes the decay of three-dimensional isotropic turbulence and provides fairly accurate predictions for mixing layers was introduced. In particular, the work suggested that the eddy viscosity should depend on a wave number magnitude based on spectral eddy viscosity in situations when the eddy viscosity reaction with different wave number is being considered. More importantly, a dynamic SGS model in which the turbulent stresses are decomposed differently to the Smagorinsky model was developed by Germano et al. (1991). Métais and Lesieur (1992) proposed the 'structure function model', a direct alternative to the Smagorinsky model, in which action of the spectral eddy viscosity was in physical space recreated. Vreman et al. (1997) provides a more in-depth review on the capabilities of the different SGS models. For further information on the LES the reader is directed to the studies in Lesieur and Metais (1996); Mason (1994) and Meneveau and Katz (2000).

2.4.3 Reynolds-Average Navier-Stokes Method

The Reynolds-averaged Navier-Stokes modelling approach which only solves the time-averaged equations of motion for turbulent flows is said to be the traditional approach to engineering modelling due to its ability to handle industrial scale flows and within reasonable computational costs. In this method, the equations are obtained through the decomposition of flow variables into mean and unsteady components, with only the average fluid quantities solved, and the resulting fluid turbulence effect on the average flow modelled using additional turbulence model. This way, detailed information on the instantaneous turbulence fluctuations are sacrificed, creating a number of unknown correlations which then triggers the need for a closure model in order to adequately account for the effect of the turbulence stresses generated in the flow field. Closing the RANS equation in turbulence modelling involves different levels of approximation depending on the computational model used. Speziale (1991) provides an extensive review of the various closure models, with each having different levels of complexity and accuracy. However, some of the models in increasing order of complexity include the algebraic (zero equation), k-ε (one- and two-equation) and the Reynolds Stress models, RSM; of which the k-ε two-equation model remains one of the most commonly applied turbulence models for solving practical engineering problems due to the low computational effort it requires.

Two-equation turbulence models: are the most commonly utilised Reynolds stress models for solving scientific and engineering problems. It is also the most preferred in most computational codes for single and two-phase flows (Crowe et al., 1996), with low computational cost when compared to other complex models. Unlike the preceding models, two-equation models only require the initial and boundary conditions to be specified in order to provide solutions to problems. For instance, the model would provide a closure to the unknown Reynolds stresses without any set requirement for the flow turbulent structures; hence, are regarded as the first simple and complete Reynolds stress model developed. Also, the main difference between this model and the zero- and one-equation models is that they solve two separate modelled transport equations to compute the turbulent length and time scales, either as a combination or independently. Most frequently, one model transport equation solves for the turbulent kinetic energy, K and the other for the turbulent energy dissipation rate, ε or the specific dissipation, ω. A specific example of the two-

equation turbulence models is the $k - \varepsilon$ model which is based on the turbulent energy dissipation rate. This version which was initially proposed by Jones and Launder (1972) and improved by Launder and Spalding (1974) is better utilized for industrial and scientific calculations. Other examples of the two-equation turbulence model include the $k - l$ model of Mellor and Herring (1973), which is based on the solving a modelled transport equation for the integral length scale; and the $k - \omega$ model of Wilcox (1988), which is based on solving a modelled transport equation for the reciprocating time scale. The drawback of the two-equation model is its inaccuracy in predicting the normal Reynolds stresses, which consequently leads to poor performance in predictions involving recirculation and secondary flows (Speziale, 1987).

Studies using this model include that of Jones and Launder (1973) who presented predictions of numerous turbulent shear flows where the flow is being influenced by the structure of the viscous sub-layer for low Reynolds number pipe flows. Cheng et al. (2003) used the model for computing a fully developed turbulent flow over a matrix of cubes in a channel. The authors made comparisons with other numerical models and also the experimental data of Meinders and Hanjalić (1999). Other researches using the model include Naik and Bryden (1999), and Mohanarangam and Tu (2007) amongst others.

Reynolds stress model approach: also known as the second-moment or second-order closure model is also widely used in engineering and industrial applications due to the nature of the complexity of the flow geometries encountered in these industries; were flow Reynolds numbers are higher than those accessible to direct simulations (Piomelli et al., 1990). It is based on the Reynolds stress transport equation which is solved for each second moments of the turbulence. The model is a notable improvement from previous turbulence models as the unknown higher-order terms in the transport equations for each of the turbulent stresses are directly modelled.

It was in the landmark study by Rotta (1951) that the foundation for closing a full Reynolds stress turbulence was laid, which ultimately changed the course of Reynolds stress modelling. However, this had limitations in its application to turbulent flow since it was not feasible to solve the additional transport equations required for each component of the Reynolds stress tensor due to low computing capabilities at

the time. With the advancement of high-speed computing in the 1970s, there was a renewed push towards developing and implementing the second-order closure model (Daly and Harlow, 1970; Donaldson, 1972). A further improvement on the earlier work of Rotta (1951) was made by Launder et al. (1975) demonstrating that it was possible to calibrate and apply the second-moment closure models to solving practical turbulent flows by deriving more systematic models for the pressure-strain correlation and turbulent transport terms. Subsequently, there have been several attempts by research modellers to improve on the second-order closures including those by Lumley (1979) who made a significant improvement in modelling the pressure-strain correlation and buoyancy effects. Haworth and Pope (1987) using a pdf-based Langevin equation developed a model for the second-order closure. An advantage of second-moment turbulence closures is that they enable a precise and accurate calculation of the mean flow properties and Reynolds stresses across many simple and complex flow geometries. However, the substantially high computational effort required to resolve the additional transport equations for the components of the Reynolds stress tensor makes the model less attractive for many engineering applications when compared to the two-equation models. For a further review on the development of the second-moment turbulence closure models, the reader is referred to Speziale (1991).

2.4.4 Other Methods for Fluid Phase Prediction

These include detached eddy simulation, coherent vortex simulation, discrete vortex method, vorticity confinement method and the linear eddy model.

The Detached Eddy Simulation (DES): proposed by Spalart (2009) is generally a modification of the RANS model and tends to combine other methodologies (LES and RANS) during predictions. Travin et al. (2000) defined it as "a three-dimensional unsteady numerical solution using a single turbulence model which functions as a subgrid-scale model in regions where the grid density is fine enough for an LES, and as a RANS model in regions where it is not" This technique was created in a quest to solve the difficulties associated with the LES around the wall regions of a flow system. This approach is also classified as hybrid due to its ability to treat near-wall turbulent regions by RANS technique and then the rest of the flow using the LES technique (Spalart, 2009). Viswanathan and Tafti (2006) applied the DES technique to evaluate hydrodynamic and thermally developed turbulent flow in a stationary duct

with square ribs. Result obtained showed good agreement with LES and experimental data gathered.

The Coherent Vortex Simulation: technique is a semi-deterministic model aimed at computing fully developed turbulent flows. Its approach is based on decomposing turbulent flow fields into coherent and random incoherent vortices by the use of wavelet filtering. Wavelet coefficients of the vorticity field are used to reconstruct the coherent and incoherent velocity fields (Farge et al., 2001). This technique resolves only filtered portion of the flow by using linear low pass filters (does not adapt to flow evolution).

Vortex method: is a grid-free technique which uses vortices as elements for computing in cases were the vorticity field is non-zero, therefore eliminating a bunch of iterations. The method is based on vorticity field discretization as well as the Lagrangian interpretation of governing equations which determines the evolvement of the computational elements. One main feature of the vortex method is that it simulates both the large and small scales accurately at the same time. An advantage of applying the vortex method in the study of two-phase flows is its ability to incorporate the instantaneous velocity field in the study of the particle motion, instead of the time-averaged flows. Therefore, a large number of particles can be introduced into the flow and their trajectories mapped. Chein and Chung (1988) applied the discrete vortex method in the simulation of particle dispersion in a two-dimensional mixing layer which is dominated by large-scale structures. Results obtained from the simulation showed that particle dispersion extent is strongly dependent on the particle Stokes number. This was in good agreement with data from a previous experimental study. The previous study using the vortex method includes studies on gas-particle flows over a cylinder (Acton, 1980; Inoue, 1985; Laitone, 1981; Leonard, 1980). Kerstein (1989, 1991); McMurtry et al. (1993) combined the Linear Eddy Model with the LES and used to predict the unresolved turbulence effects on a flame structure and concluded that the combined method is well suited for premixed flame combustion modelling.

The Vorticity Confinement method is an Eulerian technique suitable for incompressible flows with high Reynolds number. The main aim is to capture essential features like vortex filaments which have the tendency to convect through

long distances, without spreading significantly. Small wakes are then modelled efficiently on an Eulerian computational grid. Wenren et al. (2003) reviewed the application of the vorticity confinement methodology in predicting flows over complex bodies as well as solving over a long time, convecting concentrated vortices without any numerical spreading. A major advantage of this model is that it provides predictions with good resolutions across wide ranges of flow conditions.

For the particle phase, there are numerous computational techniques available for predicting dispersion in a two-phase turbulent flow. Prominent examples are the Eulerian or two-fluid approach and the Lagrangian or discrete methods. Other models include the local homogenous flow and Probability Density Function Propagation (PDF) models. In the two-fluid model (Eulerian approach), both dispersed and continuous phases are considered to exist as a continuous media since the characteristics of the particles are defined at the computational nodes that match with the nodes of the continuous phase; which therefore requires for each phase sets of coupled differential equations (Abbas et al., 1981; Curtis and Van Wachem, 2004; Elghobashi et al., 1984; Lu et al., 1993; Reeks, 1977). The application of the same Eulerian treatment to both phases in this method enables the particulate phase to be treated using the same discretisation and numerical solution approach as the continuous phase. This type of treatment is widely referred to as Eulerian-Eulerian (E-E) approach and is mostly suited for dense particle-laden flows were particles are in very close proximities such that the particulate phase is regarded as a continuum within the fluid phase (Durst et al., 1984). A positive about this method is that it accounts for the relative velocity and temperature difference of the fluid-particle inter-phase based on a point volume description of the particles. However, the drawback of this method is in its inability to adequately treat different particle sizes without a considerable increase in computational effort. This is because a transport equation would be required each per particle size and subsequently, discretization and linearization; hence the cost of computation would increase as the number of particle sizes increase. The reader is referred to the work done by Enwald et al. (1996) for a detailed review of two-phase turbulent flow using the Eulerian approach.

Notable researches involving the application of the two-fluid approach includes Elghobashi and Abou-Arab (1983) whose contribution involved developing a two-fluid turbulence model for predicting two-phase flows using this method; Druzhinin and Elghobashi (1998) using the two-fluid formulation conducted a DNS study on bubble-

laden turbulent flows. In an extension of their work, Druzhinin and Elghobashi (1999) performed an investigation on the decay rate of isotropic turbulence for flows laden with micro-particles.

2.4.5 Lagrangian Particle Tracking (LPT)

The LPT or discrete particle method is a particle tracking algorithm useful for determining the particle trajectories at any given instant within the flow field. In this method, individual particle movements, are tracked through the flow field by solving the particle equation of motion with the full consideration of the relevant forces acting on the particle. The bulk properties of the particulate phase are then derived by averaging statistically over a large number of the particles. The advantage of using this method is that there are no global assumptions on the particle characteristics within the flow field.

It also has the ability to alter the physical properties (e.g. density or size) of individual particles. But, its main disadvantage is the large computational effort needed in tracking huge numbers of particles (Curtis and Van Wachem, 2004). It can be problematic and very difficult to compute if the volume of the particle is larger than the averaging volume of the fluid (Loth, 2000). However, with the advancement of high-performance computing, the LPT has gained popularity in the investigation of particulate behaviours in turbulent two-phase flows. Increased computing capabilities have also enabled researchers to model the effect of surrounding forces on the particles by incorporating additional force terms to the particle equation of motion which is then applied in the LPT. Significant forces which have been studied in recent times include the added mass, pressure gradient, basset history, Saffman and Magnus lifts, and more importantly the particle-fluid drag force (Li et al., 1999; Potic et al., 2005; Xiong et al., 2005). The pressure gradient force takes into account the buoyancy and the acceleration pressure gradient within the fluid flow, which involves the basset history force (not considered) and added mass force. The added mass which is sometimes referred to as the apparent or virtual mass force is the inertia added in other to accelerate the surrounding fluid (Clift et al., 1978). However, in certain conditions, the added mass force term tend to be negligible, particularly for flows with low fluid-particle density ratio (Hjelmfelt and Mockros, 1966). The Magnus lift force is an attribute of the particle rotation. Saffman lift force occurs as a result of the velocity gradient and pressure difference during particle movement. The lift force is a resulting effect of particle rotation which creates a velocity gradient that

eventually leads to the development of a pressure gradient on the particle surface. The drag or friction force is a resistance force which acts opposite to the relative motion of the particles with respect to its surrounding fluid.

When the Eulerian approach is coupled with the Lagrangian approach, the approach becomes the Eulerian-Lagrangian approach (E-L) and solves the continuous fluid phase, where the instantaneous velocities are obtained directly. However, when coupling the LPT and RANS technique it becomes necessary to incorporate an additional model to recreate the instantaneous velocities of the fluid which is lost during the Reynolds averaging procedure. Crowe et al. (1996) provide an extensive account of the various LPT techniques available but in an earlier study (Crowe et al, 1977) was where one of the earliest Lagrangian models, where the particle field could now be represented by the particle trajectories was developed. This was derived through the integration of the particle equation of motion, in which the particle velocity, mass and temperature were concurrently solved along the trajectories. However, the approach did not account for the dispersion of particles due to turbulent velocity fluctuations but instead accounted for particle dispersion due to only the mean flow.

In this work, the E-L approach is used to model the transport process of the particle as it accurately simulates particle trajectories. Further information on the numerical models coupled with the Lagrangian particle tracking technique for two-phase flow predictions can be found in Crowe et al. (1996).

2.4.6 Probability Density Function Propagation Models

Probability density function (PDF) propagation models are based on solving the instantaneous spatial dispersion of particles in fluid flows. In the PDF method, it is not a requirement to compute large amounts of particle trajectories which makes them to be considered efficient. In Pope (1985), the use of evolution equations for PDF's in calculating the properties of turbulent reactive flows was originally described. A group of particles having the same initial conditions and physical properties are represented by a single PDF in this model. This way, it becomes possible to derive information on the particle statistics, although the properties of the Lagrangian particle is still required for the use of Taylor's theory. In the study of Derevich (2000) the PDF model was developed and applied in investigating the mass

transfer of the particle phase in a turbulent two-phase vertical pipe flow. Further information concerning reviews and the application of the PDF models can be found in Minier and Peirano (2001).

2.4.7 Local Homogeneous Flow

The local homogeneous flow (LHF) model is an Eulerian approach that is based on the assumption that the continuous phase and the dispersed phase are both in local thermal and kinetic equilibrium. This way the numerical procedure is simplified and eliminates the assumptions of dilution as well as the equations used in the characterisation of the inter-phase rates of mass, momentum and energy transfer. For two-phase flows, the model is based on approximations which imply that the velocities of both phases are equal and in thermodynamic equilibrium at each point within the flow (Mao et al., 1980), meaning the temperature of both phases are equal and that phase equilibrium is constantly maintained. This modelling technique was employed in the evaluation of spray combustion in Mao et al. (1980) and extended to investigating turbulent bubbly jet flows in Sun and Faeth (1986). However, the LHF approach is a simplified model and not understood to be as accurate as other more complex and robust models available. In the study Faeth (1987), errors as large as 50% were reported to be found in the LHF modelling approach when compared to experimental results obtained for particle concentration and velocity. Further information on the LHF model can be obtained in Faeth (1987).

2.4.8 Remarks on the Computational Methods

From the computational methods reviewed for the fluid phase, it is reasonable to conclude that the DNS approach is the most accurate as it solves directly the instantaneous three-dimensional Navier-Stokes equations without resorting to any turbulence modelling; although it is largely restricted in application due the high cost of computation required. It is also clear that the two-equation and second-order closure RANS models, although deficient in accuracy when compared with DNS and RANS, are most commonly applied in resolving industrial flows due to the relatively low computational effort involved. However, the LES is preferred in this study since it is computationally balanced in terms of cost and speed relative to RANS and DNS. Specifically, its ability to accommodate high Reynolds number with the relatively low computational effort required makes it preferred over the DNS. Also, it is preferred over the RANS method since it provides more accurate predictions.

For the particle phase, considering the methods reviewed herein, the LPT approach is advantageous when compared to other methods for predicting the particle phase and can be attributed to a number of reasons. Firstly the LPT unlike the rest is able to measure and track the trajectories of individual particles, which therefore produces detailed information on the physics of the flow. Furthermore, with the inclusion of appropriate models the LPT allows for studies concerning particle-turbulence and particle-particle interactions, which gives it an edge over the two-fluid approach, were the particle phase is treated as a continuum within the fluid phase due to their close proximity. With the advancement in computational capabilities, it is now even possible for the LPT to be applied in dense particle systems which makes it best suited for this research work where events concerning particle collision, agglomeration and their resulting effects on the fluid turbulence is of interest and will be extensively studied .

2.5 Review of Experimental Studies in Channels, Pipes and Ducts

A number of experimental investigations concerning fully developed flows have been conducted over the years on turbulent fluid flows in channels, pipes and ducts. This is mainly due to the simplicity of the flow geometry, which makes it attractive for both numerical and theoretical investigations of complex flow behaviours around the wall regions of wall-bounded flows. Some of these experiments have focused on measuring the Reynolds stresses and average velocity of the continuous phase. While others included the measurement of the particle statistics, including the concentration, mean and root-mean-square velocities of the particles (Balachandar and Eaton, 2010).

2.5.1 Experimental Studies of Single- and Two-Phase Flows in Channels

The simplicity of the channel flow geometry makes it one of the most frequently used flow geometries employed by researchers for measuring both single and two-phase turbulent flows. Notable examples date back to the study by Nikuradse (1929) who was among the first to study a fully developed channel flow. However, his work was limited to mean flow measurements only. Reichardt (1938) however, reported velocity fluctuations along the streamwise and wall-normal directions of a turbulent channel flow but it was not until the study of Laufer (1951) that a detailed turbulent

statistics, based on the effect of Reynolds number on the inner-scaling of turbulence intensity in the streamwise direction was documented. The statistics presented measurements on Reynolds numbers 12300, 30800 and 61600, based on the channel half-width and the mean centerline velocity. Unfortunately, results lack accuracy as the peak value of turbulent intensity appeared to decrease with increase in Reynolds number, owing to decreasing resolution of the hot-wire probe used. Similar conclusion was reached in (Alfredsson and Johansson, 1984); Johansson and Alfredsson (1982) who used hot-film probe to study the effect of Reynolds number on the inner scaling of turbulent fluctuation in water channel flows of Re range, 6900 to 244500 but just like the study in Laufer (1951), lacked accuracy (Wei and Willmarth, 1989). This was further extended in Comte-Bellot (1963) to account for high-order statistics like energy spectra, two-point correlations, skewness and flatness factors. The measurements reported were for a Reynolds number ranging between $15\,000$ to $45\,600$ but was also deficient in accuracy. Patel and Head (1968) by using hot-wire approach measured the skin-friction and average velocity profiles in a flow with low bulk Reynolds number range $(1000 - 10000)$, covering the transition from laminar to turbulent flow regime. Their result showed a burst of turbulence at an approximate Re_b of 1380.

The study on turbulent structures in channel flows continued developing through pioneering research investigations like that of Clark (1968) whose work was based on studying the boundary layers of incompressible turbulent channel flows. Hussain and Reynolds (1975) then used an extremely long two-dimensional channel in their experiment in order to establish that the state of the high-order turbulent statistics reached full development. Other investigations performed by Kreplin and Eckelmann (1979); Wallace et al. (1972) were based on turbulent structures around the near wall regions of a channel flow. Wei and Willmarth (1989) who through the use of the LDV method performed an extensive investigation on the streamwise and wall-normal turbulent fluctuations at bulk Reynolds number ranging between 30000 to 40000. The main conclusion of the study was that the streamwise Reynolds normal stress in the buffer layer increased with Reynolds number through the duration of the study. This was in contrast to previous investigations which lacked insufficient spatial resolutions, showing the opposite and more acceptable trend. The findings were later validated after showing good agreements with DNS (Hoyas and Jiménez, 2006) and experimental (Ng et al., 2011) investigations.

Years later, Zanoun et al. (2009) challenged the accuracy of skin-friction measurements in turbulent channel flows, by using the mean streamwise pressure gradient and oil film interferometry methods to provide an estimate on the wall skin-friction relation, $c_f = f(Re_m)$ for a fully developed turbulent channel flow. The work allowed measurements at higher Reynolds numbers than previously possible while maintaining sufficiently high spatial resolution. Schultz and Flack (2013) using a High Reynolds Number channel flow facility, performed an experiment based on Reynolds number scaling in a smooth-wall, fully developed, turbulent channel flow. The work examined the scaling of quantities like the mean flow, Reynolds stresses and skin friction with Reynolds numbers flows, based on the channel height and bulk mean velocity (10 000 to 300 000). The results were quantitatively in agreement with results from experimental and boundary layer flows.

For two-phase flows, one of the earliest work was in the investigation of Matsumoto and Saito (1970) where the behaviours of large copper and glass beads of mass loading, 0.5, were studied in a narrow and long horizontal channel. The study used a cinematographic photographic technique to measure the collision and concentration distribution of the particles. Results reported for different flow conditions showed a considerable increase in migration of particles towards the lower wall regions of the channel due to the influence of gravity on the flow. Burmester De Bessa Ribas et al. (1980) performed an experiment on a two-phase flow in which glass beads of diameter $0.5\ mm$ with varying mass loadings were measured in a gas flow, using a rectangular horizontal channel. The main aim of the study was to validate predictions based on the Monte Carlo kinetic model. The results showed the effect of particle size, velocity and mass loading on the vertical distribution of the particles as well as the effect of two-way coupling.

Kulick, Fessler et al. (1994) analysed experimentally particle response to turbulence and their effect on turbulent modulations in fully developed $40\ mm$ high channel flows using a centreline gas velocity of approximately $10.5\ m/s$ and a channel length of about 130 channel heights. Using the LDA technique, different mass loadings of small spherical copper beads were measured and analysed. Their work revealed attenuation of turbulence by particles. The experiment similar to Kulick, Fessler et al. (1994) investigated a fully developed particle in downwards channel flow. The study used the LDA to measure the fluid and particle velocities using glass beads of size $50\ \mu m$ and $90\ \mu m$ and spherical copper beads of $70\ \mu m$ in air. The study was aimed

at understanding the influence of particle sizes on the flow dynamics. Their results indicate that particle attenuates turbulence with an increase in the size, mass loading and distance from the wall. Kussin and Sommerfeld (2002) extended this study by accounting for the wall roughness in a horizontal flow where parameters like the particle velocity, mass loading and conveying velocity was varied. The measurements were based on the PDA technique and used spherical glass beads of range $60\,\mu m$ to $1\,mm$. The study demonstrated that with the inclusion of wall roughness, the particles influenced turbulence modulation. This is attributed to the increased slip velocity between the enhanced momentum transfer and the phases. Laín et al. (2002), studied experimentally four-way coupled particle-laden flows in a horizontal channel. Their experiment involved the measurement of different particle sizes and loading ratios, using a phase-Doppler anemometry method. The particles used in the experiment were spherical glass beads with varying mean diameter. Results observed showed that experimental measurements using the PDA coupled with other models like the Reynold stress turbulent model, is appropriate in predicting the behaviour of turbulent particle-laden gas flows in channels. Fairly recently, Li et al. (2012) investigated turbulence modulation in the near wall boundary layer of a one-way coupled channel flow. The measurements were done using a two-phase Particle Image Velocimetry, PIV technique. They reached a similar conclusion as that of Kulick et al. (1994), stating that the addition of particles (Polythene beads) noticeably modifies the turbulence intensity and the turbulence structure as well as the mean velocity of the gas phase. Prior to this, using the same technique, an experiment conducted by Sato and Hishida (1996) on the interactions between the dispersed phase and the fluid turbulence in a fully developed particle-laden turbulent channel flow showed a similar conclusions for particle size $340\,\mu m$ and $500\,\mu m$ glass beads and $420\,\mu m$ cellulose particles.

2.5.2 Experimental Studies of Single- and Two-Phase Flows in Pipes

Numerous experimental investigations have been conducted on single-phase turbulent pipe flows over the years, during which the flow parameters are varied, depending on the area of interest. In this section, the review is focused on notable experiments on turbulent single phase flows which are particularly relevant to this study.

Early research on turbulent single-phase flows includes the pioneering work by Laufer (1954) who, according to the author's knowledge, was the first to comprehensively investigate the turbulence structure of a fully developed pipe flow. The study used hot-wire anemometer technique to measure the relationship between turbulence and the mean velocity, with emphasis on the transfer, diffusion and the energy dissipation rates. The work however suffered criticism (Lawn, 1971) as inconsistencies in the measurements where identified. In earlier studies, Barbin and Jones (1963) reported measurements on turbulence intensities, Reynolds stresses and the mean velocities in the inlet region of a turbulent pipe flow with smooth walls at a Reynolds number of $388\,000$. The work reported discrepancies in the velocity profiles obtained at successive sections of the inlet region. Patel and Head (1969) using a similar technique as Laufer (1954) measured the skin-friction and mean velocity profiles in a fully developed pipe. Spectral measurements of turbulent momentum transfer were made by Bremhorst and Walker (1973) in a fully developed pipe flow, where more emphasis was made to the regions close to the pipe wall. Sabot and Comte-Bellot (1976) however, extended this work by providing a detailed understanding of the turbulent structures around the core regions of a fully developed wall-bounded flow.

Years later, Eggels et al. (1994) applied the HWA, PIV and LDA in studying a fully developed turbulent pipe flow at an approximate Re_b value of 7000, based on the centreline velocity. Results obtained were found to be in good agreement when compared against data from DNS simulations performed within the group. Matching conditions of the DNS in Eggels et al. (1993), Westerweel et al. (1996) measured a fully developed turbulent pipe flow using a digital PIV technique (DPIV) and found results to be in good agreements. Den Toonder and Nieuwstadt (1997) carried out a two-dimensional LDV measurements of water in a turbulent pipe for low to moderate Reynolds number of range $5000 - 25000$. The measurements provided proof of a clear Reynolds number dependence of the turbulence statistics which was scaled on the inner variables in turbulent pipe flow for the Reynolds numbers studied. Overall, results showed reasonable agreements with the DNS data of Eggels et al. (1994). Zagarola and Smits (1998) measured the mean velocity profile and pressure drop in a fully developed, smooth pipe flow. The authors developed a new theory to explain the scaling between overlap regions for the mean velocity profiles of flows with the Reynolds number range 31×10^{-3} to 35×10^{6}, although with some uncertainties. The uncertainties were due to the velocity gradient correlations applied but, however, showed good improvements in the studies of McKeon et al. (2003); McKeon and

Smits (2002) where corrections were made on the parameters used in the Pitot probe. Based on the experimental investigations in Zagarola and Smits (1998) and McKeon and Smits (2002), a new friction factor relationship was proposed for a fully developed pipe flow from investigations performed for the Reynolds number range 10 to 3.6×10^7 (McKeon et al., 2005; 2004). Große and Schröder (2008) used a micro-pillar wall-shear stress sensor to measure the dynamic wall shear stress in a well-defined fully developed turbulent pipe flow at bulk Reynolds number in the range $Re_b = 10000 \text{ to } 20000$. Results for the mean and dynamic wall shear stress were convincingly in agreements with experimental, analytical and numerical data obtained from the literature. More recently Monty and Chong (2009) measured the streamwise mean velocity and turbulence intensity using hot-wire measurements for a high Reynolds number flow. The results were compared against data obtained from a well-documented DNS flow and showed few discrepancies. For a more detailed information on the experimental investigations performed for single-phase pipe flows, the reader is referred to Hultmark et al. (2010) where further information on scaling of turbulence in the near wall regions of a fully developed pipe flow can also be obtained.

For two-phase flows in pipes, earliest experimental studies include the experimental work of Friedlander and Johnstone (1957), where the deposition of particles in suspension within a turbulent gas flow was investigated. The results from the studies concluded that the inertia effect of the turbulent eddies has the most dominant influence on particle movement. Experimental study on turbulent deposition rate of aerosol particles in a vertical pipe was conducted by Liu and Agarwal (1974) using a mono-dispersed aerosol generator with a particle diameter of the olive spherical droplets ranging from $1.4 \ \mu m - 21 \ \mu m$, and at Reynolds numbers 10000 and 50000. The authors argued that deposition rate of the particles are dependent on the dimensionless particle relaxation time, t^+. The work was further extended by McCoy and Hanratty (1977) for the measurement of droplets deposition rate in pipes. Similar studies on two-phase pipe flows during this time include those performed by Farmer et al. (1970); Ilori (1972); Liu and Agarwal (1974); Liu and Ilori (1974); Montgomery and Corn (1970); Postma and Schwendiman (1960); Wells and Chamberlain (1967); Yoder and Silverman (1967).

A decade on, Arnason and Stock (1984) measured the local dispersion coefficient of particles for turbulent pipe flows using the LDA technique at a Reynolds number

of 50000 based on centre line velocity. The results obtained for the flow properties compared well with the experimental data of Laufer (1954). Tsuji and Morikawa (1982) investigated turbulence modification across a $30 \, mm$ horizontal pipe by the use of LDV optical technique. The work used two types of plastic particles of mean diameters $3.4 \, mm$ and $0.2 \, mm$ each. They concluded in their experiment that turbulence level is dissipated by small particles and increased by large particles. In an extended work (Tsuji, Morikawa et al. 1984), using the same photographic technique, the authors conducted an the experiment on five types of plastic particles with varying particle sizes ranging from $3 \, mm$ to $200 \, \mu m$ in a vertical pipe two-phase flow and reached the same conclusion that small particles will suppress turbulence while larger ones generally attenuate it.

Years later, Caraman et al. (2003) using a two-component phase Doppler anemometer measured particle fluctuations and the effect of collisions in a fully developed dilute pipe flow at moderate Reynolds number. The study observed the effect of particle-particle collision has a negligible effect on the fluctuating velocity near the wall region but significantly influences particle fluctuation and redistribution. The study on inter-particle collision for a fully developed two-phase flow system was further extended in Borée and Caraman (2005) where a dilute bi-dispersed pipe flow was investigated. Li et al. (2013) studied particle deposition patterns in a $180°$ pipe bend under different inlet velocities and particle concentrations. The velocity profiles were measured using the LDV technique and then validated against numerical calculations of the carrier phase. Their results showed deposition patterns under all conditions were basically similar. Li et al., (2016) studied turbulence modulation for a dilute particle flow using the PIV method. Other recent studies include those of Shwin et al., (2017); Jain (2017)

2.5.3 Experimental Studies of Single- and Two-Phase Flows in Ducts

Just as in pipes and channels, flows in ducts over the years have been of interest to researchers. Earliest researches in ducts were based on single phase turbulent fluid flow. The earliest of these was that of Nikuradse (1926) where a distinction between the flow behaviours in pipes and ducts was made; resulting in an increased interest in the investigation of duct turbulent flows. In this study, the author indicated that in contrast to pipe flows, secondary flows will exist in the near wall areas of a duct cross-section when the Reynolds number exceeds a certain value and will result in the

deformation of the mean velocity contours. The author also observed that the axial mean velocity contours in a turbulent straight duct of rectangular cross-section bulged outwards around the duct corners due to secondary fluid motion towards the corners of the duct centre. Although some explanation on the origin of the secondary motion was given by Prandtl (1952), there was no quantification of these secondary flows until the hot-wire technique was devised by Hoagland (1962). Prandtl (1927) attributed the findings to vortices moving towards the corner of the duct. The corner vortices are classified as secondary flows of Prandtl's second kind (Galletti and Bottaro, 2004) since it is believed to be generated by the turbulence and not the secondary vortices arising from the skewing of the cross-stream vorticity. With the advancement of the hot-wire anemometer technique, it became possible for Hoagland (1962) to produce in a duct flow quantitative profiles of the secondary velocities. Following from this study, Leutheusser (1963) provided details on the distribution of the local wall shear stress in a rectangular duct where it was concluded that the flow around the duct centre did not follow the outer law formulations, although the inner law provided a good description of the flows close to the wall.

It was not until the study of Brundrett and Baines (1964) that a more detailed description of the origins of the secondary flows in a square duct was reported. The study provided measurements on all six components of the mean flow velocity distribution and Reynolds stresses using the hot-wire anemometry technique. The study indicated that the source of the vorticity in the streamwise direction was as a result of the gradient of the Reynolds stresses in the plane of the cross-section. Specifically, the normal-stress gradients were observed to be dominant in the generation of velocities in the plane of the cross-section. In a later study carried out in Gessner and Jones (1965), the effect of Reynolds number on secondary flows was examined. The study reported a decrease for the non-dimensionalised secondary flow velocity as Reynolds number is increased, and that maximum skewness of the local wall shear stress vectors occur in the near wall regions where the secondary flow is also at a maximum. In a related study, Launder and Ying (1972) measured the secondary flows in a duct with a uniformly roughened surface. The study, however, concluded that the rough surfaces will show a negligible effect on the secondary flow, provided that the velocity is normalised with the average friction velocity. The study also demonstrated that secondary motions caused by turbulence in a plane duct cross-section tend to transfer momentum from the centre of the duct towards the duct walls. Melling and Whitelaw (1976 using a laser-Doppler anemometer measured a fully developed turbulent flow in a rectangular duct; with the

aim to improve the accuracy of the laser-Doppler method and provide data for validating numerical models. Similar reports on square duct flows is found in Emery et al. (1980); Po (1975); Demuren and Rodi (1984).

Years later, Zhang et al. (1997) using the HPIV measuring technique investigated turbulent square duct flows. They reported results showing good agreements with Melling and Whitelaw (1976) and Eggels et al. (1994). The same technique was implemented by Toa et al. (2000, 2002) in a study aimed at providing an understanding of the relative alignment between strain-rate, filtered vorticity and sub-grid scale stress tensors. Sheng et al. (2008) using a digital microscope, simultaneously measured the instantaneous three-dimensional flow structure in the inner part of a turbulent boundary layer of a fully developed turbulent square duct flow.   The authors reported the mean flow profiles and velocity fluctuation statistics as being in good agreement as expected. Grosse and Schröder (2009) studied turbulent duct flow using PIV. Also, using a microscope shear stress tensor, the authors examined the wall shear stress distribution and found out that the presence of the low and high shear regions in the streamwise direction of the turbulent flow was as a direct result of the wall shear stress distribution. Owolabi et al. (2016) studied the turbulent flow behaviours of a square duct at low shear Reynolds numbers of $Re_T = 81$ and 161. The results were in reasonable agreements with the DNS data of Uhlmann et al. (2007) and Gavrilakis (1992).

For turbulent duct two-phase flows, only very few experimental investigations exist relative to studies carried out over the years on channel and pipe flows. Most of the work in this field has been mainly focused on the deposition of the dispersed phase on wall surfaces. Notable examples include those performed by Alexander and Coldren (1951), which was among the first of experimental studies on duct flows. Their work elucidated the mechanism and measured typical rates of deposition of small water droplets suspended in turbulent air flows, on the walls of a straight duct. Chamberlain (1967) extended this study to measure the deposition of lycopodium spores and aerosols of various small sized particles. Sehmel (1971); (1973) carried out an experiment to investigate the deposition of particles on the floor and ceiling of a horizontal wind tunnel, with emphasis on the effects of gravity and other factors like the particle inertia and eddy diffusion on the particle deposition process.

Furthermore, Adam et al. (1996) investigated the deposition of oil smoke particles in a square duct with aim of examining the relationship between airflow and the rate of the particle deposition. In a related study, Cheong (1997) examined the contribution of the duct domain aspect ratio to the rate of deposition of the smoked particles. Sippola and Nazaroff (2004) in a similar study as Sehmel (1971, 1973), carried out studies to examine particle deposition rate for a fully developed turbulent flow in a square duct. Using a range of particle size and airspeed, the authors observed that for all cases, there was an increase in the rate of deposition towards the floor when compared with the rate at which deposition is made in the walls and ceiling regions of the duct flow. The reader is directed to the study of Sippola and Nazaroff (2002) for more information on turbulent two-phase duct flows.

2.6 Review of Numerical Studies in Channels, Pipes and Ducts

In this section, are reviews based on numerical studies performed on single- and two-phase turbulent flows using relevant modelling and simulation methods for channels, pipes and ducts. The section also includes a description on investigations with suitable numerical data for validating against the results generated in this work.

2.6.1 DNS Review for Single-phase Wall-bounded Flows

Numerical predictions for channel flow using the DNS is one of the most prominent simulated canonical wall-bounded flows due to the simplicity of the flow geometry when compared to other wall-bounded turbulent flows. Some of the investigations where the DNS has been successfully employed in the simulation of single-phase channel flows are reviewed herein. The first notable example involving this technique is found in the study carried out by Kim et al. (1987) who performed analysis on turbulent channel flows. Their work used a bulk Reynolds number of 3300 based on the channel half-width and mean centerline velocity. Results showed good agreements with experimental data. However, the study was limited to simple flows with low Reynolds number due to the low computational capabilities at the time. However, as the advancement in computing power continues through the years, as well as the improvements in modelling approach (Borrell et al., 2013; El Khoury et al., 2013; Graham et al., 2013), it is now increasingly possible to apply the DNS in the study of wall-bounded flows with higher Reynolds numbers. As an example,

Moser et al. (1999) using the DNS was able to perform simulation for a turbulent channel flow up to $Re_\tau = 590$. Del Alamo et al. (2004) made DNS predictions on a turbulent channel flow with friction Reynolds number up to $Re_\tau = 1900$ and further extended by Hoyas and Jiménez (2006) to a friction Reynolds number of $Re_\tau = 2003$ during their study on the scaling of velocity fluctuations in turbulent channel flows. Separate DNS simulations for flows with $Re_\tau \approx 590$ were carried out by Lozano-Durán and Jiménez (2014) using a relatively small sized domain and by Bernardini et al. (2014) in the study of turbulent flow behaviours of a canonical incompressible turbulent channel flow. It is now proven to be possible to make DNS predictions on wall-bounded turbulent flows with even higher Reynolds number as reported in the study by Lee and Moser (2015). In this investigation, the simulation was performed for flows of $Re_\tau = 5200$ and achieved an acceptable level of consistency in the resolution with very minimal statistical uncertainties. Furthermore, Picano et al. (2015) investigated a dense Newtonian two phase flow laden with neutrally-buoyant spheres in a plane channel using the DNS, with their result showing a significant alteration of the mean velocity profile by the particle presence. Other recent studies includes those of Xia et al., (2016) and Kajishima and Taira (2017).

The DNS is however, not restricted to channel flows only as there are numerous instances where it has been employed for resolving single-phase turbulent flows for duct and pipe flows. For duct flows, notable examples include that performed by Gavrilakis (1992) where a straight duct turbulent flow of bulk Reynolds number 4410 was investigated. The statistics obtained for the turbulence and mean flow properties provided useful information which was used for the estimation of each term in the mean streamwise vorticity equation. Huser and Biringen (1993) performed DNS studies on square duct flows and demonstrated that there is a relationship between the mean secondary flows and the ejection structures close to the wall. Based on this report, Huser et al. (1994) were able to determine all the terms in the Reynolds stress transport equations. It enabled the researcher to obtain detailed descriptions of square duct turbulent flows with emphasis on the origin of the secondary flows. Years later, Joung et al. (2007) performed analysis on secondary flows in a duct using DNS at a bulk Reynolds number of $Re_\tau = 4440$. The secondary flows were observed to play a key role in the transfer of momentum between the corner and the duct centre. Pinelli et al. (2010) also performed DNS studies on turbulent square duct flows for low Reynolds numbers.

For single phase pipe flows, the first notable DNS simulation on turbulent pipe flows was performed by Eggels et al. (1993) in which a DNS code was developed and predictions tested for cylindrical geometries. Their method was based on the finite volume technique rather the previously known spectral method. Results were in good agreement with experimental data, justifying its use in Eggels et al. (1994). Similar studies to Eggels et al. (1994), although using a second-order finite-difference method, was performed by Orlandi and Fatica (1997) but in a pipe rotating about its axis and Fukagata and Kasagi (2002). For more methods see (Friedrich et al., 2001; Loulou et al., 1997; Veenman, 2004).

Satake et al. (2000) investigated the effect of Reynolds number on the turbulent structures of a fully developed turbulent pipe flow using the DNS procedure and concluded that turbulent structures are dependent on the flow Reynolds number. Wu and Moin (2008) performed a DNS analysis on turbulent pipe flows at $Re_\tau = 1142$ using a streamwise domain length of 15 times the pipe radius. El Khoury et al. (2013) increased in the domain length to 25 times the radius for a smooth pipe turbulent flow for a shear Reynolds up to 1000. Chin et al. (2014) like Satake et al. (2000) investigated the effect of Reynolds number in DNS pipe flows. For more on the recent studies on DNS pipe flow, see the enclosed and the references therein (Ahn et al., (2013 and 2015); Chin et al., 2010; El Khoury et al., 2014; Feldmann and Wagner, 2012; Klewicki et al., 2012; Lee and Sung, 2013; Hwang et al., 2016 and Örlü et al., 2017).

2.6.2 LES Review for Single-phase Wall-bounded Flows

The LES is admittedly uneconomical for practical engineering and industrial applications, due to the great demand for processing speed and memory it imposes. However, it is still a very attractive numerical approach employed in many scientific and academic research studies for small-scale predictions of both simple and complex wall-bounded flows.

The earliest application of the LES is found in Deardorff (1970) where a three-dimensional turbulent channel flow was simulated using large Reynolds numbers. In this pioneering work, it was proven that three-dimensional turbulence computation is feasible. Using a total of 6720 uniform grid points, the author was able to predict different features of the turbulent flow with a reasonable amount of success. The work

marked the beginning of the implementation of LES for turbulence flow calculations. As a continuation from Deardorff's work, Schumann (1975) extended the LES method to cylindrical geometries and also performed calculations on a turbulent channel flow, using grid points ten times (65536) than previously used. Grötzbach and Schumann (1979) demonstrated the improved capabilities of the LES by extending the method to account for the simulation of temperature fluctuations and heat transfer for moderately high Reynolds numbers.

It was not until the study by Moin et al. (1978) that a major improvement of the LES was made. The authors demonstrated for the first time that it was possible to compute turbulent channel flows in the areas close to the wall rather than being modelled. With only few grid points, $16 \times 16 \times 25$ in the streamwise, spanwise and wall normal directions respectively, the computation displayed some of the well-established characteristics of the flow in regions close to the wall, but not enough to resolve the coherent structures in the viscous sublayer as observed through experimental measurements. The turbulent structures near the wall were however examined in details by Moin and Kim (1982). The study used up to 516096 grid points for the simulation of a turbulent channel flow with bulk Reynolds number, $Re_{\mathrm{b}} = 13800$. The work reported good agreements of the turbulent statistics, mean velocity profile, and detailed flow structures with data obtained from experiments. With further extension of the LES method (Schumann et al., 1980), it became possible to calculate secondary flows in partly roughened channel walls, and also the inclusion of buoyancy effects for wall-bounded flows. Madabhushi and Vanka (1991) applied this findings in their LES study on turbulent-driven secondary flow in straight square ducts and reported that the secondary flows and their influence on the mean flow and turbulent statistics was correctly predicted and in good qualitative agreement with experimental data. A decade on, Rudman and Blackburn (1999) performed LES study on turbulent pipe flows, with results comparable with experimental measurements. Xu and Pollard (2001) applied LES to simulate turbulent flows in a square annular duct, with results showing acceptable agreements with numerical and experimental data. Vázquez and Métais (2002) applied the LES in the simulation of turbulent flows through a heated square duct and investigated the effect of the heated wall on secondary flows. Other Recent studies includes those of Marin et al. (2016) who used LES based on high-order spectral element method to characterised the mean flow and Reynold stress tensor in a hexagonal duct; and Bose and Park (2018) who studied complex turbulence flows using the LES.

2.6.3 RANS Review for Single-phase Wall-bounded Flows

Single phase prediction for wall-bounded flows using RANS models became prominent when the turbulence was first characterized in terms of its intensity and scale by Kolmogorov (1942). Chou (1945) in an attempt to improve the model, suggested that using the model up to the third moment is adequate to characterise turbulent flows. With improvements to the model, it became possible for the authors to predict the mean profile of the channel flow. Other notable studies concerning the application of RANS to model turbulent flows include those of Hanjalic and Launder (1972), Rogallo (1981), Moin and Kim (1982) and more recently, Subramaniam and Balachandar (2018).

For pipe flows, some noteworthy predictions using the RANS method include those of Kobayashi and Yoda (1987) who developed a turbulence model which can be applied to turbulent swirling flows in straight pipes; Martinuzzi and Pollard (1989) and Martinuzzi and Pollard (1989) who carried out a two-part investigation in which a range of turbulence models for predicting turbulent pipe flows were compared for range of Reynolds numbers of value 10000 to 38000; Hrenya et al. (1995) who performed an extensive study to determine the suitability of different $k - \varepsilon$ turbulence models in the application of low Reynolds number pipe flow prediction and Myong and Kasagi (1990) who proposed a new approach to improve the performance of the $k - \varepsilon$ turbulence model for wall-bounded shear flows. More recently, He et al. (2008) applied a low Reynolds number $k - \varepsilon$ model combined with a finite volume/finite difference discretization scheme to investigate the wall friction and turbulence dynamics within an accelerating pipe flow. More recently, Dutta et al. (2016) using $k - \varepsilon$ turbulence model investigated flow separation characteristics for a high Reynolds number single phase flow through pipe bends. The implementation of the RANS model is not limited to studies in channel and pipe flows. Notable instances where it has been applied to duct flows include those of Launder et al. (1975), Mompean (1998); Nisizima (1990) and Reif and Andersson (2002).

2.6.4 DNS Review for Two-phase Wall-bounded Flows

The study of turbulent two-phase flows using DNS dates back in time to the study of McLaughlin (1989b) where particulate deposition mechanism in vertical channel flows was simulated. Their work was based on examining the ideas about initial

deposition as suggested in an earlier study by Cleaver and Yates (1975). The simulation was done at a low Reynolds number with small computational domain. Following an extension to the study (Ounis et al., 1991, 1993), a similar study was performed by Brooke et al. (1992) on a finer computational mesh and higher Reynolds number of 9000. The work involved the use of a simplified version of the particles equation of motion, such that only the Stokes drag effect was taken into account and particle influence on gas flow was assumed negligible. The authors observed that despite the simplifications, deposition of particles proved to be as a result of the same turbulent eddies responsible for turbulence generation in the viscous sub-layer. Pedinotti et al. (1992) using the DNS investigated particle behaviours in the near wall region of a turbulent channel flow. The studies reported that the initial uniform distribution of particles tends to segregate into low-speed regions of the fluid motion with resuspension occurring as particles eject from the wall. Soltani and Ahmadi (1995) studied the process of particle entrainment in a turbulent channel flow using DNS. They reported that the coherent structure of the wall plays a key role in the particle entrainment process. Zhang and Ahmadi (2000) studied particle deposition in turbulent duct flows and reported similar findings as Soltani and Ahmadi (1995).

Of particular interest, are the DNS studies of Marchioli and Soldati (2002) wherein the mechanisms of particle transfer and segregation in the wall boundary layer was reported; and Marchioli et al. (2008) where a collaborative database of investigations for turbulent particle dispersions in channel flows was reported using the DNS technique. The latter consisted of five independent investigations of the same test case problem consisting of gaseous carrier phase, spherical particles and at low Reynolds number. Only drag force was considered in the simulations. The authors were able to achieve statistically, a steady condition for particle distribution and a comprehensive database for both fluid and particle was obtained. Zhang et al. (2015), using DNS, studied the effect of particle collisions using three particle sizes in a turbulent square duct flow of shear Reynolds number 300. The investigators observed that collisions play a key role in particle redistribution and transportation within the flow, in terms of deposition and resuspension.

Aside from the study of particle deposition and other flow phenomena, the DNS over the years have been very effective in analysing turbulence modulation and particle collisions in particulate flows. For instance, Boivin et al. (1998); Elghobashi and

Truesdell (1993); Maxey et al. (1997); Squires and Eaton (1990b); Ferrante and Elghobashi (2003); analysed turbulence modulation and particle behaviours in an isotropic homogeneous turbulence using this technique. Inhomogeneous turbulence studies using DNS was carried out by Hinze (1975); Mashayek and Pandya (2003). Very recent studies using the DNS includes those of Eisenschmidt et al., (2016); Dizaji and Marshall (2017); Xie et al., (2017); and Marchioli (2017).

2.6.5 LES Review for Two-phase Wall-bounded Flows

Over the years, many researchers have combined the LES with notable particle models in order to conduct researches on particulate flows. This is due to the ability of the LES to fully resolve large-scale structures in turbulent flow simulations as well as modelling the small-scale homogeneous turbulence. This section focuses only on those investigations in which the LES was successfully combined with notable particle models to predict two-phase flow behaviours as it is particularly relevant to the study herein.

The first significant analysis using the LES was performed by Wang and Squires (1996) in their studies on particulate transport in a fully developed channel flow. Simulations were performed at Re numbers 180 and 644 based on friction velocity and channel half width. Results obtained showed good agreement with DNS data of Rouson and Eaton (1994) and experimental measurements of Kulick et al. (1994). In another study, Wang and Squires (1996) performed LES studies on particle deposition in fully developed turbulent channel flows, this time at much higher Reynolds numbers of 112160 and 79400 neglecting particle-particle interactions and flow modifications by particles. Again, particle deposition rate observations using the LES showed that particle accumulates in the near-wall region of the channel which is in good agreement with DNS results of McLaughlin (1989a).

Years later, Yao and Fairweather (2010, 2012) performed a simulation on particle deposition in a fully developed turbulent duct flow using the LES under conditions of one-way coupling. At bulk Reynolds numbers 83000, 250000 and 10320, three particle sizes $50\ \mu m,\ 100\ \mu m$ and $500\ \mu m$ were studied. The authors argued that secondary flows in a particle-laden flow are very significant influences in the particle deposition process within the square duct. Particle sizes and forces are highly influential in particle deposition. In a similar condition, the authors (Yao and

Fairweather 2010) studied particle resuspension in a turbulent square duct flow with bulk Re equals 250000, with four particle sizes ($5\ \mu m\ to\ 500\ \mu m$) examined. A similar conclusion by the authors showed that particle sizes and forces were also highly influential in particle for particle resuspension.

Other researches using the LES technique include a study on turbulence modulation by Volavy et al. (2012), under the conditions of two-way coupling in a turbulent channel flow. Inter-particle interactions were considered negligible and the simulation carried out at different volume fractions of the particles in the channel (particles assumed spherical). The authors concluded that the presence of particles tends to attenuate turbulence, particularly around the near-wall regions of the channel. Breuer and Alletto (2012) simulated particle-laden two-phase flows based on the Euler–Lagrange approach. Mallouppas and van Wachem (2013) studied spherical particulate behaviours in a horizontal turbulent channel flow using the LES approach at $Re_b = 42000$ and based on full channel height. The simulation was four-way coupled, hence particle-particle and particle-fluid interactions were all considered. Results obtained were compared with experimental data of Kussin and Sommerfeld (2002) and showed a good agreement. The authors concluded that in a four-way coupled system, wall roughness and inter-particle collisions play an important role in particle re-distribution across the channel even if the flow is dilute. This work was further extended using a DNS-LES approach (van Wachem et al., 2015) to simulate non-spherical particles behaviours in a turbulent channel flow. The authors then compared the analysis with numerical (Zastawny et al., 2012) and experimental (Kussin and Sommerfeld 2002) data for spheres at $Re_b = 42585$, based on full channel height. The simulation was performed using the Eulerian-Lagrangian framework. The authors concluded that wall roughness has a different effect on non-spherical particles when compared to spherical ones. While a spherical particle collision with a rough wall results mostly in a translational motion change of the particle direction, non-spherical particle collision induces a significant amount of energy which causes additional rotation of the particles about their axis, and also induces a re-suspension of the particles.

Most recently Njobuenwu and Fairweather (2015) studied the behaviour of non-spherical particles in turbulent channel flows using the LES method coupled with the LPT technique, Marchioli (2017) reviewed numerical inaccuracies which are incurred as a result of approximations of the filtered velocity in the LES and lastly, the influence

of Langevin subgrid-scale model on the dispersed phase of particle-laden flows was performed by Breuer and Hoppe (2017) using LES. Breuer and co-workers applied the LES for various studies on particle collisions and agglomeration and will be discussed further in the chapter. Nonetheless, more extensive and detailed review of the LES including previous researches using this method is found the study of Bini and Jones (2008).

2.6.6 RANS Review for Two-phase Wall-bounded Flows

Recent studies on RANS include those of Tian and Ahmadi (2007) who performed a simulation on particle depositions in turbulent duct flows using the RSM and the two equation $k - \varepsilon$ model for the predictions. The aim of their study was to test the accuracy of different models in terms of simulating nano- and micro-particles in turbulent flows. Their result showed good agreement with experimental data gathered with the RSM model providing the most accurate predictions of the models. Mohanarangam and Tu (2007) performed a RANS predictions on particle-laden turbulent flow over a square sectioned $90°$ bend; with results showing good agreements with the experimental data of Kliafas and Holt (1987). Following from this work, Njobuenwu et al. (2013) using the RANS model coupled with the LPT technique determined particle dispersion characteristics in a duct with $90°$ bend. Other researches using the RANS model include particle deposition patterns in complex geometries as reported by Li and Ahmadi (1995), Balásházy and Hofmann (1995), K Lai and Nazaroff (2000) and Zhang and Kleinstreuer (2001), the study of particle erosion in pipe bends (Njobuenwu et al., 2013) and the evaluation of erosion in a two-phase flow system (Niu, 2001).

More recent studies involving the RANS technique include those of Sajjadi et al, (2017) and Zhou and Liu (2018). The computational resources required for RANS predictions is relatively minimal. However, the predictive capability of the RANS technique is usually very limited. Considering the case of interaction between particles and turbulent flow in boundary layers, for instance, the result of the RANS can be questionable depending on the isotropy assumed in the turbulence model used.

2.7 Particle Agglomeration

Particle agglomeration in turbulent flows generally refers to the process of particle adhesion which occurs after collision. In most engineering applications with often turbulent and high particle-laden flow regimes, an understanding on the characteristic nature of such flows in terms of how particles disperse, agglomerate and deposit within the flow is highly significant, as particle collision and agglomeration becomes major factors in dictating the dynamics of such flows. For instance, it is well established that agglomeration will result in an increase in particle size and larger sized particles under gravitational influence will deposit faster towards the floor regions of a wall-bounded flow (Zhang et al, 2015). Increasing particle concentration in this region can ultimately lead to bed formation which restricts flow (Adams et al, 2012).

From the studies reported so far, it is noted that the dynamics and interactions of turbulent particulate flows in wall-bounded geometries have been the subject of many experimental and numerical investigations. Whilst most of these are focused on the interactions between particles as well as particle-fluid-wall interactions, deposition and resuspension, only very few investigations have been performed on particle agglomeration, despite its significance on two-phase wall-bounded flows. This possibly may be due to the high cost of computing the phenomenon. In the following sub-sections, we provide a review on some of the relevant experimental and numerical studies on particle agglomeration.

2.7.1 Numerical and Experimental Studies on Particle Agglomeration

This section explores some of the experimental and computational investigations performed so far on particle agglomeration. The existing experimental studies are mainly related to studies concerning agglomeration in fluidised beds. Notable examples includes the following and the references therein; Ardell (1972); Ennis et al., (1991); Moseley et al., 1993; Lin et al. (2011); Dosta et al., 2013 and Lei et al.(2014). However, there are a few numerical studies on particle agglomeration in wall-bounded turbulent flows, although mostly are concerned with developing algorithms (or models) for predicting the phenomenon (stochastic and deterministic agglomeration models are the most common). Two common variants of the agglomeration model are the energy-based and momentum-based agglomeration

models, although the energy barrier approach based on DLVO (named after the work of Derjaguin and Landau and Verwey and Overbeek) interactions is also known and successfully implemented (Henry, Milner 2013).The approach for the successful prediction of the phenomenon is in most cases through the extension of the hard-sphere collision model to account for particle cohesion.

One of the earliest attempts on developing suitable models was performed by Loffler and Muhr (1972) and later extended in the study by Hiller, (1981). The authors proposed an energy-based agglomeration model in which agglomeration only occurs if the normal relative velocity between the colliding particles is less than a critical value. Sommerfeld (2001) considering a homogeneous isotropic turbulent field, proposed an energy-balance stochastic detection model which was extensively applied for modelling particle agglomeration by Sommerfeld and co-workers (Ho and Sommerfeld, 2002; Sommerfeld, 2010; Stübing and Sommerfeld, 2010). Kosinski and Hoffmann (2010) extended the momentum based hard-sphere deterministic particle collision model to account for agglomeration in Eulerian-Lagrangian simulation framework. Sommerfeld and Stübing (2017) also presented a novel agglomeration model based on the Lagrangian approach which allows for the prediction of agglomerate structure and its characteristic behaviour in the point-particle approximation. Alletto (2014) building from the improved work of Jürgens (2012) applied and provided an extension of the agglomeration model to account for friction at the point of particle contact. Breuer and Almohammed (2015) improved on the original agglomeration model of Kosinski and Hoffmann (2010) to predict better collision time and utilised it for the simulation of particle agglomeration. More recently, Breuer and Almohammed (2015) and Almohammed and Breuer (2016) extended the energy-based agglomeration model of Alletto, with detailed comparisons made against an improved momentum-based agglomeration model in their work. Njobuenwu and Fairweather (2017) using the energy-based hard sphere model of Alletto (2014) presented a more efficient technique for simulating particle agglomeration in turbulent flows. Other particle agglomeration based predictions include Afkhami et al. (2015) where particle agglomeration in turbulent two-phase channel flow was modelled. The authors applied the LES coupled with the discrete element method (DEM), which allows for multiple particle contact (soft-sphere collision model) to investigate the role of particle surface energy and turbulence on particle agglomeration behaviour.

So far, the understanding on particle agglomeration in turbulent wall-bounded flows is limited, due to the low amount of work available in the literature, although significant efforts have been put into developing new models for predicting the phenomenon over the last decade. However, there is still the need to improve the understanding on the sensitivity of the flow parameters on the subject. Specifically, the contribution of gravity in the agglomeration formation process is still not explicit, although considered in previous investigations. This study, therefore, aims to extend the available literature and ultimately improve the understanding on the subject by performing sensitivity studies on the contribution of gravity to particle collision and agglomeration, and the resulting influence of the particles on the continuous phase turbulence. Here, the improved energy-based agglomeration model by Alletto, (2014) is adopted for predicting particle agglomeration.

2.8   Concluding Remarks on Literature Review

From the literature review conducted it will be fair to conclude that considerable effort has been put into the investigation of fluid transport over the years; of which the bulk of it has been concentrated in the investigation of the continuous phase. The particle phase has also been the focus of many experimental and numerical investigations over the years; particularly in the subject of inter-particle collisions and the resulting effects on the fluid and particle behaviors (turbulence modulation). However, it would appear there is still a gap in knowledge when it comes to our understanding on particle agglomeration in particle-laden flows as only very few attempts have been made over the years to detail the conditions contributing to the agglomeration of particles and the resulting effect of the particle size increase on the turbulence of wall-bounded flows. In attempt to replicate the flow conditions typical of many industrial situations, the work will be further extended to investigate the effect of gravity on the agglomeration formation process amongst other factors like the particle size, volume fraction and flow Reynolds number. This contribution should improve our understanding on the particle agglomeration phenomenon and hoped to be a useful addition to the already existing literature.

3 Numerical Methods

3.1 Background Studies on Multiphase Flows

In this chapter, the governing equations and numerical solutions for both the fluid and particle phases are presented. The section provides a description of the numerical methods adopted for the predictions and the forces which directly influences the particle transportation. The numerical methods applied for the continuous phase are described in sections 3.2 through 3.3 with that of the particle phase elucidated in section 3.4. In section 3.5, the forces acting the particles are presented. Finally, in sections.3.6 and 3.7, the models considered for detecting particle collision and agglomeration are described respectively.

3.2 Modelling the Fluid Phase

The Navier-Stokes equations for Newtonian fluid express a general conservation principle based on the Newton's second law of motion and therefore, contains all the information required to effectively describe the flow conditions in this study (Frisch, 1995). The flow is described by solving equations based on the conservation law of mass, momentum and energy and written in a Cartesian tensorial notation as:

Mass
$$\frac{\partial \rho}{\partial t} + \frac{\partial \rho u_i}{\partial x_i} = 0 \qquad \qquad 3.1$$

Momentum
$$\frac{\partial \rho u_i}{\partial t} + \frac{\partial \rho u_i u_j}{\partial x_j} = -\frac{\partial p}{\partial x_i} - \frac{\partial \tau_{ij}}{\partial x_j} + \rho g_i + \overline{S}_{m,i} \qquad 3.2$$

The stress tensor for a Newtonian fluid is expressed as:

$$\tau_{ij} = -\mu \left(\frac{\partial u_i}{\partial x_j} + \frac{\partial u_j}{\partial x_i} - \frac{2}{3} \frac{\partial u_j}{\partial x_i} \delta_{ij} \right) \qquad 3.3$$

Where δ_{ij} is the Kronecker symbol ($\delta_{ij} = 1$ if $i = j$ and $\delta_{ij} = 0$ if $i \neq j$).

3.2.1 Large Eddy Simulation

The LES separates the large and most energetic turbulent scales from the smaller eddies. This is possible by performing a direct three-dimensional computation on the large turbulent scale motions responsible for turbulent mixing while modelling mathematically the sub-grid scale (SGS) motion smaller than the computational grid. The mathematical expression for the flow decomposition is given in Eq. (3.4) showing the resolved and unresolved components of the flow.

$$f(x) = \bar{f}(x) + f_{SGS}(x) \tag{3.4}$$

where $f(x)$ is a function of the defined scales; and $\bar{f}(x)$ is the large-scale or the resolvable-scale component of f (Leonard, 1974); and defined as:

$$\bar{f}(x) = \int_V f(x')G(x,x';\overline{\Delta})\mathrm{d}x \tag{3.5}$$

V in Eq. (3.5) represents the entire flow domain, $\overline{\Delta}$ is the minimum length scales in the filtering operation (filter width) while G represents the filter function and determines the structure and size of the small scales. In practice, various filter function distributions have been used and include; the Gaussian and the box ('top-hat') and the 'sharp cut-off' filters (Ghosal and Moin, 1995; Piomelli, 1999). In this study, the top-hat filter according to Germano (1992) will be required for all simulations as it fits into a finite-volume formulation naturally. The physical representation of the top-hat filter applied is as follows:

$$G(x) = \begin{cases} \dfrac{1}{\overline{\Delta_i}\,\overline{\Delta_j}\,\overline{\Delta_k}} & |x| \leq \dfrac{\overline{\Delta}}{2} \\ 0 & otherwise \end{cases} \tag{3.6}$$

3.2.2 Filtered Navier-Stokes equations

For an incompressible Newtonian fluid where the properties are constant, applying the decomposition operation from Eq. (3.4) and Eq. (3.5) to the Navier-Stokes equation results in the filtered continuity and Navier-Stokes equations of motion given as:

$$\frac{\partial \overline{u_i}}{\partial x_i} = 0 \qquad\qquad 3.7$$

$$\frac{\partial \overline{u_i}}{\partial t} + \frac{\partial}{\partial x_j}\left(\overline{u_i}\,\overline{u_j}\right) = -\frac{1}{\rho}\frac{\partial \overline{p_i}}{\partial x_i} - \frac{\partial \overline{\tau_{ij}}}{\partial x_j} + \frac{\partial \bar{\sigma}_{ij}}{\partial x_j} + g \qquad\qquad 3.8$$

Here, the overbar denotes filtered quantities and u, p and ρ the fluid velocity, pressure and density, respectively. $\overline{\sigma_{ij}} = -2v\overline{s_{ij}}$ is the viscous stress and $\overline{s_{ij}} = 0.5\left(\partial \overline{u_i}/\partial x_j + \partial \overline{u_j}/\partial x_i\right)$ is the strain-rate tensor. The variable $\left(\overline{u_i}\,\overline{u_j}\right)$ represents the sub-grid scale stress tensor τ_{ij} arising from the top-hat filtering operation of the fluid flow and is required to close the system of equations. Its effect on the resolved scale motion is captured through a sub-grid scale (SGS) stress term:

$$\tau_{ij} = \overline{u_i u_j} - \overline{u_i}\,\overline{u_j} \qquad\qquad 3.9$$

In order for the filtered equations to be solved, this term is modelled.

3.2.3 The Sub-Grid Model

In this study, the model for the dynamic SGS stress as proposed by Germano et al. (1991) was used. We used the SGS stress model that was previously implemented in the in-house LES-BOFFIN code, which used the approximate localisation procedure of Piomelli and Liu (1995) alongside the modification as proposed in the study of di Mare and Jones (2003). In this approach, the authors represented the SGS stresses as a product of the SGS viscosity, v_{sgs} and also the resolved part of the strain tensor. The viscosity, v_{sgs} is measured as a product of a given velocity scale, $\Delta\|\bar{s}\|$ times the filter length, Δ. This therefore yields an expression for the anisotropic part of the SGS stresses, given by:

$$\tau_{ij}^a = -2(C\Delta)^2\|\bar{S}\|\overline{S}_{ij}^a \qquad\qquad 3.10$$

The parameter, C for the model expression in Eq. (3.10) must be determined in the dynamic model. This is done by the application of a second filtering operation,

expressed as ($\tilde{\bullet}$), to the filtered Navier-Stokes equation. The SGS stresses in the test-filtered equation are expressed as:

$$\tau_{ij} = \widetilde{\overline{u_i u_j}} - \widetilde{\overline{u}_i}\, \widetilde{\overline{u}_j} \qquad\qquad 3.11$$

By comparing the definition τ_{ij} and T_{ij}, an expression for L_{ij} is derived:

$$L_{ij} = T_{ij} - \tau_{ij} - \widetilde{\overline{u}_i}\, \widetilde{\overline{u}_j} \qquad\qquad 3.12$$

The expression above involving only resolved quantities is referred to as the Germano's identity (Germano et al., 1991). Some form of correlation between the model constants C and $C^2(\tilde{\bullet})$ at the test and grid filter levels must be specified in other to obtain an expression for C. On the basis that the cut-off length is within the initial sub-range. A common expression utilised here is:

$$C^2 = C^2(\tilde{\bullet}) \qquad\qquad 3.13$$

For low Reynolds number or wall-bounded flows, there is no guarantee that such a sub-range will occur, with the largest deviations from universality of the SGS motions occurring in regions where the resolved strain is weakest. Di Mare and Jones (2003), therefore proposed the equation in Eq. (3.14), based on the values of the model parameter at the two different filter levels.

$$C^2(\tilde{\bullet}) = C^2 \left(1 + \frac{\varepsilon}{2\sqrt{2}\Delta^{\sim 2} \left\| \tilde{\overline{S}} \right\| \left\| \widetilde{\overline{S^a}} \right\|^2} \right) \qquad\qquad 3.14$$

where ε is assumed to be the rate of turbulence energy dissipation, expressed in terms of a velocity scale v and a length scale l, such that:

$$\varepsilon = {v^3}/{l} \qquad\qquad 3.15$$

with v taken as the bulk velocity and l the half width of the channel.

Eq. (3.15) holds the assumption that the scale invariance of C can be invoked only when the cut-off lies within the initial sub range, and that this occurrence would mean that the entire dissipation in the flow should be represented by the modelled dissipation. Conversely, only the v and l determines the dissipation in the high Reynolds number limit, such that the ratio of ε to $\Delta^{\sim 2}\|\tilde{s}\|^3$ provides a measure of the distance of the flow from scale preserving conditions (Porté-Agel et al., 2000). A combination of Eq. (3.13) and Eq. (3.14), on contraction of both sides, using scale tensor, $\tilde{\tilde{S}}$ gives:

$$C^2 = \frac{\left[2\sqrt{2}\,(C_*^2\Delta)^2\|\overline{S}\|\,\left\|\overline{S}_{ij}^a\right\|^\sim\tilde{\tilde{S}}_{ij}^a - L_{ij}^a\tilde{\tilde{S}}_{ij}^a\right]}{\varepsilon + 2\sqrt{2}\Delta^{\sim 2}\left\|\tilde{\tilde{S}}\right\|\left\|\tilde{\tilde{S}}^a\right\|^2} \qquad 3.16$$

Where C_*^2 represents the provisional value for C^2. According to Piomelli and Liu (1995) C_*^2 is the value of the value of C^2 at the previous time step. An advantage of this method is that it avoids irregular and spiky behaviours as exhibited by some other dynamic models. Another advantage is that C^2 tends to zero as the resolved strain also tends to zero while $C^2(\tilde{\cdot})$ stays bounded. Smooth C^2 fields are generated without the need for any averaging, and maxima are of the same order of magnitude as estimated (Lilly, 1967) for the Smagorinsky model constant. This method however, does not prevent instability when C^2 is set to zero as negative values of the model parameter is still produced. This is also the case of the SGS viscosity. This research simulation, involves test-filtering in all the space directions, without any averaging of the computed model parameter field and the ratio $\Delta^\sim/\Delta$ was set to 2 and the filter width obtained from $\Delta = (\Delta_x\Delta_y\Delta_z)^3$. A stochastic Markov model which is explained in subsection 3.2.4 was applied in order to represent the influence of the unresolved fluid velocity fluctuations on the particles.

3.2.4 Sub-Grid Scale Velocity Fluctuations

The sub-grid scale (SGS) fluctuation refers to the small-scale motion usually experienced in turbulent wall-bounded flows. While the effect from the larger scales are computed for in such flows, it is difficult to compute the fluctuations of the sub-grid scales due to the size; and therefore could either be modelled separately or

neglected in total. These fluctuations can influence the motion of the particles depending on the particle inertia *(Armenio et al., 1999)*. For the motion of tracer particles, the effect of the sub-grid scale fluctuations is far more significant due to their very small inertia when compared with the effect on larger particles. However, the inclusion of a term representing the effect of the sub-grid scale in the Navier-Stokes equation should improve the accuracy of the LES predictions.

The effect of the SGS velocity fluctuations on particle motion (X_{sgs}), is evaluated by using a stochastic Markov model (Bini and Jones, 2008) which represents the influence of the unresolved fluctuations on particle acceleration using the equation:

$$X_{sgs} = \left(C_0 \frac{k_{sgs}}{\tau_t} \right)^{0.5} \partial W_t / \partial t$$

<div align="right">3.17</div>

Here, k_{sgs} represents the unresolved kinetic energy of the continuous phase, obtained using equilibrium arguments from $k_{sgs} = (2\Delta v_{sgs}\tilde{S}_{ij}\tilde{S}_{ij})^{2/3}$, ∂W_t is the increment of the Wiener process, represented by $\xi_i \times \sqrt{\Delta t}$; where ξ_i is a random variable sampled from a normal distribution with zero mean and a variance of unity which is independent for each time step and for each velocity component. C_0 represents a model constant assumed to equal unity in this study ($C_0 = 1$) and τ_t is a sub-grid time scale which affects the rate of interaction between a particle and the turbulence dynamics. The time scale τ_t is derived through the expression (Bini and Jones, 2008):

$$\tau_t = \frac{\tau_p^{2\alpha}}{\left(\Delta / \sqrt{K_{sgs}} \right)^{2\alpha-1}}$$

<div align="right">3.18</div>

where $\alpha = 0.8$. Alternative expressions for determining the time scale is given as $\tau_t = \Delta^{1/3} / |v_p|$ and $\tau_t = \Delta^{1/3} / \sqrt{K_{sgs}}$ (Bini and Jones, 2008).

3.3 Numerical Flow Solver

Using the in-house computational code LES-BOFFIN (Boundary Fitted Flow Integrator), the governing equations (filtered Navier-Stokes equations) and the transport equations for the scalar quantities were solved. It is based on a finite-volume approach using an implicit low-Mach number formulation and is second order accurate in space and time. A two-step approximate factorisation pressure correction technique is used to ensure mass conservation. All other spatial derivatives are approximated with second-order central differences and a Crank-Nicolson scheme is used for temporal discretisation.

Primitive variables including pressure and velocity are stored at cell centres by utilising a co-located storage arrangement. Due to the co-located storage arrangement, fourth-order pressure smoothing is applied in order to prevent false oscillations of the pressure field as proposed by Rhie and Chow (1983). In order to allow the mapping of complex shape domains on a rectangular domain, the Cartesian coordinates are transformed into a curvilinear coordinate system as proposed by Thompson et al. (1974). The procedure is second order accurate in space and time. Time advancement was set to yield a maximum Courant number ranging from 0.1 to 0.3 (Di Mare and Jones, 2003) as this was required for the maintenance of high accuracy (Choi and Moin, 1994). More information on the numerical algorithm and how it is implemented can be found in Jones et al. (2002) and references cited therein. In order to sufficiently generate the flow conditions described in this study, it becomes necessary to modify the existing LES-BOFFIN code. The main modification, however, was keeping the mean flow pressure gradient constant throughout the simulations and adjusted dynamically to maintain a stable mass flux through the flow geometry in each case.

3.3.1 LES-BOFFIN Applications

The BOFFIN-LES code over the years has been widely utilised in the simulations involving both reacting and non-reacting turbulent flows. Some of the recent simulations include work on turbulent flow over swept fence (Di Mare and Jones, 2003), particle flows in ducts (Fairweather and Yao, 2009), particle deposition in turbulent duct flows (Yao and Fairweather, 2012), dynamics of non-spherical

particles in turbulent channel flows (Njobuenwu and Fairweather, 2014), particle agglomeration in turbulent channel flows (Ogholaja et al., 2017a; Ogholaja et al., 2017b), and micro-bubble transport in turbulent horizontal channel flows (Asiagbe et al., 2017). Further information on the numerical algorithms and the implementations are found in the work of Di Mare and Jones (2003); Jones (1991).

3.4 Modelling the Particle Phase

As already noted, the particle phase modelling is mostly performed using the Eulerian and Langragian prediction methods. However, the latter is preferred in this study since its formulation provides details of individual particle behaviours within the flow, which makes the particle tracking more accurate and precise.

3.4.1 Lagrangian Particle Tracking Method and Procedure

In other to calculate the particle trajectories in the flow field, a Lagrangian tracking routine is coupled with the large eddy simulation. The particle motion under the Lagrangian routine is achieved based on the implementation of solutions obtained from the particle equation of motion through the application of Newton's second law of motion (Maxey and Riley, 1983). The equations as already noted, are solved for each particle in order to obtain the trajectories of the particle and given as:

$$m\frac{\mathrm{d}\vec{v}}{\mathrm{d}t} = \frac{\rho_p \pi d_p^3}{6}\frac{\mathrm{d}\vec{v}}{\mathrm{d}t} = \sum \vec{F}(\vec{x}_p, t) \qquad 3.19$$

From the equation, $\vec{v}$ is the translational velocity of the particle and expressed as:

$$\vec{v} = (u_p, v_p, w_p) \qquad 3.20$$

ρ_p is the particle density. $\vec{x}_p = (x_p, y_p, z_p)$ accounts for the particle position in the wall-normal, spanwise and streamwise directions. Represented on the left hand side of Eq. (3.19) is a term for the inertia force acting on the particle as it accelerates. While

that on the right hand side of the equation denotes the sum of the external forces which act on the particle. Typically, the forces influencing the motion of the particles in the fluid are the drag $(\overrightarrow{F_D})$, net gravity-buoyancy $(\overrightarrow{F_{GB}})$, pressure gradient $(\overrightarrow{F_{PG}})$, added mass $(\overrightarrow{F_{AM}})$ and slip-shear lift forces $(\overrightarrow{F_{SL}})$. An expression for these forces in the particle equation of motion is given in Eq. (3.21) and enables the tracking of particles within the flow:

$$\frac{\mathrm{d}\vec{v}}{\mathrm{d}t} = \left(1 - \frac{\rho}{\rho_p}\right)\vec{g} + \frac{\vec{u} - \vec{v}}{\tau_p}C_D + C_{SL}\frac{\rho}{\rho_p}[(\vec{u} - \vec{v}) \times \vec{\omega}] + \frac{\rho}{\rho_p}\frac{\mathrm{d}\vec{u}}{\mathrm{d}t}$$
$$+ \frac{\rho}{2\rho_p}\left(\frac{\mathrm{d}\vec{u}}{\mathrm{d}t} - \frac{\mathrm{d}\vec{v}}{\mathrm{d}t}\right) + \vec{X}_{sgs} \qquad\qquad 3.21$$
$$\frac{\mathrm{d}\vec{x}_p}{\mathrm{d}t} = \vec{v}$$

The terms on the right-hand side represent the gravity-buoyancy, drag, shear-lift, pressure gradient and added mass forces per unit mass, respectively. Subscript p represents the particle, while $\vec{\omega}$ is the fluid vorticity interpolated at particle location, and expressed as:

$$\vec{\omega} = 0.5\nabla \times \vec{u} \qquad\qquad 3.22$$

u is the fluid velocity, v is the particle velocity, d_p is the particle diameter, ρ_p is the particle density, g is gravity and τ_p is the particle relaxation time given by:

$$\tau_p = \frac{\rho_p d_p^2}{18\mu f_D} \qquad\qquad 3.23$$

where f_D is the drag factor and μ is the fluid dynamic viscosity.

The expression obtained through the implementation of the fourth-order Runge-Kutta scheme on Eq. (3.21) is used to determine the particle position in the flow. In this procedure, Eq. (3.21) is integrated twice in time to determine particle position every time step. The first integration is performed in order to calculate the particle velocity in the computational space (Faires and Burden, 1994). In order to determine the new position of the particle, equation is integrated once more, which is crucially important

for the overall performance of the code. The algorithm chosen for tracking the particle solves for the particle trajectories along the channel by constantly updating with time the three-dimensional location by computing from the instantaneous solution of the fluid velocity field, the particle velocity. It functions by determining the position of the particle, followed by the interpolation of the fluid data at this location, and then integrating the equation of motion. From these steps, the effect of the particle collisions can be calculated.

3.5 Forces acting on the Particle.

Here, we provide a description of the relevant forces acting on particles in liquid-solid flows, and modelling the effect of the continuous phase on the motion of particles. As indicated in the force balance equation, several forces are known to influence particle movement in two-phase wall bounded flows; of which their resulting effect on the particles varies and subject to the fluid properties, direction and the flow domain condition. Some of the forces include gravity and buoyancy, Shear lift, Brownian motion, profile lift, added mass and pressure gradient force. A numerical representation of the forces is given and briefly discussed here. The profile lift force will not be discussed further as it is applicable for non-spherical particles and therefore beyond the scope of this study.

3.5.1 Gravity and Buoyancy Force

The force of gravity is produced from the resulting force of attraction between two bodies and acts along the direction of the gravitational acceleration g. This force significantly influences the motion of particles, and becomes even more important in flow configurations where the mean flow direction is not in alignment with the acceleration due to gravity. For a high particle laden flow system, the force of gravity leads to an indirect change in characteristics of the flow as it will promote the settling of particles in the lower regions of wall-bounded two-phase flows which consequently affects the fluid flow dynamics.

The buoyancy force founded by Archimedes is generated as a result of the pressure gradient between the top and bottom part of a body immersed in a fluid. The force acts in the direction opposite to the gravitational acceleration g. The net force of the

gravitational and buoyancy forces is utilised in the force balance equation and expressed as:

$$\vec{F}_{GB} = \left(1 - \frac{\rho_f}{\rho_p}\right)\vec{g}$$

It is noteworthy that unlike the other forces mentioned in this study, the two forces described above are not hydrodynamic forces.

3.5.2 Drag Force

Probably the most significant force acting on the particle is the drag force. The drag is the force which impacts on a particle when fluid equivalent to the particle surface area is displaced. It is the force required to move the particle with a field of uniform pressure and velocity. The drag force with respect to the drag coefficient C_D is written as:

$$\vec{F}_D = \frac{1}{2}\rho_p C_D A_p \vec{U}U \qquad\qquad 3.24$$

Where the projection of the particle surface in the incoming flow direction is A_p and expressed as:

$$A_p = \frac{1}{4}\pi d_p^2 \qquad\qquad 3.25$$

$\vec{U} = (\vec{u} - \vec{v})$ is the slip velocity in all three dimensions, with its magnitude expressed as:

$$U = |\vec{u} - \vec{v}| = \sqrt{(u - u_p)^2 + (v - v_p)^2 + (w - w_p)^2} \qquad\qquad 3.26$$

Drag coefficient effect is a function of the slip velocity of the particle which is represented by the particle Reynolds number, Re_p and the drag factor, f_D. An empirical correlation obtained for spherical particles in a uniform flow (Schiller and Naumann, 1933) is frequently used in expressing C_D and given by the relation:

$$C_D = \frac{24}{Re_p} f_D \qquad\qquad 3.27$$

$$\text{with} \qquad Re_p = d_p |\vec{u} - \vec{u}_p| / \nu \qquad\qquad 3.28$$

where C_D and f_D represents the drag coefficient and the drag factor respectively. f_D has been obtained from drag coefficient and expressed as:

$$f_D = 1 + 0.15\, Re_p^{0.687} \qquad\qquad 3.29$$

3.5.3 Lift Force

The shear lift force refers to the force which acts on the particle in a direction normal to a shear fluid flow. It is generated as a result of the asymmetric pressure and shear stress distribution arising from the difference in particle and fluid velocities. According to the author's knowledge, the first analytical study describing the lift force effect on particle displacement in a linear shear fluid flow was by Saffman (1965). By means of matched asymptotic expansions, the author obtained an analytical solution where a spherical particle was shown to be displaced in a linear shear fluid flow but was, however, only valid for low Stokes flows ($Re_p < Re_G^{1/2}$). The study was further extended in McLaughlin (1991) to remove restrictions in the analytical solution of Saffman (1965) by employing a Fourier transformation to the flow. In order to obtain a relation for the lift force suitable for high Stokes flow, a lift coefficient is introduced (see Crowe et al., 1998; Sommerfeld, 2000), with the full equation expressed as:

$$\vec{F}_{SL} = \frac{\pi}{8} \rho d_p^3 C_{SL} [(\vec{u} - \vec{v}) \times \vec{\omega}] \qquad\qquad 3.30$$

where C_{SL} is the shear lift force coefficient which accounts for high particle Reynolds numbers, obtained from Mei (1992) and applied in (Laín and Sommerfeld, 2008). It is expressed as:

$$C_{SL} = \frac{4.1128}{Re_{sl}^{0.5}} f(Re_p, Re_{sl}) \qquad\qquad 3.31$$

Re_{sl} represents the Reynolds number of the shear flow and given as:

$$Re_{sl} = \rho d_p^2 |\omega| / \mu \qquad\qquad 3.32$$

The ratio of the extended lift force to that of the shear lift force yields the correction factor $f(Re_p, Re_{sl})$ as proposed by Mei (1992) given as:

$$f(Re_p, Re_{sl}) = \frac{\vec{F}_{SL}}{\vec{F}_{SL,Saff}}, \qquad\qquad 3.33$$

A systematic study conducted by Marchioli et al. (2007) on the influence of the lift force on dilute upward and downward channel flows and concluded that the lift force has a dominant effect on the particle concentration at the wall regions and negligible for other regions of the flow. The work also observed that there was a reduction in the particle concentration at the wall regions for upward flows and an increase in the concentration of the particles at the wall regions for downward flows. The study concluded by suggesting that the influence of the lift force is enhanced for smaller sized particle flows. This thesis aims to analyse the lift force for a turbulent channel particle flow of $Re_\tau = 300$ and particle diameter $d_p = 125\ \mu m$ in order to confirm the claims in Marchioli et al. (2007).

3.5.4 Added mass, Pressure Gradient and Basset Force

The added mass force, $\vec{F}_{AM}$. in a turbulent particle-laden flow occurs as a result of the acceleration or deceleration of the particles, relative to the fluid phase. Clift et al., (1978) described it as the acceleration of the fluid displaced due to particle acceleration in a system. A change in the relative velocity of the particles within the flow field will result in a corresponding gain in kinetic energy by the fluid, which is at the expense of the work done by the accelerating particle. This work done originates the added mass force around the particle as it accelerates. An expression for the added mass force on a spherical particle in an incompressible fluid is given by (Crowe et al, 1998):

$$\vec{F}_{AM} = \frac{\rho_f}{2} V_i \left(\frac{\mathrm{d}\vec{u}}{\mathrm{d}t} - \frac{\mathrm{d}\vec{v}}{\mathrm{d}t} \right)$$

3.34

Where V_i is the particle volume (Crowe et al, 1998; Kuerten, 2016).

The pressure gradient is the simply the pressure generated as a result of the differences in the particle and fluid densities as a function of the particle acceleration expressed as:

$$\vec{F}_{PG} = \frac{\rho}{\rho_p} \frac{\partial u}{\partial t}$$

3.35

The added mass and other hydrodynamic forces like the pressure gradient and the Basset force are relatively negligible forces when compared to the drag force for a high density ratio flow using the Lagrangian particle approach (Maxey and Riley, 1983). Various numerical and theoretical studies on wall-bounded two-phase flows have proven to be in good agreement to this assumption. A notable example of such study is that conducted by Armenio and Fiorotto (2001) who using DNS, compared the drag, the pressure gradient , the added mass and the Basset force in order to determine their relative importance in dilute turbulent channel flows of density ratios ranging from $\rho_p/\rho = 2.65$ to $\rho_p/\rho = 2650$ and at shear Reynolds number $Re_\tau = 175$. Findings from this study indicated that the pressure gradient was only important for

the smallest density ratio flow and that the added mass for all density ratios were at least two times smaller than the drag force. The Basset force to drag force ratio was observed to depreciate from 0.25 for the lowest density ratio flow $\rho_p/\rho = 2.65$ to 0.096 for the highest density ratio flow ($\rho_p/\rho = 2650$) so cannot be completely neglected. Nonetheless, further analysis by the authors showed that only small changes in the particle dispersion was noticed for the simulations considering only the drag force when compared to simulations considering the drag, the pressure gradient , the added mass and the Basset force; with the difference amounting only to 1.6% for flows with $\rho_p/\rho = 2.65$ and 0.97% for flows with $\rho_p/\rho = 2650$.

The findings of Armenio and Fiorotto (2001) is confirmed in the much earlier but similar studies performed by Hjelmfelt and Mockros (1966). In this investigation, the influence of the drag, the pressure gradient, the added mass and the Basset force were tested by evaluating the response of particles to the oscillating fluid motion of an oscillating flow. The study contrasted four different solutions with the aim to determine the phase shift between the fluid and particle velocities as a function of the frequency of the fluid having varying fluid to particle velocity amplitude ratio. The first solution considered only the drag force, the second considered both the drag and pressure gradient forces, the third considered the drag, pressure gradient and added mass forces while the fourth considered the drag, the pressure gradient, the added mass and the Basset force. The authors observed that there were no difference between all four solutions considered; although, a small shift in particle to fluid amplitude ratio was observed between the solution where only drag was considered and that were all forces were considered when the oscillating frequency was significantly increased.

From both the findings of Hjelmfelt and Mockros (1966) and Armenio and Fiorotto (2001) it is observed that the most significant force in a turbulent wall bounded flow system is the drag force and that neglecting other forces will not affect the accuracy of the predictions in any great deal. Their claim was also supported by Elghobashi and Truesdell (1993), where it was mentioned that the most important force acting on a particle is the drag force. However, in this study, we have considered some of these forces as the cost of computation is negligible. Analysis on the effect of the forces is presented in a later section of this thesis and correctly justifies the claims by Hjelmfelt and Mockros (1966), Armenio and Fiorotto (2001) and Elghobashi and Truesdell (1993). In the first part of this study only the drag force was considered in

validating the chosen flow solver. The second part of the simulation which involves the collision and agglomeration of particles used the relevant forces described above.

3.5.5 Two-way Coupling and Computational Specification

For a two-way coupled flow system as discussed in section 2.2.1, the fluid flow field is modified by the particles. It is, therefore, necessary to account for the feedback effect of momentum transfer between the particle and the fluid velocity fields. In the framework of the Eulerian-Lagrangian approach adopted in this work, this feedback effect is accounted for by adding source terms representing the transfer of particles momentum to the fluid Navier-Stokes equations. These source terms are computed using the Particle-Source-in-Cell method (PSI-CELL), Crowe et al (1977). This integrates the momentum transferred along individual particle paths as they cross individual fluid control volumes, with similar consideration of heat and mass transfer when applicable.

The momentum source term for the resolved scale, $\overline{S}_{m,i}$, is expressed as:

$$\overline{S}_{m,i=x,y,z} = -\frac{1}{\Delta^3} \sum_{\alpha=1}^{n_p} \left(m_p \frac{dv_i}{dt} \right)$$

3.36

where n_p represents the number of particles in a particular cell volume and m_p the mass of each particle in the given cell.

In order to reduce the complexity of the computational process and to ensure a more accurate result is obtained during tracking, the particles have been assumed perfectly spherical and rigid, with density set to $2710 \ kg/m^3$ (calcite) to replicate the conditions in nuclear flows. For each two-phase flow simulation, the particles were assumed to be mono-dispersed i.e. of same size. The Stokes number *St* used is a function of the particle diameter, d_p, hence, can be obtained from Eq. (3.37) when the particle diameter is specified. It is a measure of the relative inertial of the particle to that of the fluid.

$$St = \frac{\tau_p}{\tau_f} = \frac{\left(\frac{\rho_p d_p^2}{18\mu}\right)}{\frac{v}{w_\tau^2}}$$

3.37

where v is the volume of the fluid, and τ_p and τ_f are the relaxation times of the particle and fluid, respectively. At a small Stokes number of say $St < 1$, the particle velocity is at near equilibrium with the velocity of the carrier phase while at $St > 1$, the motion of the particle is unaffected by the continuous flow field. In other words, particles will move in the direction of a fluid element during turbulence, provided the time scale associated with the turbulence is the same as the fluid time (Crowe et al., 1996).

The injection of particles is done at the start of the simulation, with particles randomly distributed across the computational geometry and their initial velocity set to be the same as that of the local fluid at each particle location. Once the fluid velocity field at the particle location has been established, the equation of motion for the particle is solved by applying a fourth-order Runge-Kutta scheme with an integration time of 10^{-1} times the LES time step. A periodic boundary condition was imposed on the particles in the streamwise and spanwise directions so the particles can be introduced back into the flow after exiting the domain and also that there is a correspondence between the particle flow and the fluid flow. Also, in order to ensure particle-wall collision is perfectly elastic with zero particle deformation, the particle wall normal velocity is set to be unchanged (but of an opposite sign) when a particle is tracked to be one radius away from the wall.

3.6 The Collision Model

To ensure that a considerable amount of particle collision is achieved within the shortest time possible, the simulation was made four-way coupled, having a volume fraction $\phi \geq 10^{-3}$. This way, the mean distance between the particles becomes smaller and consequently promoting particle-particle collision.

3.6.1 Method and Procedure

In this study, the particle-particle collision detection is made possible using the deterministic hard-sphere collision model described in Breuer and Alletto (2012); and preferred over a stochastic model (Sommerfeld, 2001) due to its high level of accuracy. For the particle-wall collision, the particles were assumed to be homogeneous, with contact time set to be smaller than the LES time step. In this model, the particle collision handling is calculated over two collision steps. In the first step, potential collision partners are identified by dividing the computational domain into virtual cells (see, e.g., Viccione et al., 2008), as depicted in Figure 3.1, and by taking into account the smallest possible time steps in the flow. Using the minimum time step ensures that collision within a given cell is correctly detected as particle collision will be more likely to occur between neighbouring particles and thus reduce the chances of any overlap. Particles in the same cell are tagged as having the best chance of collision; hence, virtual cells are adjusted dynamically during the simulation, in order to achieve a nearly optimal virtual cell size (user dependent) so only a minimal number of particles is contained in each cell per time. This way, significant computational savings are made since the cost of collision identification is substantially reduced from order $O(N_p^2)$ to $O(N_p)$, which becomes even more crucial for systems with high particle concentrations, like in this study. For such dense flow systems, the model assumes all collisions as binary. In order to determine the virtual cells containing particles as shown in Figure 3.1(a), it becomes necessary to split the computational domain of size into cells of dimension i_c, j_c, k_c according to the expression:

$$i_c = int(n_i/d_i) + 1$$

$$j_c = int(n_j/d_i) + 1$$

$$k_c = int(n_k/d_i) + 1$$

3.38

Here n_i, n_j, n_k is the size of the computational domain and d_i is a factor adjusted dynamically in order to limit the number of particles contained in each virtual cell during the simulation to an amount specified by the user (Breuer and Alletto, 2012). The corresponding index values of the virtual cells, based on the coordinates of the particle in the computational domain (ξ_p, n_p, ζ_p) is derived according to the expressions:

$$i_p = int(\xi_p/d_i) + 1$$

$$j_p = int(n_p/d_i) + 1$$

$$k_p = int(\zeta_p/d_i) + 1$$

3.39
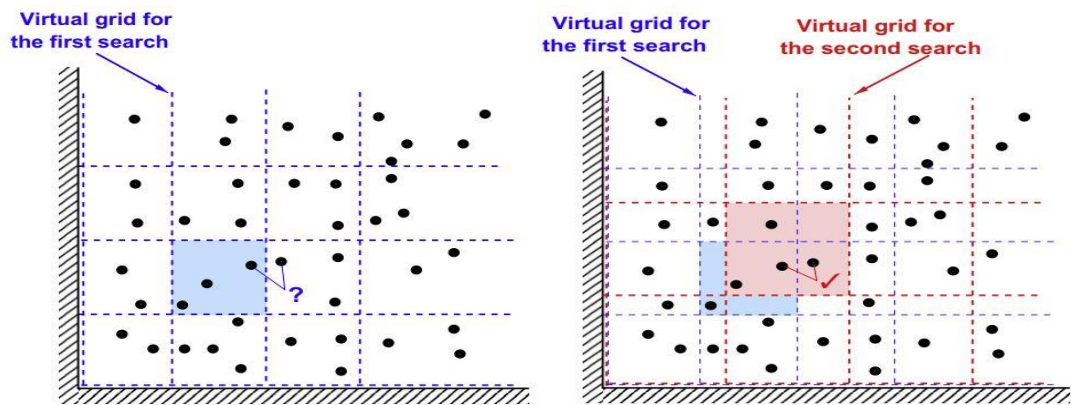
Figure 3.1 Deterministic collision handling by virtual cells (a) first search (b) second search (Breuer and Alletto, 2012)

To avoid virtual cells overlapping during the first step, it becomes necessary to carry out the collision detection procedure a second time, using slightly larger virtual cell sizes as shown in Figure 3.1(b).

In the second step, only particles contained in one virtual cell are accounted for. The collisions are detected by purely kinematic conditions. The condition for a possible binary collision is that two particle would have to approach each other, and expressed as $x_r . u_{p,r} < 0$; else particle collision is impossible. x_r and $u_{p,r}$ represents the relative distance and velocity between two colliding particles respectively. For collision to have occurred, the minimum separation distance between two colliding partners within a time step must have been less than the sum of their radii. If this condition is fulfilled then collision partners are arranged in ascending order according to their time of collision. The particles are then repositioned by using the velocities at the time of impact to the locations where the particle collision occurs. More

information on the collision model adopted is found in the study of Breuer and Alletto (2012).

3.7 The Agglomeration Model Method

The predictions model for particle agglomeration is based on the assumption that agglomeration will only happen if the relative kinetic energy of the particles post-collision is less than the energy needed to overcome the van der Waals' forces of attraction between them. The expression for this is shown in Eq. (3.40) as:

$$\frac{(v_2^- - v_1^-)^2 - [(v_2^- - v_1^-).n_c]^2(1 - e_n^2)}{|(v_2^- - v_1^-).n_c|}$$

$$\leq \frac{H^*}{6\delta_0^{*2}}\left[(1 - e_n^2)\frac{6}{\pi^2\rho_{p\overline{\sigma}^*}^*}\frac{d_{p,1}^{*3} + d_{p,2}^{*3}}{d_{p,1}^{*2}d_{p,2}^{*2}(d_{p,1}^* + d_{p,2}^*)}\right]^{1/2}$$

3.40

where, in dimensionless terms, d_p^* is the particle diameter (d_p/h), ρ_p^* is the particle density (ρ_p/ρ), $\overline{\sigma}$ is the yield pressure $(\overline{\sigma}/\rho u_b)$, H^* is the Hamaker constant $(H/\rho u_b^2 h)$ and $\delta_0^* = \delta_0/h$ is the minimum contact distance. Here, u_b is the bulk velocity and h the channel half-height. The superscript (-) represents quantities prior to particle-particle interaction while the subscripts 1 and 2 represents the two colliding particles. The amount of dissipated energy relative to the incident kinetic energy is given by $(1 - e_n^2)$, where e_n is the coefficient of restitution.

In order to avoid complexities and isolate the conditions required for agglomeration, basic assumptions were made in this model. According to Breuer and Almohammed (2015) only binary collisions between spherical particles are considered; only minimal particle deformation is allowed post-collision; purely energetic considerations was used as a criterion to decide whether an agglomeration occurs or not; and that van der Waals forces are considered solely responsible for particle adhesion after collision and the influence of the electrostatic charges or the formation of liquid bridges between particles are completely ignored.

If the condition in Eq. (3.40) is satisfied then agglomeration occurs with a new volume-equivalent spherical particle assumed. The corresponding velocity and position of the agglomerate/daughter particle is updated at the end of each time step using the equations:

$$\mathbf{v}_3^+ = \frac{\mathbf{v}_1^- d_{p,1}^3 + \mathbf{v}_2^- d_{p,2}^3}{d_{p,3}^3} \qquad 3.41$$

$$\mathbf{x}_3^+ = \frac{\mathbf{x}_{1c} + \mathbf{x}_{2c}}{2} + (t_{n+1} - t_c)\mathbf{v}_3^+ \qquad 3.42$$

where $\mathbf{v}_3$ and $\mathbf{x}_3$ denote the velocity and position of the centre of mass of the agglomerate and $d_{p,3}$ is the agglomerate diameter obtained by using the conservation of mass (Chen et al., 1999):

$$d_{p,3} = \sqrt[3]{d_{p,1}^3 + d_{p,2}^3} \qquad 3.43$$

If the condition in Eq. (3.40) is not satisfied, then no agglomeration occurs. The particles bounces off and the new position and velocity of the particles p_1 and p_2 are evaluated using the equations:

$$\mathbf{v}_1^+ = \mathbf{v}_1^- + \frac{m_{p,2}}{m_{p,1} + m_{p,2}}\{(1 + e_n)[(\mathbf{v}_2^- - \mathbf{v}_1^-).\mathbf{n_c}]\mathbf{n_c}\} , \quad \text{and}$$

$$\mathbf{v}_2^+ = \mathbf{v}_2^- + \frac{m_{p,1}}{m_{p,1} + m_{p,2}}\{(1 + e_n)[(\mathbf{v}_2^- - \mathbf{v}_1^-).\mathbf{n_c}]\mathbf{n_c}\} \qquad 3.44$$

$$\mathbf{x}_1^+ = \mathbf{x}_{1,c} + (t_{n+1} - t_c)\mathbf{v}_1^+, \quad \text{and}$$

$$\mathbf{x}_2^+ = \mathbf{x}_{2,c} + (t_{n+1} - t_c)\mathbf{v}_2^+ \qquad 3.45$$

were $\mathbf{x_{1c}}$ and $\mathbf{x_{2c}}$ are the positions of the two particles' centre of mass at the time of collision. Further information on the agglomeration model adopted may be found in Breuer and Almohammed (2015).

3.7.1 Time Step for the LPT

In order to solve the particle governing equation for the particle motion, determining the time-step for the solution is necessary. The time step chosen determines the accuracy of results generated from the simulation. A small time step would ensure that the fluid-particle interaction is captured accurately by resolving the moments where particles pass through the turbulent structure. In other words, the time step must be smaller than the lifetime of the turbulent eddy τ_e, its relaxation time τ_p, the time needed for the particle to pass through the eddy τ_r and the time needed for the particle to go through the computational cell:

$$t_{int} = min\left(\tau_p, \tau_e, \tau_r, \frac{\Delta x_{cell}}{u_x}\right)$$

3.46

Δx_{cell} represents the minimum distance across the cell.

4 Turbulent Horizontal Channel Flow: Validation, Collision and Agglomeration – Without Gravity

4.1 Introduction

In this chapter, the predictions concerning the characteristic behaviours for single phase and particle phase flows in a turbulent horizontal channel in the absence of gravity is investigated. The LES method described in the previous chapters is employed herein, with comparisons made against the more accurate DNS technique for three shear Reynolds numbers, $Re_\tau = 150$, 300 and 590; herein referred to as low, moderate and high shear Reynolds number channel flows, respectively.

Following the convergence of the single phase, particles of varying Stokes numbers were introduced into the single phase flows, with tracking made possible by coupling the LES with the LPT technique in a non-commercial code. Varying the Stokes number for the particle-laden flow was particularly necessary since the inertial of the particles determines the degree of their response to the perturbations of the underlying fluid turbulence. Other common parameters which may influence the response of the particles to turbulence and consequently alter the turbulence and flow complexity are the particle-particle interaction (or collision); particle-wall interaction, particle rotation, friction and the other surrounding forces acting on the particle. With these factors in mind, it becomes necessary to fully assess the reliability of the computational methods employed in the flow solver in order to ensure acceptable levels of accuracy in the numerical resolutions are obtainable.

In this chapter, therefore, we focus on assessing the reliability of the LES and LPT techniques and its capability to accurately predict the selective response of different inertia particles. Furthermore, the predictions of the LES is extended into four-way coupled flows where particle collisions and agglomeration is tested for varying particle sizes and volume fractions. The overall aim is to provide a justification on the use of the relatively less computationally expensive LES rather than the more

accurate but computationally expensive DNS in the prediction of turbulent two-phase flows in this thesis.

4.2 Flow Configuration and Initial Conditions

The computational domain used is a horizontal channel bounded by two infinite flat parallel walls, with the channel dimensions set to $L_x \times L_y \times L_z$, equalling $2h \times 2\pi h \times 4\pi h$ for the $Re_\tau = 150$ flow and $2h \times 2h \times 2\pi h$ for the $Re_\tau = 300$ and 590 flows. These dimensions replicate those of previous studies that employed DNS (Marchioli et al., 2002, 2008; Marchioli and Soldati, 2007; and Moser et al., 1999, respectively) which are used for validation purposes below. The channel lengths are sufficiently large in all cases to capture the elongated streamwise turbulent structures that are typical of the near wall regions of wall-bounded flows. The size of the horizontal channel domain and the number of grid points used are summarised in Table 4.1, together with the values for the direct numerical simulations (DNS) used for validation.

Table 4.1 Turbulent channel flow grid and particle parameters used for the LES simulations. Grid parameters used for DNS at $Re_\tau = 150$ (Marchioli et al.,2008), $Re_\tau = 300$ (Marchioli and Soldati, 2007) and $Re_\tau = 590$ (Moser et al., 1999) are also provided for reference.

Re_τ	$L_x \times L_y \times L_z$	$N_x \times N_y \times N_z$	Δ_x^+	Δ_y^+	Δ_z^+	$h\ (m)$
			LES Grid			
150	$2h \times 2\pi h \times 4\pi h$	$129 \times 128 \times 128$	$0.07 - 7.10$	7.42	14.84	0.02
300	$2h \times 2\pi h \times 4\pi h$	$129 \times 128 \times 128$	$0.15 - 14.20$	14.84	29.68	0.02
590	$2h \times 2\pi h \times 4\pi h$	$129 \times 128 \times 128$	$0.31 - 27.92$	29.19	58.38	0.02
			DNS Grid			
150	$2h \times 2\pi h \times 4\pi h$	$129 \times 128 \times 128$	$0.05 - 3.68$	7.42	14.84	0.02
300	$2h \times \pi h \times 2\pi h$	$257 \times 256 \times 256$	$0.02 - 3.68$	7.39	14.78	0.02
590	$2h \times \pi h \times 2\pi h$	$257 \times 384 \times 384$	$0.04 - 7.20$	4.80	9.70	0.02

In order to correctly compare cell sizes, the domains for the $Re_\tau = 300$ and 590 flows were doubled in the y and z directions to match that of the $Re_\tau = 150$ case. The cell sizes in each case is indicative of the range of scales believed to be resolved by the LES. The very small cell values depict a high resolution LES; particularly in the lowest Re_τ flow case which consequently could result in predictions close enough to DNS. The relative increase in the cell sizes for the higher Re_τ will yield to less accurate predictions of the LES but is, however, good enough to ensure the results of DNS are sufficiently reproduced.
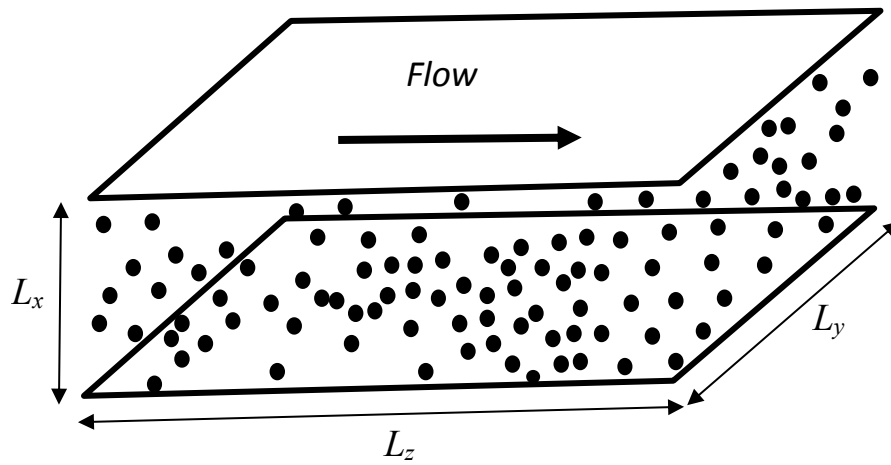
Figure 4.1. Schematic diagram of the channel geometry and co-ordinates
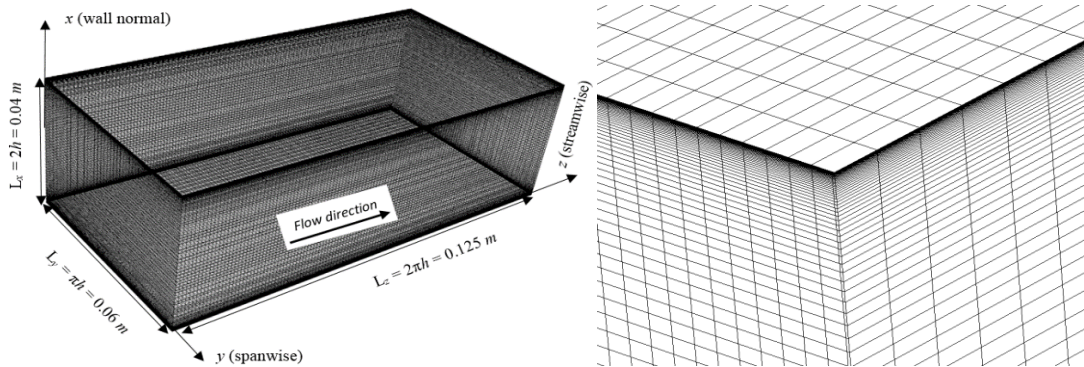
Figure 4.2. Computational channel mesh

Figure 4.2 provides a visual representation of the mesh applied in the channel. In all cases, the $x-$, $y-$ and $z-$axes represent the wall-normal, spanwise and streamwise directions. The enlarged figure in 4.2 shows the top corner of the channel and

provides a clearer view on the nodal distribution within the domain space. It indicates the distribution is made uniform along the y and z directions but is, however, made non-uniform, having a much finer resolution near the walls in the wall normal direction x of the flow. The non-uniform nodal distribution specified in the mesh is achieved by applying a hyperbolic function (Gamet et al., 1999) in the wall normal direction of the flow. No-slip boundary conditions for the fluid phase, and elastic collisions for the particle phase, is enforced at the channel walls.

The shear Reynolds numbers of $Re_\tau = 150, \ 300$ and 590 considered in the simulations is based on the channel half-height, h, and the shear velocity u_τ, defined as $u_\tau = \tau_w/\rho$ and corresponds to $0.0075, \ 0.015$ and 0.0295 m s^{-1} for the chosen Re_τ flows respectively, where τ_w is the mean shear stress at the wall. The kinematic viscosity is set to $v = 10^{-6} \, m^2 \, s^{-1}$ and the fluid density to $\rho_f = 10^3 \, kg \, m^{-3}$, equivalent to a water flow. The simulations concerning the dispersed phase used spherical particles of various initial diameter $75 \, \mu m, \ 125 \, \mu m$ and $250 \, \mu m$ and a density $2710 \, kg \, m^{-3}$ in a four-way coupled flow regime of volume fraction $O(10^{-3})$. The minimum contact distance of the particles is set at $\delta_0 = 3.36 \times 10^{-10} \, m$, with the Hamaker constant $H = 3.8 \times 10^{-20} J$, mean yield stress $\overline{\sigma} = 3.8 \times 10^8 \, Pa$, and the normal restitution coefficient $e_n = 0.4$; a representative of Calcite which is often used as a nuclear waste simulant.

The particles are injected into the flow at the start of a simulation, following the fluid phase reaching a statistically steady state, and distributed at random locations within the channel with initial velocities set equal to those of the local fluid velocity at each particle location. Once the fluid velocity at the particle location has been established, the equation of motion for each particle is solved using a fourth-order Runge-Kutta scheme for the integration. At the particle's position, a trilinear interpolation scheme was utilised to obtain the fluid velocity, u, unresolved kinetic energy, k_{sgs}, and fluid rotation, ω. Both the fluid and particles were re-introduced back into the flow on exit from the channel, with periodic boundary conditions set in both the streamwise and spanwise directions. The flow was driven using a fixed pressure gradient imposed in the streamwise direction.
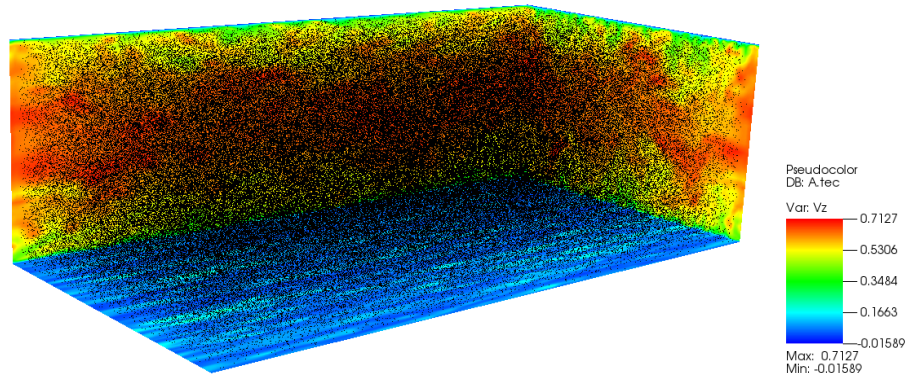
Figure 4.3 Pseudo-colour of instantaneous streamwise velocity for $Re_\tau = 590$ flow and a typical particle initial distribution.

Figure 4.3 shows the instantaneous streamwise velocity and the initial particle location in the high Reynolds number flow, and illustrates the low-speed streaks observed in such flows in close proximity to the walls (Hakansson et al., 2013), whilst the fluid velocity is at maximum around the centre of the channel.

4.3 LES solution validation

In order to establish the accuracy of the LES method adopted, results obtained for the velocity field of the fluid phase were first validated against those from DNS solutions for all shear Reynolds numbers. Similar comparisons were made for the particle phase for all Reynolds numbers considered in a dilute particle-laden flow system. In this case, similar agreement between the LES- and DNS-based particle predictions to that found for the single phase flow was evident. In order to maintain a volume fraction of 10^{-6}, a total number of $100,000$ particles were introduced in the flows.

4.3.1 DNS Test Cases

The DNS study of Moser et al. 1999; Marchioli and Soldati 2007; and Marchioli, Soldati et al. 2008 has been used as the benchmark cases for validating the LES employed in this thesis. The work of the authors were chosen due to the high accuracy of solutions obtained based on the DNS and the availability of particularly relevant raw numerical data from literature.

The first test case used was that of Marchioli et al. (2008) with simulations performed for a flow of low Reynolds number $Re_\tau = 150$ using $128 \times 128 \times 129$ grid points in the x, y and z flow directions, which corresponds to streamwise, spanwise and wall normal directions respectively. The authors in this study published results from an international collaboration involving various DNS two-phase flow investigations. The study was aimed at producing a homogeneous database for solving particle dispersion in wall-bounded turbulent flows. Simulations were performed in a smooth walled channel consisting of a gaseous continuous phase containing hard spherical particles numbering 10^5 (one-way coupled). In their simulation, only the drag force was considered in dictating particle motion, since it is the most significant force acting on a flow. All other forces were ignored owing to their relatively small magnitude when compared to the drag. Though the same flow conditions were specified for the simulations, differences in their implementations were observed. The results obtained from the various groups showed that in general the first and second order statistics of both the continuous phase and the particle phase were in good agreement except for the occasional discrepancies in quantifying the local particle concentration, which is due to the accumulation of numerical errors in the interpolation techniques used for obtaining fluid velocities, the grid discretization utilised by each group and the choice of time-step for the numerical integration. The notable differences are summarized in Table 4.2.

Table 4.2 – Summary of numerical method (from Marchioli et al. 2008)

Group	Flow Solver	Carrier phase Time-step	Particle integration method	$N_x \times N_y \times N_z$
1	PS	$\Delta t^+ = 0.045$	RK4($\Delta t^+ = 0.45$)	$129 \times 128 \times 128$
2	PS	$\Delta t^+ = 0.032$	H2	$129 \times 128 \times 128$
3	FD2	$\Delta t^+ = 0.05$	RK3	$128 \times 160 \times 190$
4	FD2	$\Delta t^+ = 0.05$	AB2	$129 \times 128 \times 128$
5	FV2	$\Delta t^+ = 0.026$	RK2	$192 \times 192 \times 192$

Flow solver – PS: pseudo-spectral, FD2: second-order finite difference, FV2: second-order finite volume. Particle integration – RK4: fourth-order Runge-Kutta, H2: second-order Heun method, RK3: third-order Runge-Kutta, AB2: second-order Adams-Bashford, RK2: second-order Runge-Kutta

The second test case used was that of Marchioli and Soldati (2007). Their publication involved a DNS study of flows in a wall-bounded horizontal channel. The aim of the study was to determine the Reynolds number effects on particle preferential

concentration scaling by comparing flows of shear Reynolds number, $Re_\tau = 150$ against a relatively more turbulent flow of shear Reynolds number, $Re_\tau = 300$ for three different sized particles of Stokes numbers $1, 5$ and 25. The simulation involving the single phase and the particle statistics at $Re_\tau = 300$ for Stokes numbers (1 and 5) have been used as the benchmark test case for the LES validation in this thesis. Their simulation was of shear Reynolds number $Re_\tau = 300$ and used a grid resolution of $257 \times 256 \times 256$ in the wall normal, spanwise and streamwise directions (x, y, z) respectively. For the selected Stokes numbers, the authors summarized the particle preferential concentration scaling behaviours using the expression in Eq. (4.1):

$$\frac{St^{300}}{St^{150}} = \frac{\tau_f^{150}}{\tau_f^{300}} = \left(\frac{u_\tau^{300}}{u_\tau^{150}}\right)^2 = 4 \qquad\qquad 4.1$$

Here the particle behaviour in the flow with $St^{300} = 25$ is described as being similar to that of $St^{150} = 5$. While the particle behaviour in the flow with $St^{300} = 5$ was concluded to be similar to that of $St^{150} = 1$, provided the shear velocity is the scaling parameter required to quantify the effect of the Reynolds number on particle preferential concentration.

The third test case employed for the validation of the of $Re_\tau = 590$ continuous phase predictions in this thesis was the DNS simulation performed by Moser et al. 1999, where numerical simulations for a fully developed turbulent channel flow was reported for three shear Reynolds number flows up to $Re_\tau = 590$. The computational domain used was of grid dimension $348 \times 257 \times 384$ in the wall normal, spanwise and stream directions, x, y, z respectively. The authors concluded that for the higher Reynolds number simulation, fewer low Reynolds number effects were exhibited when compared to previous low Reynolds number simulation for wall-bounded flows at $Re_\tau = 180$.

4.3.2 Single Phase Velocity Statistics

This section provides details on some of the relevant statistics for the fluid phase in order to benchmark the accuracy of the LES numerical approach employed in this thesis. In this method, the values of selected variables (velocity, velocity fluctuations

and shear stresses in this instance) are summed for all particles in a sampling control volume, created using wall-parallel fluid slabs, and averaged in space. To further smoothen the profiles, the statistics are averaged in time over time-steps in $100's$ of thousands. The first- and second-order moments of the fluid phase (Particularly the mean streamwise velocity and the fluctuations in all directions) and the Reynolds stresses are analysed. The dimensionless quantities, x^+ and t^+ represent the distance between the channel walls, (0 being the channel bottom) and the simulation run times for the particle phase respectively.
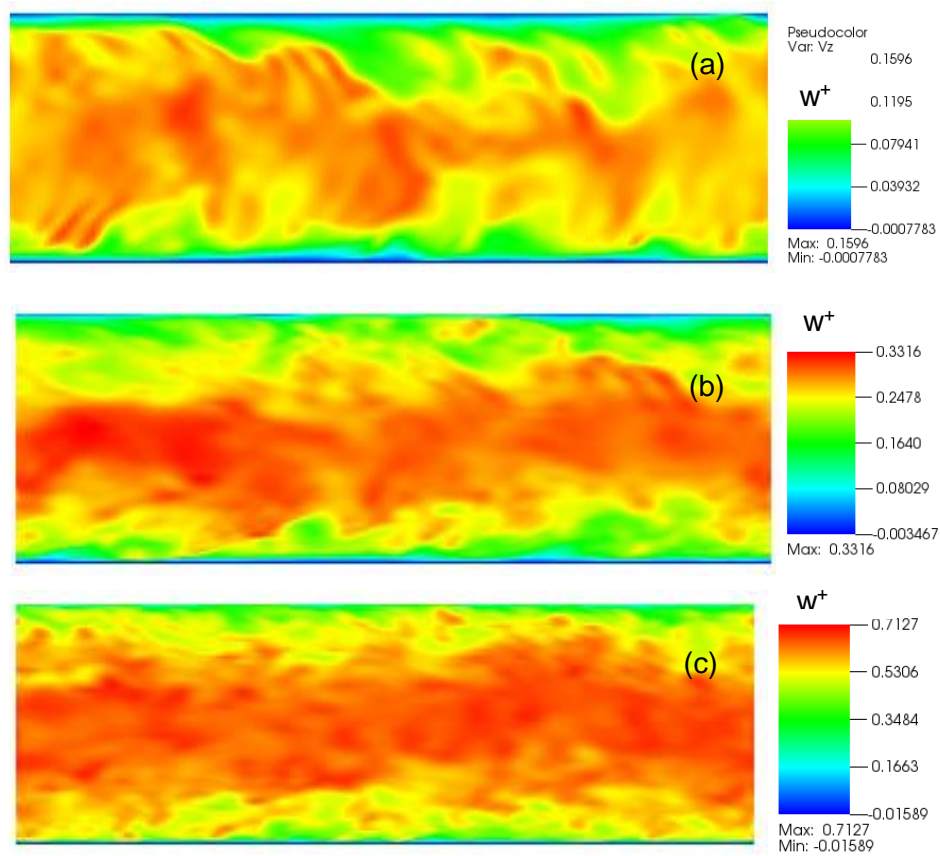
Figure 4.4 Instantaneous fluid velocity in the streamwise direction at Re_τ of (a) 150 (b) 300 (c) 590

A typical representation of the fully converged flow field with increasing Reynolds number is illustrated in Figure 4.4(a-c) where the instantaneous cross-sectional views of the streamwise velocity are shown across the wall normal position. From the figure, it is noticed that the range of scale which represents the fluid velocity increases as the flow Reynolds number increases throughout the cross-section of the channel, although for all Reynolds numbers the large scales dominate in the central region of the channel. The spacing between the near wall low speed streaks is also observed to reduce with increase in the flow Reynolds number in Figure 4.4(a) through Figure

4.4(c). The channel cross-section view in Figure 4.5(a-c) is a representation of the instantaneous streamwise vorticity in the wall normal direction at $Re_\tau = 150, 300$ and 590. It is clearly seen that the flow near the channel wall region is dominated by strong turbulent vortexes, which increase with the increase in the flow Reynolds number and reduce towards the core of the flow. This behaviour is fundamental to particle migration towards the wall regions as observed in turbulent two-phase flows.
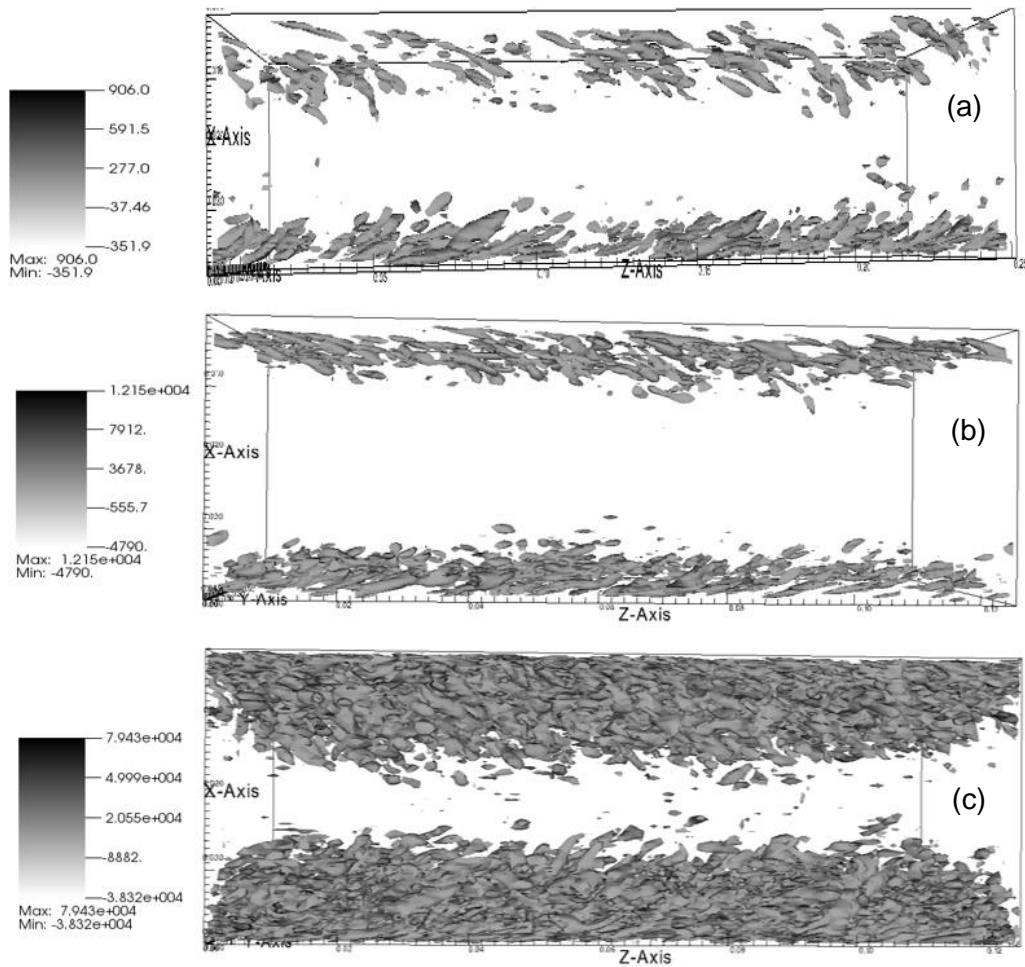
Figure 4.5 Instantaneous wall-normal vorticity in the streamwise direction at Re_τ of (a) 150 (b) 300 (c) 590

The results in Figure 4.6(a-c) give profiles of the mean streamwise velocity for the three shear Reynolds number flows, across the wall normal directions, plotted together with the DNS validation data (Marchioli, Soldati et al. 2008; Marchioli and Soldati 2007 and Moser et al. 1999) on a linear-logarithmic plot, based on the half height of the channel. In Figure 4.6(a) the mean streamwise velocity for the $Re_\tau = 150$ flow is shown. It gives an almost identical representation of the DNS flow, as all regions of the flow are predicted with a high degree of accuracy, especially towards

the wall regions of the flow where sub-grid turbulence is common. This is attributed to the very high resolution of the mesh applied for this flow, with the number of nodes exactly matching those of the DNS. Consequently, the high resolution LES acts like a DNS, as the turbulent scales are almost completely resolved. However, the low turbulence levels of the $Re_\tau = 150$ flow may also have contributed to the high accuracy in the prediction.
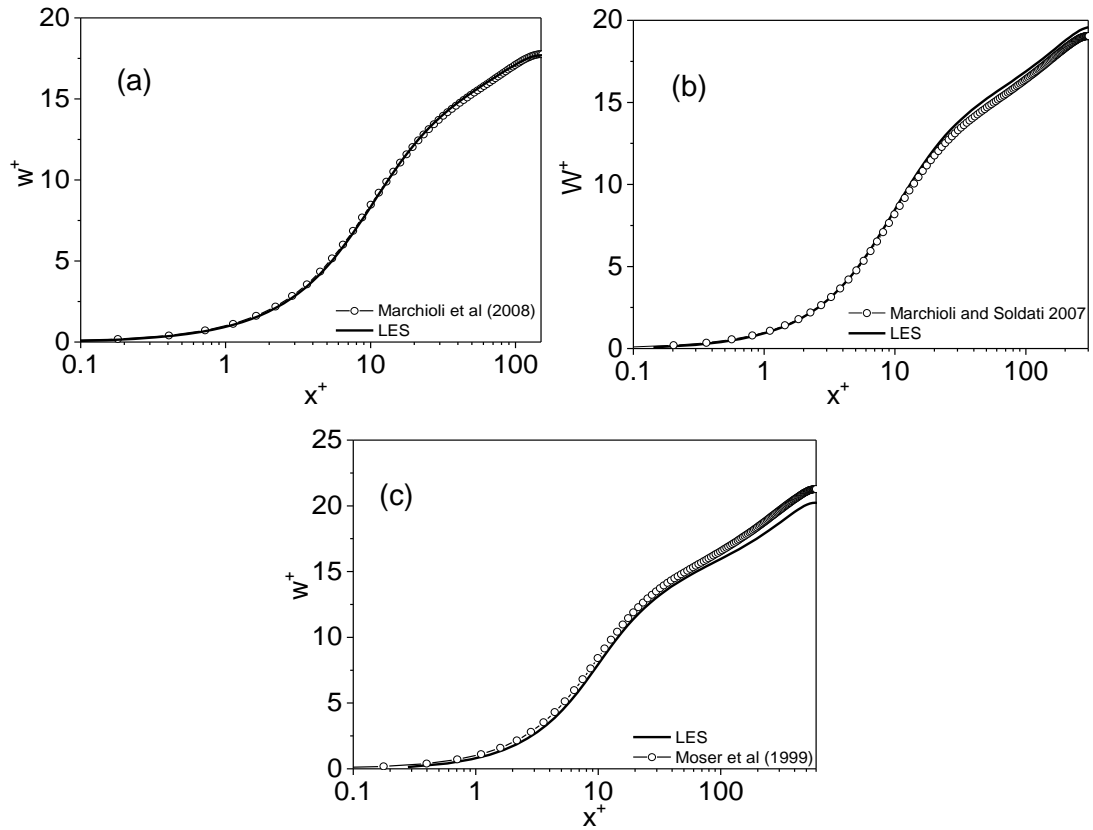
Figure 4.6 Comparison of LES and DNS-based predictions for the single phase Mean Streamwise Velocity at Re_τ of (a) 150 (b) 300 (c) 590

In order to further establish the accuracy of the LES method, the validation was extended to the higher Re_τ flows. In Figure 4.6(b), the mean streamwise velocity component w^+ is plotted for a flow of $Re_\tau = 300$ and compared against result obtained from the DNS (Marchioli and Soldati 2007). The LES result is again, in good agreement with the DNS, although not as much as in the $Re_\tau = 150$ test case, which is understandable, considering fewer nodes compared to the DNS were used. However, the LES resolution is high enough to provide a very close match in profiles to the DNS, especially in regions closest to the wall were the flow is resolved to a high degree. Only a slight LES over-prediction is noticed towards the bulk of the flow were the flow characteristics is dominated by large and very energetic scales of the fluid motion. Given that the LES directly resolves the large energetic scales of the

fluid motion, one would expect that the predicted profile in the bulk flow region would perfectly match the DNS solution, but the slight over-prediction is, however, due to the lower resolution of the LES compared to the DNS in this region. Despite this, the relatively high resolution LES employed is believed to have performed very well as most of the turbulent scales were resolved. In all, the mean streamwise velocity predicted for this Re_τ flow is in very good agreement with the DNS.

Lastly, Figure 4.6(c) shows w^+ against the DNS (Moser et al. 1999) for the highest shear Reynolds number case, $Re_\tau = 590$. Similar trend is noticed as with the previously analysed Re_τ flows, except that the profile indicates an under-prediction of the LES method across the channel space, with the level of accuracy in a constant decline towards the channel centre where the large and energetic turbulent scales are dominant. The under-prediction may be as a result of the mass flow rate of the LES being lower than the DNS cases. The increase in the rate of divergence with turbulence would indicate that the high resolution mesh used is not sufficiently fine enough to mostly resolve the flows in the near wall and bulk flow regions for the most turbulent case. Despite the discrepancies, the good agreement shown by the lesser turbulent simulations proves that the numerical procedures utilised in this study can be trusted.

The root mean square (rms) of the non-dimensional time- and space-averaged velocity fluctuations (i'^+_{rms}) for the fluid phase in the streamwise ($i = w$), spanwise ($i = v$) and wall-normal ($i = u$) directions for all three Reynolds numbers are plotted in Figure 4.7(a-c). The results showing only the resolved stresses of the LES are compared against data of the DNS, and show reasonable agreement, although with the indication of some discrepancies against those of the DNS. For the $Re_\tau = 150$ case in Figure 4.7(a), the w'^+_{rms} component of the streamwise velocity fluctuation was in good agreement with the DNS profile in the wall regions where fluctuations peak. The flow profile towards the flow center is also well predicted, although a slight under-prediction across the channel is noticed. The velocity fluctuations in the wall-normal and spanwise directions, u'^+_{rms} and v'^+_{rms} respectively, also show good agreements with the DNS data, although slight differences are observed. For the u'^+_{rms} component, deviations are noticed close to the wall, indicating a small under-prediction of the LES in the region. Nonetheless, the LES prediction maintained a close match with the DNS for the rest of the channel. The v'^+_{rms} showed a similar trend but with the prediction showing a much closer match to the DNS than the u'^+_{rms} in the near wall region and across the channel.
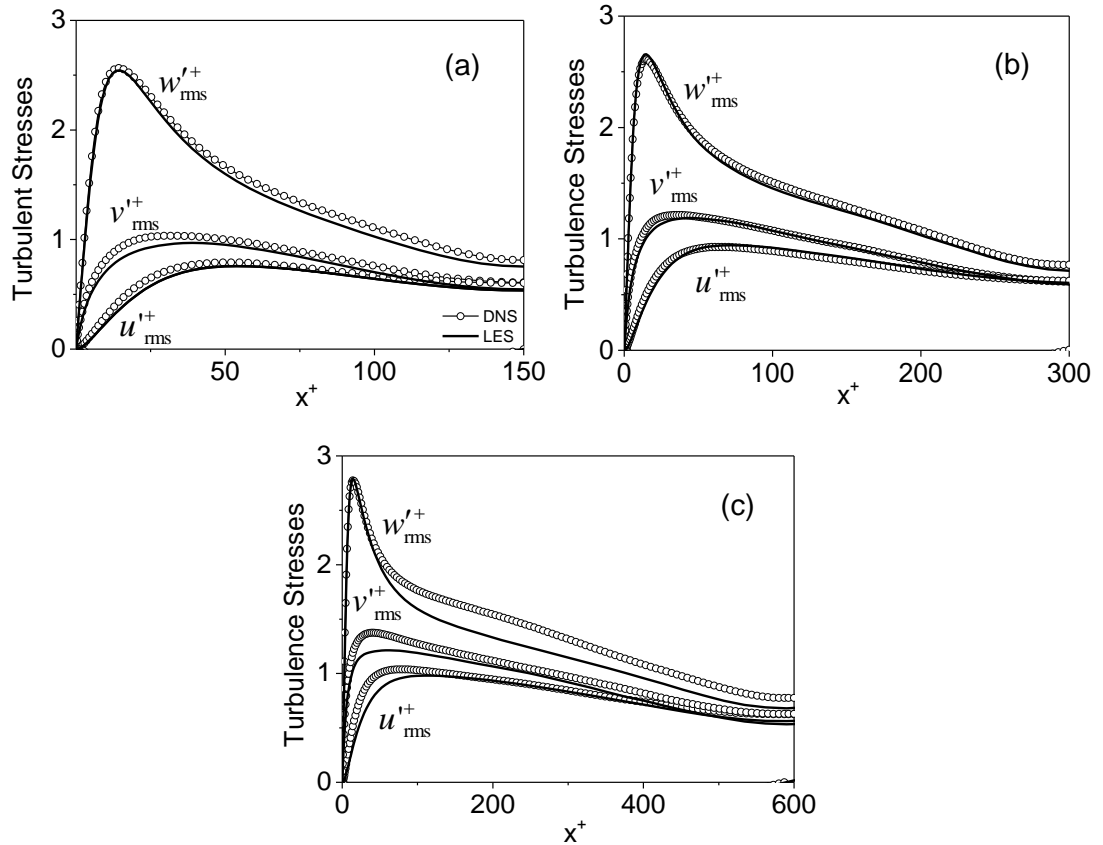
Figure 4.7 RMS Velocity Fluctuations for Single Phase at Re_τ of (a) 150 (b) 300 (c) 590.

In Figure 4.7(b), similar trends were observed for the more turbulent flow case $Re_\tau = 300$, with the LES profiles agreeing very well with those of the DNS. The agreement in this case is so good that the discrepancies becomes insignificant. However, further scrutiny reveals very slight discrepancies between the LES and DNS profiles in this case. The $w_{rms}'^+$ component showed a slightly increased rms peak close to the wall, indicating an over-prediction due to the limited computational resources in this area. This was followed by a small but consistent under-prediction of the fluid solution towards the bulk flow region. Solutions of the $u_{rms}'^+$ and $v_{rms}'^+$ were also in very good agreement. The $u_{rms}'^+$ flow indicates a deviation in the near wall region but achieved good accuracy for the rest of the flow. The $v_{rms}'^+$ solution showed really good agreement with the solution of the DNS, although a slight over-prediction in the bulk flow and an underestimation of the peak fluctuations near the boundary layer is noticed.

Similar behaviour is observed in Figure 4.7(c) for the most turbulent flow case $Re_\tau = 590$, but with a much increased under-prediction of the DNS results in all three co-

ordinate directions, and particularly for the streamwise velocity w'^+_{rms} in the bulk flow region where the deviation from the DNS prediction is observed to be at maximum. The peak region for the w'^+_{rms} component was, however, accurately predicted and fits perfectly into the DNS streamwise profile. The solutions of the u'^+_{rms} and v'^+_{rms} was also in good agreements with the DNS, with only slight deviations in the bulk flow regions. The deviations reached maximum values in the near wall regions in both cases, indicating an under-prediction of the LES, and more pronounced in the v'^+_{rms} flow direction.

As may have been observed, the predictions for the moderately turbulent flow $Re_\tau = 300$, appears to show a more matching trend contrary to the expectation that predictions of the least turbulent flow should give a much closer profile since the turbulence intensity is relatively small. It is therefore necessary to state that with an increase in the run-time for the case $Re_\tau = 150$, much improved predictions is possible but for the case of validation, the current trend is acceptable. However, from the results obtained here there is further evidence to suggest that the under-prediction of the velocity fluctuations for the high turbulence simulation is as a result of the increased turbulence intensity noted for these flows (refer to Table 4.1). Hence, despite the high resolution of the LES used, it becomes increasingly difficult to resolve the turbulent eddies.

Lastly, in Figure 4.8(a-c) the time and space-averaged $u'^+ w'^+$ component of the shear Reynolds stresses for the single phase is plotted against the DNS for all three Reynolds number flow considered in this thesis. For the $Re_\tau = 150$ case in Figure 4.8(a), the Reynolds stress showed good agreement against the DNS solution of Marchioli et al. (2008), although with minor discrepancies in both profiles. Minor offsets were seen at the near wall region of the channels, showing a slight deviation from the DNS, particularly in the region of its peak values. Overall, the agreement between the LES and DNS results of Marchioli et al. (2008) is satisfactory. For the moderately turbulent flow of $Re_\tau = 300$ shown in Figure 4.8(b), the LES profile closely follows that of the DNS and predicts the position of the stress tensor with good accuracy.
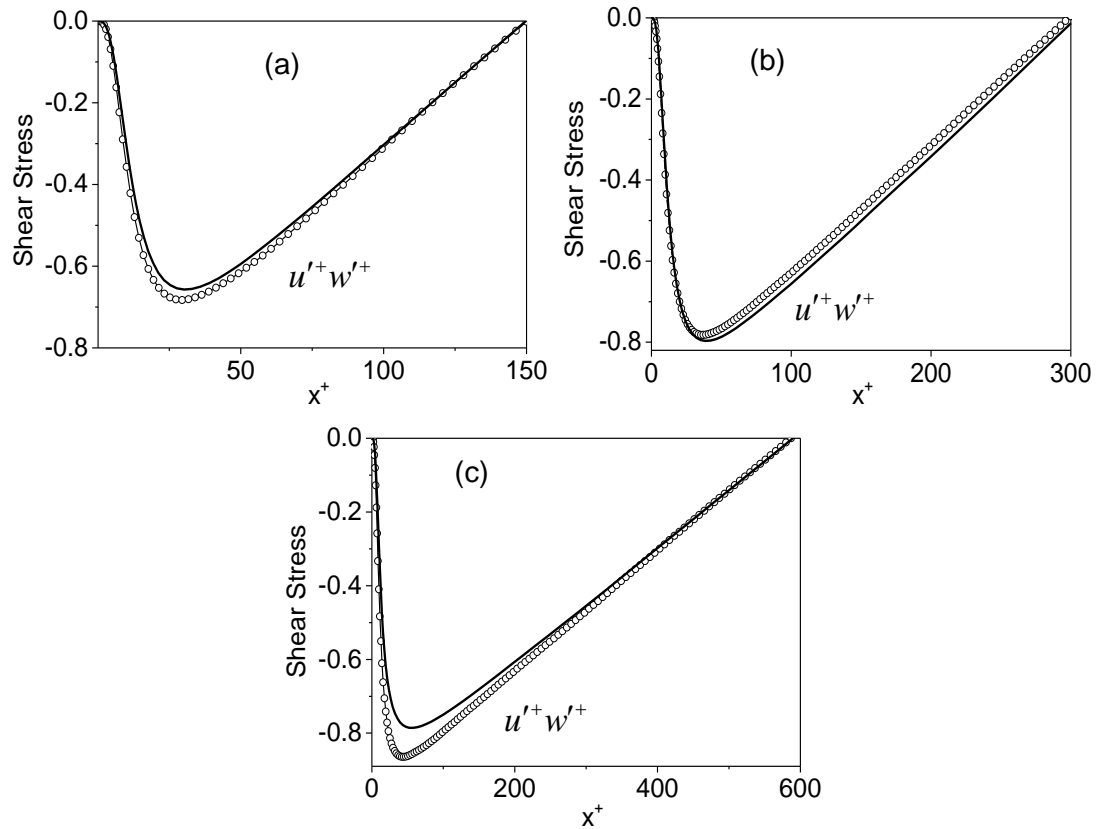
Figure 4.8 Single Phase Reynolds Stress Component at Re_τ of (a) 150 (b) 300 (c) 590

Quantitatively, the near wall regions are slightly over predicted but consistent throughout the channel wall distance. Overall, the agreement between the LES and DNS results of Marchioli and Soldati (2007) is concluded to be very satisfactory. Lastly, Figure 4.8(c) compares result of the LES against those of the DNS for the more turbulent flow of $Re_\tau = 590$, once again, the LES profile follows that of the DNS and predicts the position of the shear stress with good accuracy. Quantitatively, the entire profile across the channel walls was under predicted, with the deviation from the DNS, relative to the lower Re_τ flows, being more pronounced and reaches maximum in areas of its peak values. Overall, the agreement between the LES and DNS results of Moser et al. (1999) is in good agreement, with the discrepancies primarily due to the increase in turbulence intensity in these flows. In all, the deviations were consistent in all three flows studied and showed a good representation of the flow profile. The LES in Figure 4.7 and 4.8 was, however, observed to be reasonably close to the DNS, despite only the resolved turbulent structures being captured.

To conclude the results dedicated to the single phase statistics, a non-commercial high resolution LES code has been employed in the investigation of the turbulent flow

field in a straight channel of rectangular cross section for $Re_\tau = 150$, $Re_\tau = 300$ and $Re_\tau = 590$, with results compared against computational data obtained from the DNS studies of Marchioli et al. (2008), Marchioli and Soldati (2007) and Moser et al. (1999), respectively. Overall, the LES achieved reasonably good agreements with the DNS profiles, in particular for the lower Reynolds number flows, which confirms that the proposed simulation approach captures faithfully the turbulent velocity field within the channel flow. The minor differences noticed in the first and second-order moments of the fluctuating fluid velocity field are, of course, due to the numerical method employed by the LES flow solver for large scales and the SGS model used for small scales as well as the increase in turbulence intensity for the higher Re_τ flows. Extending the simulations to particle-laden flows where particles are included in varying concentrations is therefore anticipated to produce reliable predictions.

4.3.3 Particle Phase Velocity Statistics

As already noted, the validation was extended to dilute, one-way coupled particle-laden flows for $Re_\tau = 150$, $Re_\tau = 300$ and $Re_\tau = 590$, with the predictions again showing similar outcomes in regards to the accuracy of the LES. Overall, therefore, the LES results showed satisfactory agreements with those of the DNS and hence can justifiably be used in predicting the flows of interest in this work.

Figure 4.9(a-f), show the semi-logarithmic plots of two phase flow predictions generated using the coupled LES-LPT method. For the simulations involving all three Reynolds numbers, the analysis in each case was performed in flows laden separately with particles of Stokes numbers $St = 1$ and 5, respectively. The figures compare solutions of the particle mean velocity generated using the LES to that of the more accurate DNS, as investigated in Marchioli et al. (2008). In all cases, the simulation was one-way coupled (dilute); hence, particle movement was solely dictated by the fluid dynamics. Particle-particle interactions were also completely neglected due to the sparse distribution of the particles in the flow. It should be noted that in order to successfully make comparisons of the results generated using the LES with those of the DNS, it became necessary to match the fluid to particle density ratio of both flows for the validation purpose only. The density ratio for the DNS of Marchioli et al. (2008) was approximately 769.231 for a gas ($1.3\ kg\ m^{-3}$) to particle flow $1000\ kg\ m^{-3}$. In this study, the continuous phase used water of density $1000\ kg\ m^{-3}$; hence, the particulate phase used an arbitrary particle of density

769231. This was specified in order to match the density ratio of the DNS. Just like the DNS, the total number of particles, n_p introduced in the flow domain was 100000. All solutions were averaged in both space and time in the streamwise, spanwise and wall-normal directions.

For the least turbulent flow in Figure 4.9(a) and 4.9(b) where $Re_\tau = 150$, as anticipated, the LES predictions just like the fluid phase, is in very good agreement with the DNS, except for the slight over prediction noticed in the bulk flow region towards the channel centre in both figures. Overall, the results obtained for both Stokes numbers 1 and 5 showed an impressive agreement with the DNS data. For the more turbulent flow in Figure 4.9(c) were $Re_\tau = 300$, the LES model just like the lower Re_τ flow, showed good agreement in the near wall regions of the flow and an over-prediction in the rest of the channel length. The over prediction is, however, close enough that the overall prediction is considered in good agreement with the DNS. This is also true for the prediction in Figure 4.9(d), except that the deviation is noticeably more pronounced towards the bulk flow, although a closer match is seen towards the channel centre. In all, the prediction of the LES is confirmed to be more reliable for the lower Re_τ flow, although it predicts to a very high degree the solutions of the particulate phase as the case of the DNS.

Although, there are no data to compare the LES predictions for the most turbulent flow as shown in the Figure 4.9 (e) and 4.9(f) where $Re_\tau = 590$, it is expected that the flow characteristics would follow the same trend as that of the lower Re_τ flows. This means that the flow predictions for both Stokes numbers will be less accurate, as the LES may not sufficiently capture the turbulent scales produced at the near wall regions of the flow but it is anticipated to be of reasonable agreement with the DNS.
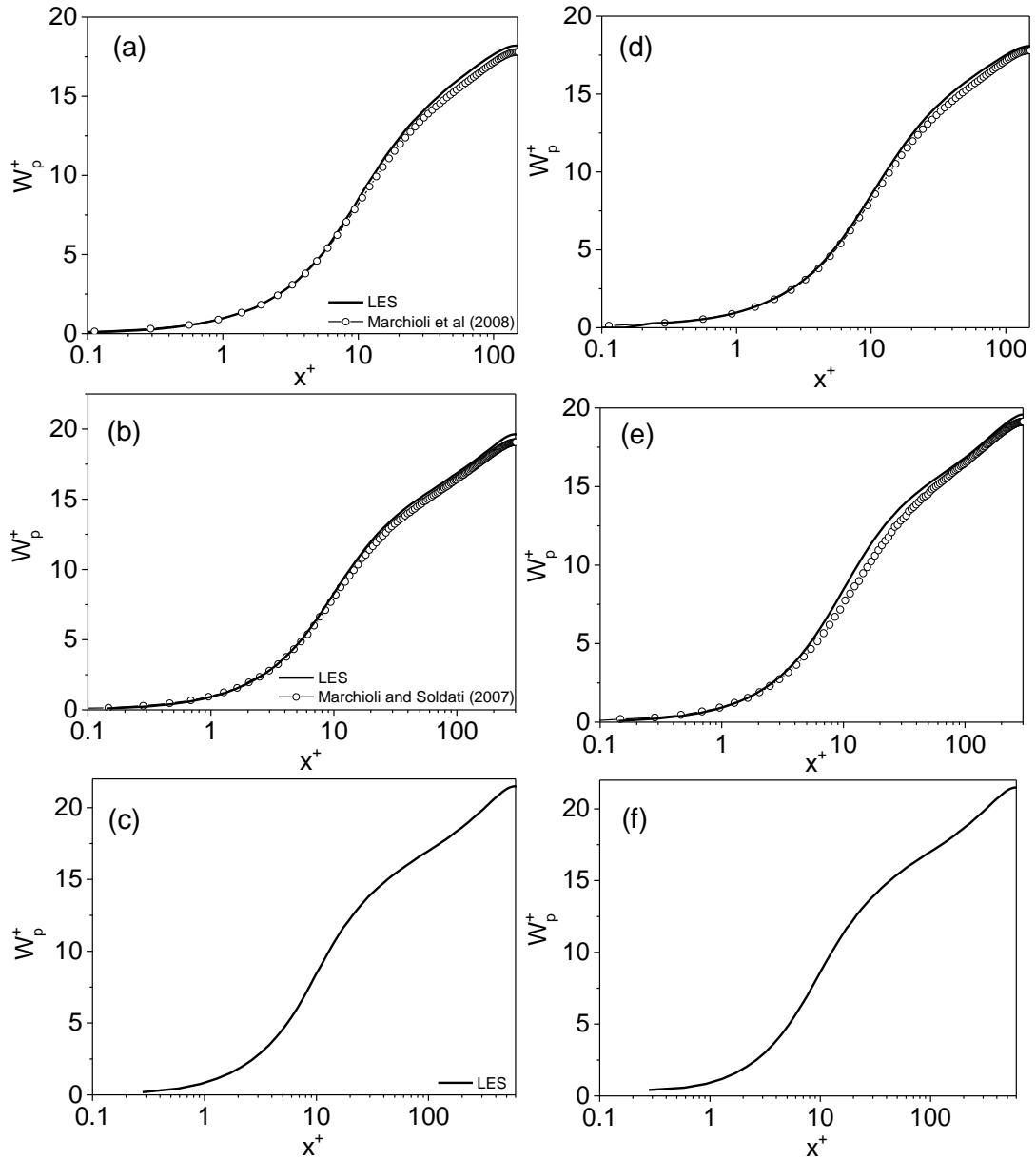
Figure 4.9 LES Particle Mean Streamwise Velocity (a) $Re_\tau = 150$, $St = 1$ (b) $Re_\tau = 300$, $St = 1$ (c) $Re_\tau = 590$, $St = 1$ (d) $Re_\tau = 150$, $St = 5$ (e) $Re_\tau = 300$, $St = 5$ and (f) $Re_\tau = 590$, $St = 5$

4.3.4 Particle Phase Velocity Fluctuations

The plots in Figure 4.10(a-c) are LES simulations showing the rms of the particle velocity fluctuations in all three coordinate directions for the particle phase ($St = 1$), validated against the DNS. From the result in Figure 4.10(a), it is clear that the flow fluctuations towards the channel centre line was under-predicted by the LES. Predictions in the near wall regions show the best agreements with the DNS, except for u'^+_{rms} where an over prediction is noticed close to the wall. The fluctuations in the moderately turbulent flow $Re_\tau = 300$ showed similar agreements as the $Re_\tau = 150$ flow. Although there are currently no DNS data to validate the most turbulent case

$Re_\tau = 590$, it is anticipated that the prediction will be fairly close to the DNS, although the under prediction is expected to increase as the turbulence intensity increases. In all, the LES predictions of the particle velocity fluctuations showed a fairly reasonable agreements with the DNS in all cases.
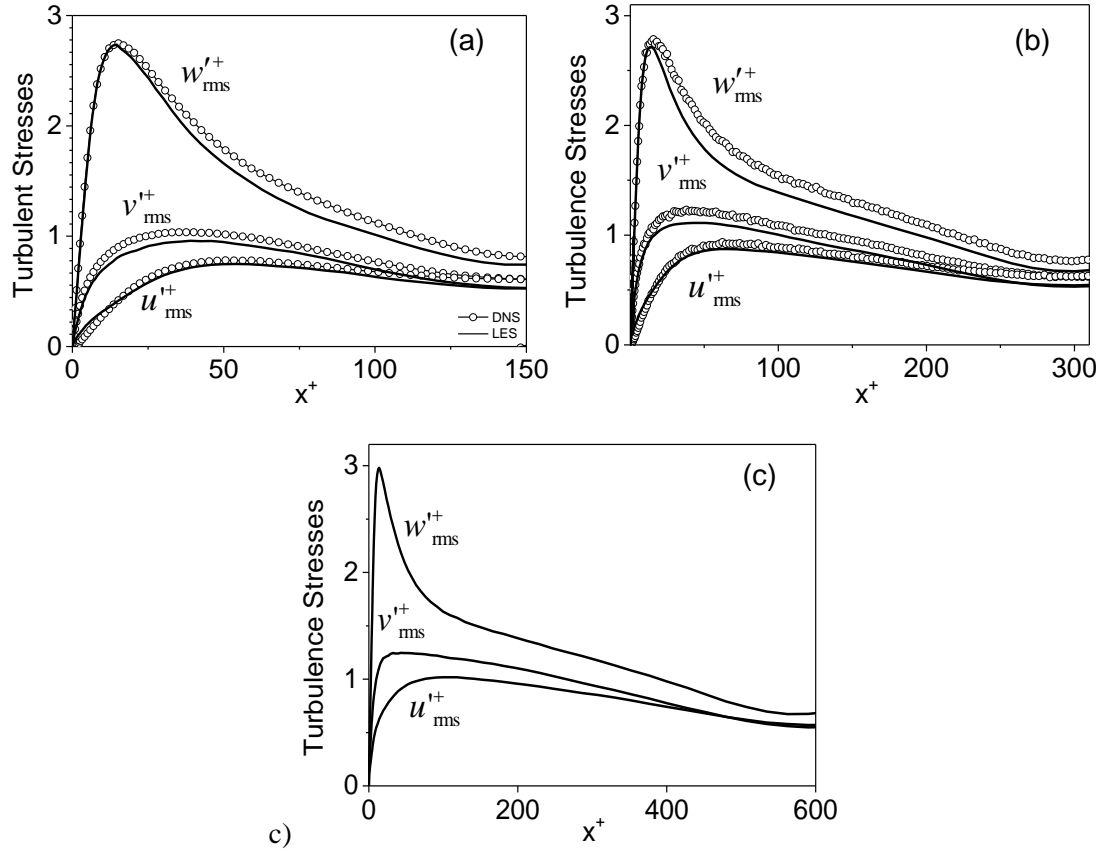
Figure 4.10 RMS Particle Velocity Fluctuations for $St = 1$ at Re_τ of (a) 150 (b) 300 (c) 590

Increasing the particle Stokes number ($St = 5$) in Figure 4.11(a-c) showed no appreciable differences in the LES prediction against the DNS in Figure 4.11(a) but however showed an increased under prediction in Figure 4.11(b), although the under prediction was constant along the channel in all coordinate directions. In all, the same trend is obtained as that of the lower Stokes number, with the best agreement between the DNS and the LES located in the near-wall regions for the streamwise and spanwise directions.
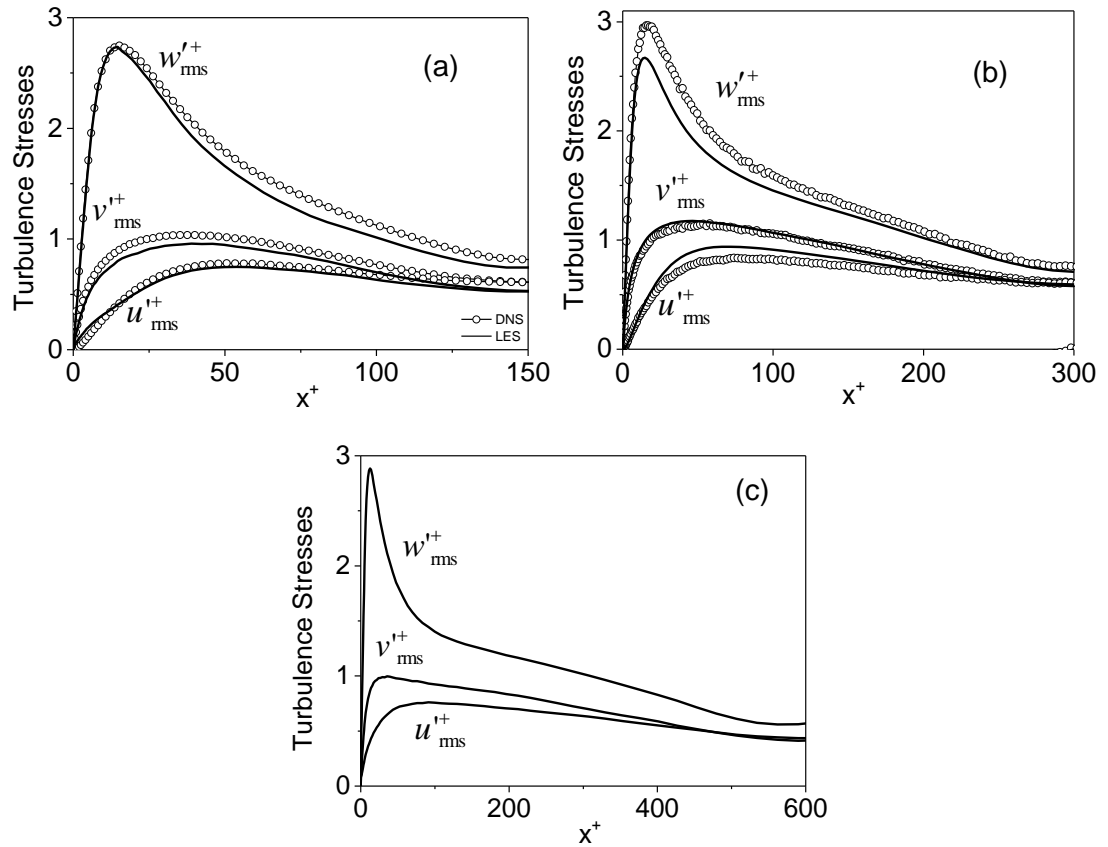
Figure 4.11 RMS Particle Velocity Fluctuations for $St = 5$ at Re_τ of (a) 150 (b) 300 (c) 590

4.3.5 Particle Phase Reynolds Stress

In order for the velocity statistics to be fully verified, the x-z component of the Reynolds shear stress of the particle phase was plotted as shown in Figure 4.12(a-f). The low Re_τ flow for both Stokes numbers follow a similar trend as that of the fluid velocity shear stresses. A good prediction of the stresses is essential, as it directly contributes to the migration of particles towards the wall regions of wall- bounded turbulent flows due to the convective wall-ward drift of particles. The theoretical model description of this phenomenon have been established through assumptions of local equilibrium between particles and fluid turbulence (Young and Leeming (1997). The trend seen in Figure 4.12(a-f) is similar to that observed for the root mean squared (rms) of velocity fluctuations components of the fluid velocities.
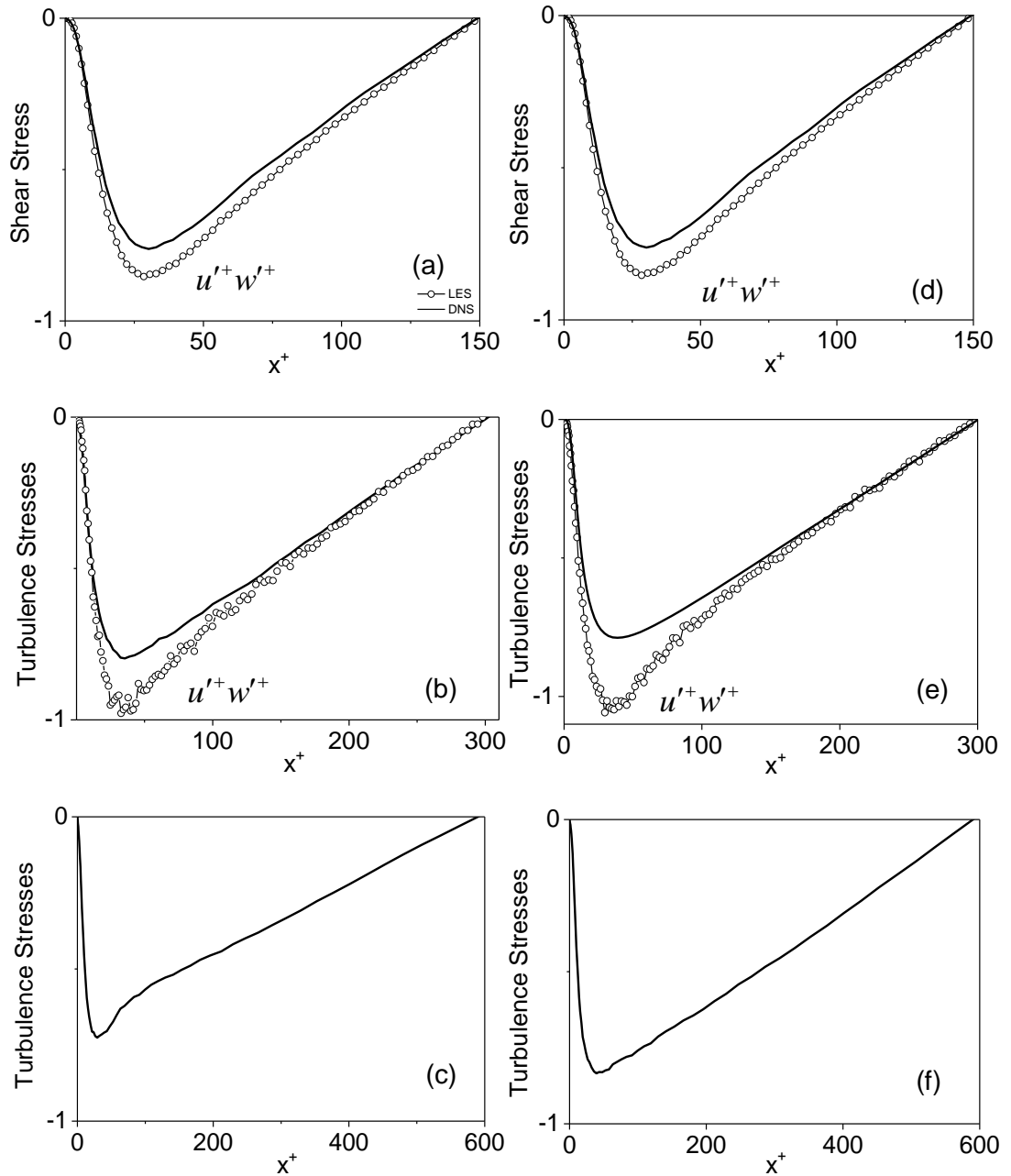
Figure 4.12 LES Particle Phase Reynolds Stress Component (a) $Re_\tau = 150$, $St = 1$ (b) $Re_\tau = 300$, $St = 1$ (c) $Re_\tau = 590$, $St = 1$ (d) $Re_\tau = 150$, $St = 5$ (e) $Re_\tau = 300$, $St = 5$ and (f) $Re_\tau = 590$, $St = 5$.

The LES predictions in Figure 4.12(a) through 4.12(f) show reasonable agreements at the channel center as well as an increasing divergence associated with the calculation of the peak values. The slight oscillatory behavior portrayed in some of the figures is mainly due to the small intervals of time averaging. A longer time span would have been sufficient to smooth out the profiles, although would not have changed the relative positions within the chart. Overall, the LES predictions for the stress tensor compare favourably with those of the DNS in all cases.

4.4 Sensitivity studies on Particle Collision and Agglomeration

For the rest of the simulations in this chapter, the sensitivity of particle-particle collisions and the resulting agglomerations from such collisions is tested for two main simulation parameters, namely, the particle size and the particle volume fraction. The flow was configured in order to match the conditions favouring particle collision and agglomeration for a fully developed turbulent channel flow. Specifically, the particle phase was considered to be dense and therefore four way coupled, with the effect of the particles on the fluid turbulence and particle-particle interactions fully accounted for. The flow considered in all cases used a fixed shear Reynolds number of $Re_\tau = u_\tau h / v = 300$, based on the channel half height, h, the shear velocity, u_τ, and the kinematic viscosity, $v = 10^{-6} \, m^2 \, s^{-1}$, with the fluid density of water, $\rho = 10^3 \, kg \, m^{-3}$. It is important to note that the difference in particle number for each case of the selected particle diameter flow was necessary to maintain the particle volume fraction at 10^{-3}, which is ideal for a four-way coupled simulation. A summary of the simulation parameters for the test cases investigated in this section is given in Table 4.3, with the visual representation of the initially random particle distribution in the channel domain shown in Figure 4.13.
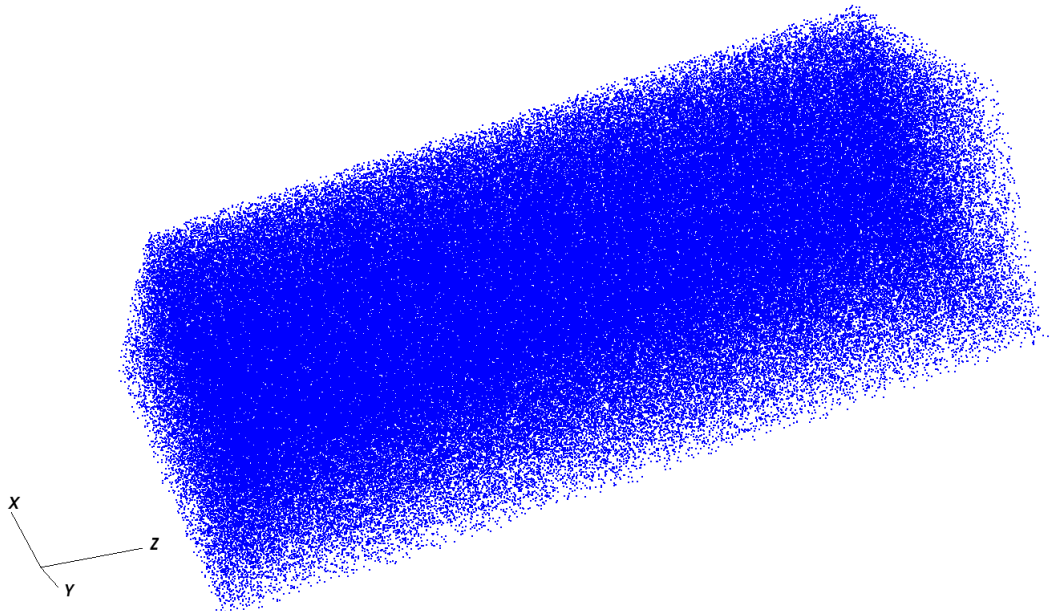
Figure 4.13 The instantaneous initial distribution of the particles in the horizontal channel without the fluid phase.

Table 4.3 Turbulent channel flow grid and particle parameters used for the LES simulations

$d_p/\mu m$	$St = \tau_p^+$	τ_p	$\emptyset_p$	Re_τ	N_{pp}
75	0.23	0.85×10^{-3}	10^{-3}	300	1430349
125 (Base Case)	0.63	2.35×10^{-3}	5×10^{-4} 10^{-3} 5×10^{-3}	300	308955
250	2.51	9.41×10^{-3}	10^{-3}	300	38620

Re_τ	$L_x \times L_y \times L_z$	$N_x \times N_y \times N_z$	Δ_x^+	Δ_y^+	Δ_z^+	$h\,(m)$
300	$2h \times \pi h \times 2\pi h$	$129 \times 128 \times 128$	$0.31 - 27.92$	14.59	14.84	0.02

4.4.1 Effect of Particle Size on Particle Collision and Agglomeration

The investigation in this section of the thesis discusses the effect of particle size on collision and agglomeration in turbulent two phase flows. The work is motivated based on the fact that the primary particle constituents typical of industrial turbulent two-phase flows are of different particle sizes. Hence, in attempt to replicate these flows, it becomes necessary to study the effect of the particle sizes on the phenomenon of interest. It is also well known that in such particle laden two phase flows the degree of response of the particles to changes in the flow perturbations, quantified by the dimensionless Stokes number *St* (described in previous chapter), becomes a key factor in determining the collision and agglomeration rate and distribution in the flow field (Breuer et al., 2006). It is of interest therefore to understand the influence of different particle sizes on collision and agglomeration. Here, all relevant forces but the force of gravity and buoyancy have been fully considered. The exclusion of the net gravity-buoyancy force at this stage of the research is necessary to isolate the desired effect of particle size on collision and agglomeration for fully developed turbulent horizontal channel flows. The analysis here, was performed using the base case Reynolds number of $Re_\tau = 300$, with the aim to check that the particle collision and agglomeration behaviour at a moderate flow velocity is still consistent with those previously observed for the lower Re_τ flow case (Njobuenwu et al., 2017). The study is further extended to check the impact of the particle interactions on the fluid turbulence. Other simulation parameters are as specified in Table 4.3. The forces considered are analysed further into the chapter.
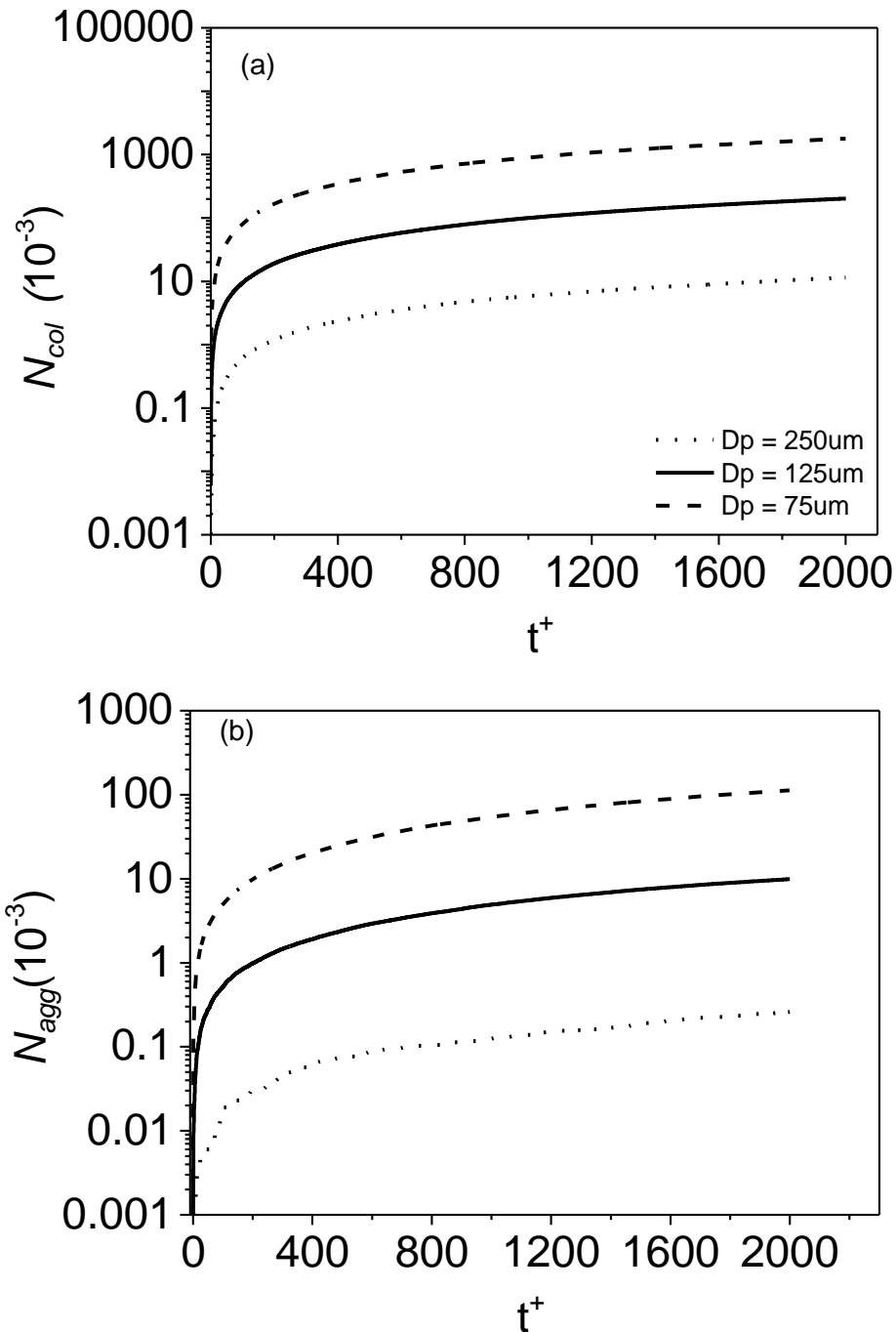
Figure 4.14 Total number of collisions and agglomeration comparison for all particle sizes (a) Number of collisions and (b) Number of agglomerations for time up to $t^+ = 2000$ at $Re_\tau = 300$

Figure 4.14 (a) and 4.14 (b) at the given shear Reynolds number flow compares predictions for the selected particle sizes, in terms of the total particle collision count, N_{col} and the resulting number of agglomeration events, N_{agg}, formed up to a simulation time of $t^+ = 2000$ (~8.9 s in real time). Here, the superscript (+) represents variables made dimensionless using u_τ and the kinematic viscosity v. From the results in Figure 4.14(a), it is noticed for all sizes that collision and agglomeration of

particles occurs at the start of the simulation. By time, $t^+ = 2000$, there were a total of $1{,}817{,}670$, $205{,}762$ and $11{,}596$ particle collisions in the $75\,\mu m$, $125\,\mu m$ and $250\,\mu m$ flows respectively. With the resulting agglomeration from such collisions amounting to $109{,}225$, $9{,}567$ and 212 in the $75\,\mu m$, $125\,\mu m$ and $250\,\mu m$ flows, respectively. For all three particle size flows, the results clearly indicate an increase in the number of collisions and agglomerations with time, and that not all collisions have resulted in the agglomeration, with the flows having far more collisions when compared to those that resulted in agglomeration. On close observation, it is revealed that there was a sharp increase in the number of collisions and agglomerations from $t^+ = 10$ in all cases, but as the simulations progressed the flow metrics approach a steady state, with the number of collision and agglomeration events decreasing at a steady rate. However, the results clearly show an inverse relationship between the rate at which particle contact is made and the particle size, indicated by the higher rate of the smaller particle size case of $d_p = 75\,\mu m$. Here, considerably more collisions and agglomeration events occurred, with a high collision to agglomeration ratio of approximately $17:1$ as to $22:1$ for the $d_p = 125\,\mu m$ particle size flow and $55:1$ observed for the particle size $d_p = 250\,\mu m$ were the lowest collision to agglomeration ratio is seen. It is necessary to note here that the differences observed in the number of collision and agglomeration events for all particle sizes may be attributed to the fact that, in an attempt to keep the volume fraction the same across all flows, more particles were introduced with decreasing particle size. This is to say the smaller particle diameter, simulations used far more particles which encouraged particle-particle interactions and consequently more agglomeration.

More importantly, smaller diameter particles also have a lower Stokes number which means they follow the instantaneous velocity field more closely into areas of high turbulence near the walls, encouraging collision and agglomeration as a result. Another reason for the increased collision and agglomeration events for the smaller sized particle is due to their larger surface area per unit volume compared to the larger size particles, which favours particle agglomeration as they tend to be more responsive to the flow perturbations (see, Lin and Wey (2004)). In contrast, in the higher Stokes flow with $d_p = 250\,\mu m$, the high inertia of the particles ensures that they become less responsive to the perturbations of the fluid flow which consequently makes them more resistive to the flow, and therefore enhances their migration into the more turbulent wall regions. Hence, only fewer particle contacts are made which then results in less agglomeration as seen in Figure 4.14(b). The difference in

characteristics observed for these flows is an indication of the importance of the Stokes number as it becomes crucial in determining the dynamics of the particles in the flow, influencing particle collision and agglomeration in the process. The rate of collision and agglomeration in the cases cited, however, continued to increase with time, although at a more steady state.

In order to effectively describe the particle size contribution to the agglomeration formation process, it becomes necessary to also analyse the sizes of the agglomerate formed as would be the case in practical applications. Figure 4.15(a-c), therefore, gives results concerning the size of the agglomerates formed over time for the selected particle sizes. The rate of depletion of the single particles and the corresponding evolution of multi-particle agglomerates is shown for each particle size, up to a simulation time of $t^+ = 2000$. At the start of all simulations, the results indicate a sharp increase in the number of two particle agglomerates formed up to time, $t^+ < 100$, which can be attributed to the influence of the initial conditions in the flow. With increasing time, larger agglomerates are observed to form through collisions between single particles and larger agglomerates, and between the agglomerates themselves. However, the rate of formation of the multi-sized particles is observed to differ with the variation in particle size. In Figure 4.15(a), up to 1000 double particle agglomerates were formed before a time $t^+ \simeq 100$, after which was the evolution of larger size agglomerates as the simulation approached a steady state. For the flow with particles of diameter $d_p = 125\,\mu m$ in Figure 4.15(b), similar trend is noticed, except that much lesser agglomeration occurred within the simulation time $t^+ = 2000$, with only 1000 double agglomerates formed before the time $t^+ \simeq 100$. This was even less for the flow with the largest particle size $d_p = 250\,\mu m$ in Figure 4.15(c) were only double agglomerates formed during the simulation time $t^+ = 2000$, with below 1000 formed by $t^+ \simeq 100$. However, the rate of formation reduces to a more steady state as interactions with the turbulent flow structures increase.

Nonetheless, the formation of agglomerates is much more prevalent for the smaller primary particles, with agglomerates consisting of up to seven primary particles formed over the time period considered ($t^+ = 2000$), contrasting with a maximum of three particle agglomerates for the $d_p = 125\,\mu m$ case and two for the $d_p = 250\,\mu m$ case. Again, this is due to the larger number of small particles present within the flow, and the relatively high inertia of the larger particles which makes them less

responsive to instantaneous variations in the velocity field. In other words, it is also observed that as the formation of larger sized agglomerates continue to occur, the rate of particle collisions reduces over time, which explains also the reason for the decline in the number of collisions and agglomerations observed for all three particle size flows as the solutions approach a more steady state. This behaviour is supported by Wang et al. (2015) where it was concluded that agglomerates formed by small particles are normally larger than those formed by coarse particles and also that small particles are the main composites of agglomerates. The authors in their experimental studies on particle diameter effects on agglomeration also established that inter-particle collisions between small particles lead to much easier formation of agglomerates compared to those between small particles and coarse particles or coarse and coarse particles. This therefore provides qualitatively, an explanation for the behaviour observed thus far.
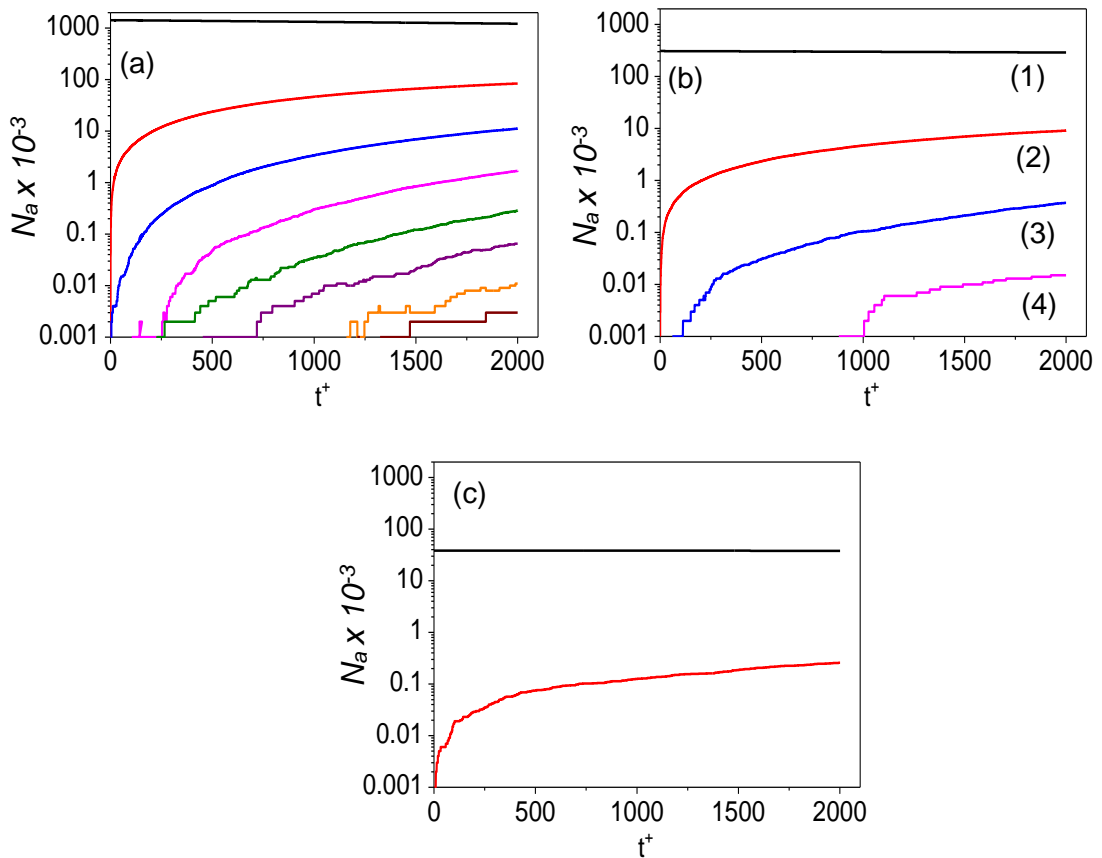
Figure 4.15 Single particle depletion and agglomerate growth with time: (a) $d_p = 75\,\mu m$ (b) $d_p = 125\,\mu m$ and (c) $d_p = 250\,\mu m$ particles. Line numbers: single (1), double (2), triple (3), quadruple (4), etc. particles.

This behaviour is further elucidated in Figure 4.16 where the particle agglomeration rate is examined for all three cases. Here, the agglomeration rate is obtained in terms

of the ratio of the collisions leading to particle agglomeration N_{agg} to the total number of collisions N_{col} for the time considered, and expressed as N_{agg}/N_{col}. For the two smaller size particles, a sharp decreasing rate of agglomeration is observed from the start of the simulation but was, however, due to the initial conditions already mentioned. Nonetheless, the flow quickly achieved a steady state. In all, the agglomeration rate was observed to increase with reduction in particle size. This behaviour is in agreement with Breuer and Almohammed, (2015) where it is shown that the rate of agglomeration increases by a factor of approximately 4.8 when the diameter of the particles is reduced by a factor of three.
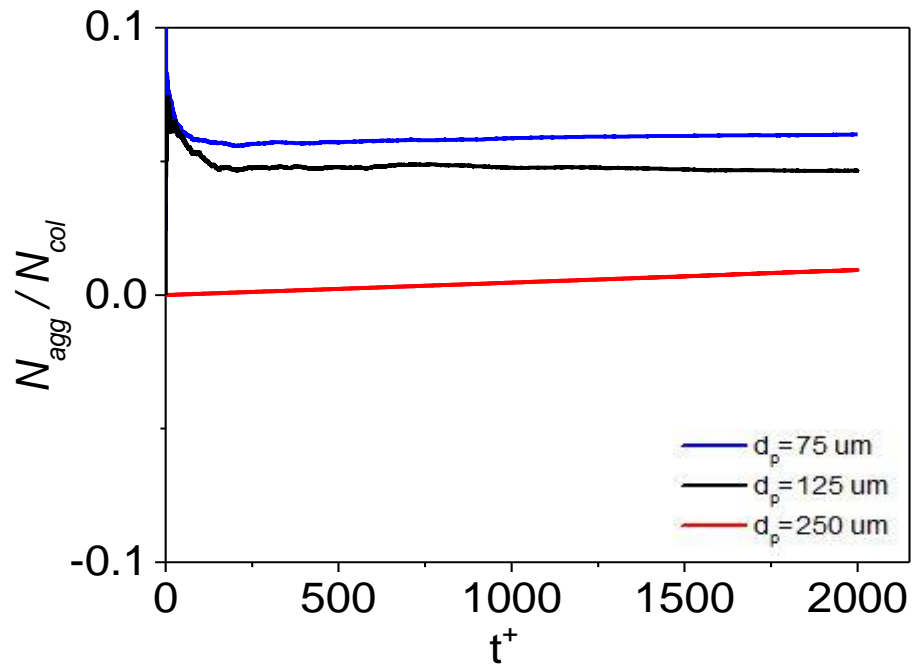
Figure 4.16 Particle rate of agglomeration comparison for a dimensionless time up to $t^+ = 2000$ at $Re_\tau = 300$. Flow without gravity.

The information concerning the collisions and agglomeration distribution across the channel and the locations where they occur for $d_p = 75\,\mu m$, $d_p = 125\,\mu m$ and $d_p = 250\,\mu m$ is given in Figure 4.17, Figure 4.18 and Figure 4.19 respectively; and at mean time values of $t^+ = 500, 1000$ and 2000 in each case, although the results are averaged over the length of the channel and over t⁺ ± 500 (mean taken 500 either side of the value i.e. $t^+ = 1000$ means $(t^+_{501} + t^+_{502} + \cdots + t^+_{1500})/1000$ to provide a sufficiently large sample for analysis. The cross-stream domain was divided into 16 equally spaced slabs in the wall normal direction in all cases. Figure 4.17(a-c) shows

the collisions and agglomeration distribution for the smallest particle size $d_p = 75\,\mu m$ at the specified non-dimensional time interval. The number of collisions was found to be near symmetry, with maximum collisions experienced in the two near wall regions. The study of Afkhami et al. (2015), where the particle concentration was found to be dominant in the near wall regions of maximum turbulence, provides an explanation for the increased collisions observed in this figure. The findings also compliment the study of Breuer and Almohammed, (2015) who reached the same conclusion in their study and attributed the particle migration towards the wall to be as a result of turbophoresis.
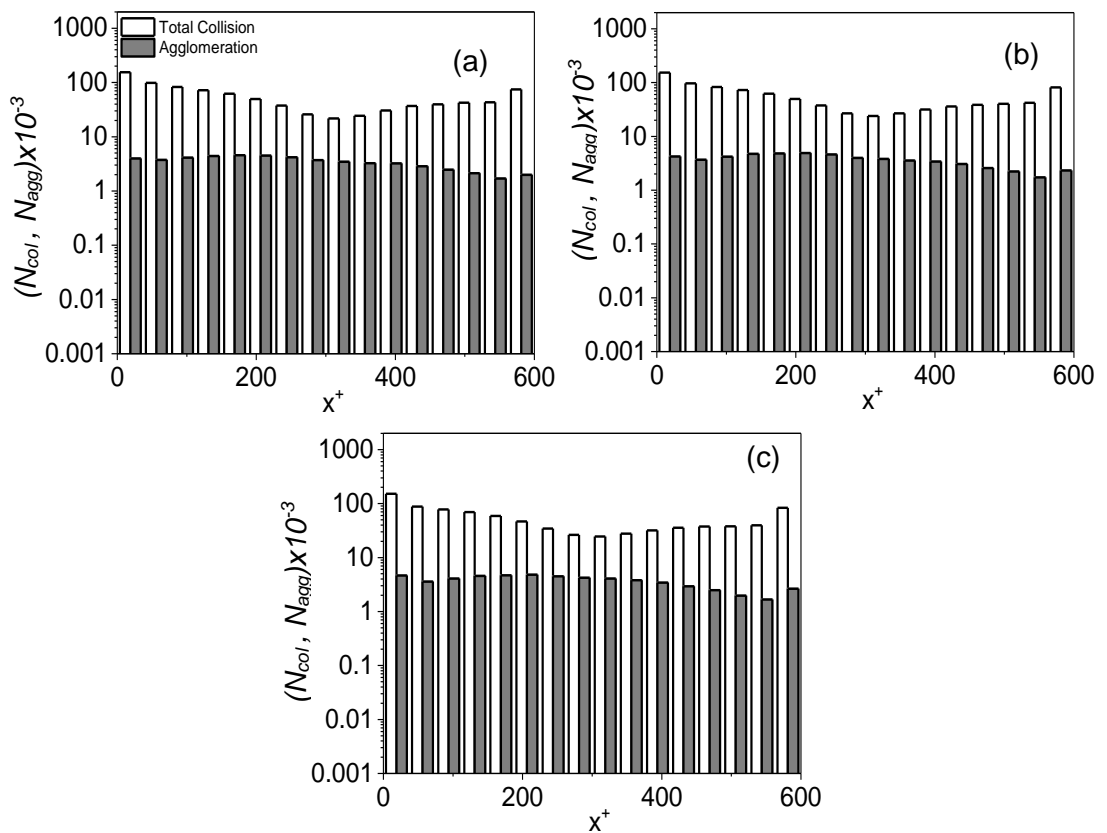
Figure 4.17 Distribution of particle collisions and agglomerations across the channel at different times at $d_p = 75\,\mu m$, for (a) $t^+ = 500$ (b) $t^+ = 1000$ and (c) $t^+ = 2000$

In Figure 4.17(a) the agglomeration events appear to be evenly distributed across the channel, although slight peaks are seen close to the walls where turbulence levels are high. The collision events close to both walls peaked at approximately 100000 and slightly lesser in the bulk flow. However, the trend is roughly stable over the simulation time as indicated in Figure 4.17(b) and 4.16(c) where there seem to be no further increases in the collisions and agglomerations. The reduction in the concentration of the collision events in the bulk flow region of the channel is as a

result of the reduced particle velocity fluctuations in this region, and also due to turbophoresis which tend to enhance particle migration towards the wall regions. However, it is also noticed that the number of agglomeration events in the bulk flow regions increased even though only minimal collisions occurred in this region. This is due to the fact that when particles collide within this less turbulent region, their combined energy post-collision is in most cases insufficient in overcoming the van da waal's energy existing between them and therefore particle agglomeration is encouraged. In other words, agglomeration is more favorable in conditions where the turbulence is in a low state. This observation compliments the findings of Breuer and Almohammed, (2015) where it was also shown that the rate of particle agglomeration is maximum in regions far away from the channel wall; and that the concentration of particle–particle collisions is decreased due to the reduction of the particle velocity fluctuations in the same region.
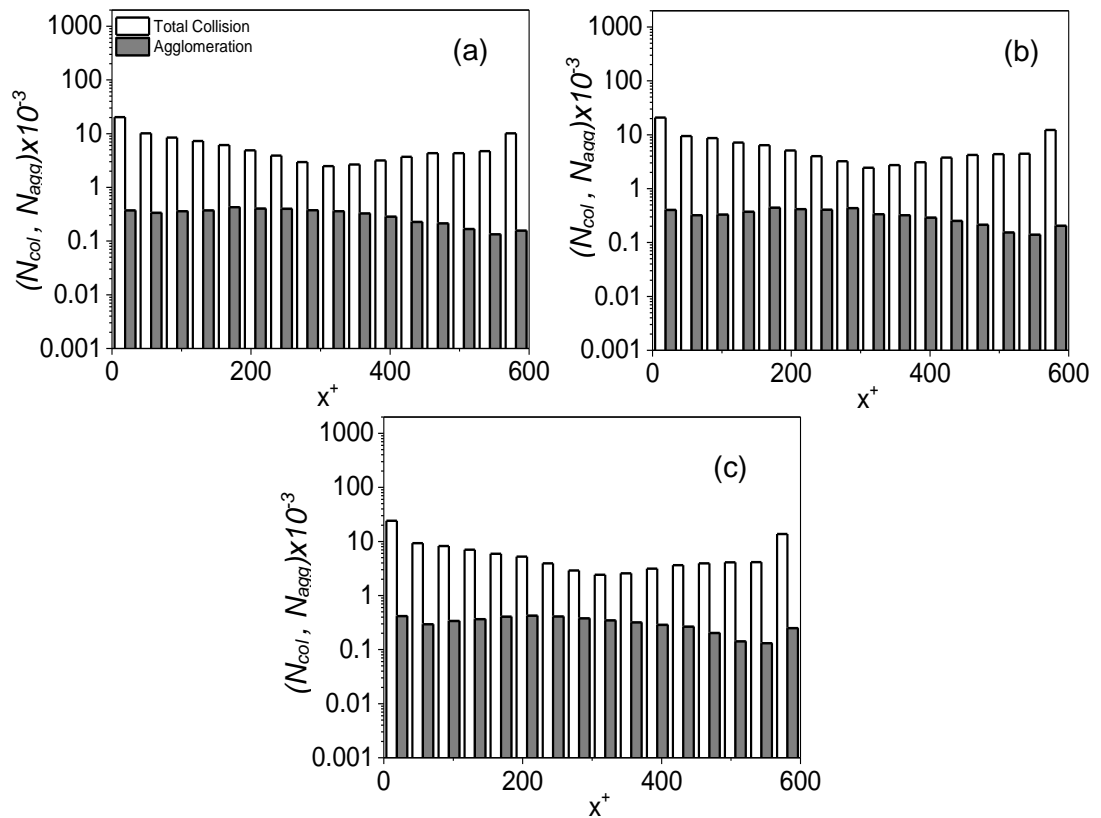
Figure 4.18 Distribution of particle collisions and agglomerates across the channel at different times at $d_p = 125 \, \mu m$, for (a) $t^+ = 500$ (b) $t^+ = 1000$ and (c) $t^+ = 2000$

Figure 4.18 (a-c) again shows the particle distribution but for the medium size particle $d_p = 125 \, \mu m$ at the specified non-dimensional time interval. The number of collisions was also found to be near symmetry, with maximum collisions experienced in the two near wall regions just as with the $d_p = 75 \, \mu m$ case, but with much fewer collisions

(near wall $\simeq$ 20000; bulk flow $\simeq$ 18000) and agglomeration. Again, the number of agglomeration appears to be evenly distributed across the channel, although slight peaks in the near wall regions where turbulence levels are high. Overall, the change in the collision and agglomeration count over time is negligible; see, Figure 4.18(b) and 4.18(c). Just as in the smaller sized particle case, closer examination of the plots, reveals that more agglomeration occurred in the bulk flow where turbulence levels is low, even though only minimal collisions occurred in this region.
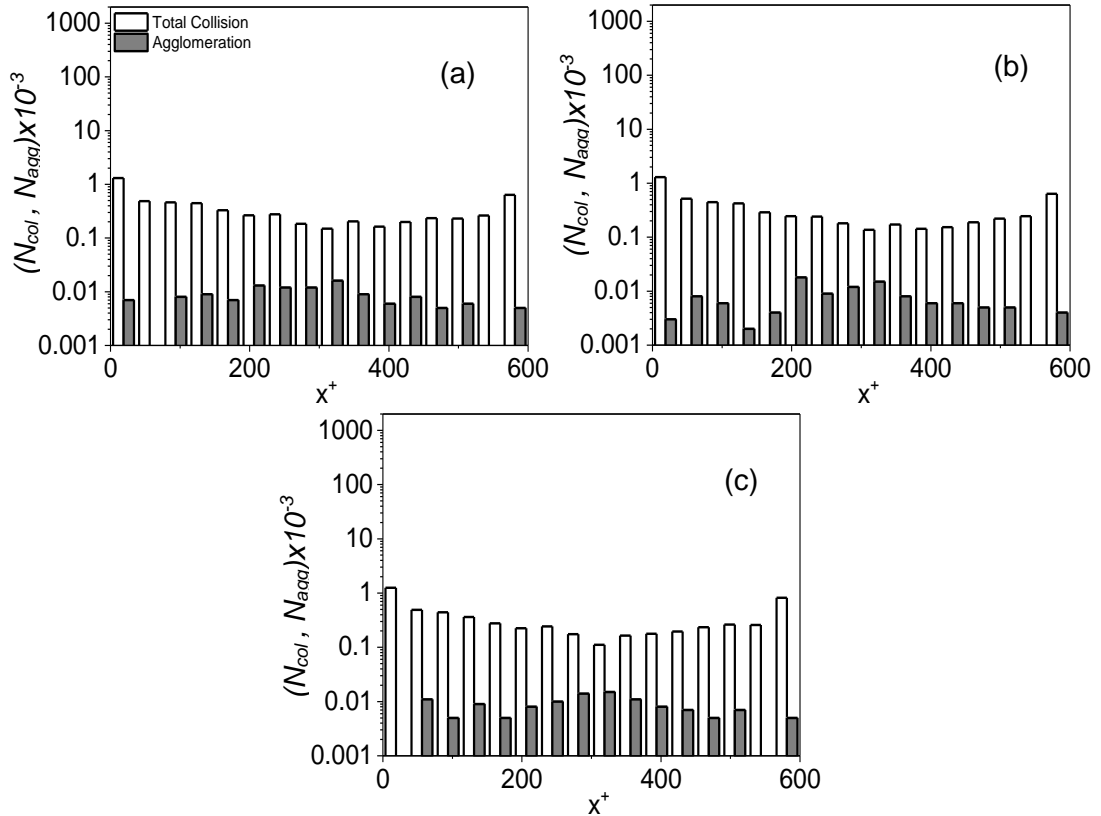
Figure 4.19 Distribution of particle collisions and agglomerates across the channel over time at $d_p = 250\ \mu m$, for (a) $t^+ = 500$ (b) $t^+ = 1000$ and (c) $t^+ = 2000$

In Figure 4.19(a) the collision and aglomeration distribution shown for the largest size particle $d_p = 250\ \mu m$ follows similar trend as the smaller size particles and also true for Figure 4.19(b) and 4.19(c), except that only small amount of particle collision (near wall $\simeq$ 1000; bulk flow $\simeq$ 100) is noticed, with the resulting agglomeration minimal for this case. From the results observed, that particle-particle collision and agglomeration is strongly influenced by the size of the particles, with increase in the phenomena observed as particle diameter is reduced. This compliments well with the findings of Breuer and Almohamed (2017) where the same conclusion is reached. Therefore, it is important to note that an industrial flow with smaller particles will be

more exposed to particle agglomeration, which could be possibly useful, and of course dependent on the application.
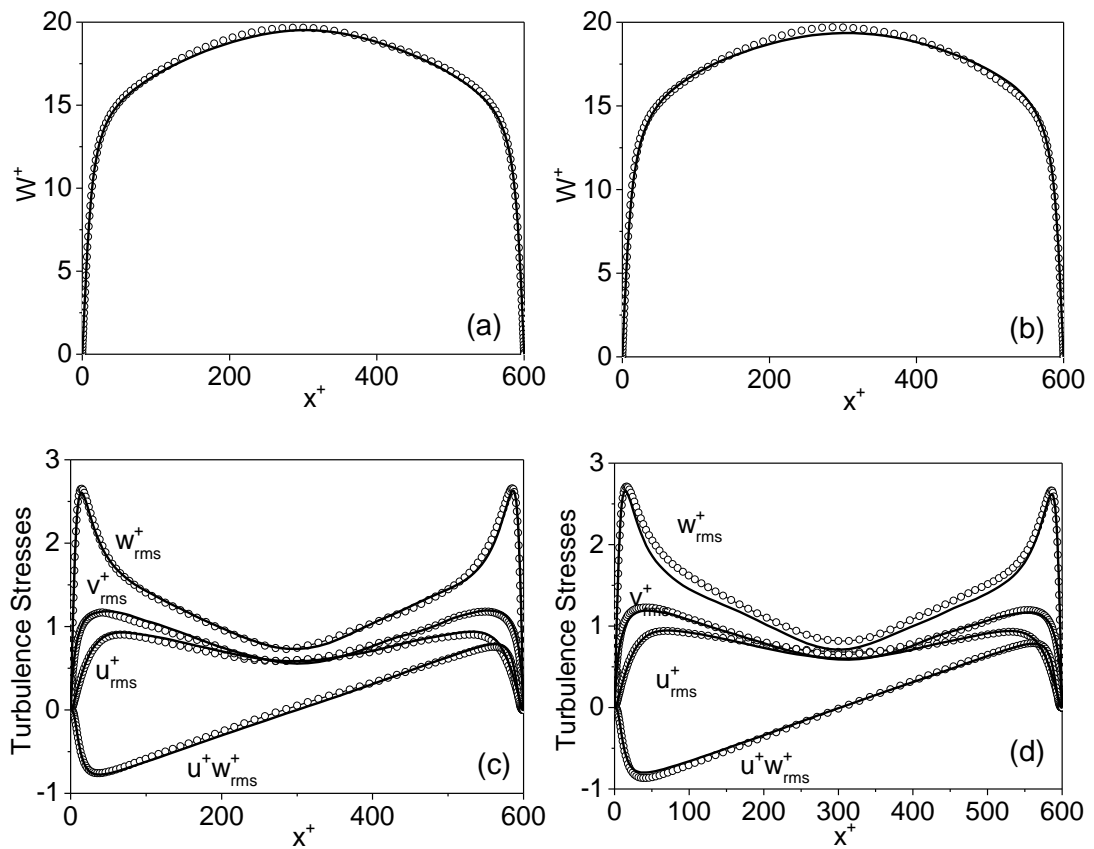
Figure 4.20 The instantaneous fluid mean streamwise velocity at time $t^+ = 1000$ for (a) $d_p = 75\,\mu m$, (b) $d_p = 250\,\mu m$; and fluid normal and shear stresses for (c) $d_p = 75\,\mu m$ and (d) $d_p = 250\,\mu m$ particles case (— single-phase flow, ○ multi-phase flow).

Lastly, the effect of particle size on the mean fluid velocity, and fluid normal and shear stresses, is considered for the smallest and largest particle sizes in Figure 4.20(a-d), and for a fixed time $t^+ = 1000$. The motivation is inspired by the work of Vreman et al. (2009) where it was concluded that the particle-particle interactions in a two-way flow system influences the flow statistics of both phases. The analysis is performed by making comparisons with the mean streamwise velocity of the unladen fluid flow. The impact of particles on the mean streamwise velocity for both particle sizes in Figure 4.20(a) and 4.20(b) is minimal, although a slight enhancement in the mean stream velocity is noticed in both cases and more pronounced in the case of the larger particle size flow. In Figure 4.20(c) and 4.20(d), normal and shear stresses are affected more significantly, especially for the larger particles, where an impact on the streamwise normal stress is noticeable for the $d_p = 250\,\mu m$ case, indicating an increase in the turbulence flow intensity. This is in agreement with literature (Crowe

et. al., 1989, Crowe, 2000, Tsuji and Morikawa, 1982, Tsuji et al., 1984 and Sommerfeld, 2002), where it is well established that larger particles augment fluid turbulence through wake shedding due to their size, and therefore intensify the turbulence.

4.4.2 Particle Force Analysis

In this section we examine the forces per unit mass acting on the particles in the direction of the wall where particle concentration is maximum for the flow of Reynolds number, $Re_\tau = 300$. The analysis in each case is performed at a fixed time ($t^+ = 1000$) as the values calculated in each node per unit time was first compared in magnitude to values obtained at the nodes at other times throughout the flow, with no significant differences observed. Hence, the figures are only a representative of a particular instant in the flow, although averaged over t$^+$ ± 100 (mean taken 100 either side of the value i.e. $t^+ = 1000$ means $(t_{901}^+ + t_{902}^+ + \cdots + t_{1100}^+)/200$. It should be noted that the averaging did not change the magnitude of the different forces acting on the flow but only performed to ensure a relatively smooth profile is obtained. The plots in Figure 4.21(a-f) are representative of all the individual forces acting on the particles of size, $d_p = 75\ \mu m,\ 125\ \mu m$ and $250\ \mu m$ across the channel at a time, $t^+ = 1000$. Specifically, the forces analysed are the hydrodynamic forces acting on the particles which in order of magnitude of their effect includes the drag, shear lift, pressure gradient and added mass forces. The net gravity/buoyancy was excluded as it has not been considered for the flow analysis in this chapter.

All the forces considered are noticed to be in symmetry and maximum in the near wall regions of the channel as expected, although very pronounced is the drag and the lift forces acting almost equally in the opposite directions of the particles, which of course, explains why collision and agglomeration events across the channel are nearly symmetric. Figure 4.21(b, d and f) is a close-up view on Figure 4.21(a, c and e), showing the magnitude of the less dominant forces. From the figures in all cases, the effect of the pressure gradient and added mass on the particle are considered very small relative to the effect of the drag and shear lift forces which are observed to be the most dominant forces and maximum in the wall regions where the particle concentration and turbulence is maximum. On a close observation, it is however, noticed that the magnitude in which the surrounding hydrodynamic forces acts on the particles varies with the variation in particle size. The effect of the drag and lift forces on the particle is observed to be increased as the size of the particle is increased.
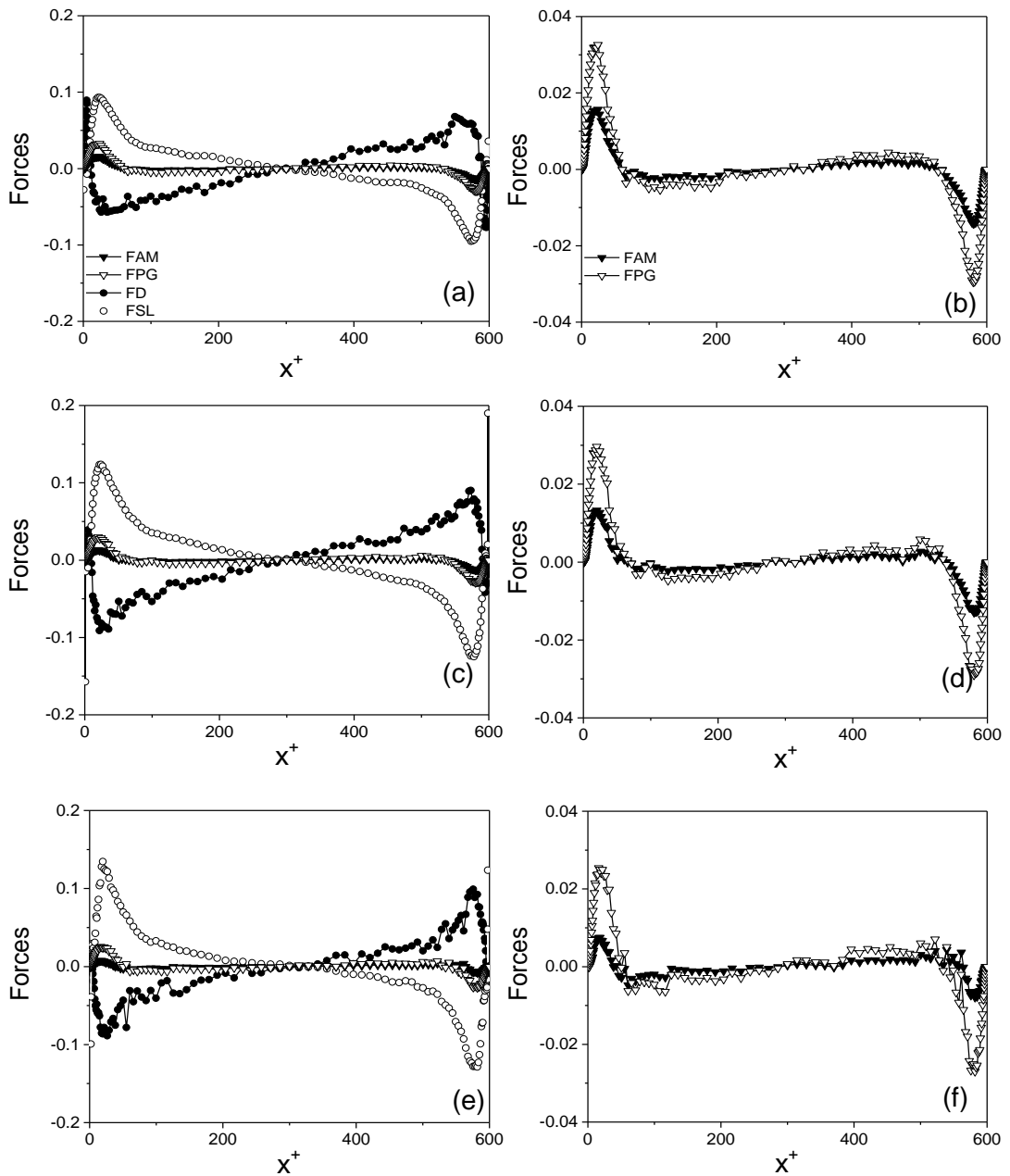
Figure 4.21 Forces (N/kg) analyses for Re_τ = 300 at t+ = 1000 (a, c, e) forces acting in the wall normal direction on particles (b, d, f) zoomed profile showing the relative magnitude of the smaller forces acting within the flow. (a, b) $d_p = 75 \, \mu m$ (c, d) $d_p = 125 \, \mu m$ and (e,f) $d_p = 250 \, \mu m$ (F_{SL} = shear lift, F_{AM} = added mass, F_D = drag, F_{PG}= pressure gradient).

This is in agreement with previous investigations as it is well known that smaller particles are more responsive to the fluid flow, and hence, would therefore follow the flow more closely, reducing the impact of the drag in the process. This further explains the reason for the increased particle collision and agglomeration rate for the flow with $d_p = 75 \, \mu m$ as these particles, having less resistance to the flow, becomes easily dispersed to areas close to the walls were turbulence is maximum, therefore enhancing collision and agglomeration. For the larger size particles the impact of the

drag and lift is much higher since the particles are less responsive to the fluid flow, which then results in an increased drag impact on the particle as in the case in Figure 4.21(c) and 4.21(e). It is necessary to highlight here that the drag force is obtained from the slip velocity between the fluid and particle $u_f - u_p$ (see LPT in methodology).

The lift on the other hand, provides a counter-balance to the drag force and increases as the drag force is increased. Further scrutiny reveals a contrasting behaviour for the effect of the smaller forces on the particles. It is noticed that the added mass and pressure gradient forces are increased as the particle size is decreased, with the added mass force having the lowest impact on the particle, which is in accordance with the investigations by Elghobashi and Truesdell (1993) were it was shown for a similar flow condition that the Stokes drag and buoyancy force are the only significant forces acting on the particle, although the force of buoyancy was neglected due to the effect of gravity not being considered herein. In all, the results obtained for all Re_τ flows showed great similarities, with the dominant forces acting on the particles being the drag and the lift for this flow condition.

4.4.3 Volume Fraction Effect on Collision and Agglomeration

In this section, the investigation on particle collision and agglomeration is extended to flows of varying volume fractions in order to understand the contribution of the volume fraction on particle collision and in the agglomeration formation process. Relatively to the particle volume fraction, Φ_p applied in the previous investigations ($\Phi_p = 10^{-3}$), the section made comparisons on flows with low and high volume fractions of values $\Phi_p = 5 \times 10^{-4}$ and $\Phi_p = 5 \times 10^{-3}$ respectively. The total number of particles introduced into the flow in each case amounts to 154478, 308955 and 1544778, respectively, for only the base case particle size $d_p = 125\ um$. Again, all relevant forces dictating the dynamics of the particles were fully considered, with the net gravity/buoyancy force, again, switched off in this section for reasons previously highlighted in section 4.4.1.

In Figure 4.22(a), the total number of particle collision events, N_{col} which occurred up to a time $t^+ = 2000$ (~8.9 s in real time) is plotted for the selected Φ_p flow cases, with comparisons made against the base case with $\Phi_p = 1 \times 10^{-3}$. From the result, it is noticed that collision is recorded from the very beginning of the simulation in all three cases. However, it is observed that N_{col} increases with increasing Φ_p, with the $\Phi_p =$

5×10^{-3} flow having the most collisions followed by the $\Phi_p = 1 \times 10^{-3}$ flow. The flow with $\Phi_p = 5 \times 10^{-4}$ is noted to have the least number of collisions.
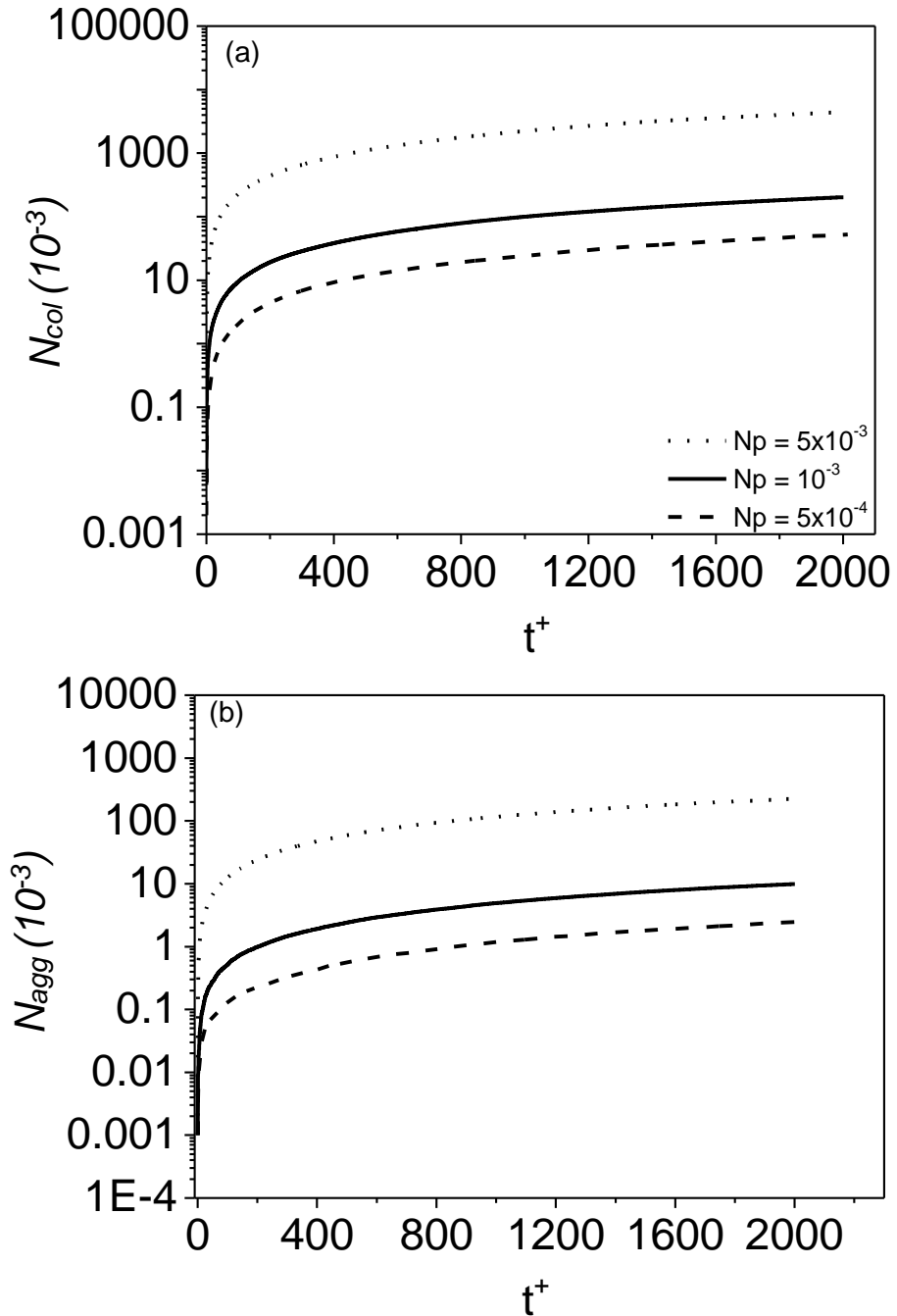
Figure 4.22 Total number of collisions and agglomeration comparison for all volume fraction cases (a) Number of collisions and (b) Number of agglomerations for a time up to $t^+ = 2000$ at $Re_\tau = 300$. Lines: Dotted ($\Phi_p = 5 \times 10^{-3}$), Solid ($\Phi_p = 10^{-3}$), Dash ($\Phi_p = 5 \times 10^{-4}$)

This is also true for the case shown in Figure 4.22(b) where the total number of collision leading to agglomeration, N_{agg} is compared for the selected Φ_p cases up to a time $t^+ = 2000$. This behaviour is not unusual as Φ_p determines the particle

proximity to each other and ultimately dictates the frequency of contact between particles (Ardell, 1972). As a result, the mean distance between particles changes with change in Φ_p, indicating that the particles disperse a greater distance before coming into contact for the low volume fraction case. However, comparing the collision to agglomeration showed no appreciable differences between both cases, with the $\Phi_p = 5 \times 10^{-3}$ case having a ratio of $20:1$ and the $\Phi_p = 5 \times 10^{-4}$ case with a similar ratio of $21:1$. Nonetheless, comparing the collisions in terms of the ratio of $\Phi_p = 5 \times 10^{-3}$ to $\Phi_p = 5 \times 10^{-4}$ showed a collision ratio of $85:1$ and that of agglomeration as $90:1$ which is quite a substantial difference in both cases.
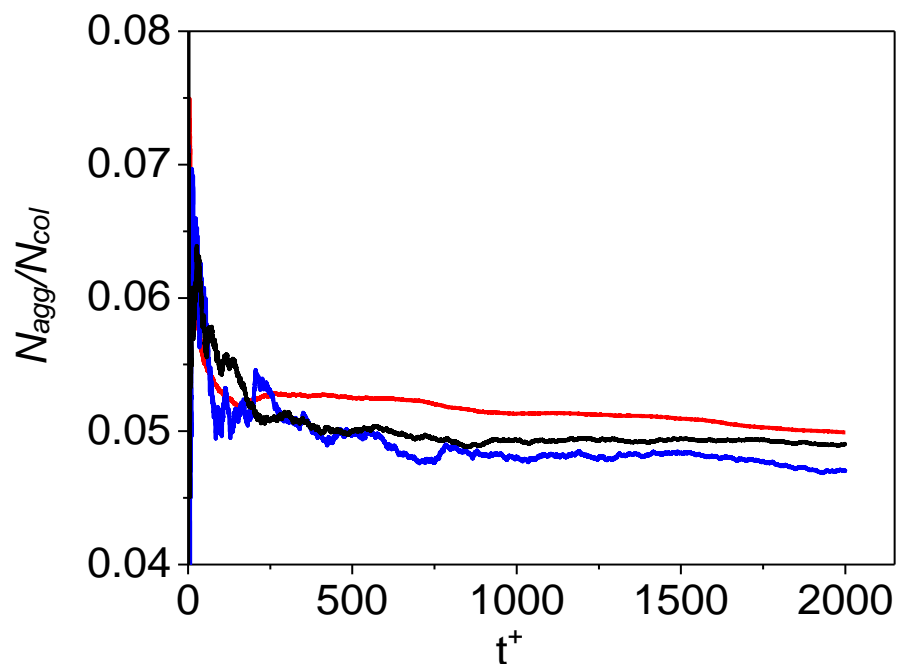
Figure 4.23 Particle rate of agglomeration comparison for all volume fraction cases for a time up to $t^+ = 2000$ at $Re_\tau = 300$. Line Colour: Blue $\Phi_p = 5 \times 10^{-4}$, Black ($\Phi_p = 10^{-3}$) and Red ($\Phi_p = 5 \times 10^{-3}$),

The trend in Figure 4.23 where the particle agglomeration rate is examined for all three cases further elucidates this behaviour. Here, the agglomeration rate is obtained in terms of the ratio of the collisions leading to particle agglomeration N_{agg} to the total number of collisions N_{col} for the time considered, and expressed as N_{agg}/N_{col}. The binning procedure is the same as those used in Figure 4.17 (i.e. concentration distribution across 16 equally spaced slabs). It should be quickly pointed out that the results in all three cases show a higher but not consistent rate of agglomeration during the initial stages of the simulations for a time up to $t^+ \approx 300$ due to the interference from the initial conditions of the flow characteristics on the

particle movement, after which a more steady state is reached where the influence of the volume fraction becomes more prevalent. The trend which also denotes the particle collision efficiency is observed to clearly indicate a higher agglomeration rate for the flow with $\Phi_p = 5 \times 10^{-3}$, and then followed by the flow with $\Phi_p = 10^{-3}$, with the smallest agglomeration rate noted for the flow with $\Phi_p = 5 \times 10^{-4}$.
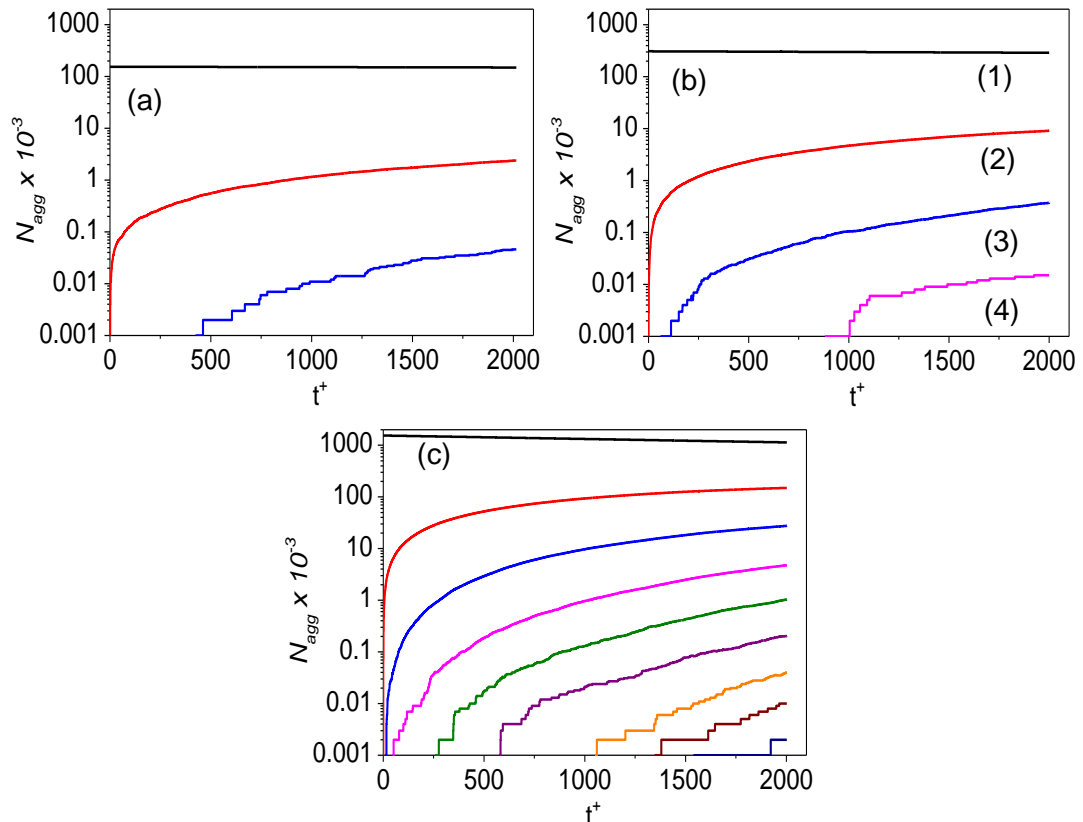
Figure 4.24 Agglomerate formation with time across the channel for $d_p = 125 \ \mu m$: without gravity (a) $\Phi_p = 5 \times 10^{-4}$ (b) $\Phi_p = 10^{-3}$ (c) $\Phi_p = 5 \times 10^{-3}$. Line numbers: single (1), double (2), triple (3), quadruple (4), quintuple (5), sextuple (6).

The rate of depletion of the single particles and the corresponding evolution of multi-particle size agglomerates for each case is shown in Figure 4.24(a-c), for a simulation time up to $t^+ = 2000$. The flow of $\Phi_p = 5 \times 10^{-3}$ is seen to have the highest rate of single particle depletion, with multi-sized particles forming up to 9 particle agglomerates for the time considered. Next is the flow of $\Phi_p = 10^{-3}$, with the multi-sized agglomerates formed consisting up to 4 primary particles; and finally was the flow of $\Phi_p = 5 \times 10^{-4}$ where only 3 particle agglomerates is formed. In Figure 4.25, the particle distribution across the channel and the positions of the collision and agglomeration is tested for the flows of minimum and maximum Φ_p, using particles of size of diameter $d_p = 125 \ \mu m$ and for a flow $Re_\tau = 300$ at mean time values of $t^+ =$

$500, 1000$ and 2000 for each case. It is noticed that quantitatively, there were no considerable changes in the collision and agglomeration distribution over time, with only slight peaks of N_{col} and N_{agg} observed in the wall regions in both cases. However, far more of these events occured in the Figure 4.25(b, d, f) where Φ_p is highest, with N_{col} and N_{agg} approximately 100 times more than those achieved for the lower Φ_p case in figures (a, c, e).
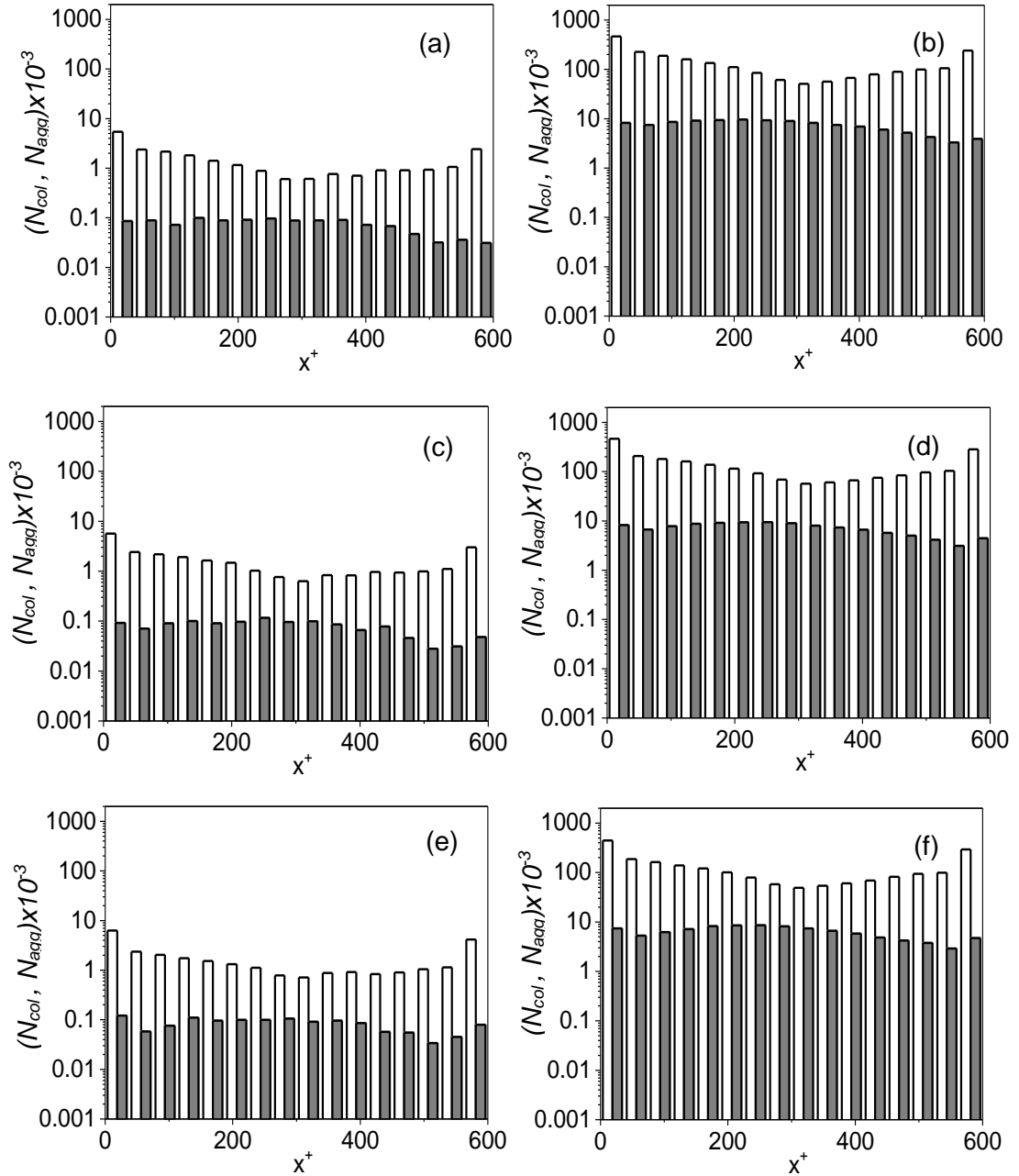
Figure 4.25 Distribution of particle collisions and agglomeration across the horizontal channel of $d_p = 125\ \mu m$ at $Re_\tau = 300$, for (a, c, e) $\Phi_p = 5 \times 10^{-4}$ (b, d, f) $\Phi_p = 5 \times 10^{-3}$ at mean time values of (a, b) $t^+ = 500$ (c, d) $t^+ = 1000$ and (e, f) $t^+ = 2000$

The trend is further illustrated in Figure 4.26(a) and 4.26(b) where N_{col} and N_{agg} is compared against the base case $\Phi_p = 10^{-3}$ flow at a mean time value of $t^+ = 2000$. The maximum values for N_{col} and N_{agg} is found in the order $\Phi_p = 5 \times 10^{-3}$, $\Phi_p = 10^{-3}$ and then $\Phi_p = 5 \times 10^{-4}$, which clearly indicates that particle collision and agglomeration is enhanced with increasing volume fraction.
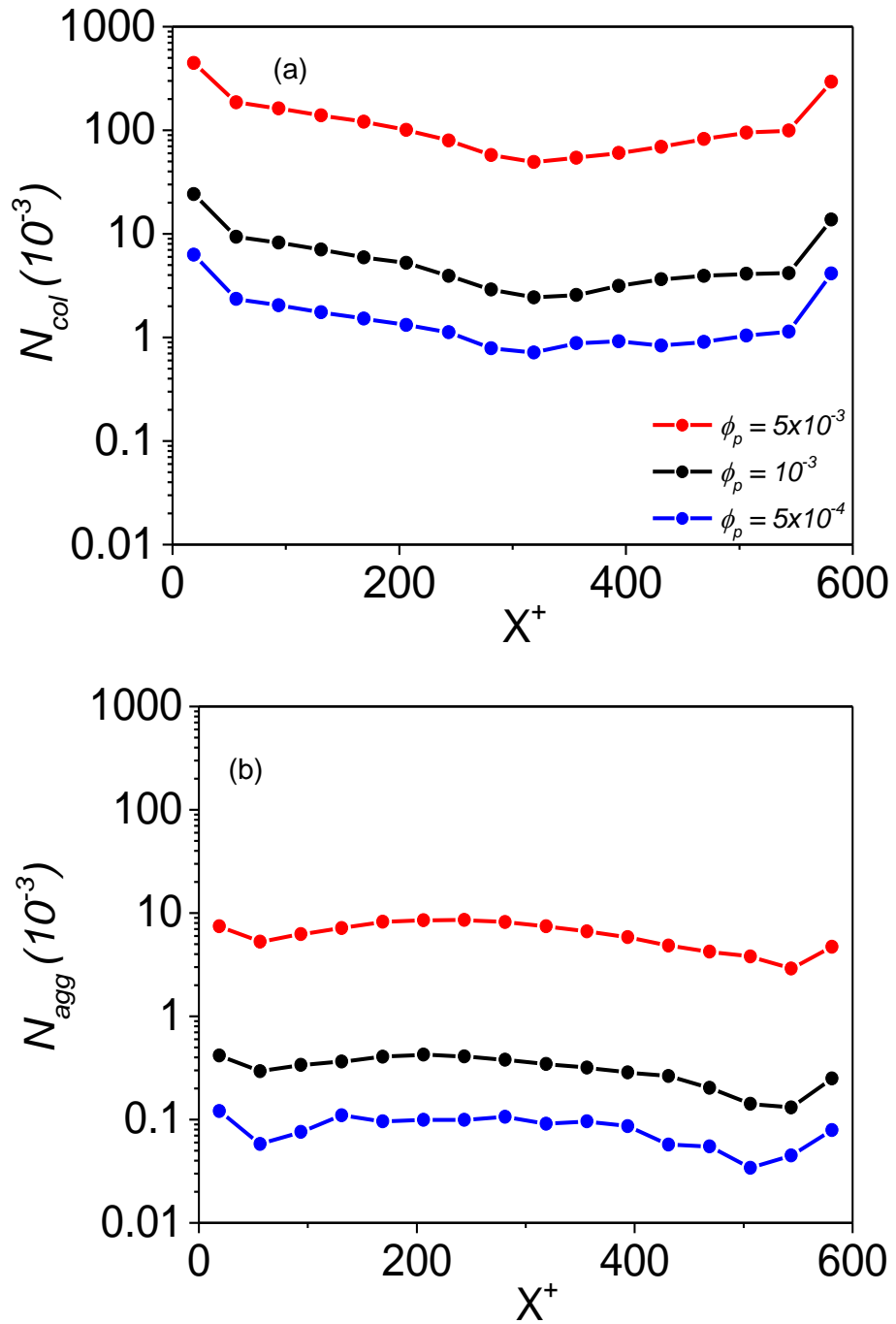
Figure 4.26 Distribution trend for particle collision and agglomeration across the horizontal channel of $d_p = 125\,\mu m$ at $Re_\tau = 300$, for (a) Number of Collision (b) Number of Agglomeration at time $t^+ = 2000$

4.4.4 Volume Fraction Effect on Fluid Turbulence and stresses

In this subsection, we consider the effect of the particles of a fixed diameter $d_p = 125\,\mu m$ on the mean fluid velocity, and the fluid normal and shear stresses. Fluid flows of particle volume fraction $\Phi_p = 5 \times 10^{-4}$ and $\Phi_p = 5 \times 10^{-3}$ are compared against the single phase solution of $Re_\tau = 300$ over time. This is carried out in order to examine the effect of volume fraction on the fluid flow characteristics with increasing time.
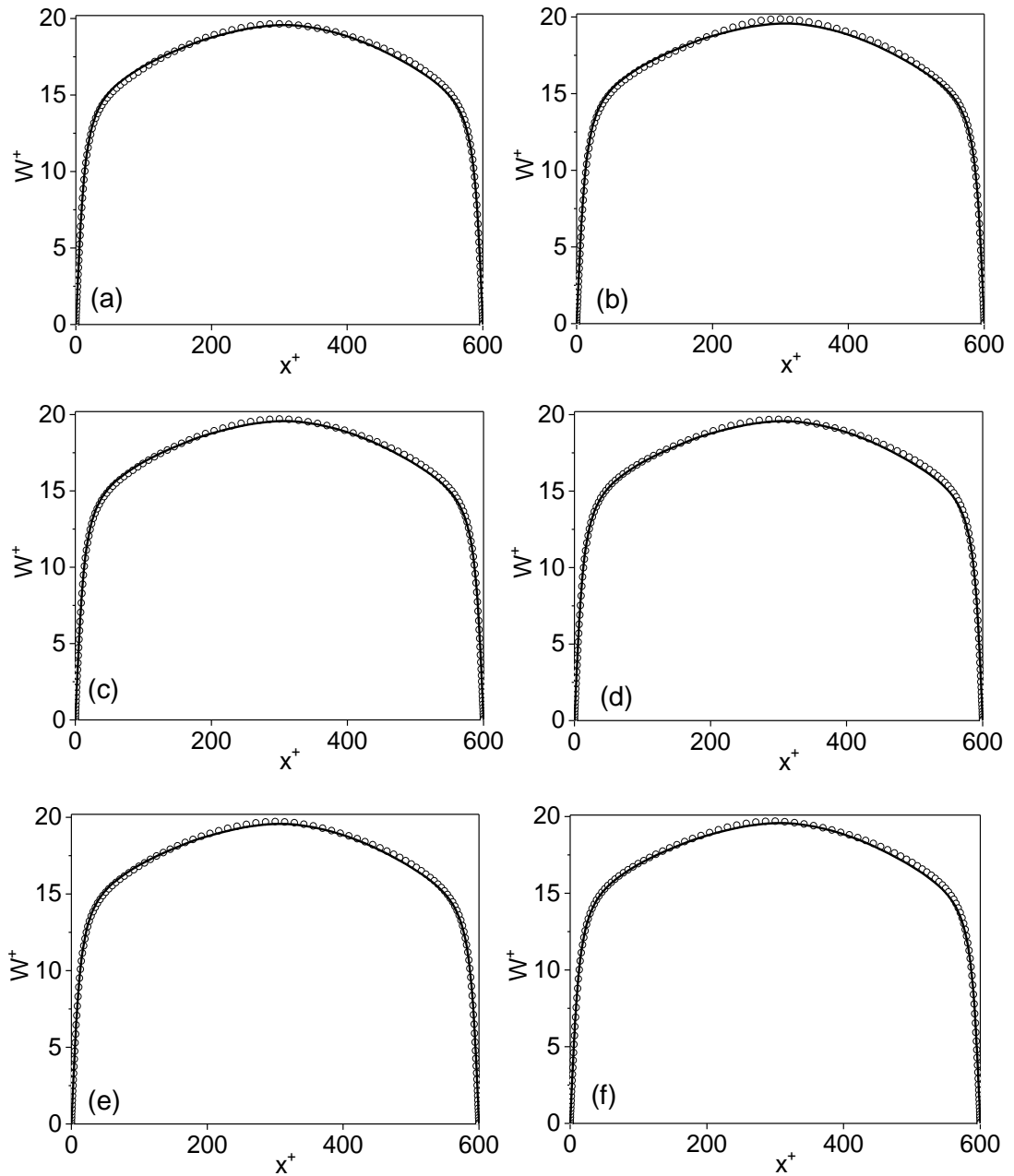
Figure 4.27 Fluid streamwise mean velocity for (a, c, e) $\Phi_p = 5 \times 10^{-4}$ (b, d, f) $\Phi_p = 5 \times 10^{-3}$, at mean time values of (a, b) $t^+ = 500$, (c, d) $t^+ = 1000$ and (e, f) $t^+ = 2000$. of $d_p = 125\,\mu m$ and $Re_\tau = 300$ (— single-phase flow, ○ multi-phase flow).

In the Figure 4.27(a-f), the effect of the particles on the mean fluid velocity is examined for the mean time values of $t^+ = 500, 1000$ and 2000. At time $t^+ = 500$, it is observed that the streamwise velocity is slightly impacted by the particles for both volume fraction flows, but with a degree of inconsistency which, again, can be attributed to the interference from the initial conditions prevalent in the flow for this time. In the $\Phi_p = 5 \times 10^{-4}$ flow in Figure 4.27(a), the streamwise velocity is seen to be enhanced in some regions of the flow and reduced in other areas, giving it a slightly wavy and unsteady profile. Although slight, the streamwise velocity is, however, noticed to be even more pronounced in the $\Phi_p = 5 \times 10^{-3}$ flow as shown in Figure 4.27(b), especially within the bulk flow regions. Nonetheless, the interference from the initial conditions for this time is still noticed from the instability in the velocity profile. As the time increases as shown in Figure 4.27(c) through to 4.26(f), the streamwise velocity is observed to gradually reach a stable state as the initial conditions becomes less prevalent from $t^+ = 1000$, with only small effect on the fluid velocity noticed. In all, the streamwise velocity is impacted with increase in the particle volume fraction, although the impact is almost negligible for this flow condition. Again, it is anticipated that for a flow with particles under the influence of gravity, which will be considered in later chapters that the impact will become more significant and obvious to the reader.

In Figure 4.28(a-f), the effect of the particles on the normal and shear stresses in the streamwise w'^+_{rms}, spamwise v'^+_{rms} and wall normal u'^+_{rms} directions are examined at mean time values of $t^+ = 500, 1000$ and 2000 for both flows of particle volume fraction $\Phi_p = 5 \times 10^{-4}$ and $\Phi_p = 5 \times 10^{-3}$. Just as in Figure 4.27, the impact on the fluid fluctuations is small in all cases. At time $t^+ = 500$, the rms fluctuations is noticed to be fairly stable for the spamwise (v'^+_{rms}) and wall normal (u'^+_{rms}) velocity components, but unsteady for that of the streamwise (w'^+_{rms}) component of the flow, and even more pronounced for the flow with $\Phi_p = 5 \times 10^{-3}$ in Figure 4.28(b). Further observation show that the flow in both cases increasingly approached a steady state with the increase in time, and that the impact on the fluctuations remains relatively enhanced by the end of the simulation. The impact is more prevalent in the bulk flow regions where the enhancement in the rms fluctuations is fairly noticeable in both cases, although clearly more pronounced in the flow with $\Phi_p = 5 \times 10^{-3}$.
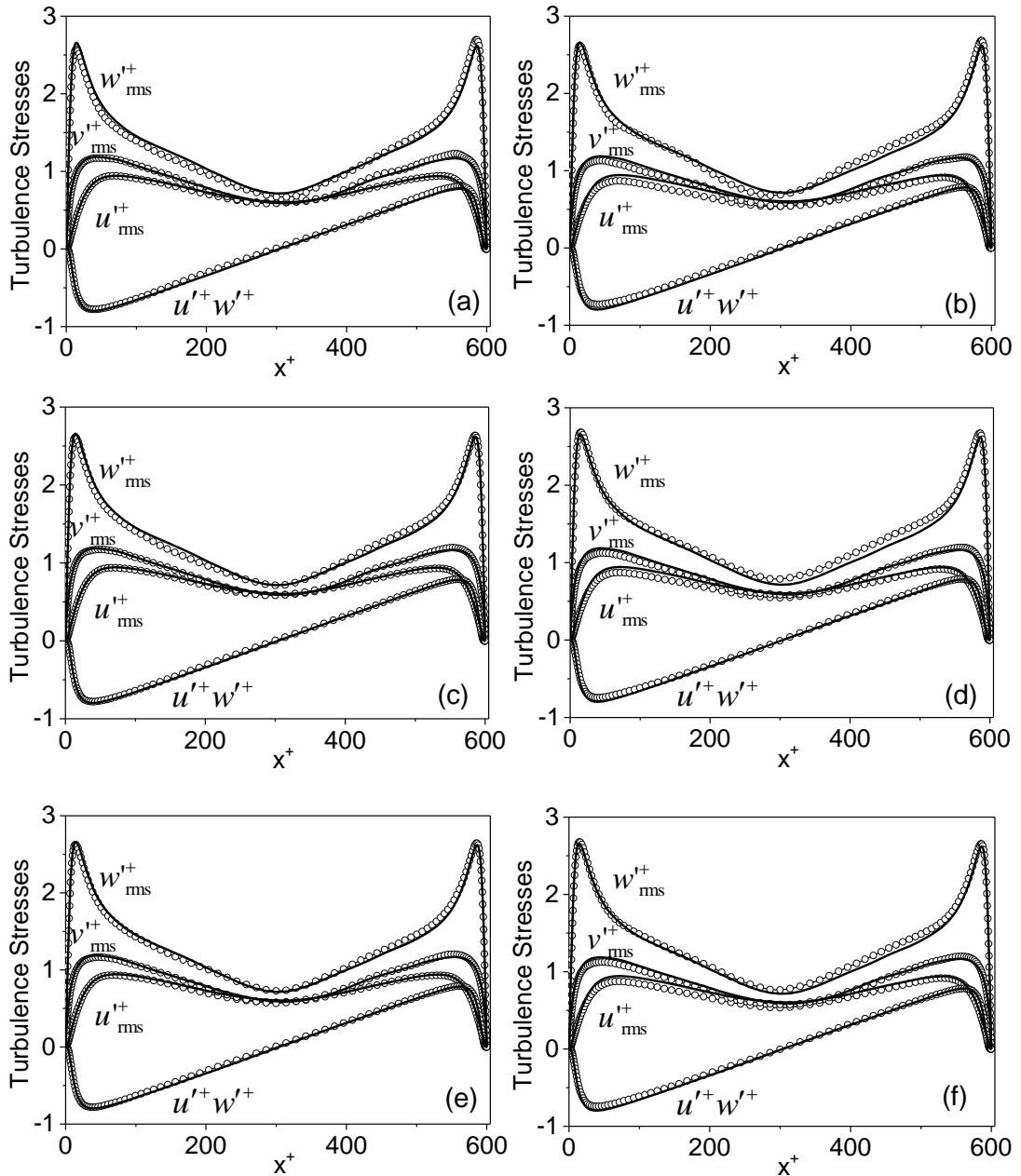
Figure 4.28 Fluid normal and stresses for (a, c, e) $\Phi_p = 5 \times 10^{-4}$ (b, d, f) $\Phi_p = 5 \times 10^{-3}$, at mean time values of (a, b) $t^+ = 500$, (c, d) $t^+ = 1000$ and (e, f) $t^+ = 2000$. of $d_p = 125 \, \mu m$ and $Re_\tau = 300$ (— single-phase flow, ○ multi-phase flow).

The change in turbulent stresses in the wall regions is negligible for the flow with $\Phi_p = 5 \times 10^{-4}$ but small changes are, however, noticed for the flow with $\Phi_p = 5 \times 10^{-3}$. The component of the shear stress ($u'^+w'^+$) is not noticed to be modified in anyway. The more pronounced modification noticed for the case with $\Phi_p = 5 \times 10^{-3}$, is as a result of the increase in the concentration and the resulting agglomeration in the flow. Further scrutiny reveals that the enhancement was more prevalent in the bulk flow because particle agglomeration is enhanced in this region. This is possible as the increase in particle size in this region enhanced the turbulence modification,

and is in line with the findings of Crowe et. al (1998) where it was suggested that turbulence is enhanced in the presence of larger particles as long as the critical value $(d_p/l_e \geq 0.1)$ is exceeded and suppressed with smaller particles $(d_p/l_e \leq 0.1)$. In all, it is shown that the turbulence modification is possible with increase particle volume fraction, although at negligible levels for this flow condition.

4.5 Conclusions on Main Findings

In this chapter the large-eddy simulation have been successfully implemented in making predictions for incompressible turbulent flow which was two-way coupled in a horizontal channel; and results presented. The LES results generated for the single phase were verified by comparing against predictions obtained using the more accurate DNS method and tested for shear Reynolds flows of $Re_\tau = 150, 300$ and 590, with results in most cases, showing highly acceptable agreements with the DNS despite minor discrepancies in the mean velocities and rms of fluctuating velocity components. The LES was then combined with the LPT by incorporating into the non-commercial code to test for particle phase behaviours. The comparison was performed for a dilute two-phase flow system and compared against DNS predictions on one-way coupled gas-particle flows, with the results again showing very good agreements with those of the DNS. The overall aim here, was to provide a justification on the use of a relatively less computationally expensive LES rather than the more accurate but computationally expensive DNS in the prediction of turbulent two-phase flows which has been successfully achieved.

In terms of the effect of particle size on particle collision and agglomeration, it was found that the rate of collision and agglomeration was greatly influenced by the size of the particles. Particle collision and agglomeration was found to be encouraged for smaller sized particles as they tend to follow the flow more closely into areas of maximum turbulence close to the walls, where even more collision and agglomeration is encouraged. It was also observed that as the particles become larger as a result of the agglomeration process, the rate of collision and agglomeration decreases over time as the particles become less responsive to the fluid phase due to their increasing inertial. Particle dispersion was also observed to be due to the influence of the fluid turbulence which causes the inertial particles to segregate towards the wall regions were turbulence is maximum. The increased particle population in this region

increases shearing at the walls; evident through the increased effect of the hydrodynamic forces in the wall regions, particularly the drag and lift forces. The fluid mean velocity, normal and shear stresses was slightly enhanced by the presence of the particles, although more pronounced for the largest particle flow.

In terms of the volume fraction effect on collision and agglomeration, the collision and agglomerate formation rate was found to increase with an increase in the particle volume fraction. Comparisons made between the flow in the four-way coupled regime and the single phase flow, showed a slightly augmented profile for the mean velocity and normal stresses, although difficult to see from the figures shown. The shear stresses was however unaffected by the increase in particle volume fraction.

5 Turbulent Horizontal Channel Flow: Collision and Agglomeration – With Gravity

5.1 Introduction

In this chapter, the modelling of particle-laden flows in a turbulent horizontal channel is extended to accommodate the effect of the net gravity-buoyancy force on particle collision and agglomeration. This has been achieved by investigating different flow characteristics. To isolate the effects of gravity on particle collisions and agglomeration the study assumed: binary collisions; particle agglomeration based on the pre-collision particle energy, van der Waals' interactions and restitution coefficient alone; minimal particle deformation post-collision; and no agglomerate break-up. The force of friction between the colliding particles and their angular velocities are neglected in the collision model.

In the first part of this work, the contribution of gravity to particle collision, agglomeration and turbulence is tested by making comparisons between two flows; one in which the gravitational force is taken as $9.81 \, m \, s^{-2}$ acting in the downwards direction and another which completely excludes the effect of the gravity force. The flow in both cases was for a fixed Reynolds number and particle size. The effect of particle size is then tested for a fixed Re_τ flow by varying particle diameter in the second part of this chapter. Lastly, in the third part of the work, by fixing the particle diameter the effect of gravity on collision and agglomeration for different shear Reynolds number horizontal flows (gravity acts in the downwards direction in both cases) was investaged. The inclusion of the gravitational force in the solutions presented in this chapter, ensures that a more realistic prediction of the flow characteristic behaviour is captured. This is particularly important as it provides solutions to flows replicating conditions typical of many industrial and engineering processes. All other flow conditions described in the previous chapter are maintained in this section.

5.2 Effects of Gravity on Collision, Agglomeration and Flow Turbulence

Figure 5.1 compares the total particle collision count, N_{col} and the resulting number of agglomerates, N_{agg} formed up to a simulation time of $t^+ = 2000$ (~ 8.9 s in real time) for a flow of shear Reynolds number $Re_\tau = 300$. Here, the superscript (+) represents variables made dimensionless using u_τ and the kinematic viscosity ν. From the results in Figure 5.1(a), it is clear that the collision and agglomeration of particles starts from the moment they are introduced into the flow. By $t^+ = 2000$, there were a total of 15,312,856 particle collisions and 220,338 agglomerations in the flow with gravity, whilst for the zero gravity flow the corresponding numbers were 205,762 and 9,567, respectively. In both the zero- and with-gravity flows, not all collisions result in the formation of agglomerates, and there are far more collisions in the flows when compared to those that resulted in agglomeration. However, there are considerably more collisions and agglomeration events in the gravity flow, with a collision to agglomeration ratio of 70:1 comparing to 22:1 for the zero gravity case. However, particle agglomeration in both cases remains relatively less compared to particle collisions.

In both cases, it is observed that during the initial stages of the simulations, particle collisions and agglomerations increase sharply, with results for the case with zero gravity achieving an approximate steady state with time, whilst in the case with gravity the number of collisions and agglomerations continues to increase with time, albeit at a decreasing rate. This decreasing rate is a result of the total number of particles within the flows reducing with time due to agglomeration, leading in turn to a reduction in the number of collisions and further agglomerations. This effect is accentuated in the flow with gravity, ultimately leading to an approximate steady state, due to the impact of gravity in promoting the downward migration of particles within the flow, leading to increased local collisions in the lower near-wall, and ultimately more collisions and agglomerations due to the high turbulence levels in this region. This is further confirmed in Figure 5.1(b) where it is shown that the particles in the zero gravity case are evenly distributed across the channel which explains the relatively less collision and agglomeration count by $t^+ = 2000$. In the same figure, it is clearly seen that the particles are migrated into the near wall regions, aided by the inclusion of gravity and therefore, explains the high collision events in the lower wall region. It is also worth mentioning that the particle fluxes towards the wall is also aided by

turbophoresis, which occurs as a result of the difference in turbulence between the bulk and wall regions of the channel.
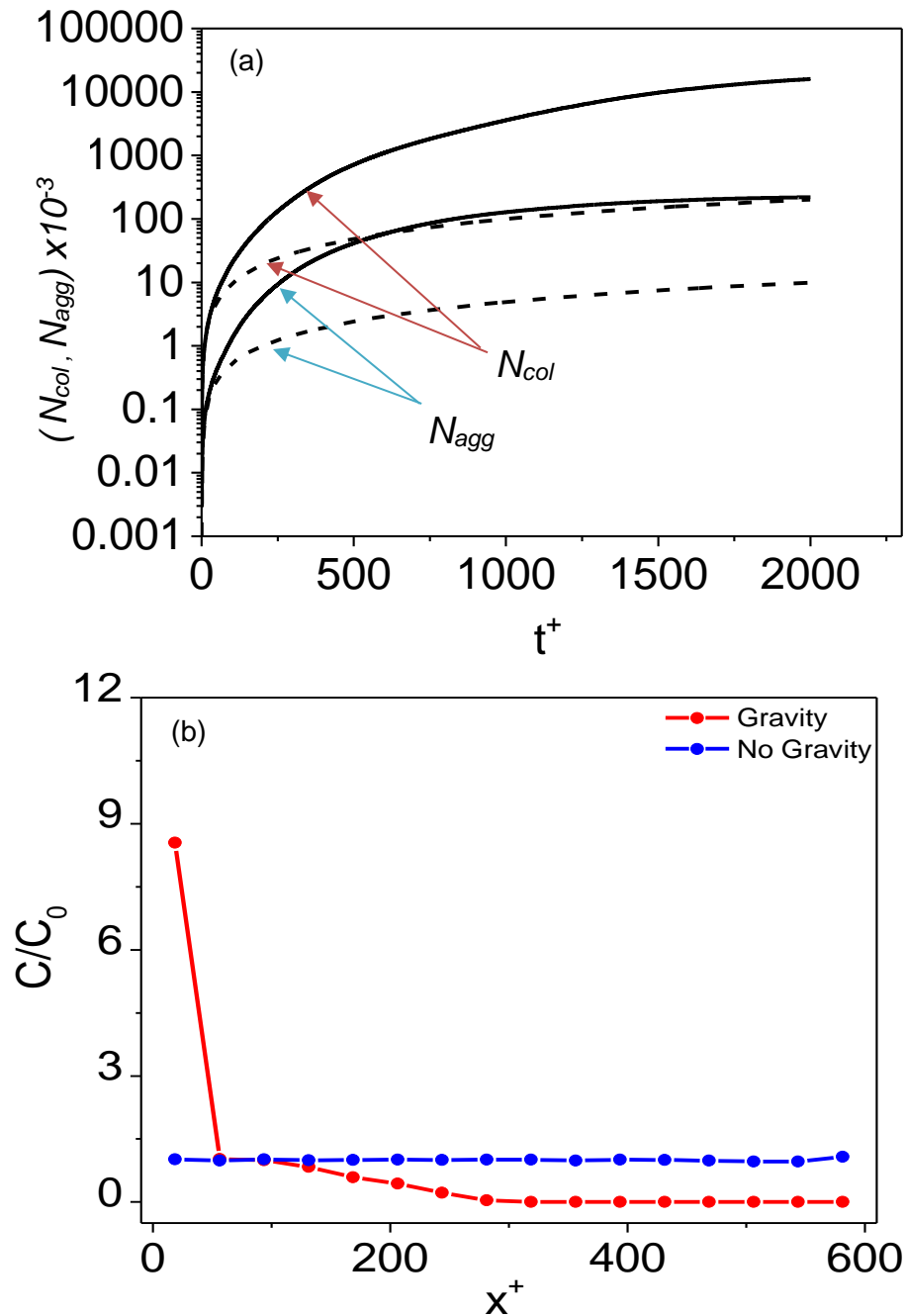
Figure 5.1 (a) Total number of particle collisions, N_{col}, and particle agglomerations, N_{agg}, as a function of time, and (b) the instantaneous particle concentration distribution on (x, z) planes at $t^+ = 2000$. $Re_\tau = 300$ and $d_p = 125\ \mu m$. Bold line: With Gravity. Dash line: Zero Gravity.

In order to further understand the influence of gravity in the formation of agglomerates, it is useful to analyse the number of agglomerates of the same type N_a formed in each flow.

Figure 5.2, therefore, gives results for the total number and sizes of the agglomerates that are formed within the flows as a function of time, in the cases with and without gravity, including the single particle depletion rate and the corresponding evolution of multi-sized particles. At the start of both simulations, the results again indicate a sharp increase in the number of agglomerates formed, although the rate of formation of multi-particle agglomerates differs significantly between the two flows.
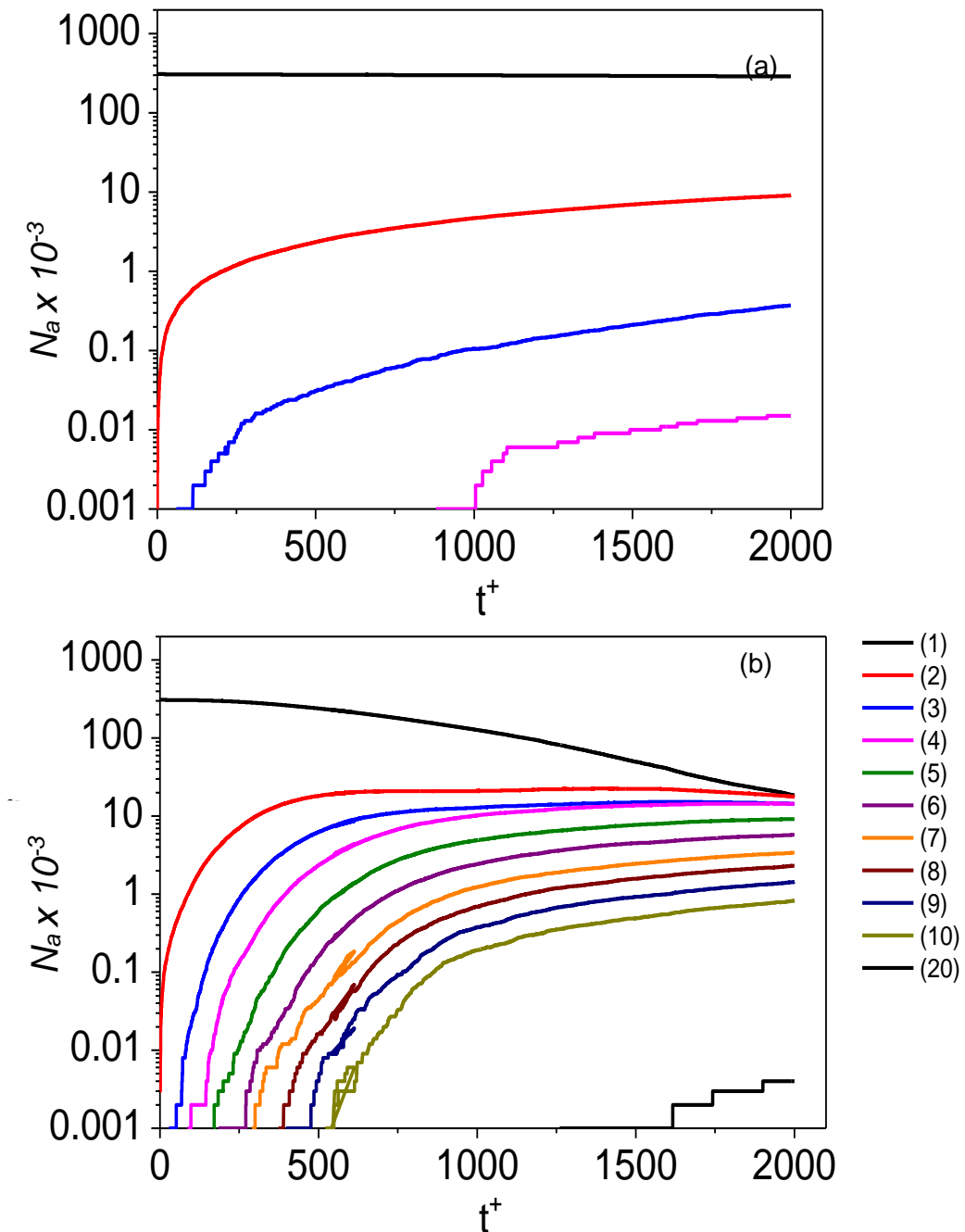
Figure 5.2 Agglomerate formation with time across the channel for $Re_\tau = 300$: (a) without gravity and (b) with gravity. Line numbers: single (1), double (2), triple (3), quadruple (4), quintuple (5), sextuple (6) etc.

The sharp increase is mainly as result of the interference from the initial conditions on the particles. In

Figure 5.2(a), where gravity is zero, after $t^+ \approx 250$ the rate of formation of two-particle agglomerates starts to reduce to an approximate steady state. In contrast, in

Figure 5.2(b), the rate of formation of multi-particle agglomerates increases exponentially, with agglomerates consisting of up to 7 primary particles formed by t^+ ≈ 400. As the simulation time increases in both cases, and the original single particles decrease in number, large agglomerates begin to form through the resulting collisions between single particles and larger agglomerates, and between the agglomerates themselves. By the end of the simulations, agglomerates consisting of up to 20 single particles were formed in the with-gravity case, contrasting with a maximum of 4 particle agglomerates in the zero gravity flow. In the zero gravity case, the number of single primary particles decreases steadily with time as the number of each agglomerate size gradually increases. However, this is not the case in the flow with gravity as the single primary particles and the smaller agglomerates are used up to form much larger agglomerates. This is particularly the case after time $t^+ =2000$ although not shown. These observations are in broad agreement with the work of Ho and Sommerfeld (2002) who concluded that for a flow system with a bimodal distribution of particle sizes, there is a tendency for smaller particles to collide and bond with larger sized particles to form multi-particle agglomerates.

The effect of gravity is further elucidated in Figure 5.3. In Figure 5.3(a) the particle agglomeration rate, obtained in terms of the ratio of the collisions leading to particle agglomeration N_{agg} to the total number of collisions, N_{col}, is examined for both cases up to a dimensionless time $t^+ = 2000$. Here, it is noticed that for the zero gravity case, the agglomeration rate N_{agg}/N_{col} decreased with time before reaching a steady state at $t^+ \approx 200$, after which no noticeable changes were observed in N_{agg}/N_{col} till the simulation end time. In contrast to this behaviour, an initial increase in N_{agg}/N_{col} is observed for the flow with gravity, which continued for a time up to $t^+ \approx 250$. After $t^+ \approx 250$, the rate is then noticed to reduce over time and continued till the end of the simulation. The continuous reduction in N_{agg}/N_{col} indicates that the primary particles and already formed agglomerates are also being used up to form even larger agglomerates. This explains the exponential increase in the number of multi-sized particles and the sharp reduction of the single particles seen in

Figure 5.2. It should be noted that the lack of tread in the results before time $t^+ \approx 200$ and $t^+ \approx 250$ for the zero gravity and gravity flows, respectively, was as a result of the interference from the initial conditions of the flow on the particles, and replicates conditions reported by Breuer and Almohammed, (2015). The term N_{agg}/N_{col} which also denotes the particle collision efficiency is observed to clearly indicate a higher agglomeration rate for the flow with gravity.
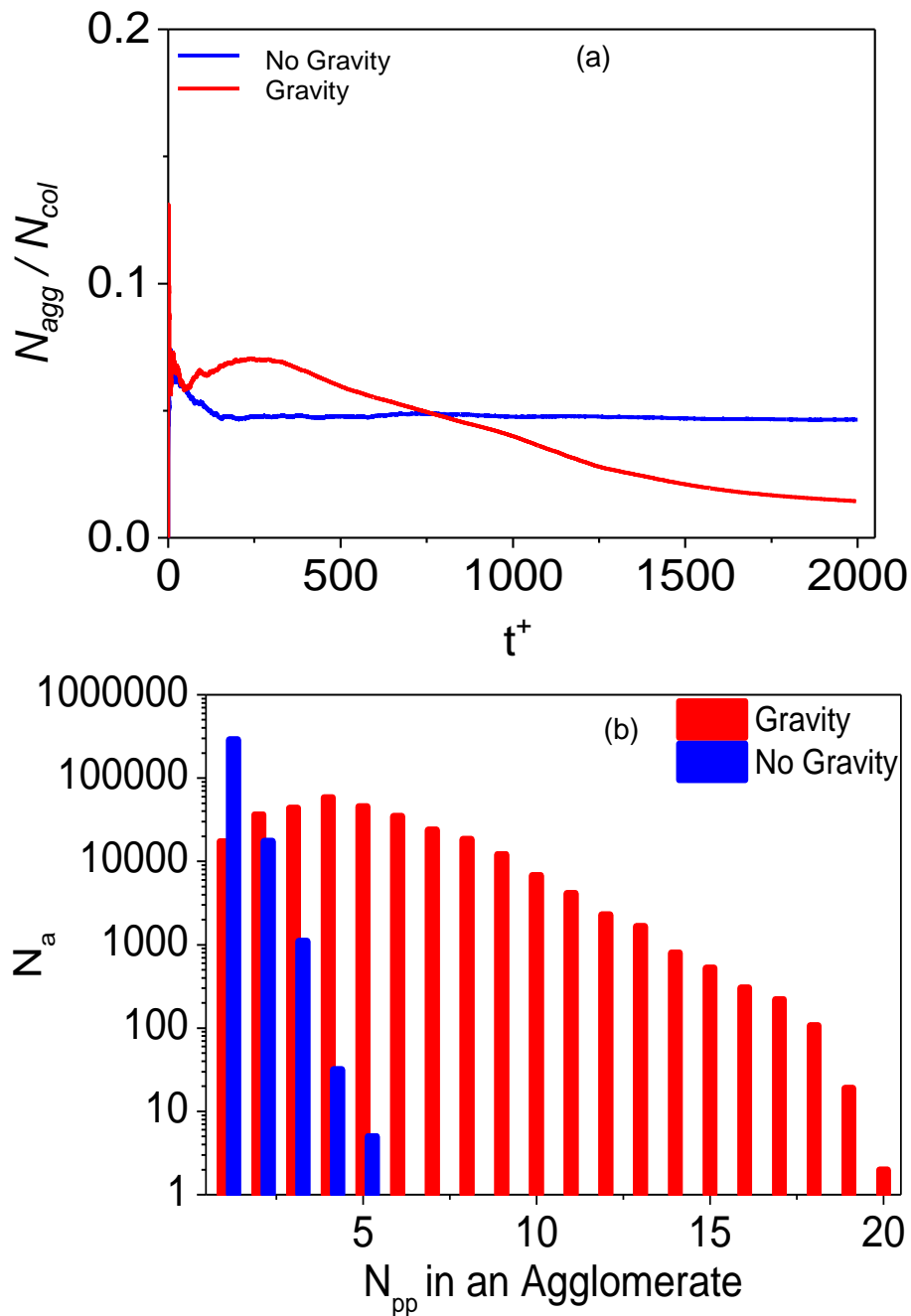
Figure 5.3 Simulation comparison of the with- and without-gravity cases for a dimensionless time up to $t^+ = 2000$ at $Re_\tau = 300$, $d_p = 125\,\mu m$ (a) Particle rate of agglomeration (b) the number of single particles [single (1)] and agglomerates of the same type [double (2), triple (3), quadruple (4), etc.]

The significance of the gravity is also seen from the result in Figure 5.3(b) where the number of primary particles N_{pp} i.e. single (1) and the different type agglomerates i.e. double (2), triple (3), quadruple (4), quintuple (5), sextuple (6), etc., formed after a dimensionless time $t^+ = 2000$ are compared for both the gravity and zero gravity cases. By the end of the simulation, it is observed that the single particles still dominate the flow for the zero gravity case, with only few agglomerates formed. This is in contrast to the gravity case where the depletion in the number of single particles are noticeable, with significantly more type agglomerates formed.

Figure 5.4 shows results for the distribution of the collisions and agglomerations across the channel, and the locations where they occur, at time t^+ = 500, 1000 and 2000. These results were obtained by averaging over the length of the channel and over t^+ ± 500 (mean taken 500 either side of the value i.e. $t^+ = 1000$ means $(t^+_{501} + t^+_{502} + \cdots + t^+_{1500})/1000$ about each time value given to provide a sufficiently large sample for analysis. The cross-stream domain is divided into 16 equally spaced zones in the wall-normal direction for the gravity and zero gravity cases considered. For the latter case, the number of collisions is effectively symmetrical about the channel centre, with the maximum number of collisions experienced in the two near-wall regions. The number of particle agglomerations in this case is relatively small and is evenly distributed across the channel. However, small peaks are again seen close to the walls where turbulence levels are high, with the trend roughly constant over all simulation times. These findings are in agreement with those of Afkhami et al. (2015) where the number of collisions and the process of agglomeration was also found to be dominant in the near-wall regions where peaks in turbulence levels occur. A small peak is also observed in the number of agglomerates formed in the bulk of the flow where turbulence levels are less significant, and where only a small number of collisions occur. This is due to the fact that when particles collide within this less turbulent region, their combined kinetic energy post-collision is in most cases insufficient to overcome the van der Waals energy existing between them and therefore particle agglomeration is highly probable for those collisions that do occur. The attraction energy between colliding particles is also greater for smaller diameter particles. For the flow with gravity the trends are noticeably different, with the number of collisions and agglomerations in the upper region of the channel decreasing over time as the flux of particles tend towards the lower wall and consequently increase their concentration in this region.

By t^+ = 500, the initial even distribution of particle collision and agglomeration events across the channel changed, with the collisions and agglomerations now occurring across each of the zones considered, although primarily in the region of the channel floor. By t^+ = 1000, collision and agglomeration events towards the lower wall increased significantly, with almost no events now occurring within the upper regions of the flow due to the low concentration of particles there.
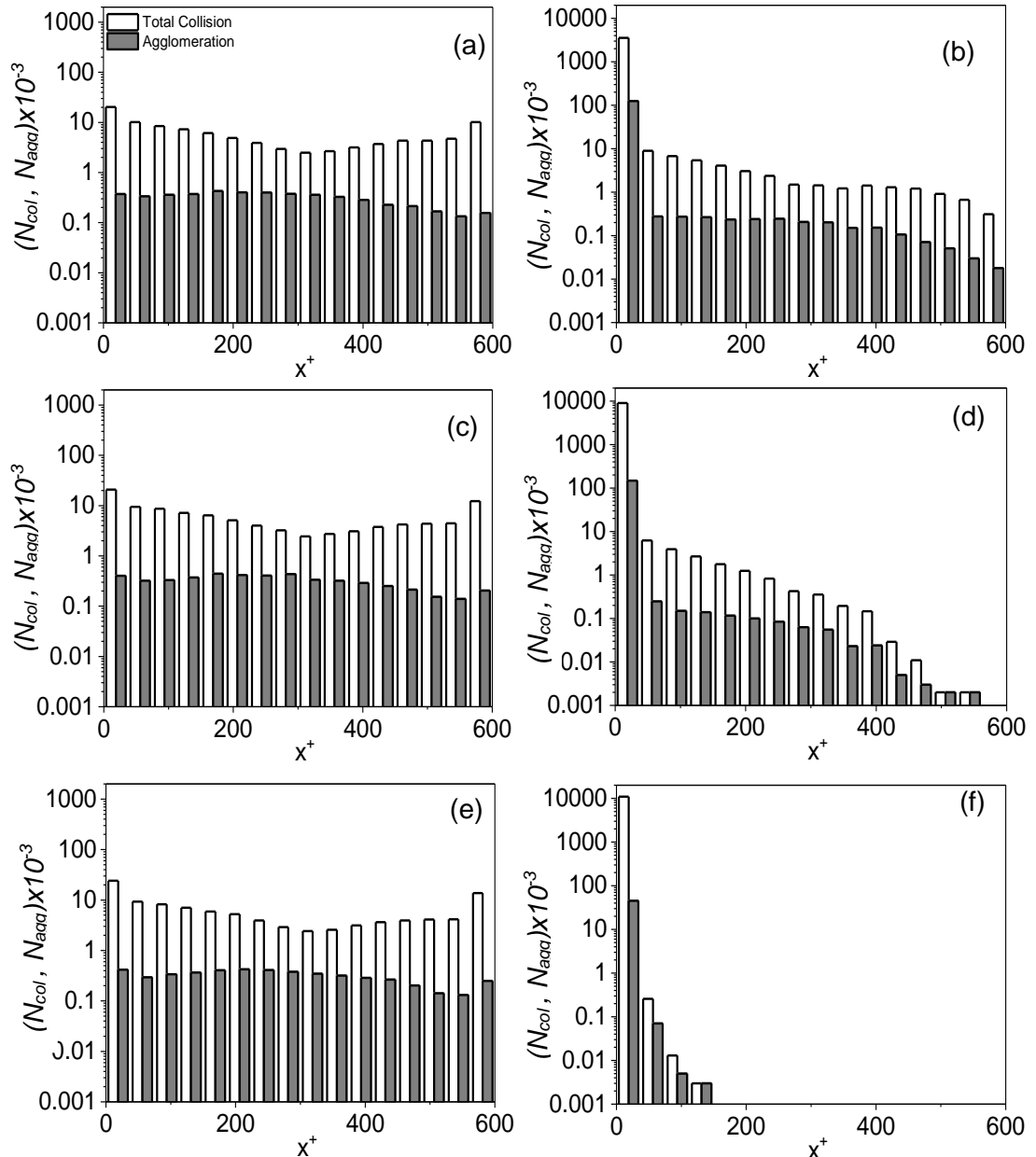
Figure 5.4 Distribution of particle collisions and agglomeration across the channel at $Re_\tau = 300$, for (a, c, e) no gravity (b, d, f) with gravity, at mean time values of (a, b) t^+ = 500, (c, d) t^+ $Re_\tau = 300$= 1000 and (e, f) t^+ = 2000

By t^+ = 2000, the depletion of particles in the upper half of the channel is complete, with the highest concentration of particles now located near the lower wall (see also Figure 5.4b). Over the times considered, it is noted that the number of collisions close to the lower wall gradually reduces with time, as does the number of agglomerations occurring in this region. This is to be expected because, as larger particles are formed through the depletion of smaller particles, the total number of particles within the flow reduces significantly and hence fewer collisions occur and agglomerates and formed over time. Beyond t^+ = 2000, a significant number of particles under the influence of gravity were observed to be out of the flow altogether. Figure 5.5 is a visual representation showing the instantaneous positions of the particles along the x, y plane of the channel domain at dimensionless time, t^+ = 1000. The figure clearly indicates the significance of the gravity force, aided by turbophoresis, on the particle dynamics and further confirms the behaviour observed in Figure 5.4, as a gradual migration of particles towards the lower wall is noticed for the flow with gravity. This behaviour is in contrast to those without gravity which appears to be evenly distributed for the times shown.
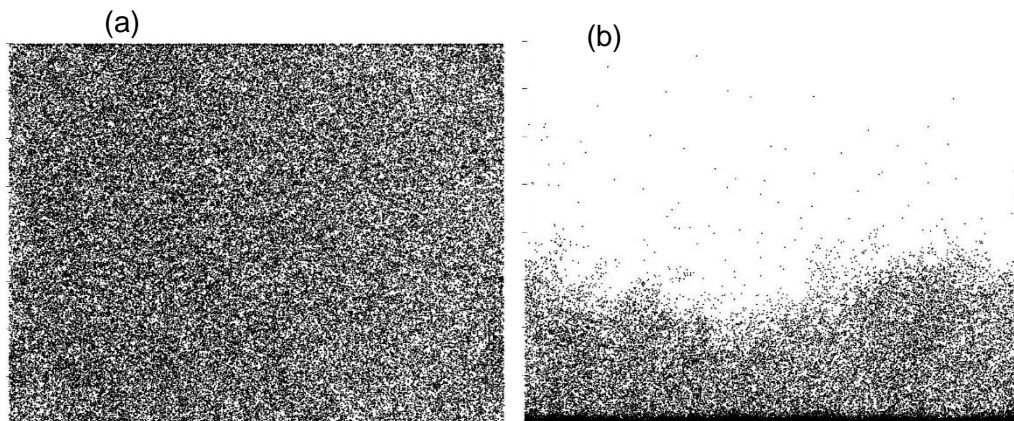
Figure 5.5 Instantaneous distribution of particles on (x, z) planes for a gravity flow at t^+ = 1000 and $Re_\tau = 300$ for $d_p = 125\,\mu m$ (a) no gravity flow (b) with gravity flow.

5.3 Effects of Particle Size on Collision, Agglomeration and Turbulence for a Flow Influenced by Gravity

In this section of the chapter, we extend the study on the effect of particle size on collision and agglomeration into flows where the contribution of the gravity and buoyancy forces are fully accounted for, as well other relevant hydrodynamic forces (i.e. drag, shear-lift, added mass, pressure gradient forces). With the inclusion of the net gravity-buoyancy force in the flow, it is anticipated that the particle movement will

be accelerated towards the lower wall region of the channel as gravity becomes the dominant force in the flow. However, the rate at which this occurs is expected to differ with the variation in particle size. The flow in this instance, is a fully developed turbulent horizontal channel flow of Reynolds number $Re_\tau = 300$. The particles introduced are of diameters $75\,\mu m$, $125\,\mu m$ and $250\,\mu m$ and of varying particle numbers. Information concerning the grid and particle parameters used for the simulations is as stated in Table 4.3. Though the particle population in each case is varied, it is worth mentioning that the global trend of the particles is believed to be comparable since the volume fraction is of a fixed value.

5.3.1 Collisions and Agglomerations

In Figure 5.6(a) and 5.6(b) the total particle collision count, N_{col} and the resulting agglomeration from such collisions, N_{agg}, formed up to a simulation time of $t^+ = 2000$ (~8.9 s in real time) is given for the selected particle sizes, with comparisons made against those of zero gravity given in Figure 5.6(c) and 5.6(d). Here, the superscript (+) represents variables made dimensionless using u_τ and the kinematic viscosity ν. From the results in Figure 5.6(a) and 5.6(b), it is noticed that the total particle collision count and those leading to agglomeration occurred from the very start of the simulation. By time, $t^+ = 2000$, there were a total of $1{,}817{,}670$, $205{,}762$ and $11{,}596$ particle collisions in the $75\,\mu m$, $125\,\mu m$ and $250\,\mu m$ flows, respectively. With the resulting agglomeration from such collisions amounting to $109{,}225$, $9{,}567$ and 212 in the $75\,\mu m$, $125\,\mu m$ and $250\,\mu m$ flows respectively. For all three particle size flows, the results clearly indicate an increase in the number of collisions and agglomerations with time, and also significantly more than those observed for the no gravity flow case in Figure 5.6(c) and 5.6(d) which is also described in the previous section. It is also observed just as in the zero gravity case that not all collisions have resulted in agglomeration, with the flows having far more collisions when compared to those leading to agglomeration.

The steep gradient observed for the collision and agglomeration at the initial stages of the simulations is an indication of the increased rate of particle contact which occurred as a result of the influence of the flow initial conditions on the particles. At a time of approximately $t^+ = 400$, the components, N_{col} and N_{agg}, in Figure 5.6(a) and 5.6(b), are observed to approach a steady state with increase in time. In Figure 5.6(a), an inverse relationship between the rate at which particle contact is made and

the particle size is noticed, and indicated by the steeper gradient of the smaller particle size case of $d_p = 75\,\mu m$ up to $t^+ = 400$, followed by the flow with $d_p = 125\,\mu m$ and then $d_p = 250\,\mu m$ for the time period. However, at about $t^+ = 1000$ an equal number of collisions is observed for all particle sizes for the gravity flow, even though far more particles were introduced in the $d_p = 75\,\mu m$ flow to fix the volume fraction at $\Phi_p = 10^{-3}$.
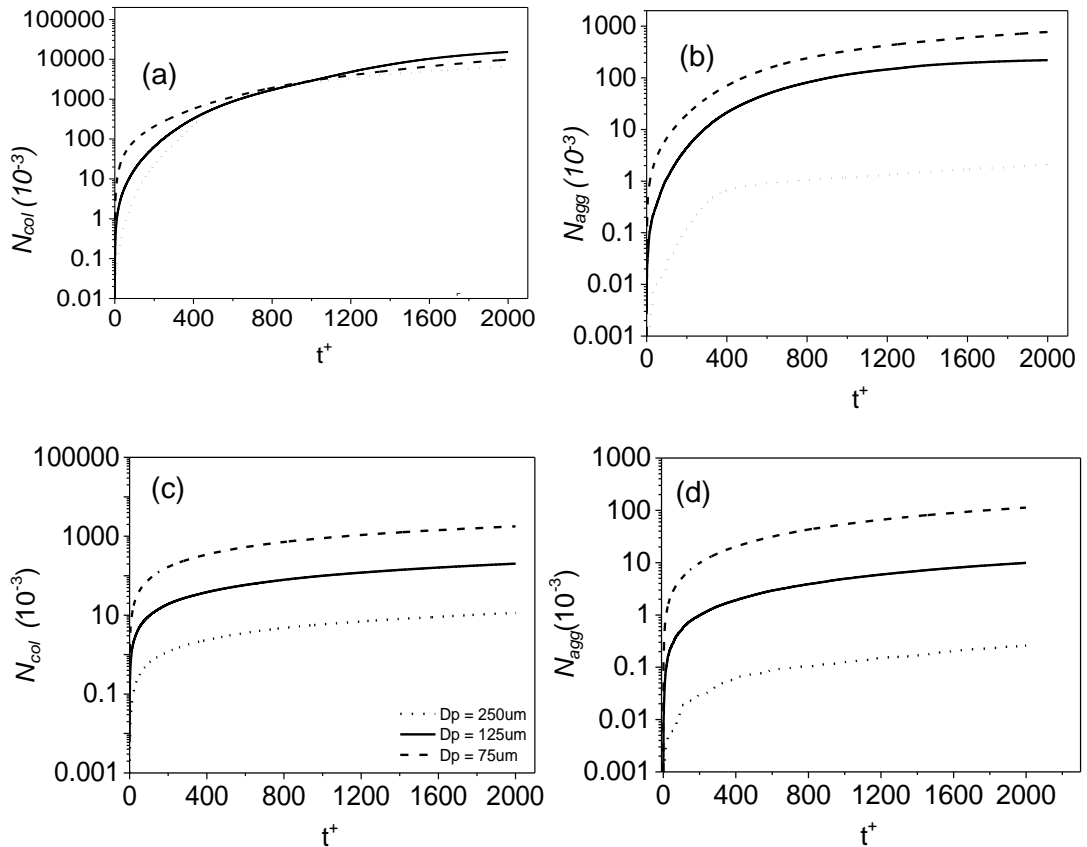
Figure 5.6 Total number of collisions and agglomeration comparison for all particle sizes (a, c) Number of collisions and (b, d) Number of agglomerations for time up to $t^+ = 2000$ at $Re_\tau = 300$. (a, b) with gravity (c, d) zero gravity

After this time, the rate of increase of N_{col} in the flow case of $d_p = 75\,\mu m$ is observed to reduce further and below both cases of $d_p = 125\,\mu m$ and $d_p = 250\,\mu m$. This is in direct contrast to the behavior observed for the zero gravity flow were collision and agglomeration is increased with decreasing particle size. This occurrence is believed to be as a result of the increased agglomeration process within the flow for the smaller diameter case, which eventually led to the reduction in the collision count and further agglomerations as larger particles continued to form through. Another reason is the inter-particle distance becomes larger with formation of agglomerates, hence, a slower rate of agglomeration. Also, smaller particles are more responsive to

turbulence, hence, are least affected by gravity and become more reluctant to migrate into areas of maximum turbulence where collision is favored. For the larger diameter particles which are less responsive to the flow, the increase in N_{col} was due to the enhanced particle migration towards these areas of high turbulence as a result of gravity on the particles. This behaviour is also aided by the impact of the turbulence on the particles which accelerates their migration towards the bottom wall. The phenomenon is often described as turbophoresis. The increase in particle concentration around the lower wall in turn increases the local collision count as the inter-particle distance becomes shortened. In 5.6(b), the agglomeration process count N_{agg} for the $d_p = 75\,\mu m$ case still appears to be highest of the three particle sizes by $t^+ = 2000$, even though the N_{col} has clearly reduced. This trend of less collision but more agglomeration noticed for the $d_p = 75\,\mu m$ case is a consequent of the flow conditions promoting particle agglomeration (see the agglomeration model in section 3.8). Unlike the larger size particles, the bulk of the $d_p = 75\,\mu m$ particles are concentrated in the channel centre where their velocity fluctuation is minimal, thus, the inter-particle kinetic energy is lesser and increases the likelihood of particle agglomeration in the flow. Also, smaller particles have larger surface area per unit volume (Lin and Wey, 2004), which increases the chances of agglomeration as the van der Waals energy becomes more predominant between the particles.

In order to further understand the influence of gravity in the formation of agglomerates, it is useful to analyse the number of agglomerates of the same type N_a formed in each flow. Figure 5.7(a)-5.7(c), therefore, gives results for the influence of particle size on the number and sizes of the resulting agglomerates for the flow under the influence of gravity. In Figure 5.7(a) and 5.7(b), the rate of depletion of the single particles during the agglomeration process, and the corresponding evolution of multi-sized particles agglomerates for each particle size, up to a simulation time of $t^+ = 2000$ is given. The formation of larger size agglomerates (double, triple, quadruple, etc.) is noticed from the very start of the simulation for all particle flows. The agglomerates are also observed to form fairly rapidly, due to the initial conditions on the flow, before gradually reducing to a steady state as interactions with the turbulent flow structures increases. However, the rate of formation of the multi-sized particles differ in all cases, with the formation being highest for the flow with particles $d_p = 75\,\mu m$ in 5.7(a) and lowest for the flow with particles $d_p = 250\,\mu m$ in 5.7(c). By the end of the simulation, agglomerates consisting of only 2 single particles were formed in the $d_p = 250\,\mu m$ flow, with the rate of depletion of the single particles

almost unchanged. This is in contrast to the flows of $d_p = 75\,\mu m$ and $d_p = 125\,\mu m$ where far more agglomerates were formed, and with visible changes in single particle depletion rate. Further observations show that the single and smaller particle agglomerates are being used up to form the larger agglomerates in both the $d_p = 75\,\mu m$ and $d_p = 125\,\mu m$ flows, although far more multi-sized particles formed for the $d_p = 75\,\mu m$ flow, specifically from time, $t^+ \approx 1000$. This further explains the reduction in N_{col} noticed for the same time in Figure 5.6(a) and the increase in N_{agg} in Figure 5.6(b).
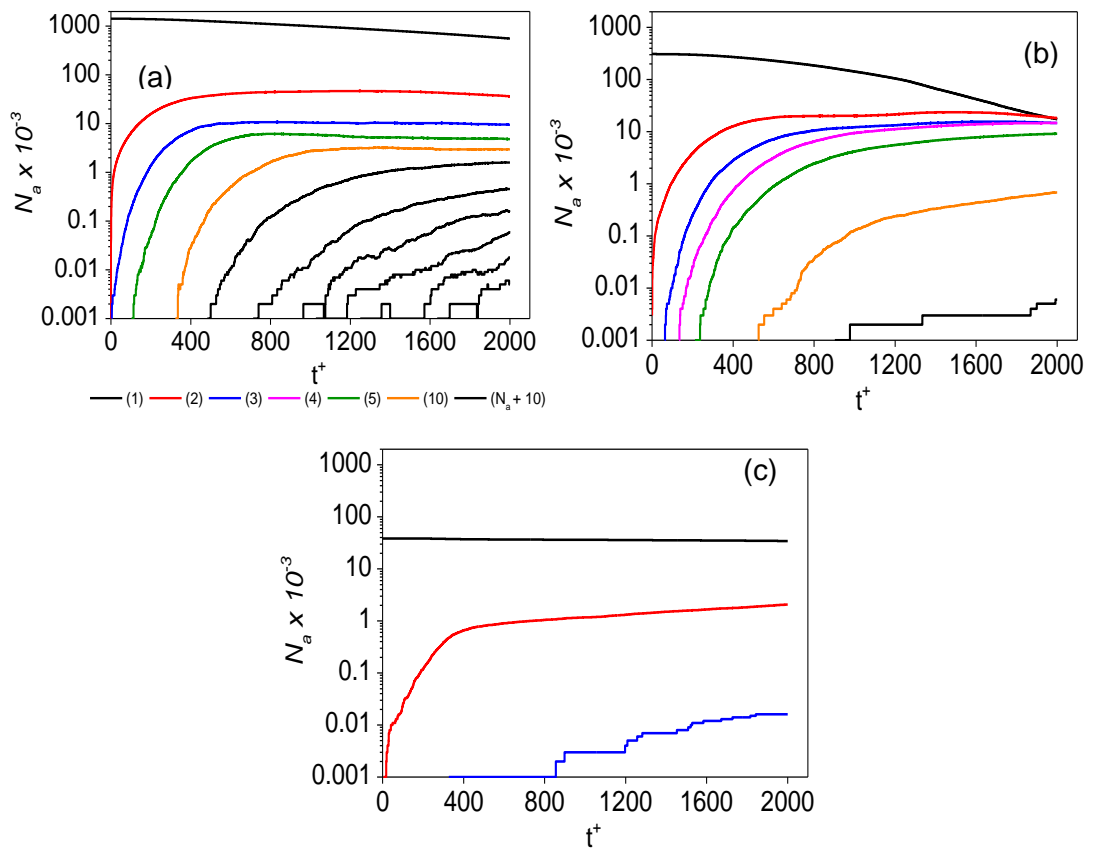
Figure 5.7: Agglomerate formation with time across the channel: (a) Dp = 75um (b) Dp = 125um (c) Dp = 250um. Line numbers: single (1), double (2), triple (3), quadruple (4), quintuple (5), sextuple (6) etc.

The behaviours shown for the different particle sizes is clearly as a result of the inclusion of gravity in the flow which causes the particles to exhibit certain characteristics, depending on their degree of response to the fluid flow. Particle collision is enhanced for larger particles as they are easily influenced by gravity which tends to enhance their migration towards the lower region of the channel into areas of high turbulence. This, in turn, increases their local particle concentration in the lower wall region, with increased turbulence levels promoting collision.

Agglomeration is enhanced for smaller sized particles as they follow the flow more closely and tend to remain in the bulk flow where turbulence levels are minimal, promoting particle agglomeration as a result.

Figure 5.8(a)-5.8(i) shows results for the distribution of the collisions and agglomerations across the channel, and the locations where they occur, at time $t^+ =$ 500, 1000 and 2000. These results were obtained by averaging over the length of the channel and over $t^+ \pm 500$ (mean taken 500 either side of the value i.e. $t^+ = 1000$ means $t_{501}^+ + t_{502}^+ + \cdots + t_{1500}^+/1000$) about each time value given to provide a sufficiently large sample for analysis, with the cross-stream domain divided into 16 equally spaced zones in the wall-normal direction for the with and without gravity cases considered (with the floor of the channel being at $x^+ = 0$). In all cases, a general migration of the particles towards the lower wall region of the channel is noticed, with the number of collisions and agglomerations in the upper wall region decreasing over time as particles migrate downwards due to the effects of gravity; consequently, increasing their concentration in this region. However, the rate at which the particles migrate is noticeably different for the selected particle sizes. By $t^+ = 500$, the initial even distribution of particle events across the channel has changed due to this migration due to gravity, with collisions and agglomerations occurring across each of the zones considered, although primarily in the region of the channel floor.

At $t^+ = 500$, the initial even distribution of particle events across the channel has changed due to gravity. For $d_p = 75\,\mu m$ the migration towards the lower wall region is gradual, with collision and agglomeration occurring across each slab at reasonable levels. A similar particle migration trend is noticed in the flows with particles $d_p = 125\,\mu m$ and $d_p = 250\,\mu m$, although the migration is much faster, with the $d_p = 250\,\mu m$ flow being most affected by gravity. By $t^+ = 1000$, the larger size particles are seen to have migrated significantly more than for the smallest particle size case. By $t^+ = 2000$, the depletion of particles in the upper half of the channel is complete, with the highest concentration of particles now located near the lower wall for particle sizes $d_p = 125\,\mu m$ and $d_p = 250\,\mu m$. Over the times considered, it is noted that the number of collisions close to the lower wall gradually reduces with time, as does the number of agglomerations occurring in this region. This is to be expected because, as larger particles are formed through the depletion of smaller particles, the total number of particles within the flow reduces significantly and hence fewer collisions occur and agglomerates and formed over time. The flow with $d_p = 75\,\mu m$, however,

continued to migrate slowly at a steady rate due to the reduce impact of gravity. As expected, the gradual migration confirms that smaller sized particles are less responsive to the force of gravity which tends to enhance the movement of larger particles into areas of high turbulence towards the lower wall region.
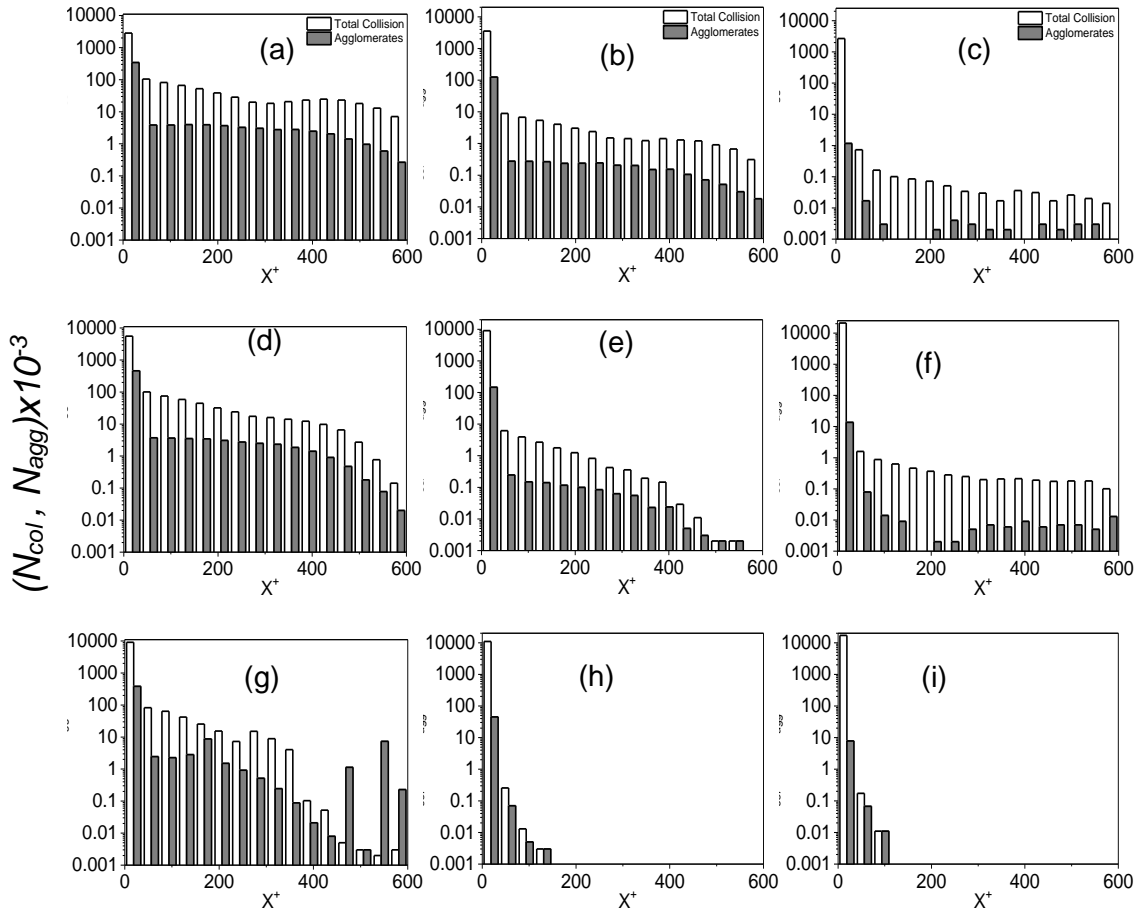
Figure 5.8 Distribution of particle collisions and agglomeration across the channel at $Re = 300$, for (a, d, g) $d_p = 75\,\mu m$ (b, e, h) $d_p = 125\,\mu m$ and (c, f, i) $d_p = 250\,\mu m$, at mean time values of (a, b, c) $t^+ = 500$, (d, e, f) $t^+ = 1000$ and (g, h, i) $t^+ = 2000$

In terms of the collision and agglomeration count, it is noticed that despite considerably more particles being present in the smaller particle flow, the number of particle collisions in the region closest to the lower wall in all cases are approximately the same, with the maximum collision reaching 5,000,000 at t$^+$ = 500. By t$^+$ = 1000 there were more collision in the flow with $d_p = 125\,\mu m$ and $d_p = 250\,\mu m$, even though the amount of particles introduced in both flows is relatively lesser than those of $d_p = 75\,\mu m$. This is again, as a result of the increase impact of the gravity force on the larger size particles, enhancing their migration towards the channel floor which then increases the number of collisions beyond those of the smaller particles. In contrast, the number of agglomeration appears to behave differently, with maximum

agglomeration counts of approximately 500,000, 150,000 and 1,000 for the flows with particles $d_p = 75\ \mu m$, $d_p = 125\ \mu m$ and $d_p = 250\ \mu m$, respectively. The significant difference observed for the agglomeration count in the results further confirms that particle agglomeration is favourable in areas of low turbulence and therefore more likely to occur in areas away from the wall region where turbulence is maximum. It is also fair to conclude that the agglomeration formation rate is not necessary dependent on the frequency of collision but more on the cohesiveness of the particles which is (a function of the particle size), the surrounding turbulence and the particle response to the force of gravity.
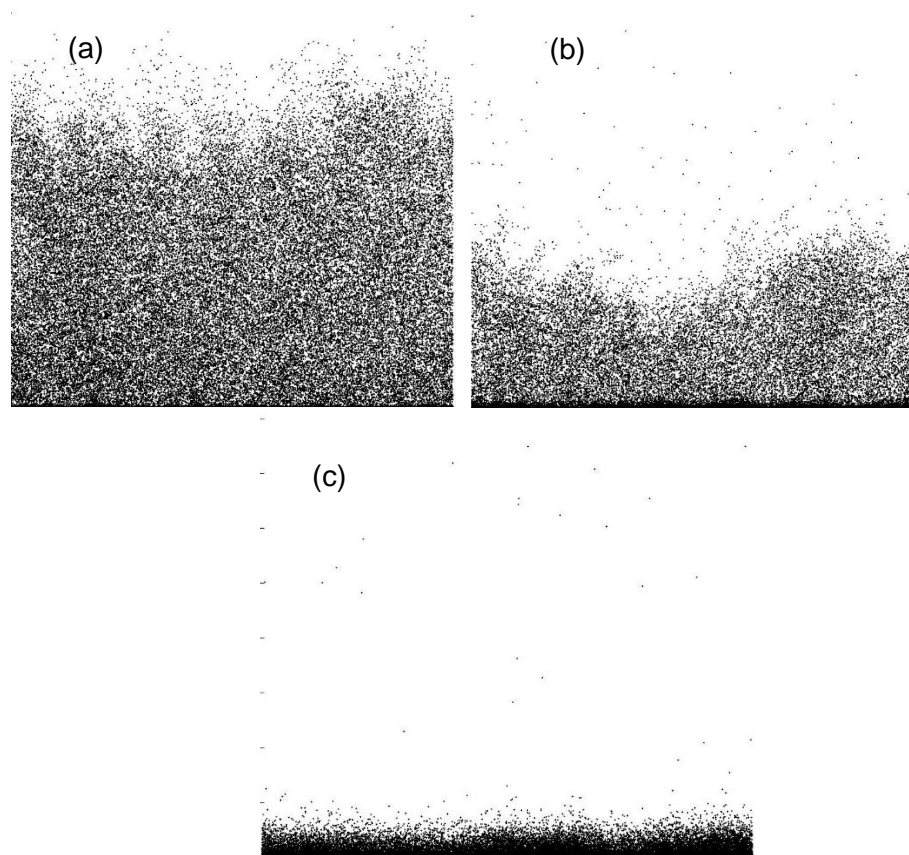
Figure 5.9 Instantaneous distribution of particles on (x, y) planes for a gravity flow at t = 1000 and Re = 300 (a) $d_p = 75\ \mu m$ (b) $d_p = 125\ \mu m$ and (c) $d_p = 250\ \mu m$

Using the visual representation showing the instantaneous positions of the particles in the channel domain at time $t^+ = 1000$ in Figure 5.9(a)-5.9(c), provides more clarity on the analysis performed so far. Here, the plots show the particle distribution along the x, y planes in flows under the influence of gravity. It clearly indicates an increase in particle migration towards the lower channel wall with increase in particle size. The largest size particle is observed to be the most influenced by gravity as the majority of the particles seem to accumulate in the channel floor region.

Finally, Figure 5.10(a) and 5.10(b) gives results for the particle agglomeration rate N_{agg}/N_{col} and the distribution of the instantaneous particle concentration C/C_0 as a function of the diameter of the primary particles, at the referenced dimensionless time, t^+ = 2000. In Figure 5.10(a), the result clearly denotes an increase in the rate of the agglomeration process with decreasing particle diameter.
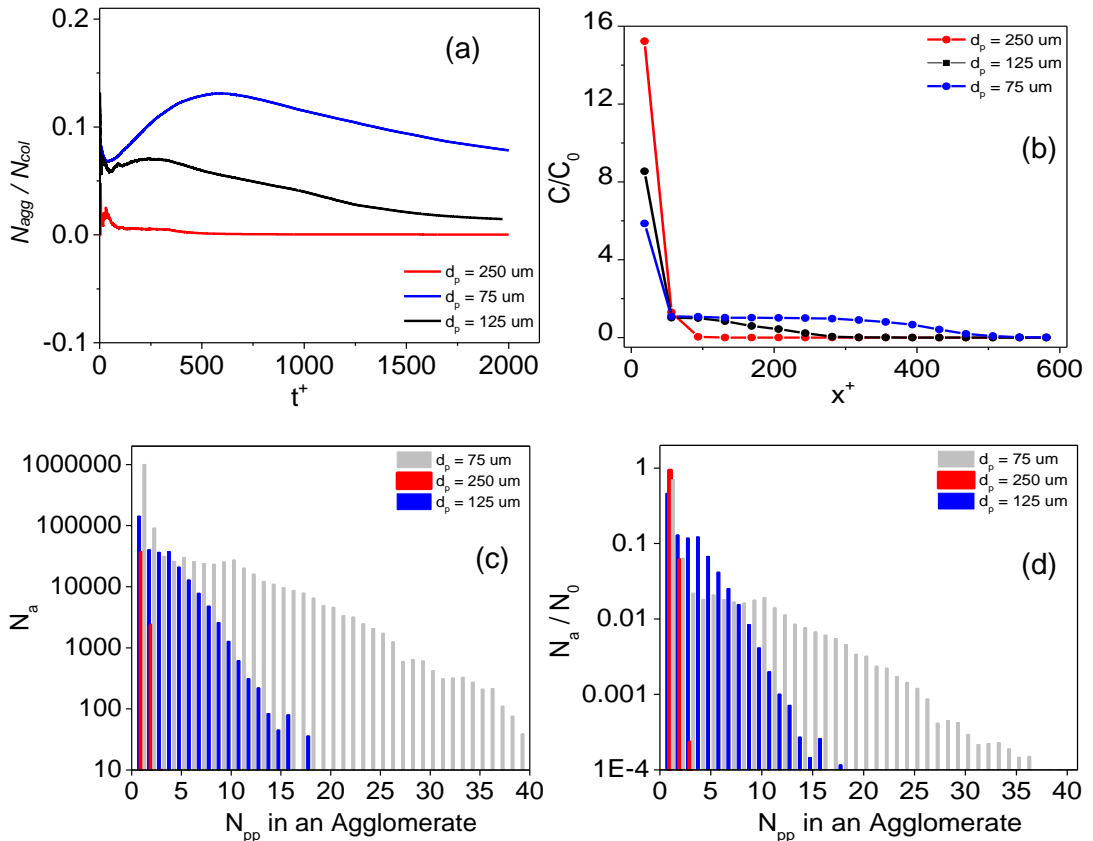
Figure 5.10 (a) Particle rate of agglomeration comparison for the selected particle sizes; (b) the instantaneous particle concentration distribution on (x, z) planes; (c) the number of single particles [single (1)] and agglomerates of the same type [double (2), triple (3), quadruple (4), etc.]; and (d) normalised form of (c). The plots show the simulation for a dimensionless time up to $t^+ = 2000$ at $Re_\tau = 300$.

The largest sized particle is observed with the lowest agglomeration rate even though the concentration for this size is highest close to the lower wall as show in Figure 5.10(b). Figure 5.10(c) is a semi- logarithmic plot showing the number of non-agglomerated primary particles i.e. single (1) and the evolution of the different type agglomerates i.e. double (2), triple (3), quadruple (4), quintuple (5), sextuple (6), etc., formed after a dimensionless time, $t^+ = 2000$. The same is shown in Figure 5.10(d) but normalised using the initial number of primary particles so that the comparisons are independent of the initial conditions imposed on the particles are shown based

on a unit agglomeration. Here it is further confirmed that the larger the diameter of the particles, the less likely they become to form agglomerates for reasons previously mentioned. In this instance, only 3 particle agglomerates are formed for the largest diameter case compared to the smallest diameter particles were agglomerates consisting of over 30 primary particles are formed. From these results, the contribution of gravity in the collision and agglomeration process is shown to be highly significant and cannot be overlooked.

5.3.2 Fluid Turbulence and stresses

Finally, in this subsection, the effect of the particle sizes on the mean fluid velocity, and fluid normal and shear stresses, is considered for a flow under the influence of gravity. As shown in Figure 5.11(a-f), the investigation was performed using particles of diameter $d_p = 75\,\mu m$ and $d_p = 250\,\mu m$ and at mean time values $t^+ = 500, 1000$ and 2000. The instantaneous two-phase solution was compared against the fluid-only solution of $Re_\tau = 300$. Though the feedback of the different particle sizes on turbulence have been successfully investigated in the last chapter, there is still the need, however, to further understand whether the fluid statistics are in anyway influenced by the inclusion of gravity in the flow; hence, the motivation for this investigation. In Figure 5.11(a) and 5.11(b) at $t^+ = 500$, the overall impact of particles on the fluid mean velocity component w^+ is minimal, with almost nothing to suggest there is any considerable influence of the gravity force on the flow at this time instance. However, as the simulation progressed over time, slight changes in the fluid mean velocity is observed for the largest size particle flow which is more noticeable at $t^+ = 2000$. The mean velocity is suppressed in the regions close to the lower wall where the particle concentration is now at maximum. Here, the influence of the gravity force on the fluid mean velocity w^+ is clearly visible as its inclusion directly resulted in the migration of the particles towards the lower wall region. The clustering of the highly inertia particles in this region, alters the mean fluid velocity by acting as an obstruction to the fluid motion, which consequently reduces the local fluid velocity in the region. The reduction in the fluid mean velocity is further enhanced with the formation of larger agglomerates in this region as it increases the resistance on the fluid flow.
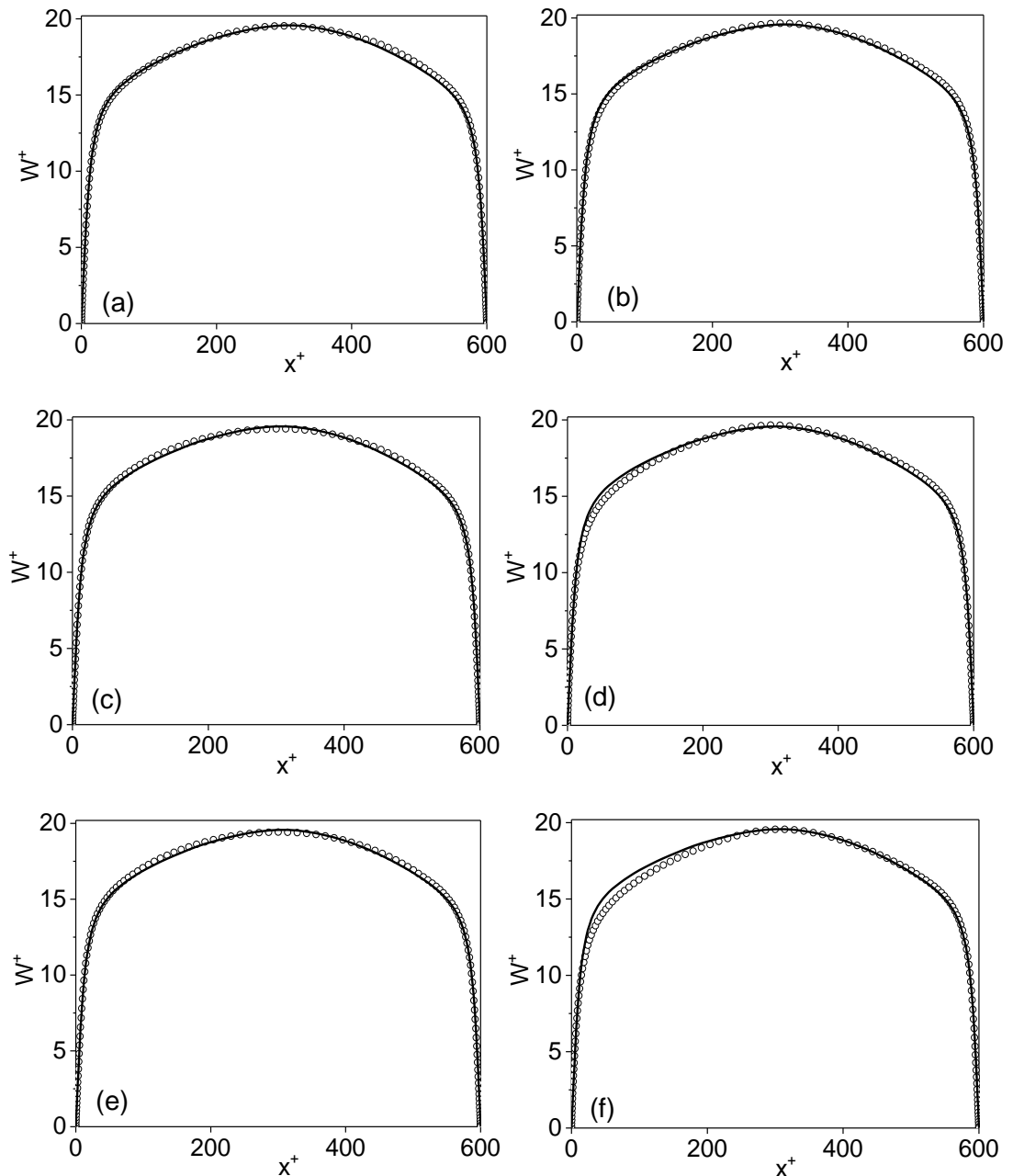
Figure 5.11 Fluid streamwise mean velocity for (a, c, e) $d_p = 75\,\mu m$ (b, d, f) $d_p = 250\,\mu m$, at mean time values of (a, b) $t^+ = 500$, (c, d) $t^+ = 1000$ and (e, f) $t^+ = 2000$. $\Phi_p = 10^{-3}$, and $Re_\tau = 300$ (— single-phase flow, ○ multi-phase flow).

For the case of the lower sized particle flow, there are no substantial changes in the fluid profile over the time shown. This is as a result of the reduced impact of the gravity force on smaller sized particles, due to their very low inertia and Stokes number. This makes the particles more likely to follow the fluid more closely and less responsive to the gravity force, as have been demonstrated from past analysis. The less impact of the gravity force on the particles ensures that the fairly even distribution of the particles across the channel is maintained for a period much longer than for larger sized particles, which consequently reduces the rate of particle clustering in

sections of the flow domain. As a result, there is less resistance on the fluid mean velocity in the lower wall as particle distribution is only slightly affected. With only minimal particle clustering now occurring, the fluid local velocity remains almost unaffected as in this case. Overall, for the selected flow conditions in this study, the impact of gravity on the fluid mean velocity is small for the time considered but enough to modify the flow dynamics of the particles, which consequently affects collisions and agglomeration.

In Figure 5.12(a-f), the effect of the particles on the normal stress (or fluctuations) in the streamwise, spanwise and wall normal directions are examined. The for the x-z plane shear stress component is also shown in the figures. For the flow with $d_p = 75\ \mu m$ particles, the stresses in the spanwise and wall normal directions of the flow remains unchanged throughout the simulation time. This is also true for the shear stress where no changes were observed for the given simulation time. However, the stresses in the streamwise ($w_{rms}'^+$) direction, although minimal, is noticed to be slightly impacted but reduces with time as the particle concentration in the upper wall region equally reduces. In contrast to this behaviour, the fluid streamwise component ($w_{rms}'^+$) is observed to be augmented in the lower wall region, with the impact gradually increased with time as particle migration towards the lower wall continues. This behaviour is as expected since this is the region where the particle concentration (see Figure 5.10b for concentration profile) reaches maximum in the flow. For the flow with $d_p = 250\ \mu m$, the fluid velocity components in all three directions in the lower wall region is impacted more significantly; which is unlike the lower sized flow where only the streamwise component is impacted. However, no impact is noticed for the $u_{rms}'^+$, $v_{rms}'^+$ and $u'^+ w'^+$ components in the upper region of the flow, but just as in the $d_p = 75\ \mu m$ flow, the augmented $w_{rms}'^+$ component is observed to gradually normalise as the particle concentration is reduced with time. More importantly, the shear stress and the normal stresses in the lower wall region was increasingly augmented with time due to the continuous increase of the particle concentration in this region. The reasoning here is similar to that in Figure 5.11 where the increase in particle concentration in the lower wall resulted in an increase in the wake generation in the local fluid flow. In conclusion, the effect of the gravity on the flow turbulence is clear in both instances, although lesser in the smaller sized particle. In all, the fluid statistics was found to be increasingly affected by the presence of gravity and enhanced for flows with larger diameter particles.
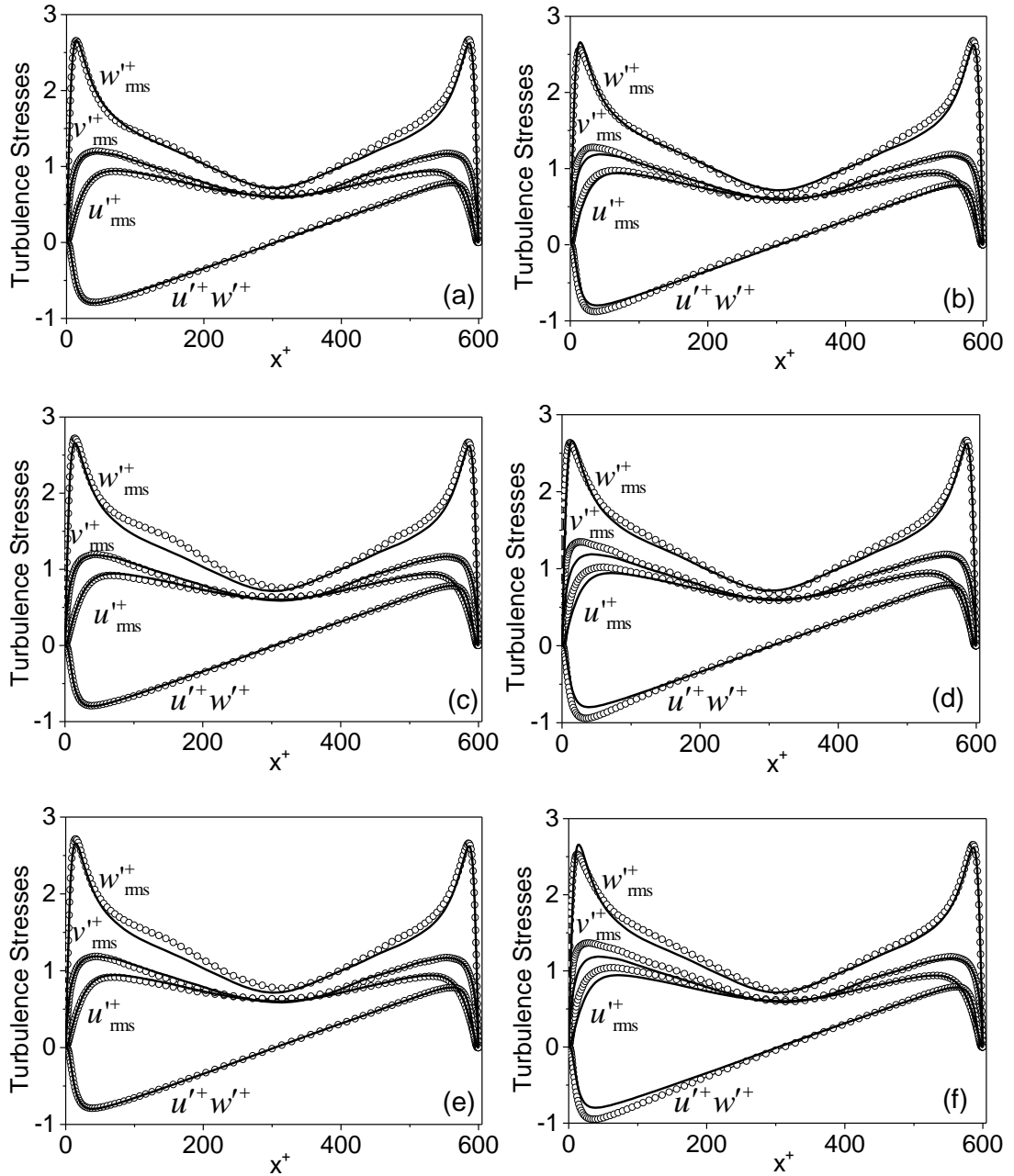
Figure 5.12 Fluid normal and shear stresses for (a, c, e) $d_p = 75\ \mu m$ (b, d, f) $d_p = 250\ \mu m$, at mean time values of (a, b) $t^+ = 500$, (c, d) $t^+ = 1000$ and (e, f) $t^+ = 2000$. $\varnothing_p = 10^{-3}$, and $Re_\tau = 300$ (— single-phase flow, ○ multi-phase flow).

5.3.3 Particle Force Analysis

In this section we examine the forces per unit mass acting on the particles in the direction of the wall where particle concentration is maximum for all particle size flow. The analysis in each case is performed at a fixed time ($t^+ = 1000$) as the values calculated in each node per unit time was first compared in magnitude to values obtained at the nodes at other times throughout the flow, with no significant differences observed. Hence, the insert in the figures is only a representative of one

particular instant in the flow, although averaged over t$^+$ ± 100 (mean taken 100 either side of the value i.e. $t^+ = 1000$ means $(t^+_{901} + t^+_{902} + \cdots + t^+_{1100})/200$.

Figure 5.13 Forces (N/kg) analyses for Re_τ = 300 at t^+ = 1000 (a,c,e) forces acting in the wall normal direction on particles (b,d,f) enlarged plot showing the relative magnitude of smaller forces acting within the flow. (a, b) $d_p = 75\,\mu m$ (c, d) $d_p =$ 125 μm and (e,f) $d_p = 250\,\mu m$ (F_{SL} = shear lift, F_{AM} = added mass, F_D = drag, F_{GB} = gravity/buoyancy, F_{PG}= pressure gradient).

It should be noted that the averaging did not change the magnitude of the different forces acting on the flow but only performed to ensure a relatively smooth profile is obtained. The results in Figure 5.13 are representative of all the individual forces acting on the particles of diameter $d_p = 75\,\mu m,\ 125\,\mu m$ and $250\,\mu m$ across the

channel at time t^+ = 1000. The forces analysed for the case with gravity, in order of magnitude of their effect on the particles, include the net gravity-buoyancy (F_{GB}), drag (F_D), shear lift (F_{SL}), pressure gradient (F_{PG}) and added mass forces (F_{AM}). Unlike the force analysis performed in the last chapter, the net gravity/buoyancy force is included in this analysis since it is proven to be highly significant in dictating the dynamics of the particles and the resulting influence on the fluid turbulence statistics. Note that Figure 5.13(b), 5.13(d) and 5.13(f) give enlarged views compared to Figure 5.13(a), 5.13(c) and 5.13(f) to better show the magnitude of the less influential forces.

In all cases, the net gravity force is observed to be the dominant force on the particles, balanced by the drag force which acts in the opposite direction. There is also little influence of the pressure gradient and added mass forces on the particles, with the impact of the lift force also significantly reduced relative to the drag and net gravity forces. From the results, it is noticed that the magnitude of the drag and net gravity forces is unchanged for the different sized particles, although the drag force on the largest particle is an exception. This is as expected, since the net gravity force is universally constant and that the drag would normally act in the opposite direction but in equal magnitude to create a balance on the particle motion. The forces are also noticed to reduce across the channel width with increase in particle diameter. Again this is due to the depletion of the particle concentration in the upper channel regions, which becomes enhanced with increasing particle diameter. Finally, the irregularity observed for the drag force on the largest diameter particle in Figure 5.13(e), occurs since the particles for this dimensionless time is predominantly settled in the lower wall region of the channel, which therefore means that the particle velocity is now almost zero. Hence, the drag on the particles becomes insignificantly small and tends to zero. However, the gravity force as expected remains unchanged. Overall, this force analysis therefore demonstrates the dominant role of the net gravity force, and the balancing effect of the drag force, generated during particle migration towards the lower wall under the influence of gravity.

5.4 Reynolds Number Effect on Collision and Agglomeration

In this section, the effect of turbulence on particle collision and agglomeration is investigated. The study considered two different flow Reynolds numbers for the simulation, namely $Re_\tau = 150$ and 590. Mono-sized particles of diameter $d_p =$

125 μm were introduced in both flows. The study is particularly motivated due to the relevance in industrial applications where there is often the need to ramp up flow velocity to boost flow assurance. It therefore becomes necessary to understand the influence of such increase in velocity on the collision and agglomeration process. It is also noted that the degree of response (relaxation times) of the mono-sized particles (measured by its Stokes number) in these flows are a function of the flow Reynolds number. Hence, the inertia for same size particles of different Re_τ flows becomes different. However, the decision to fix the particle size for the different Re_τ flows rather than the inertia was based on the intent to replicate the more practical situation earlier mentioned. Also, the global number of particles in both flows differs since the channel domain size is different in each case. Nonetheless, the particle volume fraction is fixed in both flows, hence, it is used as the bases of comparisons. Where necessary the results are made dimensionless to ensure trends of the particle parameters are comparable. The corresponding particle relaxation times, Stokes number and other relevant parameters are as stated in Table 5.1 and Table 5.2 Particle parameters used in the simulation below.

Table 5.1 Turbulent channel flow grid parameters used

Re_τ	$L_x \times L_y \times L_z$	$N_x \times N_y \times N_z$	Δ_x^+	Δ_y^+	Δ_z^+	$h\ (m)$
150	$2h \times 2\pi h \times 4\pi h$	$129 \times 128 \times 128$	$0.07 - 7.10$	7.42	14.84	0.02
590	$2h \times \pi h \times 2\pi h$	$129 \times 128 \times 128$	$0.31 - 27.92$	14.5	14.84	0.02

Table 5.2 Particle parameters used in the simulation

Re_τ	$d_p/\mu m$	$St = \tau_p^+$	τ_p	$(\emptyset_p)$	N_{pp}
150	125	0.157	2.35×10^{-3}	10^{-3}	1240000
590	125	2.425	2.35×10^{-3}	10^{-3}	308955

Figure 5.14(a) compares results for the total number of collision events, N_{col}, and the total number of the collisions leading to agglomerations, N_{agg}, in the channel, for both Re_τ flows, up to a dimensionless simulation time $t^+ = 2000$. From these results, it is clear that the collision and agglomeration of particles for the lower Re_τ case starts from the moment they are introduced into the flow. By $t^+ = 2000$, there were a total

of 34,976,175 particle collisions and 1,168,928 agglomerations in the flow. The collision and agglomeration of particles for the higher Re_τ flow begins from the simulation start time.
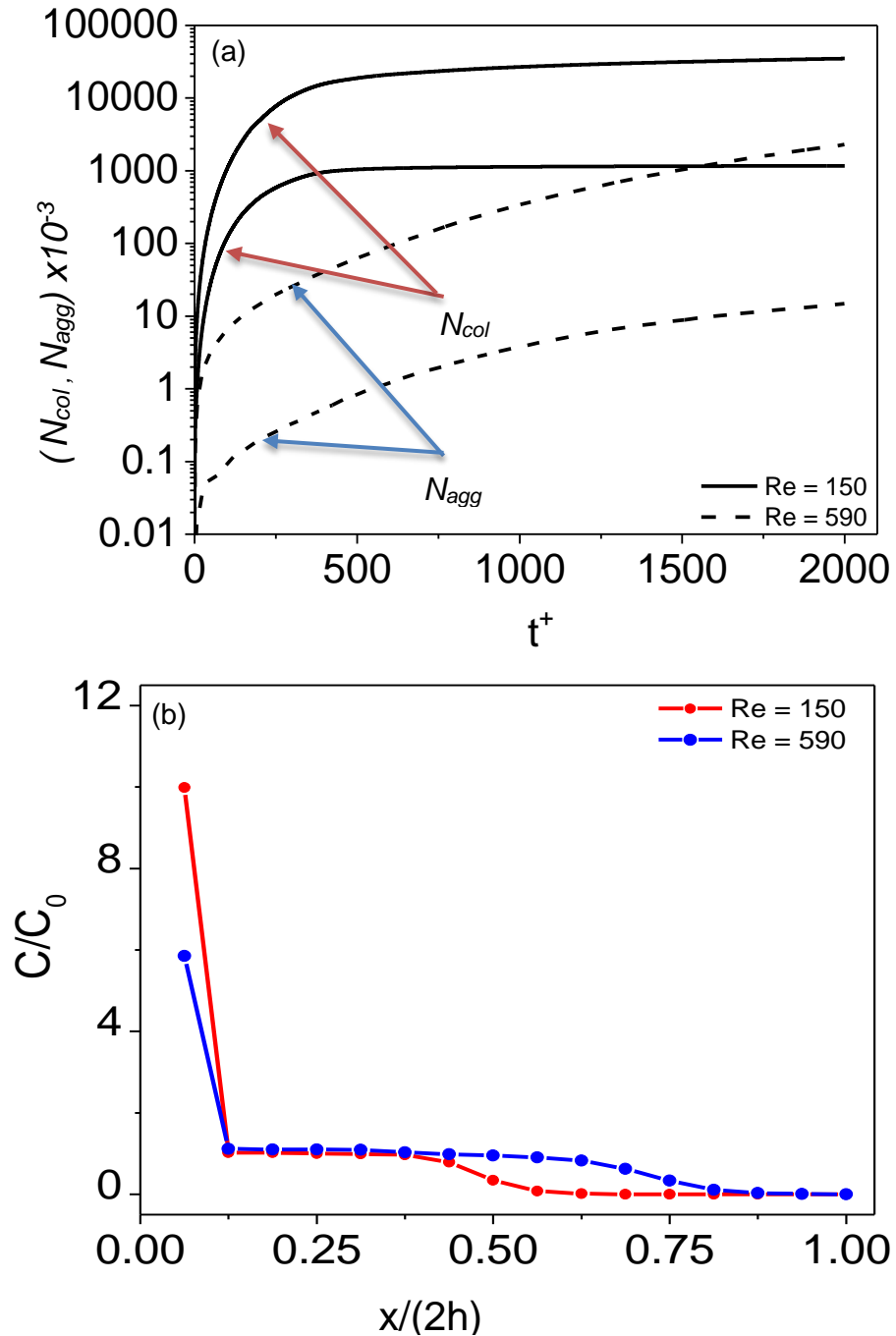
Figure 5.14 (a) Total number of particle collisions, N_{col} and particle agglomerations N_{agg} as a function of time in the $Re_\tau = 150$ flow, and (b) the instantaneous particle concentration distribution on (x, z) planes at $t^+ = 2000$, normalised using the channel full length.

By t^+ = 2000, there were a total of 2,291,290 particle collisions and 14,783 agglomerations in the flow with gravity. The results show similar trends to those

observed in the lower Re_τ flow, except that the rate of increase in collisions and agglomerations over time are decreased compared to the latter flow, with the number of collisions and agglomerations increasing at an approximate steady state. In both cases, the sensitivity of the particles to the different shear Reynolds number flows becomes more obvious when the collision to agglomeration ratio is considered. The lower Re_τ flow had a collision to agglomeration ratio of 30:1 compared to 155:1 for the higher Re_τ flow. This is to suggest that far more agglomerations occurred for the lower Re_τ flow. This owes to the fact that although the particles in the lower Re_τ flow see less turbulence, they tend to be more influenced by gravity, which enhances their migration into the lower wall regions of relatively high particle concentration. With the increase in particle concentration in this region, particle collision is enhanced as the distance between particles becomes shortened.

Also, the low turbulence levels for the lower Re_τ flow creates the ideal conditions for particle agglomeration since the relative kinetic energies of the particles which is needed to overcome the cohesive energy between them is weakened. In contrast, the high turbulence levels experienced in the higher Re_τ flow ensured that the particle distribution remained fairly even across the channel, with minimal particle clustering within the flow. The low number of agglomeration is primarily a result of the increased turbulence in the flow which leaves colliding particles having a high enough energy post-collision to overcome the van der Waals energy of attraction between them, with the majority of collisions being elastic collisions. Consequently, only a few agglomerations occurred, though the number of particle collisions is relatively high. The trend in this plot is of interest, as it would normally be expected that the more turbulent flow should result in more particle collisions, considering the understanding on the role of turbulence in promoting particle-particle interactions. The explanation for this behaviour is given in Figure 5.14(b), where it is shown that more particles migrated to the lower wall region of the channel for the lower Re_τ flow. Unlike the higher Re_τ flow, the clustering of particles in this region of high turbulence intensifies the local particle interaction, hence, the more collisions. To further understand this, it is useful to analyse the collision and agglomeration distribution across the channel for both Re_τ flows. The next figure provides this information.

Figure 5.15(a - f) show results for the distribution of the collisions and agglomerations across the channel, and the locations where they occur, at time t^+ = 500, 1000 and 2000. For the flow of $Re_\tau = 150$ the number of collisions and agglomerations in the

upper region of the channel is observed to decrease over time as particles migrate towards the lower wall which consequently increases their concentration in this region. By t^+ = 500, the initial even distribution of particle events across the channel has changed due to gravity, with collisions and agglomerations occurring across each of the zones considered, although primarily in the region of the channel floor. By t^+ = 1000, particle migration towards the lower wall has increased significantly, with almost no collisions or agglomeration now occurring within the upper regions of the flow due to the low concentration of particles there.
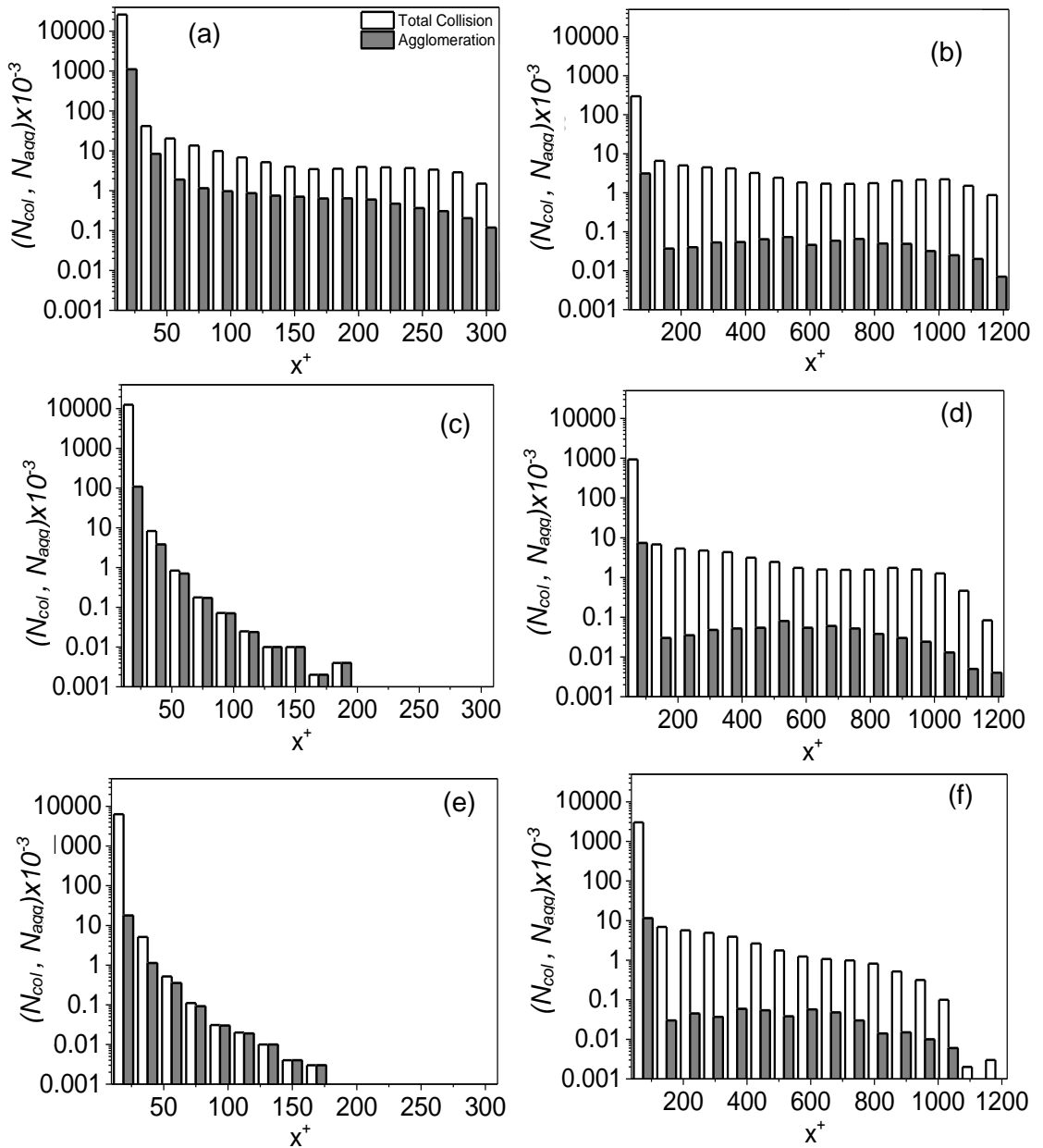
Figure 5.15 Distribution of collisions and agglomerations across the channel in the wall-normal direction: (a, c, e) $Re_\tau = 150$ and (b, d, f) $Re_\tau = 590$; times of (a, b) t^+ = 500, (c, d) t^+ = 1000 and (e, f) t^+ = 2000.

By t^+ = 2000, the depletion of particles in the upper half of the channel is complete, with the highest concentration of particles now located near the lower wall. Over the times considered, it is noted that the number of collisions close to the lower wall gradually reduces with time, as does the number of agglomerations occurring in this region. This is to be expected because, as larger particles are formed through the depletion of smaller particles, the total number of particles within the flow reduces significantly and hence fewer collisions occur and agglomerates and formed over time. Beyond t^+ = 2000, a significant number of particles under the influence of gravity were observed to be out of the flow altogether, although not shown. For the flow of $Re_\tau = 590$ the particles again clearly migrate downwards within the flow, as for the $Re_\tau = 150$ case, but at a substantially reduced rate. In contrast to the latter flow, the number of collisions and agglomerations also increases with time near the lower wall, albeit at a significantly reduced rate, whilst remaining low within the remaining regions of the channel. The increased levels of turbulence in this flow therefore prevent particle agglomeration within the main body of the flow, relative to the $Re_\tau = 150$ case, which in turn delays particle downward migration relative to that observed in the latter case. Close to the lower wall, the number of collisions and agglomerations slowly increase with time as the particle concentration in this region increases due to particle downward migration.
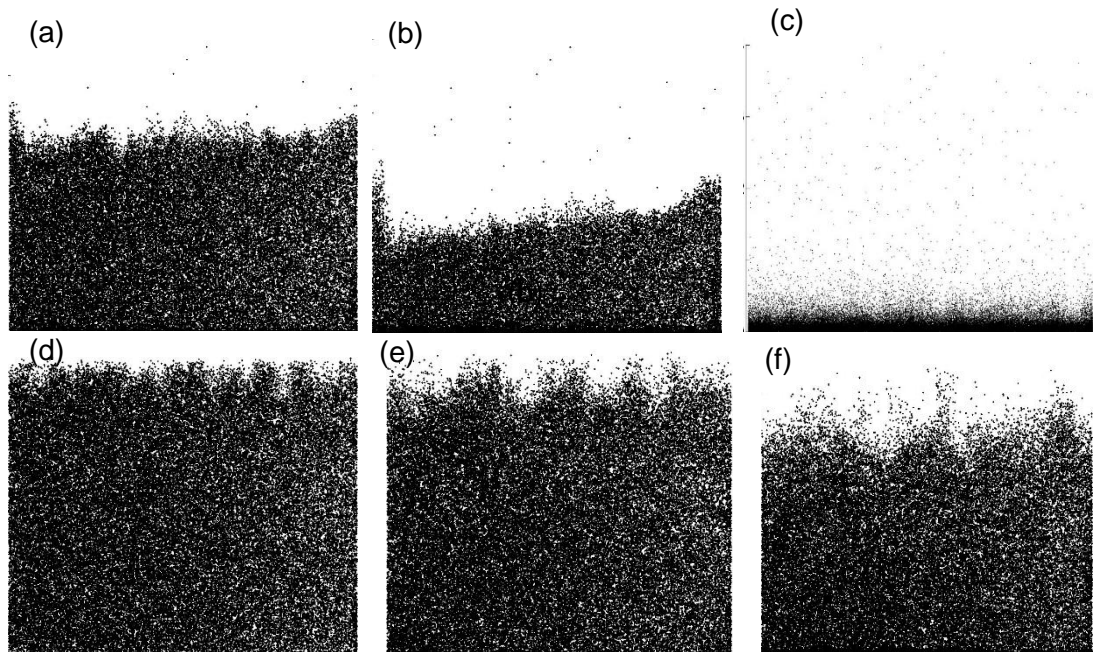
Figure 5.16 Instantaneous distribution of particles on x-y planes for gravity flows of particle diameter $d_p = 125\,\mu m$ (a, b, c) $Re_\tau = 150$ and (d, e, f) $Re_\tau = 590$; at dimensionless times (a, d) t^+ = 500, (b, e) t^+ = 1000 and (c, f) t^+ = 2000.

Visual plots of the particles introduced into the flow are shown in Figure 5.16, which gives a perspective view of the instantaneous particle distributions along the x-y planes at various wall normal locations. The existence of competing gravitational and flow turbulence is observed to influence particle dispersion differently in both flows with time. The effect of gravity results in the accumulation of particles within the lower region of both channels but clearly enhanced for the low Re_τ flow (Figure 5.16a-c), with more local particle collisions occurring in the lower wall region. For the higher Re_τ flow a much slower rate of segregation is observed due to the high turbulence levels as previously highlighted.

To further examine the effect of turbulence in the collision and agglomeration process, it is necessary to analyse the number of agglomerates of the same type N_a formed in each case. Figure 5.17, therefore, gives results for the total number and sizes of the agglomerates that form within both Re_τ flows with time, including the single particle depletion rate and the corresponding evolution of multi-sized particles. At the start of both simulations, the results again indicate a sharp increase in the number of agglomerates formed, although the rate of formation of multi-particle agglomerates differs significantly between the two flows. The sharp increase is mainly as result of the interference from the initial conditions on the particles. For the lower Re_τ case in Figure 5.17(a), the rate of formation of multi-particle agglomerates increases exponentially, with agglomerates consisting of up to 10 primary particles formed by $t^+ \approx 100$. As the simulation time increases, and the original single particles decrease in number, large agglomerates begin to form through the resulting collisions between single particles and larger agglomerates, and between the agglomerates themselves. By the end of the simulations, agglomerates consisting of up to 80 single particles were formed. The result provides an indication that the single primary particles and the smaller agglomerates are used up to form much larger agglomerates from $t^+ \approx 250$ at a much higher rate than in the case of the higher Re_τ flow.

Another reason for this is due to the higher particle inertia in the lower Re_τ flow which accentuates their migration towards the channel bottom for a flow influenced by gravity. In contrast to the Re_τ 150 case, it is observed that the rate of depletion of the single particles is minimal for the $Re_\tau = 590$ case in Figure 5.17(b), with only a few agglomerates formed by $t^+ = 2000$. Overall, the results show a steady rate of formation of multi-particle agglomerates with time, which is due to the high kinetic

energies of the particles obtained as a result of the increased turbulence levels. Figure 5.18, which is normalised using the original particle number N_0, further improves the perspective on the influence of turbulence on the primary particles (single) and the various types of agglomerates formed (double, triple, quadruple, etc.).
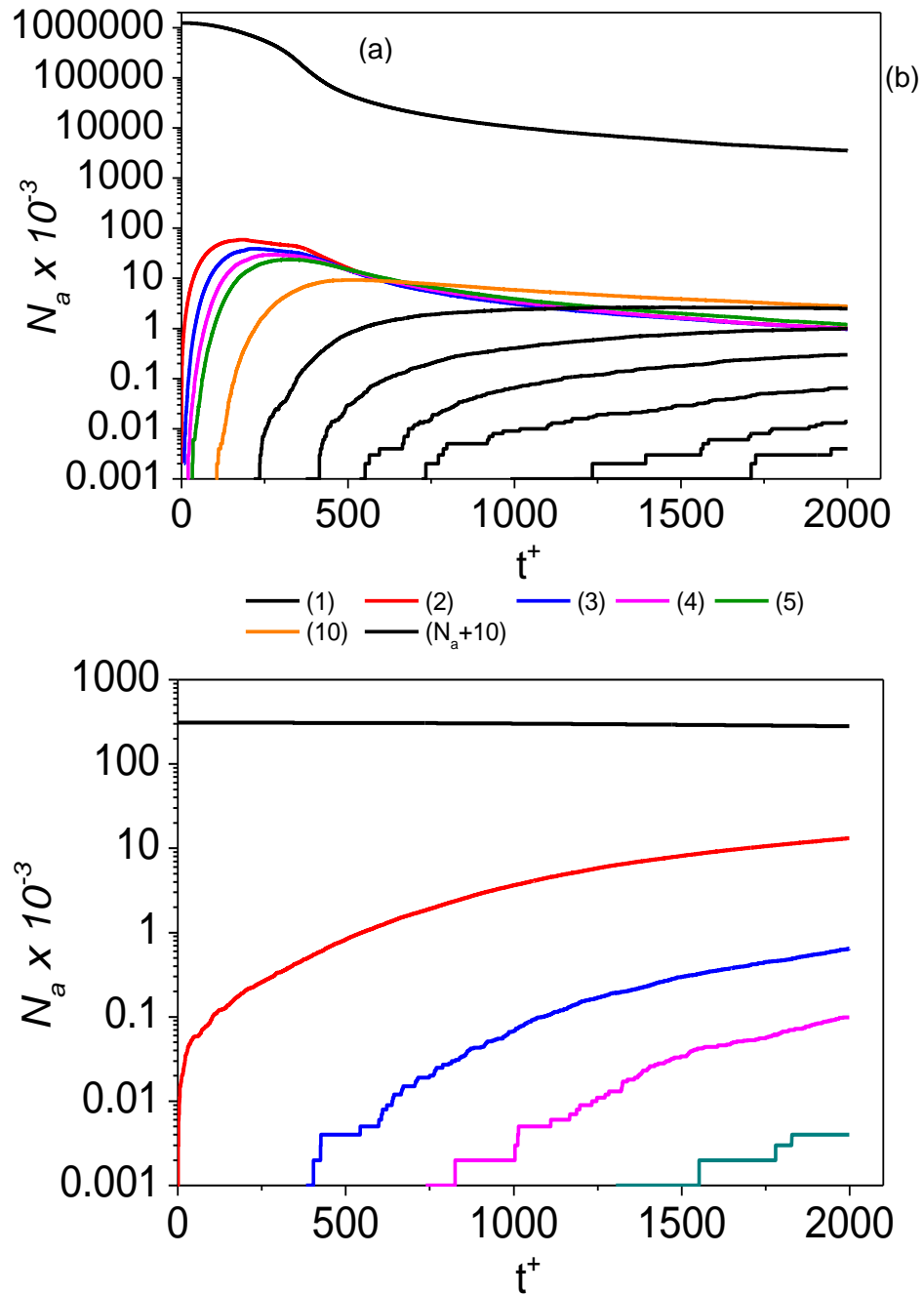
Figure 5.17 Agglomerate formation with time for a flow of $d_p = 125 \, \mu m$, (a) $Re_\tau = 150$ and (b) $Re_\tau = 590$. Key under figure gives total number of original particles (1), and total number of original particles in each agglomerate (2-80).

Here, it is seen that there are much lesser number of the single particles left in the computational domain for the lower Re_τ flow when compared to that of the higher Re_τ flow. This is believed to be as a result of the high number of agglomerate formed in the $Re_\tau = 150$ flow, which is in direct contrast to the $Re_\tau = 590$ flow where only few agglomerates formed.
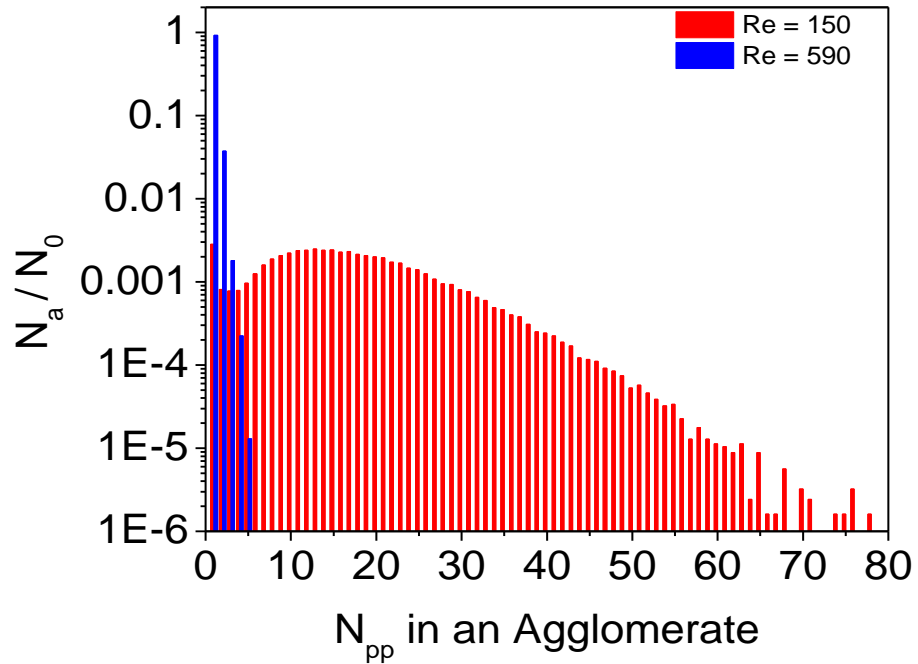
Figure 5.18 number of single particles [single (1)] and agglomerates N_a of the same type [double (2), triple (3), quadruple (4), etc.] $d_p = 125\ \mu m$
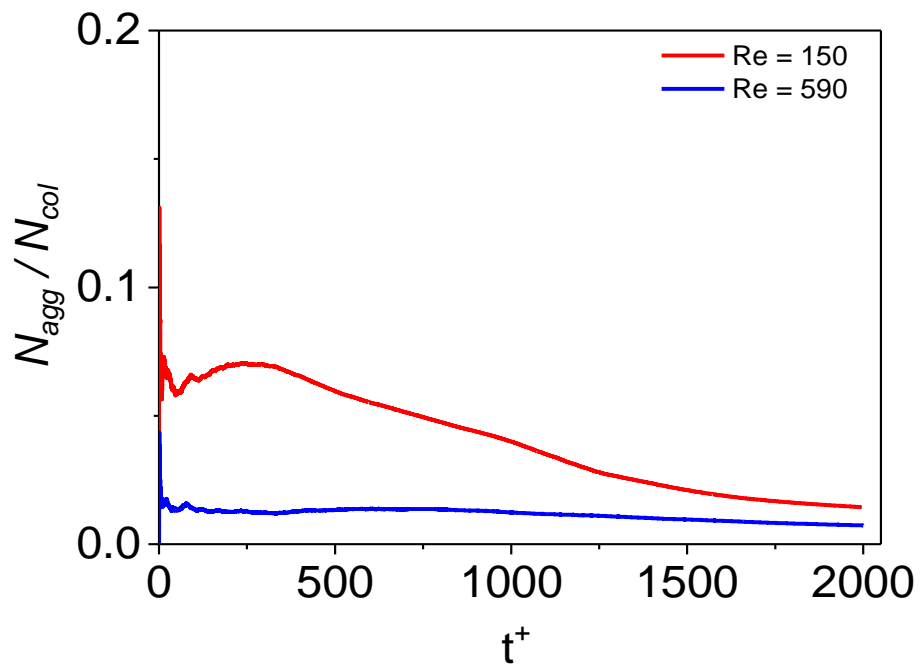
Figure 5.19 Particle rate of agglomeration comparison for both (a) Re_τ flows, for a dimensionless time up to $t^+ = 2000$. $d_p = 125\ \mu m$

Lastly, the particle agglomeration rate N_{agg}/N_{col} is examined for both cases in Figure 5.19, up to a dimensionless time of $t^+ = 2000$. The figure, depicts a strong dependency of the particle characteristics on turbulence intensity. After an initial period of bias resulting from the flow initial conditions, the rate of particle agglomeration is seen to reach a steady state for the higher shear Reynolds flow. However, the agglomeration rate continued to decrease for the lower shear Reynolds flow after an initial increased rate of agglomeration. It is also noticed that the rate is far higher in the lower shear Reynolds flow, which provides further evidence on the strong influence of gravity on the low shear Reynolds flows.

5.5 Conclusions on Main Findings

The work reported in this chapter has been concentrated on the prediction of some of the conditions favouring particle collisions and agglomeration within turbulent channel flows using a fully coupled LES-LPT approach. Particularly, simulations have been carried out to investigate the contribution of gravity and particle size variation, in the collision and agglomeration processes for a liquid-solid flow. The gravity force was observed to play a key role as it enhances the migration of the particles towards the lower regions of maximum turbulence, which ultimately increases the rate of particle collisions and agglomeration in the region. Also, particle agglomeration was observed to be mostly formed in the centre regions of the channel where the turbulence intensity is lowest; and are particularly the case for particles of low inertia, since they tend to be more responsive to the flow than the gravitational pull. In terms of the particle size effect, the agglomeration was found to be enhanced for smaller particles since the area of contact is higher than for larger sized particles, and consequently increases the forces of attraction between the particles. They are also more concentrated in the bulk flow where it has been shown to be more favourable to the agglomeration process. However, more collisions occurred for the larger sized particles. This was attributed, again, to the increased influence of the gravity force on the particles, which enhances their migration into areas of high turbulence; hence more collisions but less favourable to agglomeration due to high kinetic energies possessed by the particles post-collision.

Furthermore, analysis on the turbulence effect on collision and agglomeration was reported. The simulation used two separate horizontal channel flows of a fixed diameter but different levels of turbulence, achieved through increasing the Reynolds

number of the flow. It was found that the rate of collision and agglomeration was strongly sensitive to the level of turbulence generated in the flow, with far more collisions and agglomeration occurring for the flow of less turbulence. This was concluded to be as a result of the increased influence of gravity on the less turbulent flows, which encourages a faster migration of the particles towards the lower wall region. Hence more localised collisions and agglomerations occur as particle concentration increase in the area. On turbulence modulation, the fluid was observed to be affected by the variation in flow parameters, although only minimal. The fluid turbulence was increasingly augmented with the increase in particle size; while the mean velocity was suppressed. The effect was found to be enhanced with the inclusion of gravity in the flow, although of negligible magnitude. In all, particle collisions and agglomeration were shown to be highly influenced by the gravity and the flow turbulence, with the level of impact highly dependent on the size of the particles.

6 Collision and Agglomeration in Turbulent Vertical Channel Flows

6.1 Introduction

It is well known (Marchioli and Soldati, 2007) that a change in the direction of flow of a wall-bounded two-phase flow directly impacts on the particle velocity statistics and also their distribution in the flow domain. This is normally due to the change in magnitude of the forces acting on the particles resulting from the change in flow configurations. The investigations in this chapter are, therefore, extended into a fully developed turbulent vertical channel flow geometry. This is necessary to further understand the impact of these forces and the change in geometry on particle collisions and agglomerations, for flows pointing towards and against the direction of gravity. The analysis performed in this computational domain made contrast on flows moving in counter directions, and simulated using the LES-LPT technique.

In the first part of this work, the contribution of the surrounding forces in the collision and agglomeration process is tested by making comparisons between flows of different configurations; one in which the flow is in the positive gravity direction (downward flow) and another flowing against the direction of the gravity force (upwards flow). The second subsection, using a fixed particle diameter, reports the effect of turbulence on collision and agglomeration, with comparisons also made between both vertical channel flow cases. This was achieved by comparing particle responses to flows of varying Reynolds number in each flow direction case. It is also important to mention here that the particles in all cases were introduced at the local fluid velocity in all cases. The parameters utilised in this study are as specified in Table .5.1.

6.2 Vertical Channel Up-Down Flows: Collision, Agglomeration and Turbulence

Four different flow configurations are considered in this subsection, and categorised based on the flow Reynolds number and direction of flow. These includes, Upward flow ($Re_\tau = 150$), upward flow ($Re_\tau = 590$), downward flow ($Re_\tau = 150$) and down flow ($Re_\tau = 590$). Figure 6.1 is the schematic diagram of the vertical flow geometry and the co-ordinate system employed in this chapter.
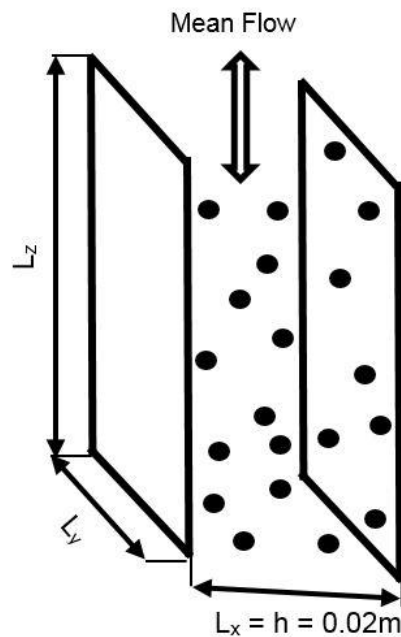
Figure 6.1 Vertical channel domain dimension sketch and the flow configuration in both upward and downward directions

6.2.1 Collision and Agglomeration: Up-down Flow Comparison

For the upward and downward channel flows, Figure 6.2 compares the total number of particle collisions, N_{col}, and agglomerations, N_{agg}, for both flows up to a dimensionless simulation time of $t^+ = 2000$ (~8.9 s in real time). A third case showing the simulation without the presence of gravity is also included in the figure for reference. Here, the superscript (+) represents variables made dimensionless using u_τ and the kinematic viscosity v. From these results, it is clear that the collision and agglomeration of particles starts from the moment they are introduced into the flow. It is also observed that there are far more collisions in the flows when compared to those that resulted in agglomeration, hence, not all collisions resulted in agglomeration. The result in Figure 6.2(a) suggests more collisions occurred for the

flow in the positive gravity direction (after $t^+ \approx 700$), followed by the no gravity case and then the upward flow. The difference in collision between the downward flow and the latter cases is observed to increase with time.
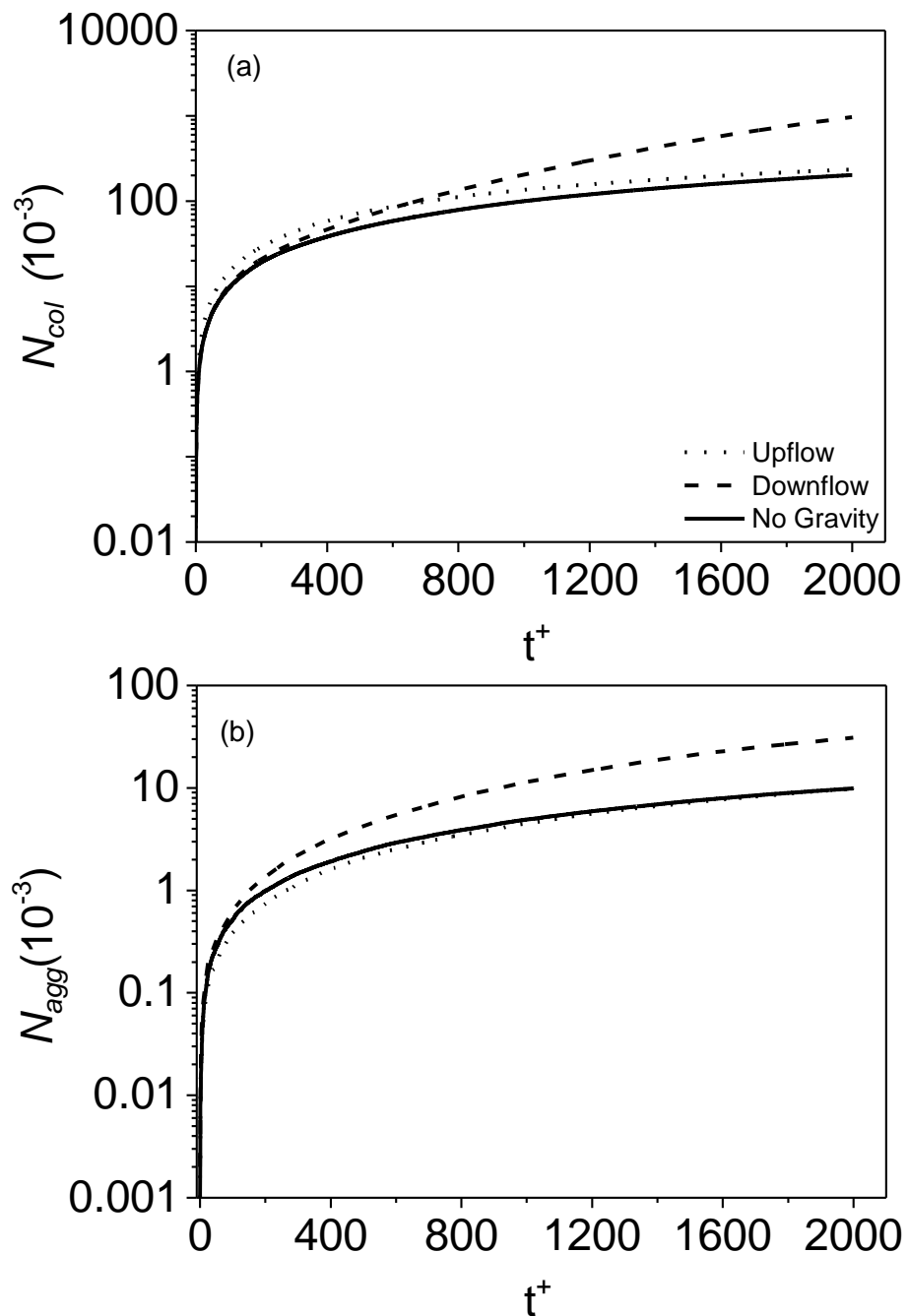
Figure 6.2 Total number of collisions and agglomeration comparison for all particle sizes (a) Number of collisions and (b) Number of agglomerations for time up to $t^+ = 2000$ at $Re_\tau = 300$

Nonetheless, the trend in the upward and no gravity flows show a close match, with only minimal differences observed. Before $t^+ \approx 700$, the upward flow is, however, noticed to have slightly higher collision count but is well known to have resulted from

the initial bias on the flow. The trend also show an almost identical behavior for the total particle agglomeration process in Figure 6.2(b), except that there were less agglomerations in the upward flow during the initial stages of the simulation, comparing to the downward and no gravity cases. In all cases, it is observed that during the initial stages of the simulations, particle collisions and agglomerations increase sharply, with results for the upward and no gravity flow cases achieving an approximate steady state with time, whilst in the downward flow the number of collisions and agglomerations continues to increase with time and do not asymptote to an approximate steady state. By $t^+ = 2000$, there were a total of 15,312,856 particle collisions and 220,338 agglomerations in the downwards flow, while for the upward flow the corresponding numbers were 205,762 and 9,567, respectively. This yields a collision to agglomeration ratio of 70:1, which is relatively high compared to the upward flow case of ratio 22:1. In general, the particle collision and agglomeration count is seen to be more in the flow pointing in the direction of gravity (downward flow case), which is attributed to the reduced drag in this flow direction, and more importantly, the increased lift effect (Wang and Squires, 1996) on the particles which enhances particle migration into regions of high turbulence near the channel walls. This consequently increases the local particle interactions in the near-wall regions, leading to more collisions and agglomerations in the regions.

In the case of the upward flow, the particle movement towards the wall is suppressed due to the presence of the lift force which tends to promote their migration into the bulk flow region, consequently leading to lesser collisions and agglomerations. This is in agreement with the DNS study of Marchioli and Soldat (2007) where the effect of lift force on particle distribution in a vertical channel flow was investigated. The authors successfully demonstrated that for a flow in the positive gravity direction, the mean particle drift velocity toward the wall (Stokes number dependent) is significantly as a result of the lift force on the particles which acts towards the wall direction and increases over time. In contrast, the authors also demonstrated that for a flow in the direction opposite to the gravity force (upward flow), lift force tend to promote particle migration away from the wall regions and into the bulk flow. Fan and Ahmadi (1993) reached similar conclusion where it was reported that the rate of particle deposition in a vertical channel flow is enhanced when pointing in the positive gravity direction and reduced when gravity is in the opposite direction. This is further confirmed by the particle concentration profiles in Figure 6.3 which clearly indicate particle migration towards the wall regions in the downward flow, whilst in the case of the upward flow

the particles are noticed to be depleted in the wall region and increasingly accumulate in the bulk flow.

The result depicts the strong dependency of the particle distribution on the gravity and lift forces. However, the contribution of gravity is not directly linked with this behaviour, but the drag force, since the gravitational acceleration is constant. This is confirmed in McLaughlin (1989) and Wang and Squires (1996), where it was suggested that for vertical flows the force due to gravity does not directly lead to particle deposition but on drag and the Saffman lift forces. Fan and Ahmadi (1993) in agreement showed that particle deposition rate in the walls of a vertical duct flow is affected by gravity via the shear-induced lift force. They reported an enhancement in the deposition rate by the shear-induced lift force when gravity is in the direction of the flow and a reduction when gravity is opposing the flow. It is therefore safe to infer that other than flow turbulent structures, the particle collisions and agglomeration process are predominantly determined by the gravity and lift forces, since the particle dynamics is dictated by both forces.
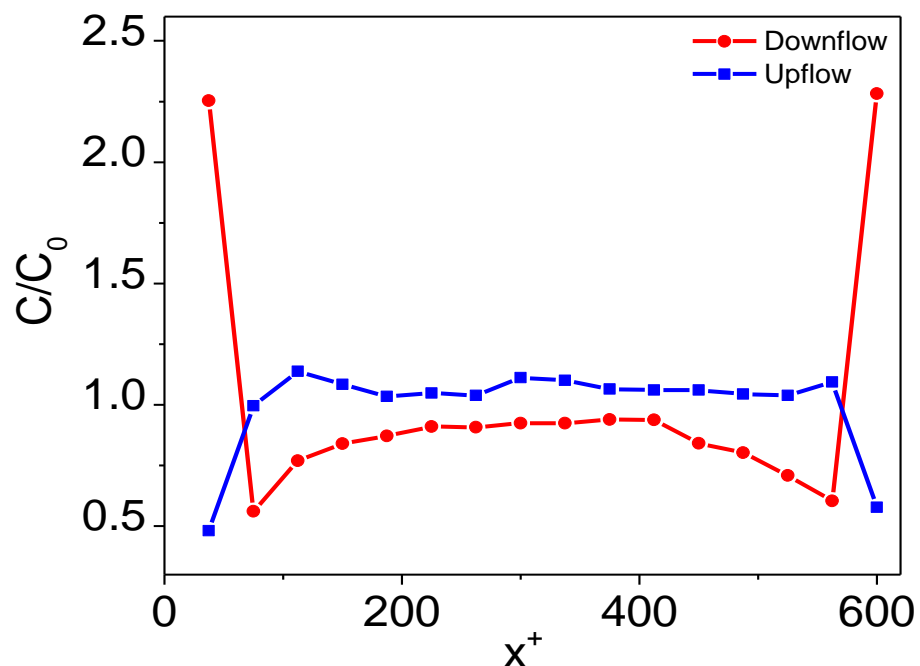
Figure 6.3 the instantaneous particle concentration distribution in the wall normal flow direction at $t^+ = 2000$. $Re_\tau = 300$ and $d_p = 125\ \mu m$.

In order to further understand the significance of the flow direction in the formation of agglomerates, it becomes necessary to analyse the number of agglomerates of the same type N_a formed in each flow. Figure 6.4, therefore, gives results for the total number and sizes of the agglomerates that was formed within the flows as a function

of time, in both flow directions, including the single particle depletion rate and the corresponding evolution of multi-sized particles. In both cases, only minimal depletion of the single particle is noticed, and decreases steadily with time as larger agglomerates begin to form. At the start of both simulations, the results again indicate a sharp increase in the number of agglomerates formed, although the number of multi-particle agglomerates differs in both flow cases. The sharp increase is mainly as result of the interference from the initial conditions on the particles.

In Figure 6.4(a) showing the upward flow, agglomerates consisting of just 3 single particles are formed by $t^+ = 1000$. The number is slightly increased for the downward flow case shown in Figure 6.4(b), where up to 4 single particle agglomerates were formed by $t^+ = 1000$. By the end of the simulations, agglomerates consisting of up to 9 single particles were formed in the downward flow case, contrasting with a maximum of 4 particle agglomerates in the upward flow case. Again, the behaviour observed in both flow directions further indicates the strong sensitivity of the particles to the direction of flow, as this dictates the degree of their response to the flow. In the case of the downward flow, larger agglomerates are formed due to the lift effect in this flow direction which tends to enhance their migration towards the wall regions of high turbulence. With the increase in particle concentration in the wall region beyond the time shown, more agglomerates are expected to form through since particle interaction will be increased.

(a)

(b)
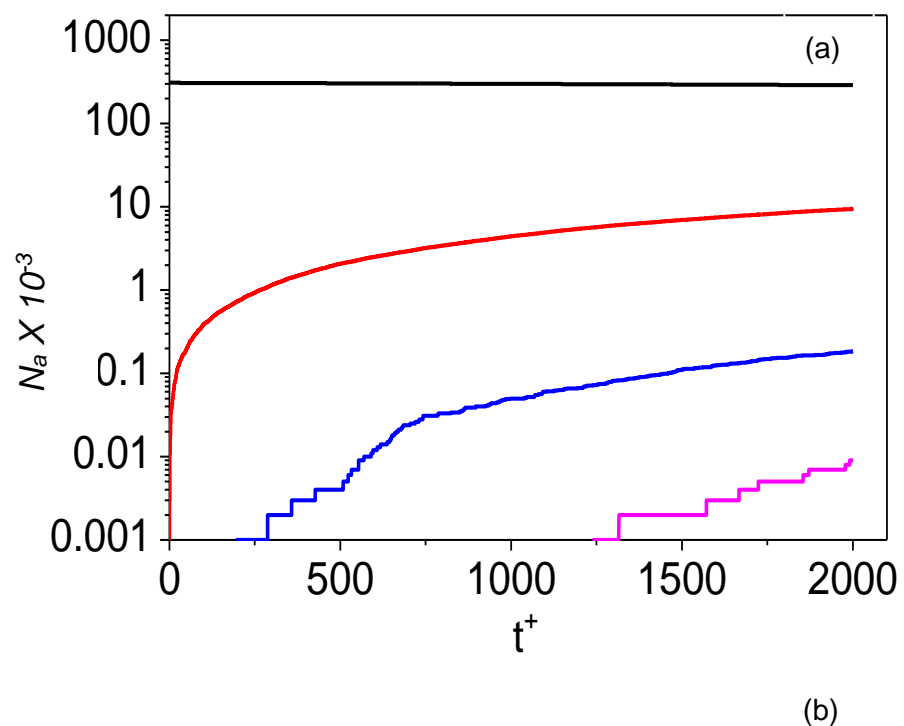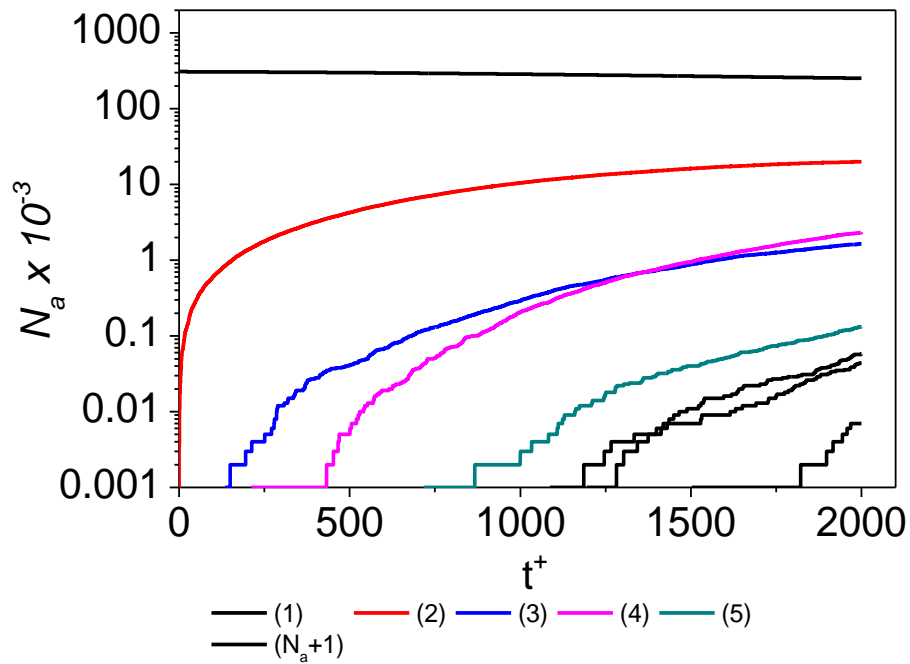
Figure 6.4 Agglomerate formation with time across the channel for $Re_\tau = 300$: (a) Upward flow and (b) Downward flow. Line numbers: single (1), double (2), triple (3), quadruple (4), quintuple (5), sextuple (6) etc.

In Figure 6.5(a) the rate at which particles agglomerate, also known as agglomeration rate or collision efficiency, is examined for both cases up to a dimensionless time $t^+ = 2000$. The agglomeration rate is obtained in terms of the ratio of the collisions leading to particle agglomeration N_{agg} to the total number of collisions N_{col}. Here, it is noticed that for the upward flow case, the agglomeration rate, given as N_{agg}/N_{col} decreased with time up to $t^+ \approx 100$, after which a slight increase in N_{agg}/N_{col}, which continued as the simulation approached a statistically steady state. In contrast to this behaviour, an initial increase in N_{agg}/N_{col} is observed for the downward flow, which continued for a time up to $t^+ \approx 400$, after which the rate is noticed to reduce over time and continued till the end of the simulation.
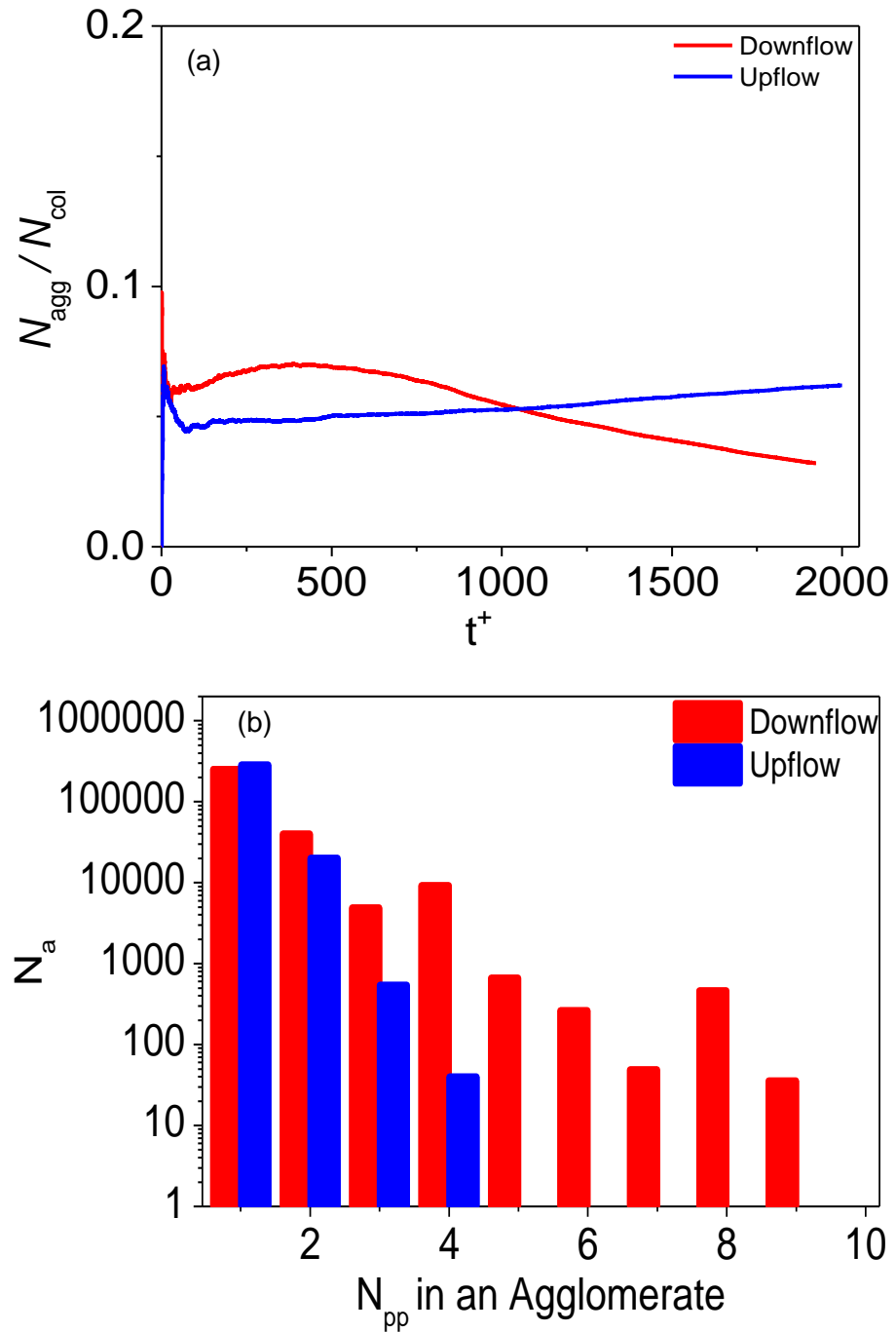
Figure 6.5 Simulation comparison of the upward and downward channel flow cases for a dimensionless time up to $t^+ = 2000$ at $Re_\tau = 300$, $d_p = 125\,\mu m$ (a) Particle agglomeration rate (b) the number of single particles [single (1)] and agglomerates of the same type [double (2), triple (3), quadruple (4), etc.]

The continuous reduction in N_{agg}/N_{col} indicates that the primary particles and/or other agglomerates are also being used up to form larger agglomerates, which clearly supports the trend observed in Figure 6.4(b). It should be noted that the initial decrease and increase in the upward and downward flows respectively, is as a result of the interference from the initial conditions of the flow on the particles, and replicates conditions reported by Breuer and Almohammed, (2015). The term N_{agg}/N_{col} which

also denotes the particle collision efficiency is observed to indicate a higher agglomeration rate for the downward flow up to the time $t^+ \approx 1100$, after which the rate reduces due to the reduction in the total number of colliding particles as larger agglomerates begin to form through over time. Figure 6.5(b) clearly depicts this behaviour. Here the number of primary particles N_{pp} i.e. single (1) and the different type agglomerates i.e. double (2), triple (3), quadruple (4), quintuple (5), sextuple (6), etc., formed after the dimensionless time $t^+ = 2000$ are compared for both the upward and downward flow cases. By the end of the simulation, it is observed that although the single particles still dominate the flow in both cases, the depletion in the number of single particles in the downward flow, and the corresponding evolution of larger size agglomerates (than those found in the upward flow) is noticeable.

The information concerning the collisions and agglomeration distribution across the channel and the locations where they occur for both the upward and downward flow is given in Figure 6.6. The results are shown for the cross-stream domain divided into 16 regions in the wall-normal direction at mean time values of $t^+ = 500, 1000$ and 2000 in each case, although the results are averaged over the length of the channel and over $t^+ \pm 500$ (mean taken 500 either side of the value i.e. $t^+ = 1000$ means $(t^+_{501} + t^+_{502} + \cdots + t^+_{1500})/1000$ to provide a sufficiently large sample for analysis. The cross-stream domain was divided into 16 equally spaced slabs in the wall normal direction in both cases. For the upward flow simulation in Figure 6.6(a), 6.6(c) and 6.6(e) the number of collisions is effectively symmetrical about the channel centre. The number of collisions is noticed to be slightly increased in the near-wall region, even though the local particle concentration is depleted in the region. This is due to the increased turbulence levels in the near-wall region which causes an increase in the local particle-particle interactions in the region. This agrees with Sommerfeld and Soldati, (2007) where it was concluded that the non-homogeneity of the particle distribution is because of the dynamic interaction occurring between particles and near-wall turbulent structures. However, the collision N_{col} is observed to reduce with increase in simulation time due to the increase in agglomeration N_{agg}.
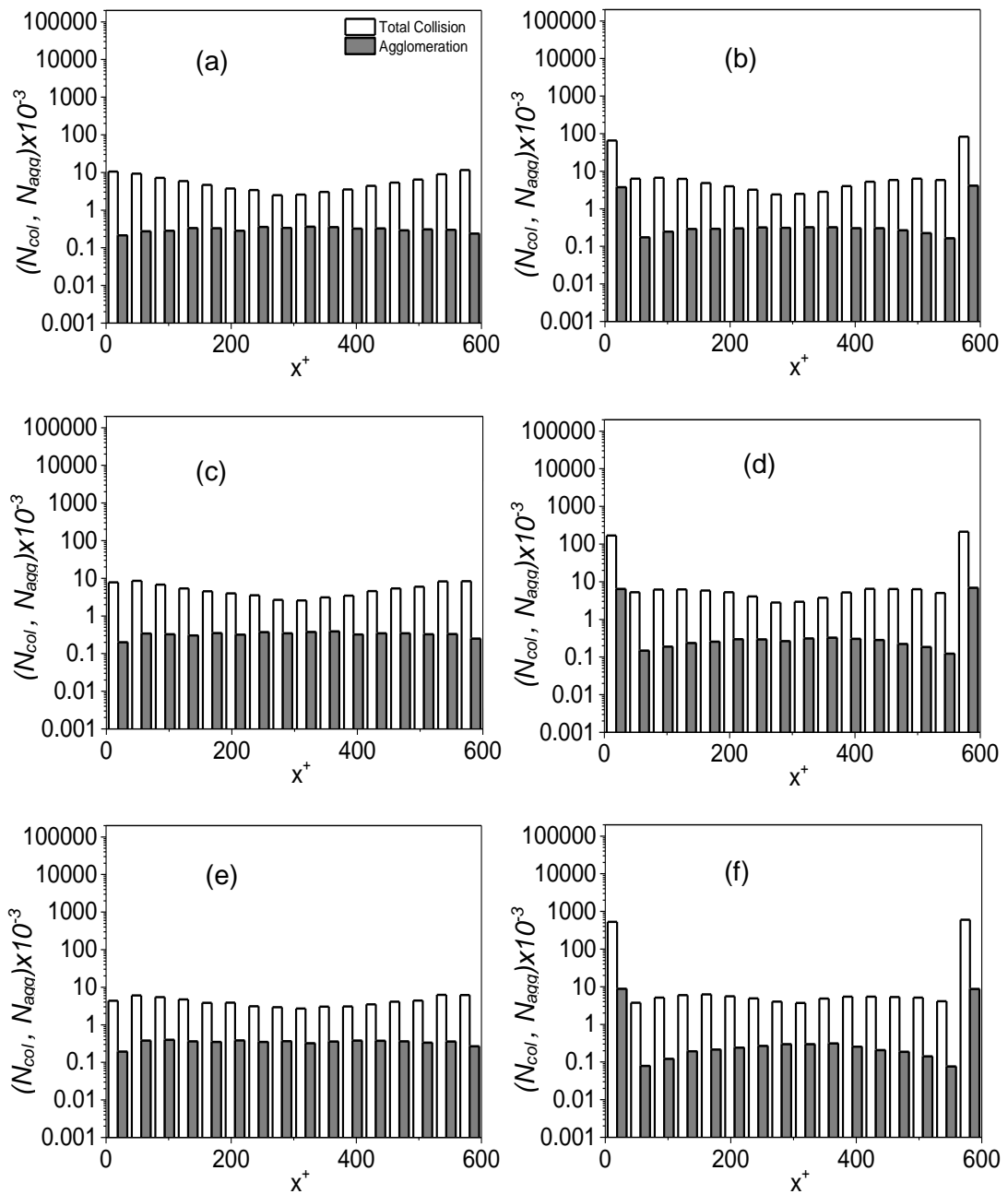
Figure 6.6 Distribution of particle collisions and agglomeration across the horizontal channel of $d_p = 125\,\mu m$ at $Re_\tau = 300$, for (a, c, e) upward flow (b, d, f) downward flow; at mean time values of (a, b) $t^+ = 500$ (c, d) $t^+ = 1000$ and (e, f) $t^+ = 2000$

The changes in the agglomeration count across the channel over time appear to be negligible for the upward flow, with the maximum formation in the middle channel region where turbulence is low. In downward flow in Figure 6.6(b), 6.6(d) and 6.6(f), the trends are noticeably different, with collision and agglomeration reaching maximum levels in the two wall regions due to the migration of particles from the bulk flow towards the walls. As already noted, the lift force is responsible for the continuous increase in particle concentration in the wall regions as it enhances the turbophoretic drift by increasing the particle wall-normal velocity. This consequently

enhances the collisions and agglomerations due to the high turbulence levels close to the wall.

Over the times considered, it is noted that the number of collisions close to the walls gradually decreases with time. This is to be expected because, as larger particles are formed through the depletion of smaller particles, the total number of particles within the flow reduces significantly and hence fewer collisions occur and agglomerates and formed over time. In all, the effect of the lift, gravity and turbulence is seen to be primarily responsible for the particle distribution within the flow, which consequently determines the collision and agglomeration count in the flow. Sommerfeld et al, (2003) describes the conditions in which the lift acts towards and away from the wall and agrees with the behaviour observed here for both flow configurations.

6.2.2 Effect on Fluid Turbulence: Up-Down Flow Comparison

It is well known from the literature (Kulick et al., 1994; Vreman et al., 2009; Kuerten et al., 2011) that in a particle-laden turbulent flow, the presence of particles, if of adequate mass loading, modifies the fluid turbulence. The effect tested for the horizontal channel flow simulations only showed minimal effects of the particles on the fluid turbulence. In this subsection, therefore, the effect of N_{col} and N_{agg} (reported in section 6.2.1) on the mean fluid velocity, and fluid normal and shear stresses is repeated to investigate the contributions for vertical channel flows; and at mean time values $t^+ = 500, 1000 \text{ and } 2000$. The instantaneous two-phase solution was compared against the fully developed fluid-only solution of $Re_\tau = 300$ for both upward and downward flow cases over time. The simulation utilized here is four-way coupled.

In Figure 6.7 the particle feedback effect on the upward and downward flow streamwise mean velocities are shown. In Figure 6.7(a, c and e) the fluid streamwise mean velocity is observed to be attenuated, with the attenuation increasingly pronounced as the simulation progresses with time. By $t^+ = 2000$, the attenuation of the fluid streamwise mean velocity becomes even more pronounced.
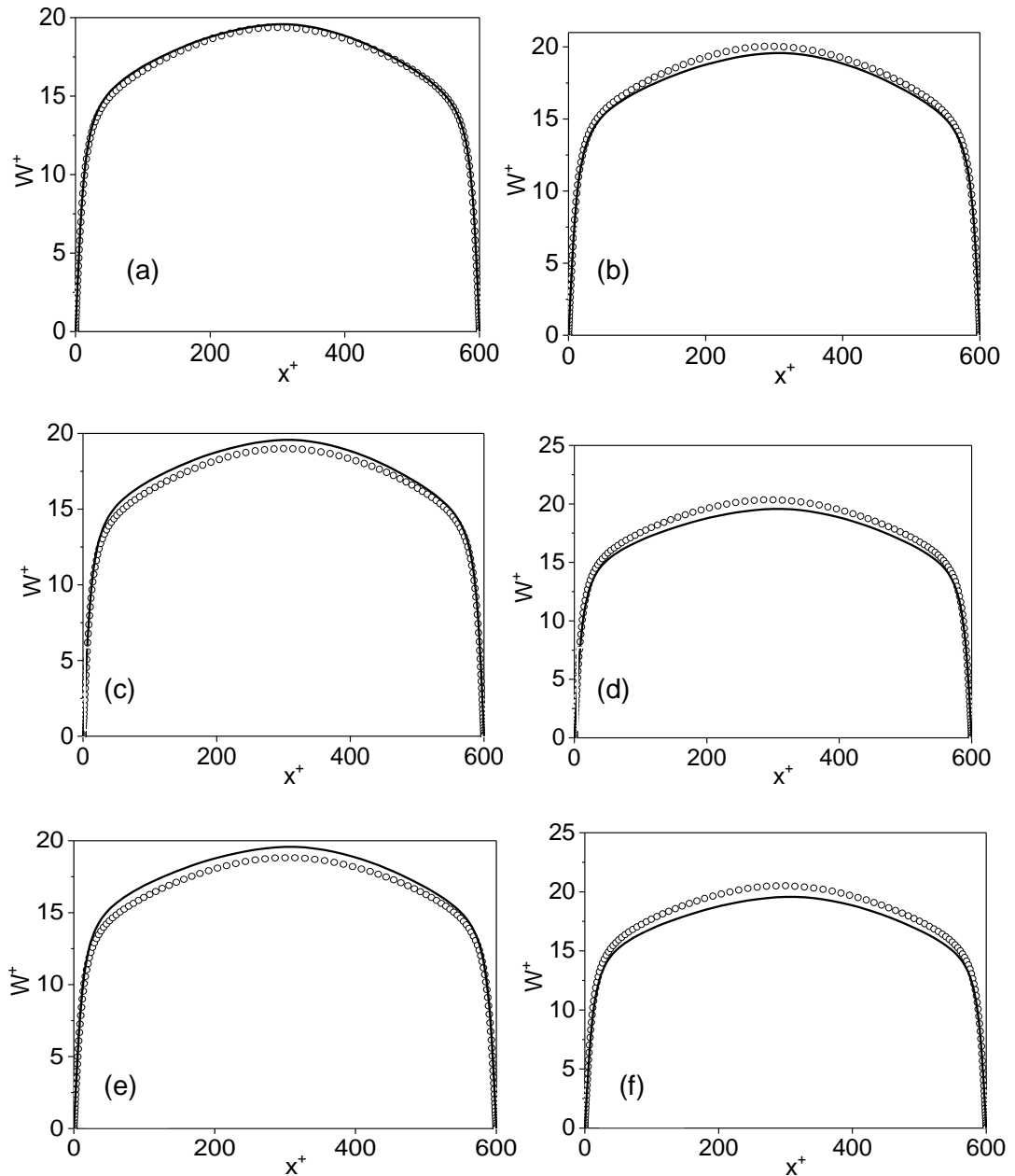
Figure 6.7 Fluid streamwise mean velocity for (a, c, e) upward flow (b, d, f) downward flow, at mean time values of (a, b) $t^+ = 500$, (c, d) $t^+ = 1000$ and (e, f) $t^+ = 2000$. $d_p = 125 \ \mu m$ and $Re_\tau = 300$ (— single-phase flow, ○ multi-phase flow).

This occurs due to the increased drag on the particles which, depending on their inertia, gradually suppresses their velocity. Over time, the drag on the particles results in a velocity gradient between the particles and the fluid, which ultimately forces the fluid flow to lag as seen in the figure. The impact is, as expected, predominant around the channel centre where the fluid velocity is at maximum. In contrast, the streamwise mean velocity is observed to be enhanced in the downward flow as shown in Figure 6.7(b, d and f), with the resulting impact, again, predominant in the channel centre region where the flow is of maximum velocity. The reason for

the enhancement is attributed to the reduced impact of the drag resistance on the fluid flow which causes the fluid to accelerate in the positive gravity direction. Just like the upward flow, the figures depicts the enhancement is increased with the increase in simulation time. In both cases, the results observe is, quantitatively, in very good agreement with those of Marchioli and Soldat (2007) where similar conclusion is reached. The authors suggested the well-known crossing-trajectory effect (Csanady, 1963; Wells and Stock, 1983; Maxey, 1987) as a reasonable explanation for the occurrence. A phenomenon which denotes that particles influenced by a potential field (gravity in this case) become separated from the fluid turbulence and quickly travel through the fluid eddies.

In Figure 6.8, the effect of the particles on the normal and shear stresses in the streamwise w'^+_{rms}, spamwise v'^+_{rms} and wall normal u'^+_{rms} directions are given at mean time values of $t^+ = 500, 1000$ and 2000 for both the upward and downward flows. For the upward flow, at time $t^+ = 500$, the root mean square (rms) velocity fluctuations is noticed to be fairly stable across the velocity components w'^+_{rms} , v'^+_{rms} and u'^+_{rms}. However, the fluctuations are noticed to be increasingly suppressed as the simulation progresses over time, although only minimal. This is also the case for the component of the fluid shear stress, $u'w'^+$, as it is observed to be increasingly suppressed in the near-wall region of the channel with time. In the case of the downward flow, the behaviour is observed to be in the reverse, with w'^+_{rms} , v'^+_{rms} and u'^+_{rms} enhanced increasingly across the channel wall distance. The fluctuation is also observed to peak in the regions close to the wall and highest in the streamwise direction. The reasoning here is similar to that of the mean stream velocity where gravity and the lift force is observed to be vital in terms of the redistribution of the single particles and the agglomerates, and modifying the fluid in the process. This again is in agreement with the findings of Marchioli and Soldat (2007).

In all, the behaviour observed here further confirms the reason for the low and high collision and agglomeration events encountered in the upward and downward flows, respectively. This owes to the knowledge that high turbulence encourages particle-particle interaction (as in the case of the downward flow) while low turbulence decreases interaction (as in the case of the upward flow). However, the difference in turbulent modification is very small, hence, there are not much difference in terms of the collisions and agglomerations in both flow configurations. It is, however, possible

for the differences to be more pronounced if the particle mass loading is significantly increased.
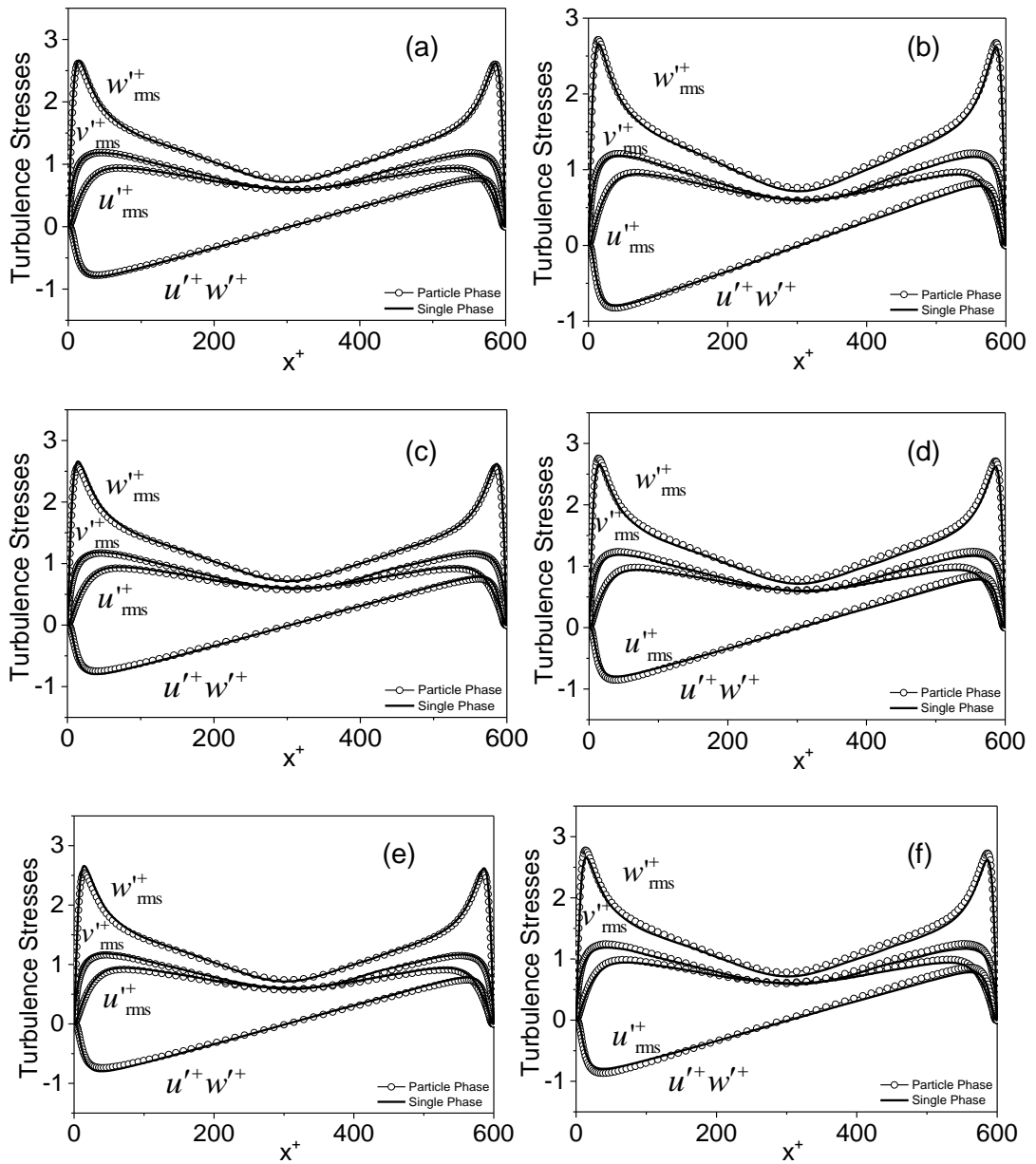
Figure 6.8 Fluid normal and stresses for (a, c, e) upward flow (b, d, f) downward flow, at mean time values of (a, b) $t^+ = 500$, (c, d) $t^+ = 1000$ and (e, f) $t^+ = 2000$. $d_p = 125\ \mu m$ and $Re_\tau = 300$ (— single-phase flow, ○ multi-phase flow).

6.2.3 Particle Force Analysis

Lastly, to complete the statistical analysis on the collision and agglomeration in the different flow configurations, it becomes necessary to analyse the particle surrounding forces (gravity included) and their contribution to the collision and agglomeration formation process. Particularly, we examine the forces per unit mass

acting on the particles in the direction of the wall where particle concentration is maximum for all particle size flow. The analysis in each case, as already noted, is performed at a fixed time ($t^+ = 1000$) as the values calculated in each node per unit time was first compared in magnitude to values obtained at the nodes at other times throughout the flow, with no significant differences observed. Hence, the insert in the figures is only a representative of one particular instant in the flow, although averaged over $t^+ \pm 100$ (mean taken 200 either side of the value i.e. $t^+ = 1000$ means $(t^+_{901} + t^+_{902} + \cdots + t^+_{1100})/200$. It is also worth mentioning that the averaging did not change the magnitude of the different forces acting on the flow, but only performed to ensure a relatively smooth profile is obtained.

The results in Figure 6.9 are representative of all the individual forces acting on the particles of diameter $d_p = 125\,\mu m$ across the channel at time $t^+ = 1000$. Note that Figure 6.9(b, c) give enlarged views compared to Figure 6.9(a, b) to better show the magnitude of the less influential forces. For the upward flow in Figure 6.9(a), the lift force is observed to the most dominant force acting on the particles, and closely followed by the drag. However, the lift being slightly dominant explains why the particles are depleted in the channel wall regions for the upward flow, otherwise, a more balanced particle distribution would be expected, if the lift is equally balanced by the drag force. The impact of the lesser forces where observed to be relatively negligible compared to the lift and drag forces, the magnitude of their impact on the particles in the order; shear lift, drag, pressure gradient and added mass forces. In the case of the downward flow, the impact of the lift force is much greater relatively to the upward flow. The drag force, although still prominent, is still noticed to be less influential on the particle dynamics when compared to the lift. The impact of both forces in found to be much enhanced in the near-wall region of the flow where turbulence is maximum. Nonetheless, the difference between both forces, enhances the particle drift towards the wall regions into these areas of high turbulence. This therefore, explains the reason for the more collisions and agglomerations observed in the downward flow.
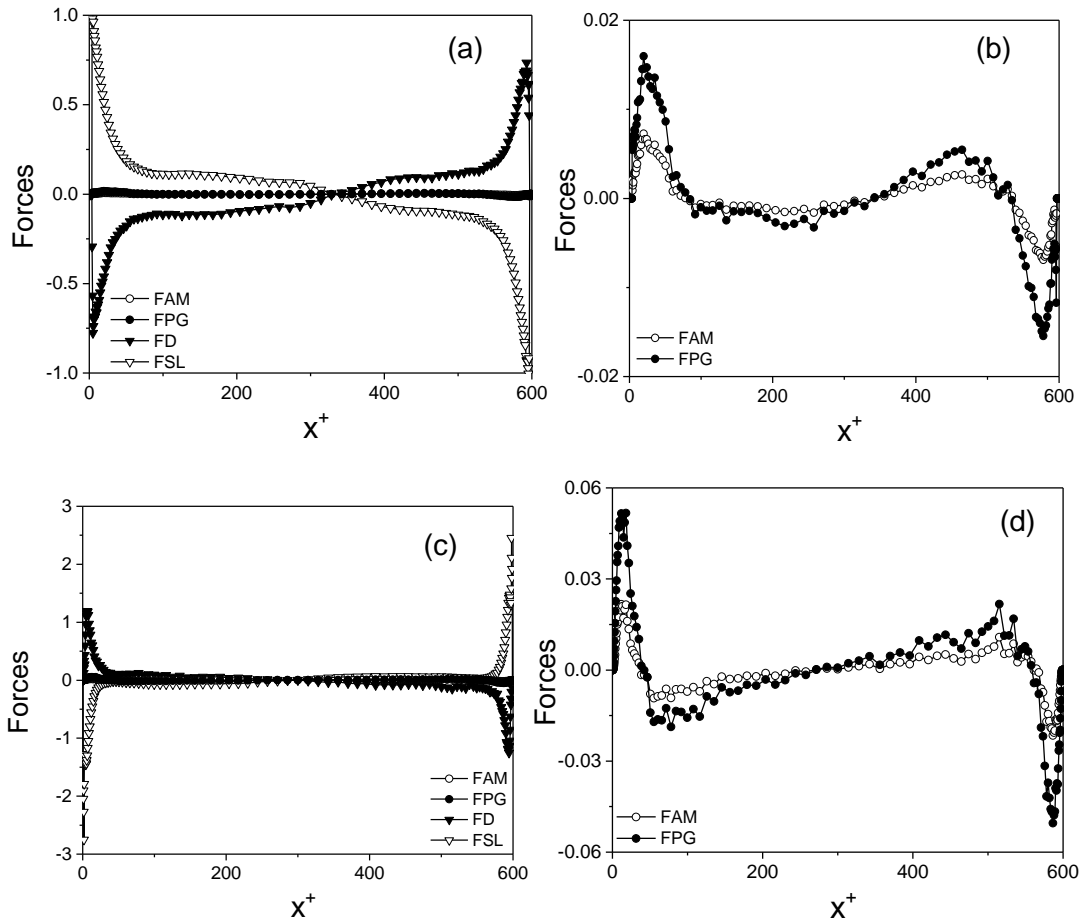
Figure 6.9 Forces (N/kg) analyses for $Re_\tau = 300$ at $t^+ = 1000$ (a, c) forces acting in the wall normal direction on particles (b, d) zoomed profile showing the relative magnitude of the smaller forces acting within the flow. (a, b) upward flow (c, d) downward flow (F_{SL} = shear lift, F_{AM} = added mass, F_D = drag, F_{GB} = gravity/buoyancy, F_{PG} = pressure gradient).

6.3 Reynolds Number Effect on Vertical Channel Flows: Collision and agglomeration

In this section, the effect of turbulence on particle collision and agglomeration for a fully developed vertical channel flow is investigated. The study considered two different flow Reynolds numbers for the simulation, namely $Re_\tau = 150$ and 590. Mono-sized particles of diameter $d_p = 125\,\mu m$ were introduced in both flows. The study is particularly motivated due to the relevance in industrial applications where there is often the need to ramp up flow velocity to boost flow assurance. It is worth mentioning that a similar study was conducted in the last chapter, where the effect of turbulence on the collision and agglomeration statistics, for a horizontal channel turbulent flow under the influence of gravity was investigated. However, with the

change in flow direction for the vertical flow, the impact of the turbulence on the particle statistics is expected to change. Therefore, it becomes necessary to understand the impact of these changes on the particle collision and agglomeration process. It is also noted that the degree of response (relaxation times) of the mono-sized particles (measured by its Stokes number) in the Re_τ flow is a function of the flow Reynolds number. Again, the decision to fix the particle size for the different Re_τ flows rather than the inertia was based on the intent to replicate the more practical situation earlier mentioned. Also, the global number of particles in both flows differs since the domain size is different. Nonetheless, the particle volume fraction is fixed in both flows, hence, it is used as the bases of comparisons. Where necessary the results are made dimensionless to ensure trends of the particle parameters are comparable. The corresponding particle relaxation times, Stokes number and other relevant parameters remains as stated in Table 5.1.

6.3.1 Upward flow

Figure 6.10 (a) shows results for two upward flow cases, comparing the total number of collision events, N_{col}, and the total agglomeration process, N_{agg}, in the channel. Both flows were of shear Reynolds numbers 150 and 590; performed up to a dimensionless simulation time $t^+ = 2000$. In both cases, it is clear that the collision of particles starts from the moment they are introduced into the flow, whilst there is a very slight time lag before agglomeration occurs ($t^+ \approx 0.08$ and 0.88 for $Re_\tau = 150$ and 590, respectively).

The lower Reynolds number flow, however, showed a distinctive trend which was not encountered in the previous analysis. It was observed that at approximately $t^+ = 500$, the number of N_{col} and N_{agg} accelerated, illustrating the occurrence of rapid collision and agglomeration. The occurrence continued up to a simulation time $t^+ \approx 800$, after which the rate of change in N_{col} and N_{agg} is observed to reduce as the simulation progressed towards a statistically steady state. In the higher Reynolds number flow, however, the number of collisions and agglomerations is observed to increase at an approximately steady state, and also with far less collision and agglomeration events. The decrease in the rate of change of N_{col} and N_{agg} is as a result of the total number of active particles within the flows reducing with time due to agglomeration. The rapid increase in the number of N_{col} and N_{agg} during the initial

stages (up till $t^+ \approx 100$) of the simulation was as a result of the initial bias on the flow, which gradually faded out as the fluid-particle mixing increased with time.
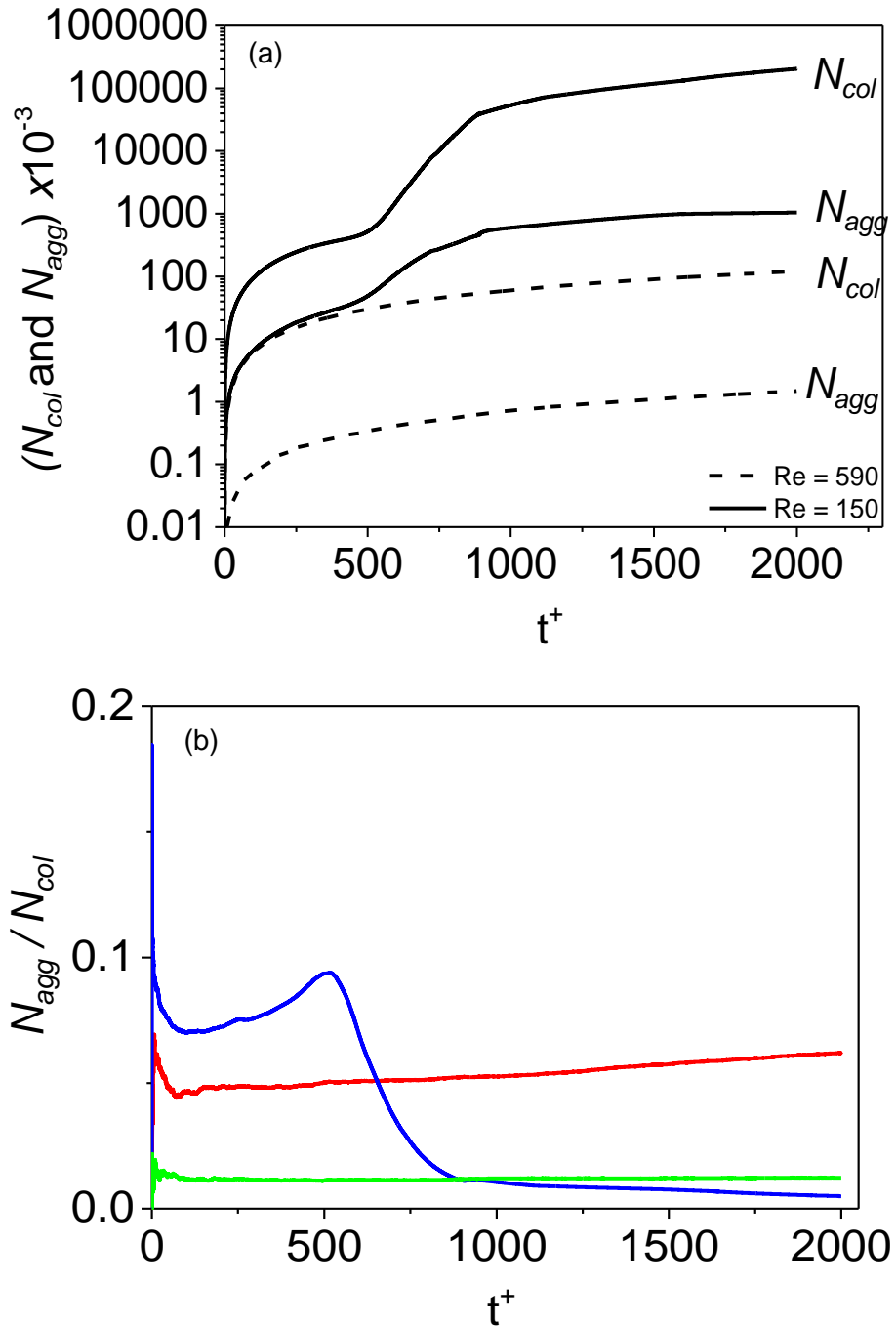
Figure 6.10 (a) Total number of particle collisions, N_{col} and particle agglomerations N_{agg} as a function of time in the upward flow, and (b) Particle rate of agglomeration comparison for both Re_τ flows. Line Colour: Blue - $Re_\tau = 150$, Red - $Re_\tau = 300$ and Green - $Re_\tau = 590$

From the figure, it is strongly believed that due to the relatively low velocity of the $Re_\tau = 150$ flow, the transport of the particles of $d_p = 125\ \mu m$ up the channel becomes

challenging as they tend to flow backwards in the direction of the positive gravity force, due to the high inertia developed. Hence, the particles over time become less responsive to the fluid velocity and therefore lag the flow. The same lagging effect was seen by Marchioli and Soldati (2007) in their investigation on gravity and lift effects in upward particle flows. In this case, the lag is enhanced due to the diameter of particles utilised, which consequently depletes the particles in the upper flow region. This further results in the increase in particle concentration in the lower flow region, leading to an acceleration of the particle collisions since the distance between each particle is shortened. This is believed to be the most likely explanation for the much enhanced particle collision and agglomeration observed in the lower Re_τ flow. However, more analysis is still required before conclusions can be drawn. It is also necessary to mention that the computational code employed for the vertical flows was made periodic only in the positive streamwise direction, which means that particles only exit the channel from the top. Hence, particles moving backwards end up accumulating in the bottom regions of the flow as they are not allowed to leave the domain when they reach that point (nor are they returned to the top boundary). This is necessary to isolate the effect being studied and avoid any complications that may arise if periodicity is in both streamwise directions.

In Figure 6.10(b) the particle agglomeration rate N_{agg}/N_{col} is examined to further understand the behaviour observed in both flows. The agglomeration rate is shown up to a time $t^+ = 2000$, which is also the entire simulation run-time. The figure also includes result showing the agglomeration rate for the base case shear Reynolds number ($Re_\tau = 300$) in the upward flow. This was previously shown in Figure 5.3 but has been included here just for reference. In all the three flows, it is seen that N_{agg}/N_{col} decreases with an increase in the Reynolds number. This is as expected since agglomeration is more likely to occur under conditions of low fluid velocity and turbulence as previously described. However, whilst the profiles remains linear and statistically steady throughout the simulation run-time for both the $Re_\tau = 300$ and 590 flow cases, a deviation in the trend is observed in the lower Re_τ flow. Here, an initial increase in N_{agg}/N_{col} is observed as expected, after which an unusually sharp rate reduction occurs from $t^+ \approx 500$. It however, increased slightly at time $t^+ \approx 800$ and continued as the rate approached a steady state. This suggests there were far more collisions compared to the agglomeration that occurred within the time period ($t^+ \approx 500$ and 800), a behavior only known for highly turbulent flows and also for high particle volume fraction flows. This strongly supports the explanation provided for this

behavior, as the sharp drop in agglomeration rate depicts a high particle collision frequency. In other words, that the particles are being used up more frequently to form larger size agglomerates. The rapid formation of these agglomerates over the short period, consequently results in a sharp drop in the number of active particles in the flow; leading to the drop in N_{agg}/N_{col} as particles becomes further apart from each other.

The sensitivity of the collision and agglomeration process to the different shear Reynolds number flows becomes more obvious when the collision to agglomeration ratio N_{agg}/N_{col} is considered. Table 6.1 show values of N_{agg}/N_{col} for different dimensionless times in both flow cases. It is seen that N_{agg}/N_{col} increased fairly rapidly between $t^+ = 500$ and 800 and continued till the end of the simulation for the lower Re_τ flow but was fairly constant for the higher Re_τ flow. This further suggests that the particles cluster in regions of the flow and consequently collide more frequently in the regions; with collisions increasingly outweighing agglomeration (although still much higher than expected) to cause an increase in N_{agg}/N_{col}.

Table 6.1 Instantaneous particle collision (N_{col}) to agglomeration (N_{agg}) ratio at selected dimensionless times for both Re_τ flows.

$Re_\tau = 150$

t^+	300	500	800	1000	2000
N_{col}/N_{agg}	$13:1$	$10:1$	$53:1$	$94:1$	$202:1$

$Re_\tau = 590$

| N_{col}/N_{agg} | $89:1$ | $89:1$ | $88:1$ | $83:1$ | $82:1$ |

Figure 6.11 shows results for the distribution of the collisions and agglomerations across the channel, and the locations where they occur, at time t^+ = 500, 1000 and 2000. These results were obtained by averaging over the length of the channel and over $t^+ \pm 500$ (mean taken 500 either side of the value i.e. $t^+ = 1000$ means $(t_{501}^+ + t_{502}^+ + \cdots + t_{1500}^+)/1000$ about each time value given to provide a sufficiently large sample for analysis, with the cross-stream domain divided into 16 equally spaced zones in the wall-normal direction for both flow cases considered. From the

result, the collision (N_{col}) and agglomeration (N_{agg}) distribution clearly indicates that way more events occurred in the lower Re_τ flow case, when compared to the higher Re_τ flow. N_{col} in both flow cases is observed to reach peak values at the wall regions which, as already mentioned, is due to the increased fluctuations in the wall regions which enhances the collision between the particles.
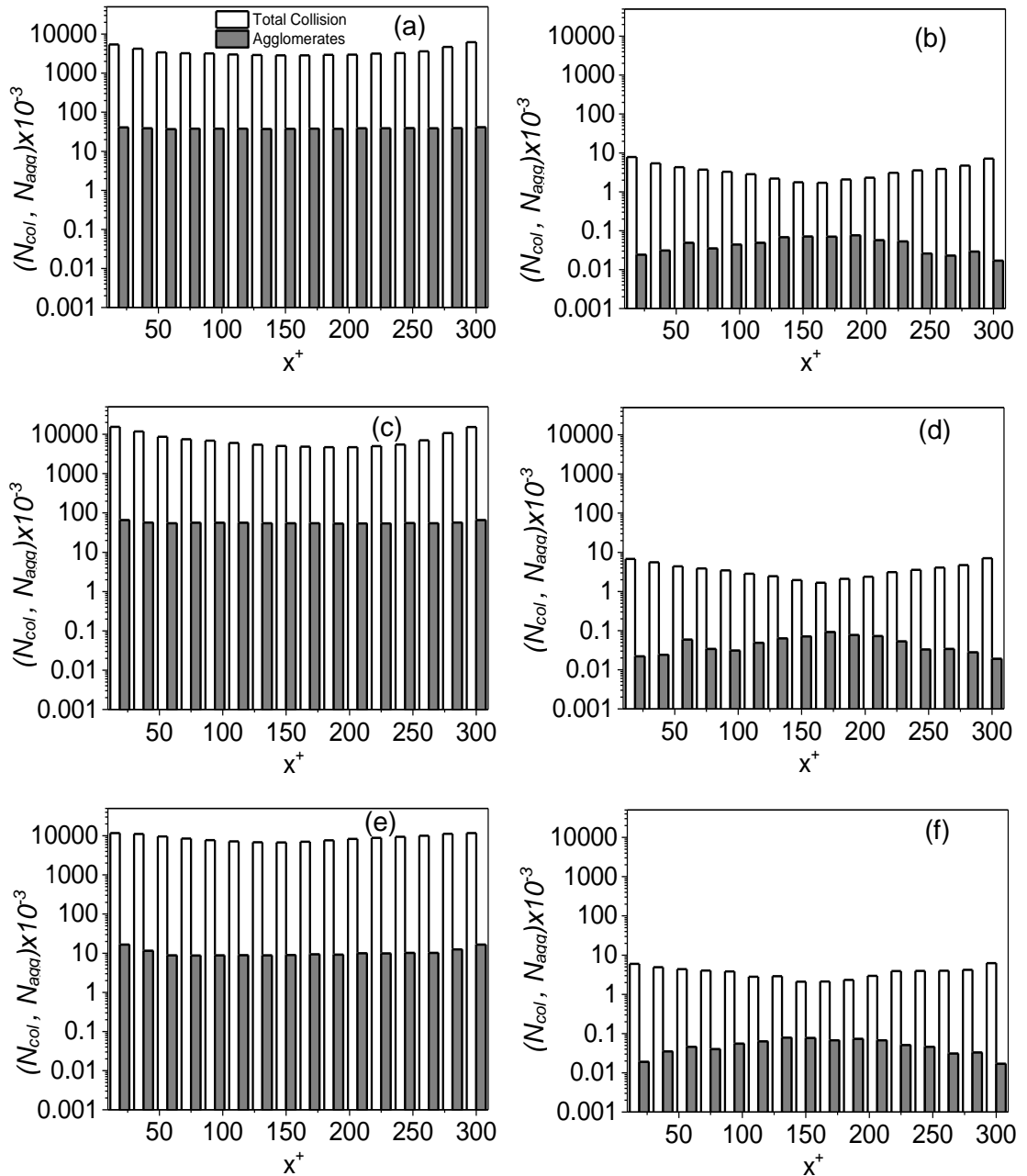
Figure 6.11 Distribution of collisions and agglomerations across the channel in the wall-normal direction of the upward flow: (a, c, e) $Re_\tau = 150$ and (b, d, f) $Re_\tau = 590$. (a, b) $t^+ = 500$, (c, d) $t^+ = 1000$ and (e, f) $t^+ = 2000$.

On agglomeration, N_{agg} is noticed to be evenly distributed across the channel for the lower Re_τ flow but peaked in the channel centre in the case of the higher Re_τ flow. The behaviour in the higher Re_τ flow is as expected, since agglomeration is favourable in the channel centre where the fluid is less turbulent. However, the even distribution of N_{agg} in the case of the lower Re_τ flow, reveals that the agglomeration is occurring across the channel width, due to the dense concentration of the particles across the channel width. In other words, agglomeration on average becomes equally favourable across the channel, and not preferentially occurring within the main body of the flow, as was the case in the $Re_\tau = 590$ flow. Hence, the even distribution observed in the figure.
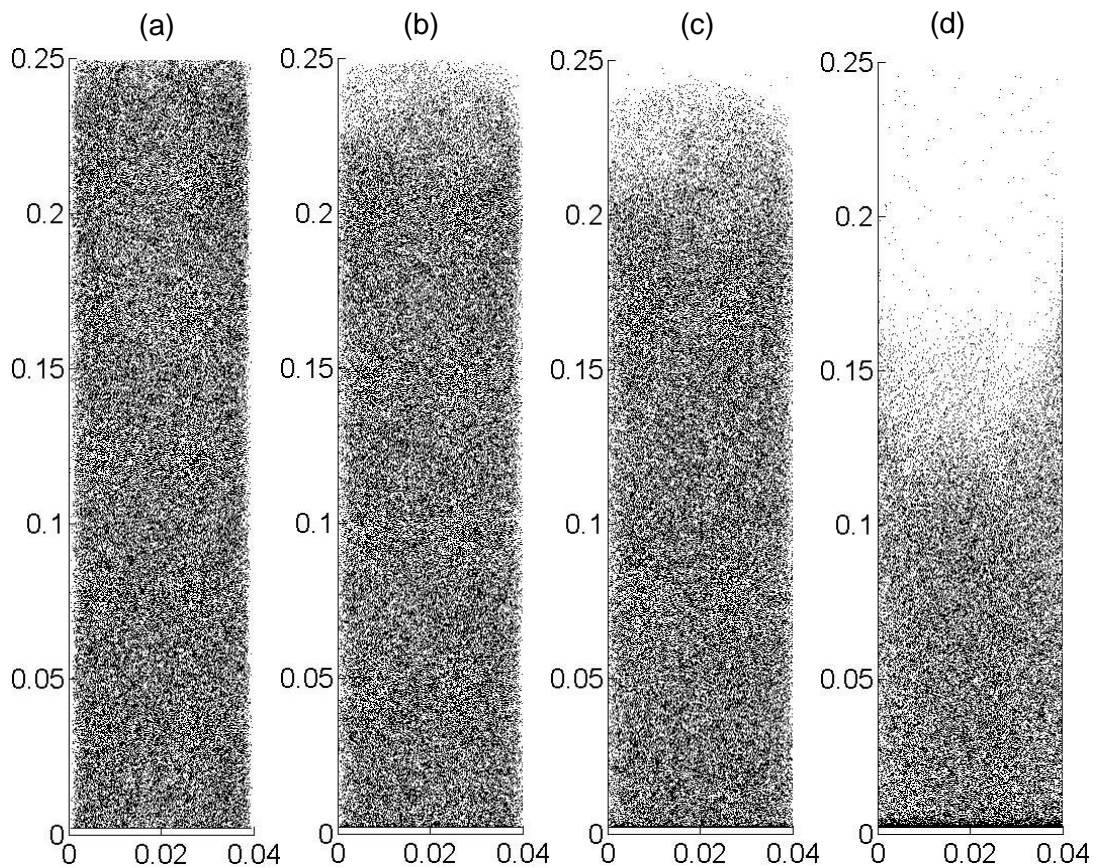
Figure 6.12 Instantaneous distribution of particles on (x, z) planes for the $Re_\tau = 150$ flow, at selected dimensionless times for the upward flow (a) $t^+ = 500$, (b) $t^+ = 530$, (c) $t^+ = 650$ and (d) $t^+ = 1000$.

To better picture the events in the lower Re_τ flow, Figure 6.12 provides a visualisation of the particles introduced into the flow for selected dimensionless times. The selected times were chosen to capture specific moments in the flow were the instantaneous particle distributions along the x, z plane is of interest. From the time trail, it is noticed that at $t^+ = 500$, the particles were still, on the average, evenly

distributed across the channel. However, from t^+ = 530, a cluster of particles begin to form in the lower flow region as particles depletes in the upper flow. This indicates a lag in the particle velocities due to the gravity force acting opposite to the stream direction.

With the increase in time (up to t^+ = 1000), the images depict the particles to become increasingly resistant to the stream flow, owing to the gravity force. Although not quite evident from the picture but as larger sized agglomerates continue to form through with time, the particles which are now heavier, were observed to accumulate towards the start of the channel, indicating a reverse particle flow velocity in the gravity direction. This reverse flow behaviour is, however, clearer in Figure 6.13 where the concentration of the particles, C/C_0 at selected times are plotted in the wall-normal flow direction. Here, particles are observed to drift towards both walls over time – a behaviour typical of downward particle flows, in which the lift force enhances particle movement towards the walls.
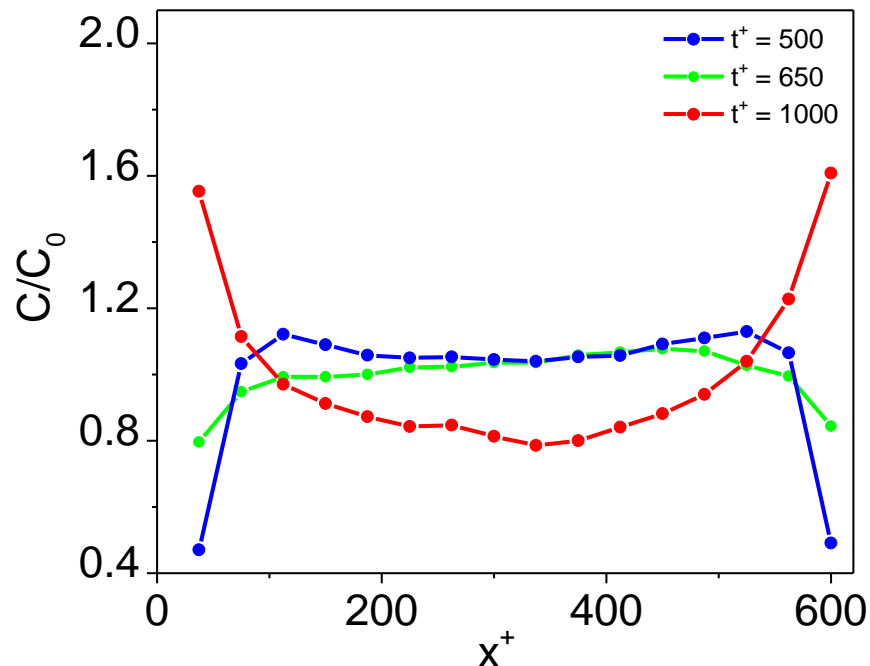
Figure 6.13 the instantaneous particle concentration distribution in the wall-normal direction for the upward flow. $Re_\tau = 300$ and $d_p = 125\ \mu m$

Figure 6.14, gives results for the number and sizes of the agglomerates that form for both Re_τ flow over time, including the single particle depletion rate and the corresponding evolution of multi-sized particles. At the start of both simulations, the

results again indicate a sharp increase in the number of agglomerates formed, due to the interference from the initial conditions on the particles. From the figure, the trend in both Re_τ flows noticeably different, with agglomerates consisting of up to 10 primary particles formed in the lower Re_τ case, compared to just two agglomerates in the higher Re_τ case by t^+ = 500.
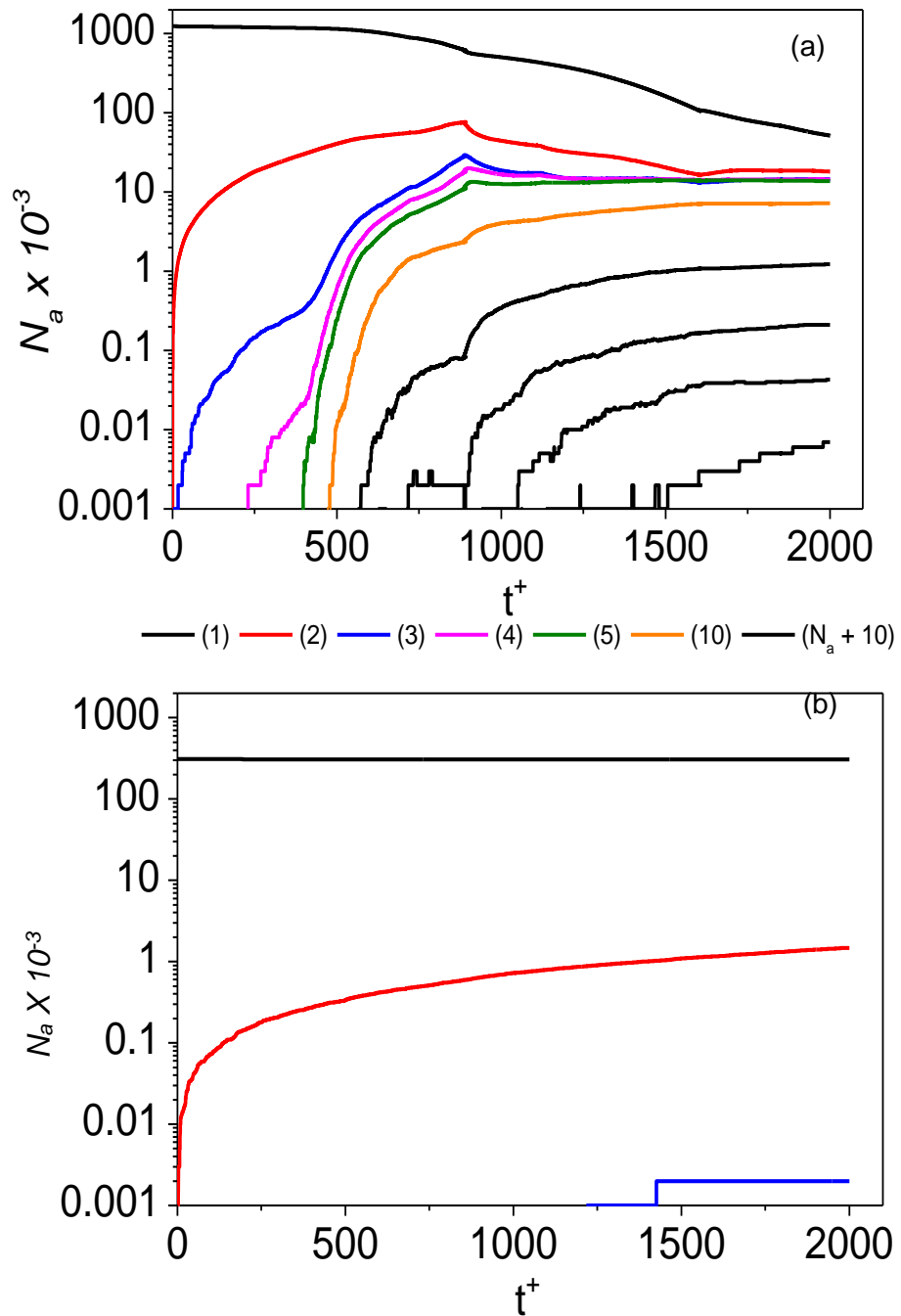
Figure 6.14 Agglomerate formation with time for the upward flow of $d_p = 125\ \mu m$, (a) $Re_\tau = 150$ and (b) $Re_\tau = 590$. Key under figure gives total number of original particles (1), and total number of original particles in each agglomerate.

The single particles are also observed to be significantly depleted in the lower Re_τ case, unlike the higher flow case. The low formation rate in the higher case is due to the increase turbulence which reduces the likelihood of particle agglomeration over the period as expected. In the case of the lower Re_τ flow, the multi-sized agglomerates are observed to quickly form through (typical of low Re_τ flows), as both the single and lower sized agglomerates collide to form even larger particle agglomerates. It is, however, reduced with the reduction in the number of colliding particles in the domain. To summarise the effect of turbulence for the upward flow, it was shown from the results analysed that particles with high enough inertia would tend to lag in the flow (depending on fluid velocity) and possibly flow backwards in the positive gravity direction. Thus, increasing the likelihood of particle collisions and agglomeration since the particle lag would result in the segregation (or cluster) of the particles in the flow, which consequently increases the particle-particle interaction in the channel regions as the inter-particle distance becomes shortened. Considering the contrasting behaviour in the higher flow case, it is, therefore, possible to infer that by sufficiently increasing the flow velocity the occurrence could adequately be prevented.

6.3.2 Downward flow

Just as in the upward flow, Figure 6.15(a) shows results for the two Re_τ flow cases but in the downward direction (flow points in the direction of gravity). The plot provides details on the total number of collision events, N_{col}, and the total agglomeration process, N_{agg}, in both flow configurations, up to the dimensionless simulation time $t^+ = 2000$. Again, the collision of particles is observed to start from the moment they are introduced into the flow in both cases, whilst there is a very slight time lag before agglomeration occurs ($t^+ \approx 0.08$ and 0.73 for $Re_\tau = 150$ and 590, respectively). From the figure, the only noticeable difference between both flow cases is that there are more collisions and agglomerations in the lower Re_τ flow when compared the flow of $Re_\tau = 590$. This occurs as a result of the increased influence of gravity on the less turbulent flows, which encourages a faster migration of the particles towards the near-wall region. Hence more localised collisions and agglomerations occur as particle concentration increase in the near-wall areas. The reduced collision and agglomeration events in the higher Re_τ flow is as a result of the increased flow velocity and turbulence, which ensured particles remain evenly distributed across the channel for the simulation time. In all, the flow trend is progressed as expected. In Figure 6.15(b), N_{col} and N_{agg} is normalized using the initial number of particles, N_0,

for each case, but no appreciable differences from Figure 6.15(a) is seen. The normalised N_{col} and N_{agg} was still observed to be higher in the lower Re_τ flow. Similar to the upward flow, N_{col} and N_{agg} is observed to increase rapidly during the initial stages of the simulation but gradually reduces as the particles increasingly interacts with the fluid as well as with the formation of agglomerates.
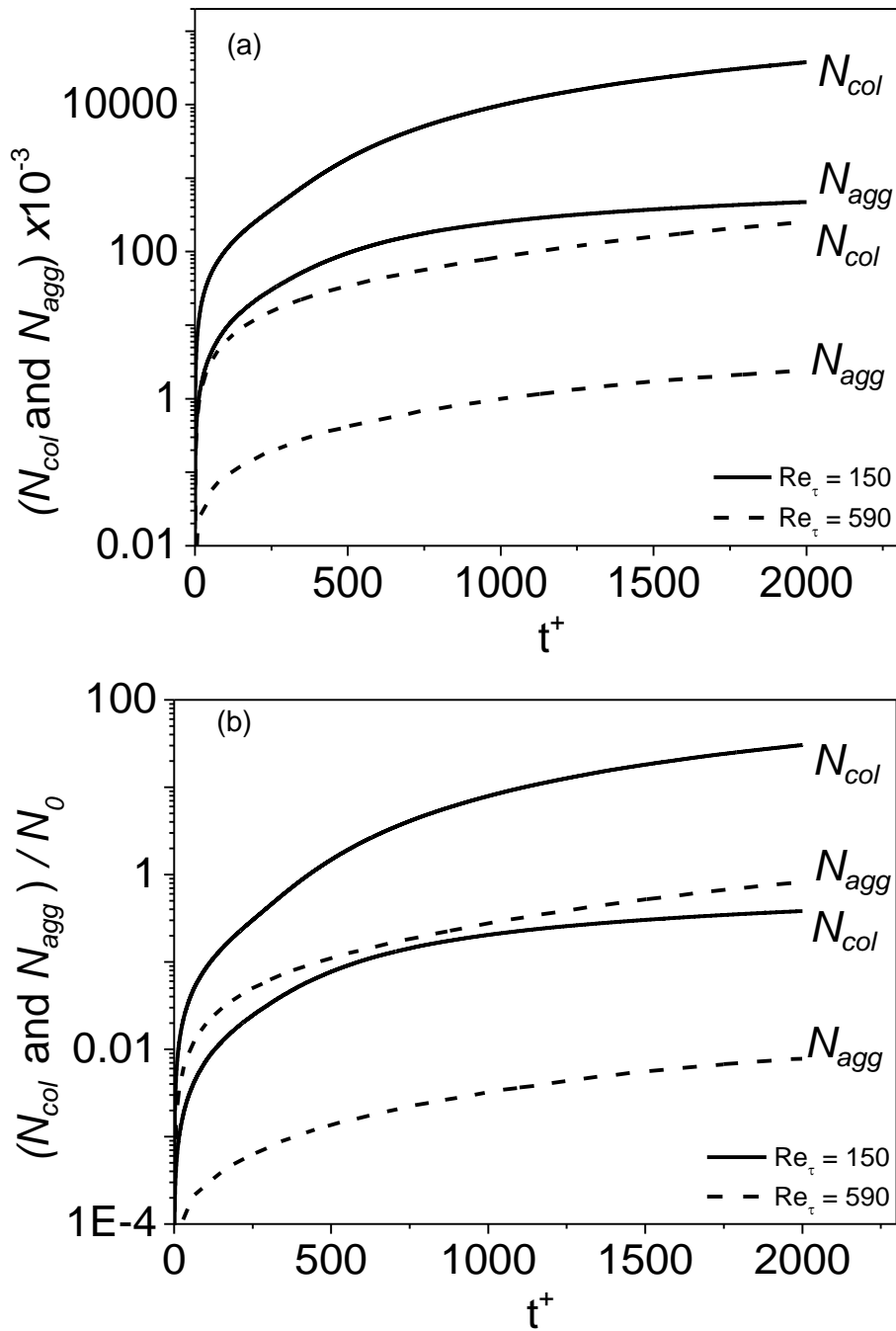
Figure 6.15 Total number of particle collisions, N_{col} and particle agglomerations N_{agg} as a function of time in the downward flow (a) N_{col}, N_{agg} and (b) N_{col}/N_0, N_{agg}/N_0

In Figure 6.16 the agglomeration rate, N_{agg}/N_{col}, is examined for both downward flow cases, up to a dimensionless time $t^+ = 2000$. The agglomeration rate for the base case shear Reynolds number ($Re_\tau = 300$) in the downward flow has also been include but only as a reference case. In all three flows, it is seen that N_{agg}/N_{col} increases with a decrease in the Reynolds number. However, N_{agg}/N_{col} is observed to be constant for the higher Re_τ flows but it is continuously decreased in the lower Re_τ flow. Similar to the upward flow, the reduction is as a result of the particles being used up to form larger sized agglomerates, which consequently reduces the agglomerate rate as active particles are continually depleted and the inter-particle travel distance increases.
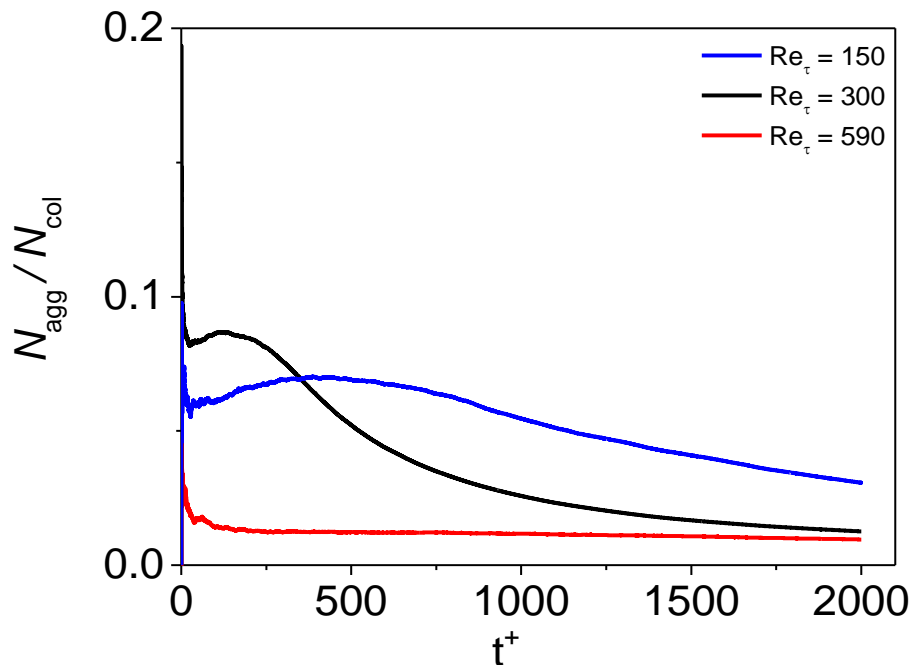
Figure 6.16 Particle rate of agglomeration comparison for both Re_τ flows in the downward flow direction. $d_p = 125\,\mu m$.

Figure 6.17 shows results for the distribution of N_{col} and N_{agg} across the channel for the downward flow, and the location of the events at time t^+ = 500, 1000 and 2000. N_{col} and N_{agg} in both flow cases are observed to reach peak values at the wall regions as expected, and increases with time. The high N_{col} and N_{agg} events in the lower Re_τ flow occur as agglomeration is favoured in low velocity flows. The particle distribution in the wall normal (x, z) direction of both vertical channel flows are shown in Figure 6.18. The trend of the particle concentration, C/C_0, denotes a high particle concentration in the near-wall areas of both flows, which explains the high N_{col} and

N_{agg} events near the walls in each case. The particles drift towards the wall, again, depicts the dominance of the lift force in both downward flow cases.
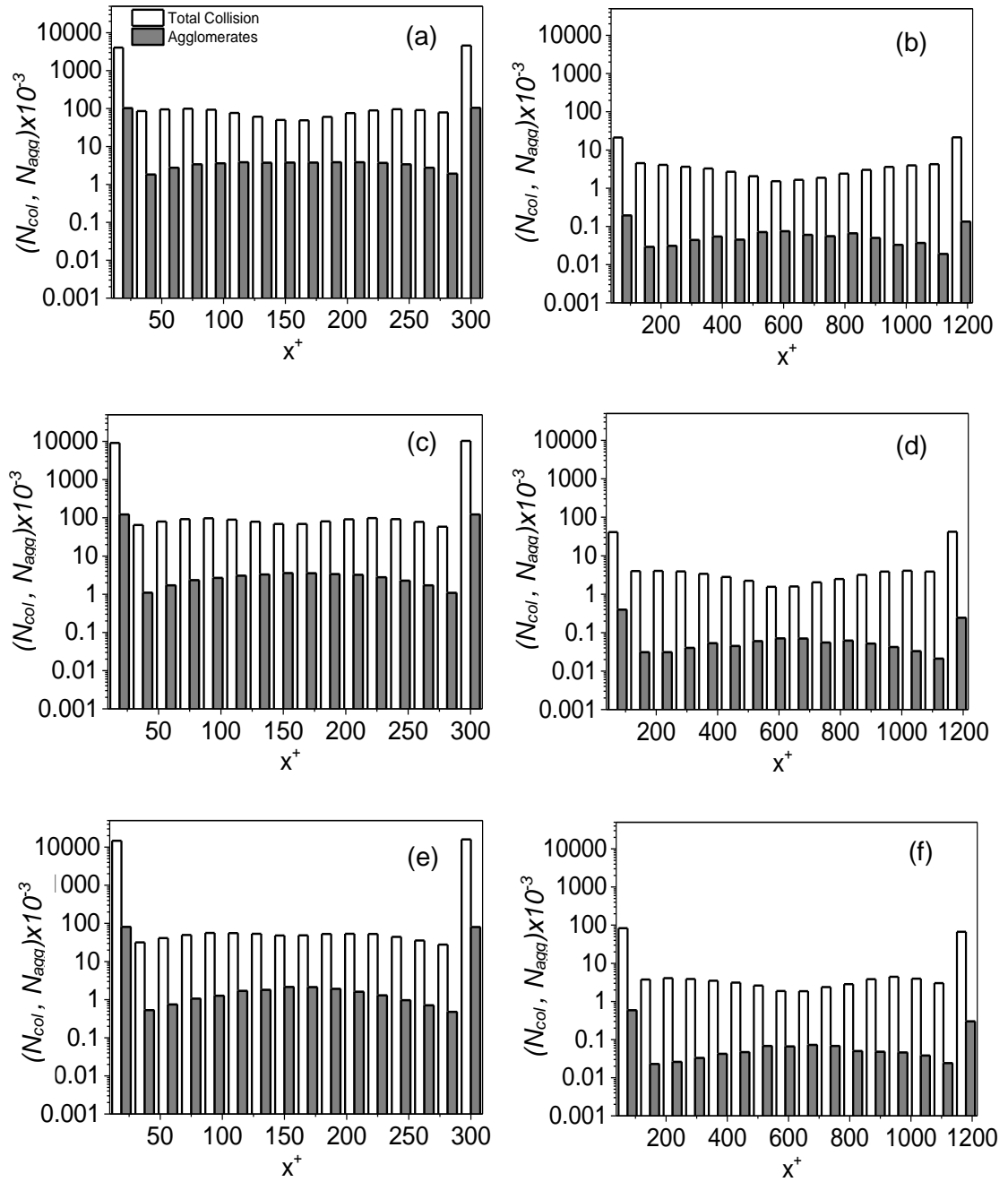
Figure 6.17 Distribution of collisions and agglomerations across the channel in the wall-normal direction for the downward flow: (a, c, e) $Re_\tau = 150$ and (b, d, f) $Re_\tau = 590$. (a, b) $t^+ = 500$, (c, d) $t^+ = 1000$ and (e, f) $t^+ = 2000$.
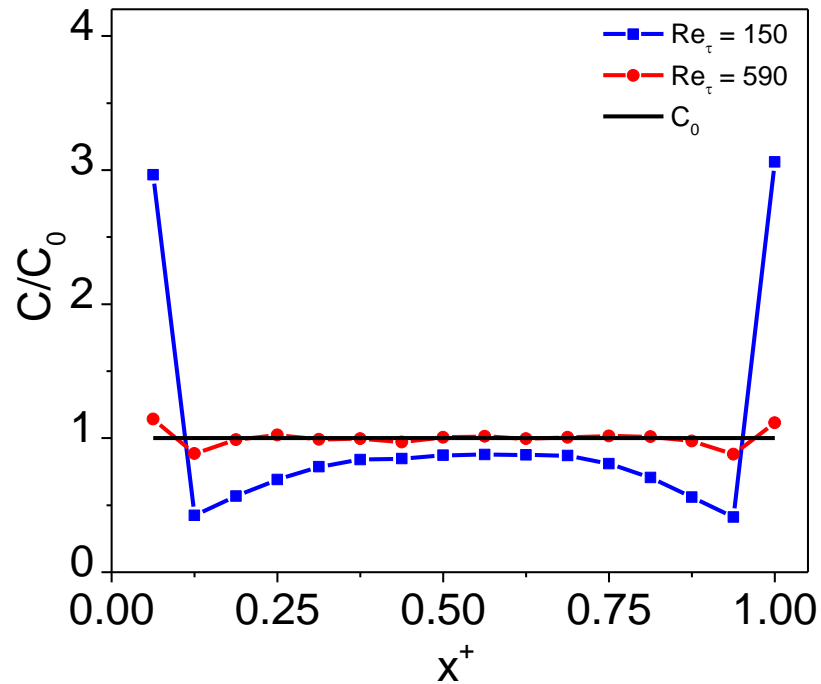
Figure 6.18 the instantaneous particle concentration distribution in the wall normal direction at $t^+ = 2000$ for both Re_τ downward flows. $d_p = 125\ \mu m$.

Lastly, Figure 6.19 gives results for the number and sizes of the agglomerates that formed for both Re_τ flows over time in the downward flow. This includes the single particle depletion rate and the corresponding evolution of multi-sized. From the figure, the trend in both Re_τ flows noticeably different, with agglomerates consisting of up to 15 primary particles formed in the lower Re_τ case, compared to just two agglomerates in the higher Re_τ case by $t^+ = 2000$. The single particles are also observed to be significantly depleted in the lower Re_τ case, unlike the higher flow case. The low formation rate in the higher case is due to the increase turbulence which reduces the likelihood of particle agglomeration over the period as expected. In the case of the lower Re_τ flow, the multi-sized agglomerates are observed to quickly form through (typical of low Re_τ flows), as both the single and lower sized agglomerates collide to form even larger particle agglomerates. It is, however, reduced due to the reduction in the number of colliding particles in the domain. In all, the simulations are as expected, with the results again demonstrating the importance of the lift and gravity force in enhancing collisions and agglomerations for flows in the downward direction. Turbulence is another vital parameter which enhances the rate for the downward flow as demonstrated from the results.
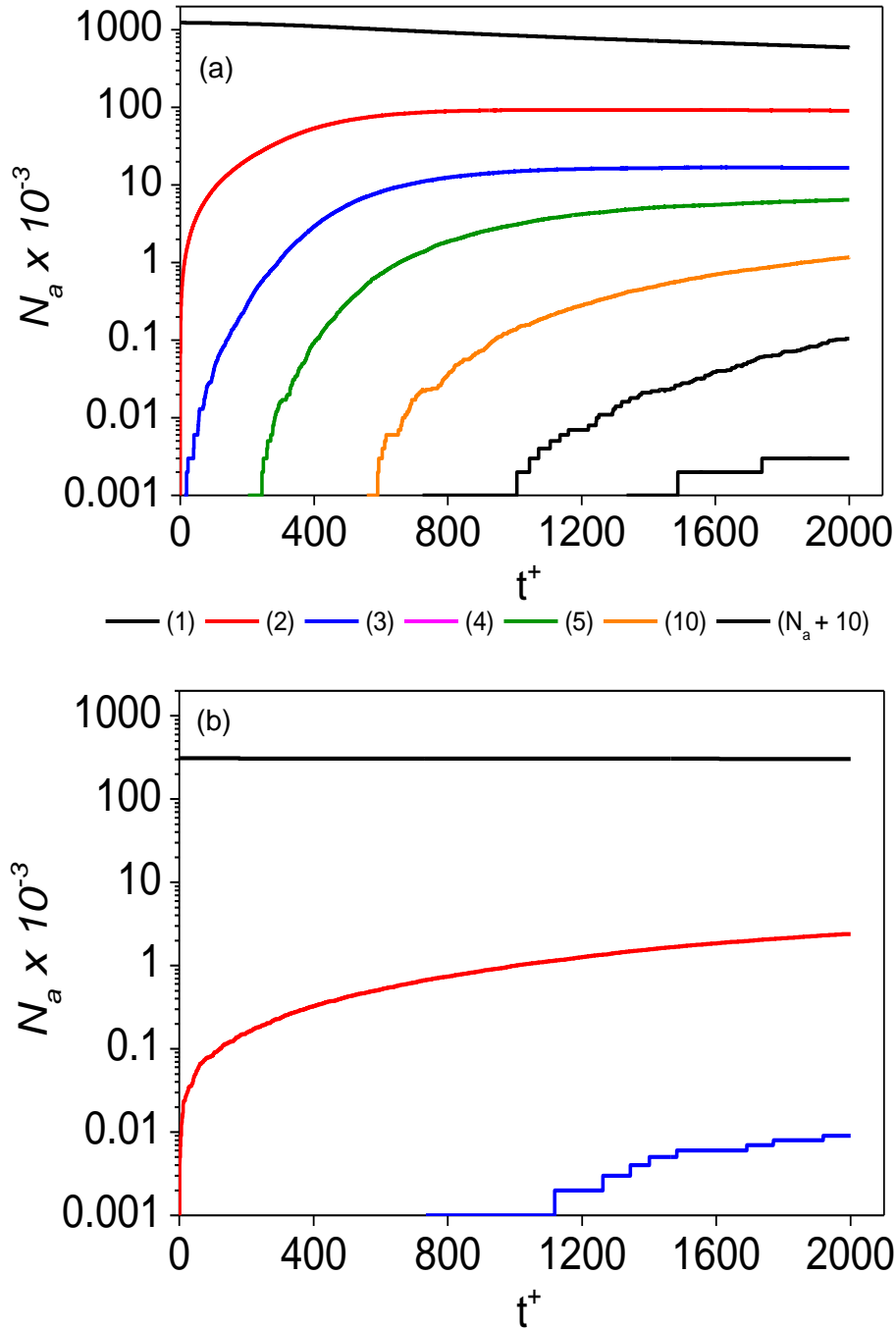
Figure 6.19 Agglomerate formation with time for the downward flow of $d_p = 125\ \mu m$, (a) $Re_\tau = 150$ and (b) $Re_\tau = 590$. Key under figure gives total number of original particles (1), and total number of original particles in each agglomerate.

6.4 Conclusions in Main Findings

In conclusion, the LES-LPT predictions in this chapter has been focused on examining particle collision and agglomeration behaviours in vertical channel flows. The influence of the surrounding forces on the particle motion was successfully investigated, with the lift force particularly responsible for particle drift towards and

away from the channel walls, depending on the flow direction. With the consideration of two separate flows pointing towards (downward flow) and against (upward flow) the direction of gravity, it was shown that particle collision and agglomeration is enhanced when flow is in the positive gravity direction. This was found to be as a result of the lift force which enhances particle migration towards the wall where turbulence is maximum. The drag force was also found to be less dominant in this flow direction; hence, particle downward migration is accelerated. More importantly, it was shown that although particle collision is maximum in the near wall areas of maximum turbulence, agglomeration on the other hand is favoured in the bulk flow where turbulence is minimal.

The second part of this chapter examined the effect of turbulence on particle collision and agglomeration for each flow direction. The analysis in each case compared flows of different levels of turbulence, achieved through increasing the Reynolds number of the flow. It was found that the rate of collision and agglomeration was strongly sensitive to the level of turbulence generated in the flow, with far more collisions and agglomeration occurring for the flow of less turbulence in both flow directions. This was attributed to the segregation of particles in the lower Re_τ flow, which then resulted in more collisions and agglomeration as particle contact distance becomes increasingly reduced. The reduced collision and agglomeration events in the higher Re_τ flow was attributed to the increased flow velocity and turbulence, which ensured particles remain evenly distributed across the channel for the simulation time; thus, prevented localised particle collisions. In all, the lift and gravity force and turbulence was seen to be the primary factors responsible for particle distribution within the flow; and consequently determined the collision and agglomeration counts.

7 Conclusions and Further Work

In this final chapter, the conclusions on key findings obtained from the numerical results of the three chapters are given consecutively in Section 7.1, after which suggestions for future work is provided in Section 7.2.

7.1 Conclusions

The work described in this thesis was undertaken to gain insight into fundamental aspects of turbulent fluid-particle flows with relevance to processes employed over a wide range of industrial applications, such as flow assurance in oil and gas, sludge transportation in nuclear waste ponds, to name but a few. In particular, a fundamental study on the influence of gravity on particle collision and agglomeration in turbulent channel flows was performed. The collision and agglomeration model was applied based on the framework of a four-way coupled Eulerian-Lagrangian approach and the collision detection based on the deterministic collision model. The mathematical modelling technique used is based on the large eddy simulation (LES) methodology embodied in a non-commercial CFD code BOFFIN, with flow solutions provided by this approach coupled with the Lagrangian particle tracker (LPT). Worthy of note is that the particles are described as point-particles in the LPT approach.

In the first result chapter, the LES results generated for the single phase were verified by comparing against predictions obtained using the more accurate DNS method and tested for shear Reynolds flows of $Re_\tau = 150, 300$ and 590 (DNS of Marchioli et al, 2008; Marchioli and Soldati, 2007; and Moser et al, 1999, respectively). The validation became necessary in order to provide a justification on the use of a relatively less computationally expensive LES rather than the more accurate but computationally expensive DNS; and also to establish the reliability of the LES in the prediction of turbulent two-phase flows. The validations were tested for three separate flow configurations for each Re_τ case. The first set of simulations were performed for the single-phase only solutions. The results in all Re_τ single-phase flow cases, showed highly acceptable agreements with the DNS despite minor discrepancies in the mean velocities and rms of fluctuating velocity components.

With the combination of the LES with the LPT, it became possible to extend the validation to two-phase flows of dilute particle concentration (one-way coupled). In the second set of simulations, LES and DNS solutions obtained from two-phase flow simulations of dilute particle concentration (one-way coupled, $St = 1$) are compared. The validation in the second set was repeated in the third case but for a flow entrained with particles of much lower response times ($St = 5$). In all instances, the results again showed very good agreements with those of the DNS, although the LES solutions were over and under predicted in all directions in some instances. Overall the LES showed good levels of accuracy and was justifiably employed in this research study.

Post validation, the LES-LPT technique was employed in studying selected turbulent channel flow conditions of various configurations; with particular interest in the role of gravity and other hydrodynamic forces in the collision, agglomeration and dispersion of particles of varying particle sizes and volume fractions. In order to fully isolate the effects of the particle sizes and the concentrations, the gravity force was excluded in the first result chapter. For the study on particle size effect, the particle density was set at $2710 \, kg \, m^{-3}$ (calcite) to replicate the conditions in nuclear flow; and of diameter $75 \, \mu m$, $125 \, \mu m$ and $250 \, \mu m$ for a fixed flow of $Re_\tau = 300$. For the study on particle concentration, the investigation compared flows of volume fraction 5×10^{-4}, 10^{-3}.and 5×10^{-3}.

In terms of the effect of particle size on particle collision and agglomeration, the collisions in all cases were found to reach peak values in the wall regions. The agglomeration on the other hand was shown to be favourable in the mid channel regions where turbulence is of minimal magnitude. It was also shown that the rate of collision and agglomeration is greatly influenced by the size of the particles, with collisions and agglomerations enhanced for smaller sized particles due to their small surface area, and the fact that they tend to follow the flow more closely. Further observation shows that as the particles become larger as a result of the agglomeration process, the rate of collision and agglomeration decreases over time since the particles become less responsive to the fluid phase due to their increasing inertial. Particle dispersion was also observed to be maximum near the walls due to the influence of the fluid turbulence which causes the inertial particles to segregate towards the wall regions were turbulence is maximum. This explains the high collision events observed in this area. The increased particle population in this region

increases shearing at the walls; evident through the increased effect of the hydrodynamic forces in the wall regions, particularly the drag and lift forces. The fluid mean velocity, normal and shear stresses were slightly enhanced by the presence of the particles, although more pronounced for the largest particle flow. In terms of the volume fraction effect on collision and agglomeration, the collision and agglomerate formation rate was found to increase with an increase in the particle volume fraction. Comparisons made between the flow in the four-way coupled regime and the single phase flow, showed a slightly augmented profile for the mean velocity and normal stresses, although difficult to see from the figures shown. The shear stresses were however unaffected by the increase in particle volume fraction.

With the inclusion of gravity, however, the migration of the particles was observed to increase exponentially towards the lower regions of maximum turbulence, with the concentration in the upper wall region reduced gradually over time. The turbulence in the wall region was also observed to be modulated by the increased particle concentration. The increase in particle migration was possible since gravity decouples particle motion from the structure of the fluid turbulence, therefore altering the wall- normal distribution and downward migration rate of the particles. This ultimately increased the rate of particle collisions and agglomeration in the region. Also, particle agglomeration was observed to be mostly formed in the centre regions of the channel where the turbulence intensity is lowest; and are particularly the case for particles of low inertia, since they tend to be more responsive to the flow than the gravitational pull. In terms of the particle size effect, the agglomeration was found to be enhanced for smaller particles since the area of contact is higher than for larger sized particles, and consequently increases the forces of attraction between the particles. They are also more concentrated in the bulk flow where it has been shown to be more favourable to the agglomeration process. However, more collisions occurred for the larger sized particles, which was attributed, again, to the increased influence of the gravity force on the particles, which enhanced their migration into areas of high turbulence. In contrast to the collision events, less agglomerations occurred for the larger sized particles due to the high kinetic energies possessed post-collision, which is less favourable to agglomeration as typically this results in larger forces than the force of attraction between both colliding partners.

Furthermore, analysis on the turbulence effect on collision and agglomeration was reported. The simulation used two separate horizontal channel flows of a fixed

diameter but different levels of turbulence, achieved through increasing the Reynolds number of the flow. It was found that the rate of collision and agglomeration was strongly sensitive to the level of turbulence generated in the flow, with far more collisions and agglomeration occurring for the flow of less turbulence. This was concluded to be as a result of the increased influence of gravity on the less turbulent flows, which encourages a faster migration of the particles towards the lower wall region. Hence, the increased collision and agglomeration events for the less turbulent flow was as a result of localised particle concentrations in this flow, accentuated by gravity towards the lower wall. On turbulence modulation, the fluid was observed to be affected by the variation in flow parameters, although only minimal. The fluid turbulence was increasingly augmented with the increase in particle size which encouraged vortex shedding and wake generation within the flow; while the mean velocity was suppressed. The effect was found to be enhanced with the inclusion of gravity in the flow, although of negligible magnitude. In all, particle collisions and agglomeration were shown to be highly influenced by the gravity force and the flow turbulence, with the level of impact highly dependent on the size of the particles.

In the final result chapter, the investigation on collision and agglomeration was extended into vertical channels flows using a flow of Reynolds number, $Re_\tau = 300$. The investigation studied the phenomenon of interest by making contrast of flows in the positive gravity direction (downward flow) and another flowing against the direction of the gravity force (upwards flow). The influence of the surrounding forces on the particle motion was successfully investigated, with the lift force particularly responsible for particle drift towards and away from the channel walls, depending on the flow direction. With the consideration of both counter direction flows, it was shown that particle collision and agglomeration is enhanced when flow is in the positive gravity direction. This was found to be as a result of the lift force which enhances particle migration towards the wall where turbulence is maximum. The drag force was also found to be less dominant in this flow direction; hence, particle downward migration occurred at a faster rate. Similarly to the horizontal channel flow, it was also shown for both vertical flows that although particle collision is maximum in the near wall areas of maximum turbulence, agglomeration on the other hand is favoured in the bulk flow where turbulence is minimal.

In terms of the effect of turbulence on particle collision and agglomeration for the vertical flow, the analysis in each case compared flows of low and high turbulence

levels ($Re_\tau = 150$ and 590, respectively). It was found that the rate of collision and agglomeration was strongly sensitive to the level of turbulence generated in the flow, with far more collisions and agglomeration occurring for the flow of less turbulence in both flow directions. This was attributed to the segregation of particles in the lower Re_τ flow, which then resulted in more collisions and agglomeration as particle contact distance becomes increasingly reduced. The collision and agglomeration events in the higher Re_τ flow was observed to be much reduced, owing to the increased flow velocity and turbulence, which ensured particles remain evenly distributed across the channel for the simulation time; thus, prevented localised particle collisions. In all, the lift and gravity force and turbulence was seen to be the primary factors responsible for particle dynamics within the flow; and consequently determined the collision and agglomeration events. In summary, the gravity force has been successfully demonstrated to play a significant role in the formation of agglomerates in wall bounded flows, with its impact accentuated with increase in particle size and for flows in the direction positive to gravity were the drag impact is of less significance.

The investigation presented is a novel contribution to literature that addresses fundamentally, the issue as related to the collision and agglomeration of solid particles and provide basic understandings on the physics that underpins their behaviour in industrial flow processes. In particular, it extends the existing knowledge on particle collision and agglomeration in turbulent flows by examining the effect of gravity on such flows. This is useful in the processing and transportation of fluid-solid flows, where particle agglomeration adds to their propensity to form solid beds, and can result in flow blockages. The understanding on the physical conditions promoting these interactions and the consequent re-distribution, collision and agglomeration of the dispersed phase is of clear benefit to more cost-effective process design and improved flow assurance.

7.2 Recommendations for Further Work

A list of improvements to the current model and suggestions for future work, based on the findings of this study, are highlighted below:

1. An improvement in the LES prediction of the fluid phase is possible, particularly in the near-wall regions. A possible way of achieving this is through the use of better refined mesh and more grid nodes. Although would

require more computational resources, this would ensure that smaller energetic scales of turbulence are sufficiently captured and resolved; reducing the modelling and computational run-time requirements.

2. An improvement in the LPT code to account for multiple particle collisions as to the present limitation of only binary collisions is required, although this will be very challenging to implement and may dramatically increase the cost of computation.

3. The current LPT model assumes the dispersed phase as a collection of point particles. Therefore, interesting flow behaviours around the mass of the particles are neglected. For flows with agglomerating particles like the case herein, a correction to the point-particle assumption is necessary to better describe the behaviour of the agglomerates and their impact on turbulence.

4. The break-up of already formed agglomerates due to hydrodynamic forces and inter-particle or particle-wall collisions have not been accounted for in this investigation. An extension of the current agglomeration model to account for particle breakup would allow for more realistic agglomeration predictions, which is of industrial interest. Furthermore, the variables studied here could be extended into flow geometries with rough walls and also for flows ladened with non-spherical particles.

5. The consideration of particle deposition and resuspension in the current LES-LPT code will also be very useful in improving the understanding on the effects of the variables investigated.

6. The inclusion of the force of friction at point of contact between the colliding particles and their angular velocities as derived in the much improved agglomeration model of Alletto (2014) should provide an improvement in the agglomeration predictions.

7. The effect of turbulence on the agglomeration formation process for a gravity flow could be extended to more complex flow geometries such as pipes and ducts. This is necessary to gain insight into the effect of generated secondary flows (prevalent in complex geometry flows) on collision and agglomeration. A more efficient approach would involve the use of very small particles, since they follow the flow more closely and are more affected by secondary flow velocities.

8. The mass loading of the flow considered could be increased to better understand the particle feedback effects on the flow, i.e. turbulence modulation.

9. In an attempt to replicate typical industrial flow conditions, it may be useful to further extend the study herein, into pipes with beds as the effect of secondary flow becomes more pronounced; and could be key to particle resuspension and break-ups.

10. It may also be useful to repeat the study for a gas-particle flow to further understand the effects of the aerodynamic forces on collision and agglomeration. The effect of the high gas-particle density ratio is expected to influence the dynamics of the particles in the fluid and thus influence collision and agglomeration.

11. Finally, a detailed experimental study on particle agglomeration will be useful, as it will help validate the predictions on the contribution of gravity to the particle and agglomerate dispersion behaviours; and can help identify possible lapses in the agglomeration model employed in this investigation.

8 References

Abbas, A., Koussa, S., Lockwood, F., 1981. The prediction of the particle laden gas flows, Symposium (International) on Combustion. Elsevier, pp. 1427-1438.

Acton, E., 1980. A modelling of large eddies in an axisymmetric jet. Journal of Fluid Mechanics 98, 1-31.

Adam, N., Everitt, P., Riffat, S., 1996. Aerosol deposition in ventilation ducts. International journal of energy research 20, 1095-1101.

Adams, J.F., Biggs, S.R., Fairweather, M., Yao, J., Young, J., 2012. Transport of nuclear waste flows-a modelling and simulation approach-59136.

Adrian, R.J., 1984. Scattering particle characteristics and their effect on pulsed laser measurements of fluid flow: speckle velocimetry vs particle image velocimetry. Applied optics 23, 1690-1691.

Adrian, R.J., 1991. Particle-imaging techniques for experimental fluid mechanics. Annual review of fluid mechanics 23, 261-304.

Afkhami, M., Hassanpour, A., Fairweather, M., Njobuenwu, D.O., 2015. Fully coupled LES-DEM of particle interaction and agglomeration in a turbulent channel flow. Computers & Chemical Engineering 78, 24-38.

Ahn, J., Lee, J.H., Jang, S.J. and Sung, H.J., 2013. Direct numerical simulations of fully developed turbulent pipe flows for Re_τ = 180, 544 and 934. International Journal of Heat and Fluid Flow, 44, pp.222-228.

Ahn, J., Lee, J.H., Lee, J., Kang, J.-h., Sung, H.J., 2015. Direct numerical simulation of a 30R long turbulent pipe flow at Re_τ = 3008. Physics of Fluids 27, 065110.

Alexander, L., Coldren, C., 1951. Droplet transfer from suspending air to duct walls. Industrial & Engineering Chemistry 43, 1325-1331.

Alfredsson, P.H., Johansson, A.V., 1984. On the detection of turbulence-generating events. Journal of Fluid Mechanics 139, 325-345.

Alletto, M., 2014. Numerical investigation of the influence of particle-particle and particle-wall collisions in turbulent wall-bounded flows at high mass loadings. Ph.D. thesis, Department of Fluid Mechanics, Helmut-Schmidt-University Hamburg, Germany.

Alletto, M., Breuer, M., 2015. Four-Way Coupled LES Predictions of Dense Particle-Laden Flows in Horizontal Smooth and Rough Pipes, Direct and Large-Eddy Simulation IX. Springer, pp. 605-612.

Almohammed, N., Breuer, M., 2016. Modelling and simulation of agglomeration in turbulent particle-laden flows: A comparison between energy-based and momentum-based agglomeration models. Powder Technology 294, 373-402.

Ardell, A.J., 1972. The effect of volume fraction on particle coarsening: theoretical considerations. Acta metallurgica, 20(1), pp.61-71.

Armenio, V., Fiorotto, V., 2001. The importance of the forces acting on particles in turbulent flows. Physics of Fluids 13, 2437-2440.

Armenio, V., Piomelli, U., Fiorotto, V., 1999. Effect of the subgrid scales on particle motion. Physics of Fluids (1994-present) 11, 3030-3042.

Arnason, G., Stock, D., 1984. A new method to measure particle turbulent dispersion using laser Doppler anemometer. Experiments in fluids 2, 89-93.

Asiagbe, K.S., Fairweather, M., Njobuenwu, D.O., Colombo, M., 2017. Large eddy simulation of microbubble transport in a turbulent horizontal channel flow. International Journal of Multiphase Flow 94, 80-93.

Attanasi, E.D., Freeman, P.A., 2014. Commercial possibilities for stranded conventional gas from Alaska's North Slope. Natural resources research 23, 175-193.

Balachandar, S., Eaton, J.K., 2010. Turbulent dispersed multiphase flow. Annual Review of Fluid Mechanics 42, 111-133.

Balásházy, I., Hofmann, W., 1995. Deposition of aerosols in asymmetric airway bifurcations. Journal of Aerosol Science 26, 273-292.

Baldwin BS, Barth TJ. A one-equation turbulence transport model for high Reynolds number wall-bounded flows. AIAA 91-0610, 1991.

Barbin, A., Jones, J., 1963. Turbulent flow in the inlet region of a smooth pipe. Journal of Basic Engineering 85, 29-33.

Bauckhage, K., 1988. The Phase-Doppler-Difference-Method, a New Laser-Doppler Technique for Simultaneous Size and Velocity Measurements. Part 1: Description of the method. Particle & Particle Systems Characterization 5, 16-22.

Bernardini, M., Pirozzoli, S., Orlandi, P., 2014. Velocity statistics in turbulent channel flow up to $Re_{\tau}= 4000$. Journal of Fluid Mechanics 742, 171-191.

Bini, M., Jones, W., 2008. Large-eddy simulation of particle-laden turbulent flows. Journal of Fluid Mechanics 614, 207-252.

Bird, R.B., Stewart, W.E., Lightfoot, E.N., 1960. Transport Phenomena John Wiley & Sons. New York, 413.

Boivin, M., Simonin, O., Squires, K.D., 1998. Direct numerical simulation of turbulence modulation by particles in isotropic turbulence. Journal of Fluid Mechanics 375, 235-263.

Borée, J., Caraman, N., 2005. Dilute bidispersed tube flow: Role of interclass collisions at increased loadings. Physics of Fluids 17, 055108.

Borrell, G., Sillero, J.A., Jiménez, J., 2013. A code for direct numerical simulation of turbulent boundary layers at high Reynolds numbers in BG/P supercomputers. Computers & Fluids 80, 37-43.

Bose, S.T. and Park, G.I., 2018. Wall-Modeled Large-Eddy Simulation for Complex Turbulent Flows. Annual Review of Fluid Mechanics, 50-1.

Bradshaw, P., Ferriss, D., Atwell, N., 1967. Calculation of boundary-layer development using the turbulent energy equation. Journal of Fluid Mechanics 28, 593-616.

Bremhorst, K., Walker, T., 1973. Spectral measurements of turbulent momentum transfer in fully developed pipe flow. Journal of Fluid Mechanics 61, 173-186.

Brenn, G., Braeske, H., Durst, F., 2002. Investigation of the unsteady two-phase flow with small bubbles in a model bubble column using phase-Doppler anemometry. Chemical engineering science 57, 5143-5159.

Breuer, M., Alletto, M., 2012. Efficient simulation of particle-laden turbulent flows with high mass loadings using LES. International Journal of Heat and Fluid Flow 35, 2-12.

Breuer, M., Almohammed, N., 2015. Modeling and simulation of particle agglomeration in turbulent flows using a hard-sphere model with deterministic collision detection and enhanced structure models. International Journal of Multiphase Flow 73, 171-206.

Breuer, M. and Hoppe, F., 2017. Influence of a cost–efficient Langevin subgrid-scale model on the dispersed phase of large–eddy simulations of turbulent bubble–laden and particle–laden flows. International Journal of Multiphase Flow, 89, pp.23-44.

Brooke, J.W., Kontomaris, K., Hanratty, T., McLaughlin, J.B., 1992. Turbulent deposition and trapping of aerosols at a wall. Physics of Fluids A: Fluid Dynamics (1989-1993) 4, 825-834.

Brundrett, E., Baines, W., 1964. The production and diffusion of vorticity in duct flow. Journal of Fluid Mechanics 19, 375-394.

Burmester De Bessa Ribas, R., Lourenco, L., Riethmuller, M., 1980. A kinetic model for a gas-particle flow. Pneumotransport 5, Proceedings of the Fifth International Conference on the Pneumatic Transport of Solids in Pipes, Paper B, pp. 99-112.

Caraman, N., Borée, J., Simonin, O., 2003. Effect of collisions on the dispersed phase fluctuation in a dilute tube flow: Experimental and theoretical analysis. Physics of Fluids 15, 3602-3612.

Chamberlain, A., 1967. Transport of Lycopodium spores and other small particles to rough surfaces, Proceedings of the Royal Society of London A: Mathematical, Physical and Engineering Sciences. The Royal Society, pp. 45-70.

Chein, R., Chung, J., 1988. Simulation of particle dispersion in a two-dimensional mixing layer. AIChE Journal 34, 946-954.

Chen, M., Kontomaris, K., McLaughlin, J., 1999. Direct numerical simulation of droplet collisions in a turbulent channel flow. Part II: collision rates. International journal of multiphase flow 24, 1105-1138.

Cheng, Y., Lien, F., Yee, E., Sinclair, R., 2003. A comparison of large eddy simulations with a standard k–ε Reynolds-averaged Navier–Stokes model for the prediction of a fully developed turbulent flow over a matrix of cubes. Journal of Wind Engineering and Industrial Aerodynamics 91, 1301-1328.

Cheong, K., 1997. Deposition of aerosol particles in ductwork. Applied energy 57, 253-261.

Chin, C., Monty, J., Ooi, A., 2014. Reynolds number effects in DNS of pipe flow and comparison with channels and boundary layers. International Journal of Heat and Fluid Flow 45, 33-40.

Chin, C., Ooi, A., Marusic, I., Blackburn, H., 2010. The influence of pipe length on turbulence statistics computed from direct numerical simulation data. Physics of Fluids 22, 115107.

Choi, H., Moin, P., 1994. Effects of the computational time step on numerical solutions of turbulent flow. Journal of Computational Physics 113, 1-4.

Chou, P., 1945. Pressure flow of a turbulent fluid between two infinite parallel planes. Quarterly of Applied Mathematics 3, 198-209.

Clark, J., 1968. A study of incompressible turbulent boundary layers in channel flow. Journal of Basic Engineering 90, 455-467.

Cleaver, J., Yates, B., 1975. A sub layer model for the deposition of particles from a turbulent flow. Chemical Engineering Science 30, 983-992.

Clift, R., Grace, J., Weber, M., 1978. Bubbles, Drops and Particles, Acad. Press, New York, 117-120.

C.-L. Lin and M.-Y. Wey, "The effect of mineral compositions of waste and operating conditions on particle agglomeration/defluidization during incineration," Fuel 83, 2335 (2004).

Comte-Bellot, G., 1963. Contribution a letude de la trubulence de conduite. These presente a la faculte des sciences de l'Universite de Grenoble.

Crabtree, M., Eslinger, D., Fletcher, P., Miller, M., Johnson, A., King, G., 1999. Fighting scale—removal and prevention. Oilfield review 11, 30-45.

Crowe, C., Troutt, T., Chung, J., 1996. Numerical models for two-phase turbulent flows. Annual Review of Fluid Mechanics 28, 11-43.

Crowe, C.T., 2000. On models for turbulence modulation in fluid–particle flows. International Journal of Multiphase Flow 26, 719-727.

Crowe, C.T., 2005. Multiphase flow handbook. CRC press.

Crowe, C.T., Sharma, M.P., Stock, D.E., 1977. The particle-source-in cell (PSI-CELL) model for gas-droplet flows. Journal of fluids engineering 99, 325-332.

Curtis, J.S., Van Wachem, B., 2004. Modeling particle-laden flows: A research outlook. AIChE Journal 50, 2638-2645.

Daly, B.J., Harlow, F.H., 1970. Transport equations in turbulence. The Physics of Fluids 13, 2634-2649.

Deardorff, J.W., 1970. A numerical study of three-dimensional turbulent channel flow at large Reynolds numbers. Journal of Fluid Mechanics 41, 453-480.

Deegan, D., Chapman, C. and Ismail, S., Tetronics (International) Ltd, 2013. Treatment of nuclear sludge. U.S. Patent 8,404,919.

Del Alamo, J.C., Jiménez, J., Zandonade, P., Moser, R.D., 2004. Scaling of the energy spectra of turbulent channels. Journal of Fluid Mechanics 500, 135-144.

Demadis, K.D., Mavredaki, E., Stathoulopoulou, A., Neofotistou, E., Mantzaridis, C., 2007. Industrial water systems: problems, challenges and solutions for the process industries. Desalination 213, 38-46.

Demuren, A.O., Rodi, W., 1984. Calculation of turbulence-driven secondary motion in non-circular ducts. Journal of Fluid Mechanics 140, 189-222.

Den Toonder, J., Nieuwstadt, F., 1997. Reynolds number effects in a turbulent pipe flow for low to moderate Re. Physics of Fluids 9, 3398-3409.

Derevich, I., 2000. Statistical modelling of mass transfer in turbulent two-phase dispersed flows—1. Model development. International journal of heat and mass transfer 43, 3709-3723.

Di Mare, L., Jones, W., 2003. LES of turbulent flow past a swept fence. International Journal of Heat and Fluid Flow 24, 606-615.

Di Mare, L., Klein, M., Jones, W., Janicka, J., 2006. Synthetic turbulence inflow conditions for large-eddy simulation. Physics of Fluids 18, 025107.

Dizaji, F.F. and Marshall, J.S., 2017. On the significance of two-way coupling in simulation of turbulent particle agglomeration. Powder Technology, 318, pp.83-94.

Donaldson, C.d.P., 1972. Calculation of turbulent shear flows for atmospheric and vortex motions. AIAA J 10, 4-12.

Dosta, M., Antonyuk, S. and Heinrich, S., 2013. Multiscale simulation of agglomerate breakage in fluidized beds. Industrial & Engineering Chemistry Research, 52(33), pp.11275-11281.

Dou, Z., Bragg, A.D., Hammond, A.L., Liang, Z., Collins, L.R. and Meng, H., 2018. Effects of Reynolds number and Stokes number on particle-pair relative velocity in isotropic turbulence: a systematic experimental study. Journal of Fluid Mechanics, 839, pp.271-292.

Druzhinin, O., Elghobashi, S., 1998. Direct numerical simulations of bubble-laden turbulent flows using the two-fluid formulation. Physics of Fluids 10, 685-697.

Druzhinin, O., Elghobashi, S., 1999. On the decay rate of isotropic turbulence laden with microparticles. Physics of Fluids 11, 602-610.

Durst, F., Miloievic, D., Schönung, B., 1984. Eulerian and Lagrangian predictions of particulate two-phase flows: a numerical study. Applied Mathematical Modelling 8, 101-115.

Durst, F., Zaré, M., 1976. Laser Doppler measurements in two-phase flows, The accuracy of flow measurements by laser Doppler methods, pp. 403-429.

Dutta, P., Saha, S.K., Nandi, N. and Pal, N., 2016. Numerical study on flow separation in 90 pipe bend under high Reynolds number by k-ε modelling. Engineering Science and Technology, an International Journal, 19(2), pp.904-910.

E. Forum and U. Technical, Environmental management in oil and gas exploration and production, First. Oxford: Words and Publications, 1997, pp. 1–76.

Eggels, J., Unger, F., Weiss, M., Westerweel, J., Adrian, R., Friedrich, R., Nieuwstadt, F., 1994. Fully developed turbulent pipe flow: a comparison between direct numerical simulation and experiment. Journal of Fluid Mechanics 268, 175-210.

Eggels, J., Westerweel, J., Nieuwstadt, F., Adrian, R., 1993. Direct numerical simulation of turbulent pipe flow. Applied Scientific Research 51, 319-324.

EIA, 2010. Energy information administration. Department of Energy 92010, 1-15.

Eisenschmidt, K., Ertl, M., Gomaa, H., Kieffer-Roth, C., Meister, C., Rauschenberger, P., Reitzle, M., Schlottke, K. and Weigand, B., 2016. Direct numerical simulations for multiphase flows: An overview of the multiphase code FS3D. Applied Mathematics and Computation, 272, pp.508-517.

El Khoury, G.K., Schlatter, P., Brethouwer, G., Johansson, A.V., 2014. Turbulent pipe flow: Statistics, Re-dependence, structures and similarities with channel and boundary layer flows, Journal of Physics: Conference Series. IOP Publishing, p. 012010.

El Khoury, G.K., Schlatter, P., Noorani, A., Fischer, P.F., Brethouwer, G., Johansson, A.V., 2013. Direct numerical simulation of turbulent pipe flow at moderately high Reynolds numbers. Flow, turbulence and combustion 91, 475-495.

Elghobashi, S., 1994. On predicting particle-laden turbulent flows. Applied scientific research 52, 309-329.

Elghobashi, S., Abou-Arab, T., Rizk, M., Mostafa, A., 1984. Prediction of the particle-laden jet with a two-equation turbulence model. International Journal of Multiphase Flow 10, 697-710.

Elghobashi, S., Abou-Arab, T., 1983. A two-equation turbulence model for two-phase flows. The Physics of Fluids 26, 931-938.

Elghobashi, S., Truesdell, G., 1993. On the two-way interaction between homogeneous turbulence and dispersed solid particles. I: Turbulence modification. Physics of Fluids A: Fluid Dynamics (1989-1993) 5, 1790-1801.

Emery, A., Neighbors, P., Gessner, F., 1980. The numerical prediction of developing turbulent flow and heat transfer in a square duct. Journal of Heat Transfer 102, 51-57.

Ennis, B.J., Tardos, G., Pfeffer, R., 1991. A microlevel-based characterization of granulation phenomena. Powder Technology 65, 257-272.

Enwald, H., Peirano, E., Almstedt, A.-E., 1996. Eulerian two-phase flow theory applied to fluidization. International Journal of Multiphase Flow 22, 21-66.

Faeth, G.M., 1987. Mixing, transport and combustion in sprays. Progress in Energy and Combustion Science 13, 293-345.

Faires, J.D., Burden, R.L., 1994. Numerische Methoden-Näherungsverfahren und ihre praktische Anwendung.

Fairweather, M., Yao, J., 2009. Mechanisms of particle dispersion in a turbulent, square duct flow. AIChE Journal 55, 1667-1679.

Farge, M., Pellegrino, G., Schneider, K., 2001. Coherent vortex extraction in 3D turbulent flows using orthogonal wavelets. Physical Review Letters 87, 054501.

Farmer, R., Griffith, P., Rohsenow, W.M., 1970. Liquid droplet deposition in two-phase flow. Journal of Heat Transfer 92, 587-594.

Feldmann, D. and Wagner, C., 2012. Direct numerical simulation of fully developed turbulent and oscillatory pipe flows at. Journal of Turbulence, (13), p.N32.

Ferrante, A., Elghobashi, S., 2003. On the physical mechanisms of two-way coupling in particle-laden isotropic turbulence. Physics of fluids 15, 315-329.

Friedlander, S., Johnstone, H., 1957. Deposition of suspended particles from turbulent gas streams. Industrial & Engineering Chemistry 49, 1151-1156.

Friedrich, R., Hüttl, T., Manhart, M., Wagner, C., 2001. Direct numerical simulation of incompressible turbulent flows. Computers & fluids 30, 555-579.

Frisch, U., 1995. Turbulence: the legacy of AN Kolmogorov. Cambridge university press.

Fukagata, K., Kasagi, N., 2002. Highly energy-conservative finite difference method for the cylindrical coordinate system. Journal of Computational Physics 181, 478-498.

Galletti, B., Bottaro, A., 2004. Large-scale secondary structures in duct flow. Journal of Fluid Mechanics 512, 85-94.

Gavrilakis, S., 1992. Numerical simulation of low-Reynolds-number turbulent flow through a straight square duct. Journal of Fluid Mechanics 244, 101-129.

Germano, M., 1992. Turbulence: the filtering approach. Journal of Fluid Mechanics 238, 325-336.

Germano, M., Piomelli, U., Moin, P., Cabot, W.H., 1991. A dynamic subgrid-scale eddy viscosity model. Physics of Fluids A: Fluid Dynamics 3, 1760-1765.

Gessner, F., Jones, J., 1965. On some aspects of fully-developed turbulent flow in rectangular channels. Journal of Fluid Mechanics 23, 689-713.

Ghosal, S., Moin, P., 1995. The basic equations for the large eddy simulation of turbulent flows in complex geometry. Journal of Computational Physics 118, 24-37.

Gore, R., Crowe, C.T., 1989. Effect of particle size on modulating turbulent intensity. International Journal of Multiphase Flow 15, 279-285.

Graham, J., Lee, M., Malaya, N., Moser, R., Eyink, G., Meneveau, C., Kanov, K., Burns, R., Szalay, A., 2013. Turbulent channel flow data set. Technical report, John Hopkins University.

Große, S., Schröder, W., 2008. Dynamic wall-shear stress measurements in turbulent pipe flow using the micro-pillar sensor MPS 3. International Journal of Heat and Fluid Flow 29, 830-840.

Große, S., Schröder, W., 2009. Wall-shear stress patterns of coherent structures in turbulent duct flow. Journal of fluid mechanics 633, 147-158.

Grötzbach, G., 1987. Direct numerical and large eddy simulation of turbulent channel flows. Encyclopedia of fluid mechanics 6, 1337-1391.

Grötzbach, G., Schumann, U., 1979. Direct numerical simulation of turbulent velocity, pressure, and temperature fields in channel flows, Turbulent Shear Flows I. Springer, pp. 370-385.

Hanjalic, K., Launder, B., 1972. A Reynolds stress model of turbulence and its application to thin shear flows. J. Fluid Mech 52, 609-638.

Haworth, D., Pope, S., 1987. A pdf modeling study of self-similar turbulent free shear flows. The Physics of fluids 30, 1026-1044.

He, S., Ariyaratne, C., Vardy, A., 2008. A computational study of wall friction and turbulence dynamics in accelerating pipe flows. Computers & fluids 37, 674-689.

Hetsroni, G., 1989. Particles-turbulence interaction. International Journal of Multiphase Flow 15, 735-746.

Hinze, J.O., 1975. Turbulence McGraw-Hill. New York, 218.

Hjelmfelt, A., Mockros, L., 1966. Motion of discrete particles in a turbulent fluid. Applied Scientific Research 16, 149-161.

Ho, C.A., Sommerfeld, M., 2002. Modelling of micro-particle agglomeration in turbulent flows. Chemical Engineering Science 57, 3073-3084.

Hoagland, L.C., 1962. Fully developed turbulent flow in straight rectangular ducts: secondary flow, its cause and effect on the primary flow (Doctoral dissertation, Massachusetts Institute of Technology).

Hoyas, S., Jiménez, J., 2006. Scaling of the velocity fluctuations in turbulent channels up to Re τ= 2003. Physics of fluids 18, 011702.

Hrenya, C., Bolio, E., Chakrabarti, D., Sinclair, J., 1995. Comparison of low Reynolds number k− ε turbulence models in predicting fully developed pipe flow. Chemical Engineering Science 50, 1923-1941.

Hultmark, M., Bailey, S.C., Smits, A.J., 2010. Scaling of near-wall turbulence in pipe flow. Journal of Fluid Mechanics 649, 103-113.

Huser, A., Biringen, S., 1993. Direct numerical simulation of turbulent flow in a square duct. Journal of Fluid Mechanics 257, 65-95.

Huser, A., Biringen, S., Hatay, F.F., 1994. Direct simulation of turbulent flow in a square duct: Reynolds-stress budgets. Physics of Fluids 6, 3144-3152.

Hussain, A., Reynolds, W., 1975. Measurements in fully developed turbulent channel flow. Journal of Fluids Engineering 97, 568-578.

Hwang, J., Lee, J. and Sung, H.J., 2016. Influence of large-scale accelerating motions on turbulent pipe and channel flows. Journal of Fluid Mechanics, 804, pp.420-441.

Hyatt, N., Biggs, S., Livens, F., Young, J., Evans, N., 2009. DIAMOND: Academic Innovation in Support of UK Radioactive Waste Management, Workshop TRePro II, p. 22.

Ilori, T.A., 1972. Turbulent deposition of aerosol particles inside pipes. 2737-2737.

Inoue, O., 1985. Vortex simulation of a turbulent mixing layer. AIAA Journal (ISSN 0001-1452) 23, 367-373.

Jain, A., 2017. Experimental Investigation of Turbulent Flow in a Pipe Bend using Particle Image Velocimetry (Doctoral dissertation).

Johansson, A.V., Alfredsson, P.H., 1982. On the structure of turbulent channel flow. Journal of Fluid Mechanics 122, 295-314.

Jones, W., 1991. BOFFIN: A computer program for flow and combustion in complex geometries. Dept. Mech. Eng., Imperial College of Science, Technology and Medicine.

Jones, W., Launder, B., 1972. The prediction of laminarization with a two-equation model of turbulence. International journal of heat and mass transfer 15, 301-314.

Jones, W., Launder, B., 1973. The calculation of low-Reynolds-number phenomena with a two-equation model of turbulence. International Journal of Heat and Mass Transfer 16, 1119-1130.

Jones, W.P., di Mare, F., Marquis, A.J., 2002. LES-BOFFIN: User's Guide, Technical Memorandum. Department of Mechanical Engineering, Imperial College of Science, Technology and Medicine. Journal.

Joung, Y., Choi, S.-U., Choi, J.-I., 2007. Direct numerical simulation of turbulent flow in a square duct: analysis of secondary flows. Journal of engineering mechanics 133, 213-221.

Jürgens, D., 2012. Modellierung und Simulation der Partikelagglomeration in turbulenten, dispersen Mehrphasenströmungen. Master's thesis, Professur für Strömungsmechanik Helmut-Schmidt-Universität, Hamburg, Germany.

Kajishima, T. and Taira, K., 2017. Numerical simulation of turbulent flows. In Computational Fluid Dynamics (pp. 207-235). Springer, Cham.

K Lai, A.C., Nazaroff, W.W., 2000. Modeling indoor particle deposition from turbulent flow onto smooth surfaces. Journal of Aerosol Science 31, 463-476.

Kerstein, A.R., 1989. Linear-eddy modeling of turbulent transport. II: Application to shear layer mixing. Combustion and Flame 75, 397-413.

Kerstein, A.R., 1991. Linear-eddy modeling of turbulent transport. Part V: Geometry of scalar interfaces. Physics of Fluids A: Fluid Dynamics 3, 1110-1114.

Kim, J., Moin, P., Moser, R., 1987. Turbulence statistics in fully developed channel flow at low Reynolds number. Journal of fluid mechanics 177, 133-166.

Klewicki, J., Chin, C., Blackburn, H., Ooi, A., Marusic, I., 2012. Emergence of the four layer dynamical regime in turbulent pipe flow. Physics of Fluids 24, 045107.

Kliafas, Y., Holt, M., 1987. LDV measurements of a turbulent air-solid two-phase flow in a 90 bend. Experiments in Fluids 5, 73-85.

Kobayashi, T., Yoda, M., 1987. Modified k-ε Model for Turbulent Swirling Flow in a Straight Pipe: Fluids Engineering. JSME international journal 30, 66-71.

Kolmogorov, A., 1942. Equations of motion of an incompressible turbulent fluid. Izv Akad Nauk SSSR Ser Phys 6, 56-58.

Kosinski, P., Hoffmann, A.C., 2010. An extension of the hard-sphere particle–particle collision model to study agglomeration. Chemical Engineering Science 65, 3231-3239.

Kraichnan, R.H., 1976. Eddy viscosity in two and three dimensions. Journal of the Atmospheric Sciences 33, 1521-1536.

Kreplin, H.P., Eckelmann, H., 1979. Behavior of the three fluctuating velocity components in the wall region of a turbulent channel flow. The Physics of Fluids 22, 1233-1239.

Kuerten, J.G., 2016. Point-Particle DNS and LES of Particle-Laden Turbulent flow-a state-of-the-art review. Flow, turbulence and combustion, 97(3), pp.689-713.

Kulick, J.D., Fessler, J.R., Eaton, J.K., 1994. Particle response and turbulence modification in fully developed channel flow. Journal of Fluid Mechanics 277, 109-134.

Kussin, J., Sommerfeld, M., 2002. Experimental studies on particle behaviour and turbulence modification in horizontal channel flow with different wall roughness. Experiments in Fluids 33, 143-159.

Laín, S., Sommerfeld, M., 2008. Euler/Lagrange computations of pneumatic conveying in a horizontal channel with different wall roughness. Powder technology 184, 76-88.

Laín, S., Sommerfeld, M., Kussin, J., 2002. Experimental studies and modelling of four-way coupling in particle-laden horizontal channel flow. International journal of heat and fluid flow 23, 647-656.

Laitone, J.A., 1981. A numerical solution for gas-particle flows at high Reynolds numbers. J. Appl. Mech 48, 465-471.

Laufer, J., 1951. Investigation of turbulent flow in a two-dimensional channel.

Laufer, J., 1954. The structure of turbulence in fully developed pipe flow.

Launder, B., Reece, G.J., Rodi, W., 1975. Progress in the development of a Reynolds-stress turbulence closure. Journal of fluid mechanics 68, 537-566.

Launder, B., Ying, W., 1972. Secondary flows in ducts of square cross-section. Journal of Fluid Mechanics 54, 289-295.

Launder, B.E., Spalding, D.B., 1974. The numerical computation of turbulent flows. Computer methods in applied mechanics and engineering 3, 269-289.

Lawn, C., 1971. The determination of the rate of dissipation in turbulent pipe flow. Journal of Fluid Mechanics 48, 477-505.

Lee, J.H., Sung, H.J., 2013. Comparison of very-large-scale motions of turbulent pipe and boundary layer simulations. Physics of Fluids 25, 045103.

Lee, M., Moser, R.D., 2015. Direct numerical simulation of a turbulent channel flow up to Re_τ = 5200. J. Fluid Mech. 744, 395–415.

Lee, S., Durst, F., 1982. On the motion of particles in turbulent duct flows. International Journal of Multiphase Flow 8, 125-146.

Leonard, A., 1974. Energy cascade in large-eddy simulations of turbulent fluid flows, Turbulent Diffusion in Environmental Pollution, pp. 237-248.

Leonard, A., 1980. Vortex methods for flow simulation. Journal of Computational Physics 37, 289-335.

Lesieur, M., Metais, O., 1996. New trends in large-eddy simulations of turbulence. Annual Review of Fluid Mechanics 28, 45-82.

Leutheusser, H.J., 1963. Turbulent flow in rectangular ducts. J. Hydraul. Div., Am. Soc. Civ. Eng., HY3, 1-19.

Li, A., Ahmadi, G., 1995. Computer simulation of particle deposition in the upper tracheobronchial tree. Aerosol science and technology 23, 201-223.

Li, J., Wang, H., Liu, Z., Chen, S., Zheng, C., 2012. An experimental study on turbulence modification in the near-wall boundary layer of a dilute gas-particle channel flow. Experiments in fluids 53, 1385-1403.

Li, Q., Song, J., Li, C., Wei, Y., Chen, J., 2013. Numerical and experimental study of particle deposition on inner wall of 180° bend. Powder technology 237, 241-254.

Li, Y., McLaughlin, J.B., Kontomaris, K., Portela, L., 2001. Numerical simulation of particle-laden turbulent channel flow. Physics of Fluids (1994-present) 13, 2957-2967.

Li, Y., Zhang, J., Fan, L.-S., 1999. Numerical simulation of gas–liquid–solid fluidization systems using a combined CFD-VOF-DPM method: bubble wake behavior. Chemical Engineering Science 54, 5101-5107.

Lilly, D.K., 1967. The representation of small-scale turbulence in numerical simulation experiments, Proc. IBM Sci. Compt. Symp. Environ. Sci., White Plains, IBM, 1967.

Lin, C.L., Peng, T.H. and Wang, W.J., 2011. Effect of particle size distribution on agglomeration/defluidization during fluidized bed combustion. Powder technology, 207(1-3), pp.290-295.

Lin, C.-L., Wey, M.-Y., 2004. The effect of mineral compositions of waste and operating conditions on particle agglomeration/defluidization during incineration. Fuel 83, 2335-2343.

Liu, B.Y., Agarwal, J.K., 1974. Experimental observation of aerosol deposition in turbulent flow. Journal of Aerosol Science 5, 145IN1149-1148IN2155.

Liu, B.Y., Ilori, T.A., 1974. Aerosol deposition in turbulent pipe flow. Environmental Science & Technology 8, 351-356.

Liu, Z.-C., Landreth, C., Adrian, R., Hanratty, T., 1991. High resolution measurement of turbulent structure in a channel with particle image velocimetry. Experiments in fluids 10, 301-312.

Li, J., Wang, H., Xiong, Y., Jiang, G., Liu, Z. and Zheng, C., 2016. Experimental investigation on turbulence modification in a dilute gas-particle axisymmetric opposed jets flow. Chemical Engineering Journal, 286, pp.76-90.

Löffler, F. and Muhr, W., 1972. Die Abscheidung von Feststoffteilchen und Tropfen an Kreiszylindern infolge von Trägheitskräften. Chemie Ingenieur Technik, 44(8), pp.510-514.

Loth, E., 2000. Numerical approaches for motion of dispersed particles, droplets and bubbles. Progress in Energy and Combustion Science 26, 161-223.

Loulou, P., Moser, R.D., Mansour, N.N., Cantwell, B.J., 1997. Direct numerical simulation of incompressible pipe flow using a B-spline spectral method.

Lozano-Durán, A., Jiménez, J., 2014. Effect of the computational domain on direct simulations of turbulent channels up to Re τ= 4200. Physics of Fluids 26, 011702.

Lu, Q., Fontaine, J., Aubertin, G., 1993. A Lagrangian model for solid particles in turbulent flows. International journal of multiphase flow 19, 347-367.

Lumley, J.L., 1979. Computational modeling of turbulent flows. Advances in applied mechanics 18, 123-176.

Madabhushi, R.K., Vanka, S., 1991. Large eddy simulation of turbulence-driven secondary flow in a square duct. Physics of Fluids A: Fluid Dynamics 3, 2734-2745.

Mallouppas, G., George, W., van Wachem, B., 2013. New forcing scheme to sustain particle-laden homogeneous and isotropic turbulence. Physics of Fluids 25, 083304.

Mao, C.-P., Szekely, G., Faeth, G., 1980. Evaluation of a locally homogeneous flow model of spray combustion. Journal of Energy 4, 78-87.

Marchioli, C., Soldati, A., 2002. Mechanisms for particle transfer and segregation in a turbulent boundary layer. Journal of Fluid Mechanics 468, 283-315.

Marchioli, C., Soldati, A., 2007. Reynolds number scaling of particle preferential concentration in turbulent channel flow, Advances in Turbulence XI. Springer, pp. 298-300.

Marchioli, C., Soldati, A., Kuerten, J., Arcen, B., Taniere, A., Goldensoph, G., Squires, K., Cargnelutti, M., Portela, L., 2008. Statistics of particle dispersion in direct numerical simulations of wall-bounded turbulence: results of an international collaborative benchmark test. International Journal of Multiphase Flow 34, 879-893.

Marin, O., Vinuesa, R., Obabko, A., Schlatter, P., 2016. Characterization of the secondary flow in hexagonal ducts. Physics of Fluids 28, 125101.

Martinuzzi, R., Pollard, A., 1989. Comparative Study of Turbulence Models in Predicting Turbulent Pipe Flow. Part I: Algebraic Stress and k-Models. AIAA journal 27, 29-36.

Mashayek, F., Pandya, R., 2003. Analytical description of particle/droplet-laden turbulent flows. Progress in Energy and Combustion Science 29, 329-378.

Mason, P.J., 1994. Large-eddy simulation: A critical review of the technique. Quarterly Journal of the Royal Meteorological Society 120, 1-26.

Matsumoto, S., Saito, S., 1970. On the mechanism of suspension of particles in horizontal pneumatic conveying: Monte Carlo simulation based on the irregular bouncing model. Journal of Chemical Engineering of Japan 3, 83-92.

Maxey, M., Patel, B., Chang, E., Wang, L., 1997. Simulations of dispersed turbulent multiphase flow. Fluid Dynamics Research 20, 143.

Maxey, M.R., Riley, J.J., 1983. Equation of motion for a small rigid sphere in a nonuniform flow. The Physics of Fluids 26, 883-889.

McCoy, D., Hanratty, T., 1977. Rate of deposition of droplets in annular two-phase flow. International Journal of Multiphase Flow 3, 319-331.

McKeon, B., Li, J., Jiang, W., Morrison, J., Smits, A., 2003. Pitot probe corrections in fully developed turbulent pipe flow. Measurement science and technology 14, 1449.

McKeon, B., Smits, A., 2002. Static pressure correction in high Reynolds number fully developed turbulent pipe flow. Measurement Science and Technology 13, 1608.

McKeon, B., Zagarola, M., Smits, A., 2005. A new friction factor relationship for fully developed pipe flow. Journal of fluid mechanics 538, 429-443.

Mckeon, B.J., Li, J.-d, Jiang, W., Morrison, J.F., Smits, A.J., 2004. Further observations on the mean velocity distribution in fully developed pipe flow. Journal of Fluid Mechanics 501, 135-147.

McLaughlin, J.B., 1989. Aerosol particle deposition in numerically simulated channel flow. Physics of Fluids A: Fluid Dynamics 1, 1211-1224.

McLaughlin, J.B., 1991. Inertial migration of a small sphere in linear shear flows. Journal of Fluid Mechanics 224, 261-274.

McMurtry, P., Menon, S., Kerstein, A., 1993. Linear eddy modeling of turbulent combustion. Energy & fuels 7, 817-826.

Mei, R., 1992. An approximate expression for the shear lift force on a spherical particle at finite Reynolds number. International Journal of Multiphase Flow 18, 145-147.

Meinders, E., Hanjalić, K., 1999. Vortex structure and heat transfer in turbulent flow over a wall-mounted matrix of cubes. International Journal of Heat and fluid flow 20, 255-267.

Melling, A., Durst, F., Whitelaw, J., 1976. Principles and Practice of Laser-Doppler Anemometry. London: Acad. Press Merzkirch, W.(1974): Flow visualisation. New York: Acad. Press Strickert, H.(1973): Hitzdraht-und Hitzfilmanemometrie. Berlin: VEB Verl. Technik.

Mellor, G.L., Herring, H.J., 1973. A survey of the mean turbulent field closure models. AIAA journal 11, 590-599.

Meneveau, C., Katz, J., 2000. Scale-invariance and turbulence models for large-eddy simulation. Annual Review of Fluid Mechanics 32, 1-32.

Métais, O., Lesieur, M., 1992. Spectral large-eddy simulation of isotropic and stably stratified turbulence. Journal of Fluid Mechanics 239, 157-194.

Minier, J.-P., Peirano, E., 2001. The pdf approach to turbulent polydispersed two-phase flows. Physics reports 352, 1-214.

Mohanarangam, K., Tu, J., 2007. Two-fluid model for particle-turbulence interaction in a backward-facing step. AIChE journal 53, 2254-2264.

Moin, P., Kim, J., 1982. Numerical investigation of turbulent channel flow. Journal of fluid mechanics 118, 341-377.

Moin, P., Mahesh, K., 1998. Direct numerical simulation: a tool in turbulence research. Annual review of fluid mechanics 30, 539-578.

Moin, P., Reynolds, W., Ferziger, J.H., 1978. Large eddy simulation of incompressible turbulent channel flow. Rep. No. TF-12 Dept. of Mech. Eng, Stanford University.

Mompean, G., 1998. Numerical simulation of a turbulent flow near a right-angled corner using the Speziale non-linear model with RNG k–ε equations. Computers & Fluids 27, 847-859.

Montgomery, T.L., Corn, M., 1970. Aerosol deposition in a pipe with turbulent airflow. Journal of Aerosol Science 1, 185IN3195-194213.

Monty, J., Chong, M., 2009. Turbulent channel flow: comparison of streamwise velocity data from experiments and direct numerical simulation. Journal of Fluid Mechanics 633, 461-474.

Morsi, S.A.J. and Alexander, A.J., 1972. An investigation of particle trajectories in two-phase flow systems. Journal of Fluid mechanics, 55(2), pp.193-208.

Örlü, R., Fiorini, T., Segalini, A., Bellani, G., Talamelli, A. and Alfredsson, P.H., 2017. Reynolds stress scaling in pipe flow turbulence—first results from CICLoPE. Phil. Trans. R. Soc. A, 375(2089), p.20160187.

Moseley, J. L.; O'Brien, T. J. A model for agglomeration in a fluidized bed. Chem. Eng. Sci. 1993, 48, 3043−3050.

Moser, R.D., Kim, J., Mansour, N.N., 1999a. Direct numerical simulation of turbulent channel flow up to Re τ= 590. Physics of fluids 11, 943-945.

Moser, R.D., Kim, J., Mansour, N.N., 1999b. Direct numerical simulation of turbulent channel flow up to Re= 590. Phys. Fluids 11, 943-945.

Myong, H.K., Kasagi, N., 1990. A new approach to the improvement of k-ε turbulence model for wall-bounded shear flows. JSME international journal. Ser. 2, Fluids engineering, heat transfer, power, combustion, thermophysical properties 33, 63-72.

Naik, S., Bryden, I., 1999. Prediction of turbulent gas–solids flow in curved ducts using the Eulerian–Lagrangian method. International Journal for Numerical Methods in Fluids 31, 579-600.

Ng, H., Monty, J., Hutchins, N., Chong, M., Marusic, I., 2011. Comparison of turbulent channel and pipe flows with varying Reynolds number. Experiments in fluids 51, 1261-1281.

Nikuradse, J., 1926. Untersuchung über die Geschwindigkeitsverteilung in turbulenten Strömungen. Vdi-verlag.

Nikuradse, J., 1929. Untersuchungen über die Strömungen des Wassers in konvergenten und divergenten Kanälen. VDI-Verlag.

Nisizima, S., 1990. A numerical study of turbulent square-duct flow using an anisotropic k-ε model. Theoretical and Computational Fluid Dynamics 2, 61-71.

Niu, Y.Y., 2001. Evaluation of erosion in a two-way coupled fluid–particle system. International journal for numerical methods in fluids 36, 711-742.

Njobuenwu, D., Fairweather, M., 2015. Dynamics of single, non-spherical ellipsoidal particles in a turbulent channel flow. Chemical Engineering Science 123, 265-282.

Njobuenwu, D., Fairweather, M., Yao, J., 2013. Coupled RANS–LPT modelling of dilute, particle-laden flow in a duct with a 90 bend. International Journal of Multiphase Flow 50, 71-88.

Njobuenwu, D.O., Fairweather, M., 2016. Simulation of inertial fibre orientation in turbulent flow. Physics of Fluids 28, 063307.

Odar, F., 1966. Verification of the proposed equation for calculation of the forces on a sphere accelerating in a viscous fluid. Journal of Fluid Mechanics 25, 591-592.

Odar, F., Hamilton, W.S., 1964. Forces on a sphere accelerating in a viscous fluid. Journal of Fluid Mechanics 18, 302-314.

Ogholaja, T., Njobuenwu, D., Fairweather, M., 2017. Particle Size Effects on Collision and Agglomeration in Turbulent Channel Flows, Computer Aided Chemical Engineering. Elsevier, pp. 79-84.

Orlandi, P., Fatica, M., 1997. Direct simulations of turbulent flow in a pipe rotating about its axis. Journal of Fluid Mechanics 343, 43-72.

Ounis, H., Ahmadi, G., McLaughlin, J.B., 1991. Dispersion and deposition of Brownian particles from point sources in a simulated turbulent channel flow. Journal of Colloid and Interface Science 147, 233-250.

Ounis, H., Ahmadi, G., McLaughlin, J.B., 1993. Brownian particle deposition in a directly simulated turbulent channel flow. Physics of Fluids A: Fluid Dynamics 5, 1427-1432.

Ouriev, B., Windhab, E., 2002. Rheological study of concentrated suspensions in pressure-driven shear flow using a novel in-line ultrasound Doppler method. Experiments in fluids 32, 204-211.

Owolabi, B.E., Poole, R.J., Dennis, D.J., 2016. Experiments on low-Reynolds-number turbulent flow through a square duct. Journal of Fluid Mechanics 798, 398-410.

Pang, M., Wei, J., Yu, B., 2011. Effect of particle clusters on turbulence modulations in liquid flow laden with fine solid particles. Brazilian Journal of Chemical Engineering 28, 433-446.

Patel, V., Head, M., 1969. Some observations on skin friction and velocity profiles in fully developed pipe and channel flows. Journal of Fluid Mechanics 38, 181-201.

Patel, V., Head, M.R., 1968. Reversion of turbulent to laminar flow. Journal of Fluid Mechanics 34, 371-392.

Patro, P., Dash, S.K., 2014. Computations of particle-laden turbulent jet flows based on Eulerian model. Journal of Fluids Engineering 136, 011301.

Pedinotti, S., Mariotti, G., Banerjee, S., 1992. Direct numerical simulation of particle behaviour in the wall region of turbulent flows in horizontal channels. International journal of multiphase flow 18, 927-941.

Picano, F., Breugem, W.P. and Brandt, L., 2015. Turbulent channel flow of dense suspensions of neutrally buoyant spheres. Journal of Fluid Mechanics, 764, pp.463-487.

Pinelli, A., Uhlmann, M., Sekimoto, A., Kawahara, G., 2010. Reynolds number dependence of mean flow structure in square duct turbulence. Journal of fluid mechanics 644, 107-122.

Piomelli, U., 1999. Large-eddy simulation: achievements and challenges. Progress in Aerospace Sciences 35, 335-362.

Piomelli, U., Chasnov, J.R., 1996. Large-eddy simulations: theory and applications, Turbulence and transition modelling. Springer, pp. 269-336.

Piomelli, U., Liu, J., 1995. Large-eddy simulation of rotating channel flows using a localized dynamic model. Physics of Fluids (1994-present) 7, 839-848.

Piomelli, U., Zang, T.A., Speziale, C.G., Hussaini, M.Y., 1990. On the large-eddy simulation of transitional wall-bounded flows. Physics of Fluids A: Fluid Dynamics 2, 257-265.

Po, J.K.-o., 1975. Developing turbulent flow in the entrance region of a square duct. University of Washington.

Pope, S.B., 1985. PDF methods for turbulent reactive flows. Progress in Energy and Combustion Science 11, 119-192.

Porté-Agel, F., Meneveau, C., Parlange, M.B., 2000. A scale-dependent dynamic model for large-eddy simulation: application to a neutral atmospheric boundary layer. Journal of Fluid Mechanics 415, 261-284.

Postma, A., Schwendiman, L., 1960. Studies in micromeritics. I. Particle deposition in conduits as a source of error in aerosol sampling. General Electric Co. Hanford Atomic Products Operation, Richland, Wash.

Potic, B., Kersten, S.R., Ye, M., van der Hoef, M.A., Kuipers, J., van Swaaij, W.P.M., 2005. Fluidization with hot compressed water in micro-reactors. Chemical Engineering Science 60, 5982-5990.

Prandtl, L., 1925. Uber die ausgebildete Turbulenz. ZAMM. Z. angew. Math. Mech 5, 136-139.

Prandtl, L., 1927. The generation of vortices in fluids of small viscosity. The Aeronautical Journal 31, 718-741.

Reeks, M., 1977. On the dispersion of small particles suspended in an isotropic turbulent fluid. Journal of fluid mechanics 83, 529-546.

Reichardt, H., 1938. Messungen turbulenter Schwankungen. Naturwissenschaften 26, 404-408.

Reif, B.P., Andersson, H., 2002. Prediction of turbulence-generated secondary mean flow in a square duct. Flow, Turbulence and Combustion 68, 41.

Rhie, C., Chow, W., 1983. Numerical study of the turbulent flow past an airfoil with trailing edge separation. AIAA journal 21, 1525-1532.

Rogallo, R.S., 1981. Numerical experiments in homogeneous turbulence. NASA TM-81315

Rogers, C., Eaton, J., 1989. Particle Response and Turbulent Modification in a Flat Plate Turbulent Boundary Layer. ASME, FED 80, 15.

Rogers, C., Eaton, J., 1991. The effect of small particles on fluid turbulence in a flat-plate, turbulent boundary layer in air. Physics of Fluids A: Fluid Dynamics (1989-1993) 3, 928-937.

Rotta, J., 1951. Statistische theorie nichthomogener turbulenz. Zeitschrift für physik 129, 547-572.

Rouson, D., Eaton, J., 1994. Direct numerical simulation of particles interacting with a turbulent channel flow, Proceedings of the 7th Workshop on Two-Phase Flow Predictions, Erlangen, Germany.

Rudman, M., Blackburn, H.M., 1999. Large eddy simulation of turbulent pipe flow, Second International Conference on CFD in the Minerals and Process Industries, Melbourne, Australia, Dec, pp. 6-8.

Sabot, J., Comte-Bellot, G., 1976. Intermittency of coherent structures in the core region of fully developed turbulent pipe flow. Journal of Fluid Mechanics 74, 767-796.

Saffman, P., 1965. The lift on a small sphere in a slow shear flow. Journal of fluid mechanics 22, 385-400.

Sajjadi, H., Salmanzadeh, M., Ahmadi, G. and Jafari, S., 2017. Lattice Boltzmann method and RANS approach for simulation of turbulent flows and particle transport and deposition. Particuology, 30, pp.62-72.

Satake, S.-i., Kunugi, T., Himeno, R., 2000. High Reynolds number computation for turbulent heat transfer in a pipe flow, International Symposium on High Performance Computing. Springer, pp. 514-523.

Sato, Y., Hishida, K., 1996. Transport process of turbulence energy in particle-laden turbulent flow. International Journal of Heat and Fluid Flow 17, 202-210.

Schiller, L., 1935. A drag coefficient correlation. VDI Zeitung 77, 318.

Schultz, M.P., Flack, K.A., 2013. Reynolds-number scaling of turbulent channel flow. Physics of Fluids 25, 025104.

Schumann, U., 1975. Subgrid scale model for finite difference simulations of turbulent flows in plane channels and annuli. Journal of computational physics 18, 376-404.

Schumann, U., Grotzbach, G., Kleiser, L., 1980. Direct numerical simulation of turbulence in prediction methods for turbulent flows. Hemisphere Publ., New York.

Sehmel, G., 1971. Particle diffusivities and deposition velocities over a horizontal smooth surface. Journal of Colloid and Interface Science 37, 891-906.

Sehmel, G., 1973. Particle eddy diffusivities and deposition velocities for isothermal flow and smooth surfaces. Journal of Aerosol Science 4, 125-138.

Sheng, J., Malkiel, E., Katz, J., 2008. Using digital holographic microscopy for simultaneous measurements of 3D near wall velocity and wall shear stress in a turbulent boundary layer. Experiments in fluids 45, 1023-1035.

Shwin, S., Hamdani, A., Takahashi, H. and Kikura, H., 2017. Experimental Investigation of Two-Dimensional Velocity on the 90° Double Bend Pipe Flow Using Ultrasound Technique. World Journal of Mechanics, 7(12), p.340.

M. Sippola and W. Nazaroff. Particle Deposition from Turbulent Flow: Review of Published Research and Its Applicability to Ventilation Ducts in Commercial Buildings. LBNL Report 51432, Lawrence Berkeley National Laboratory, Berkeley, California, 2002. 74

Sippola, M.R., Nazaroff, W.W., 2004. Experiments measuring particle deposition from fully developed turbulent flow in ventilation ducts. Aerosol Science and technology 38, 914-925.

Smagorinsky, J., 1963. General circulation experiments with the primitive equations: I. The basic experiment. Monthly weather review 91, 99-164.

Soldati, A., Marchioli, C., 2009. Physics and modelling of turbulent particle deposition and entrainment: Review of a systematic study. International Journal of Multiphase Flow 35, 827-839.

Soltani, M., Ahmadi, G., 1995. Direct numerical simulation of particle entrainment in turbulent channel flow. Physics of fluids 7, 647-657.

Sommerdijk, N.A., With, G.d., 2008. Biomimetic $CaCO_3$ mineralization using designer molecules and interfaces. Chemical reviews 108, 4499-4550.

Sommerfeld, M., 2001. Validation of a stochastic Lagrangian modelling approach for inter-particle collisions in homogeneous isotropic turbulence. International Journal of Multiphase Flow 27, 1829-1858.

Sommerfeld, M., 2010. Modelling particle collisions and agglomeration in gas–particle flows. In: International Conference on Multiphase Flow, ICMF 2010, May 30–June 4, 2010. Tampa, FL, USA.

Sommerfeld, M. and Stübing, S., 2017. A novel Lagrangian agglomerate structure model. Powder Technology, 319, pp.34-52.

Spalart, P., Allmaras, S., 1992. A One-Equation Turbulence Model for Aerodynamic Flows. AIAA-Paper 92-0439, 1992, 30th Aerospace Sciences Meeting & Exhibit, Jan, pp. 6-9.

Spalart, P.R., 2009. Detached-eddy simulation. Annual review of fluid mechanics 41, 181-202.

Speziale, C.G., 1991. Analytical methods for the development of Reynolds-stress closures in turbulence. Annual Review of Fluid Mechanics 23, 107-157.

Squires, K.D., Eaton, J.K., 1990a. Particle response and turbulence modification in isotropic turbulence. Physics of Fluids A: Fluid Dynamics 2, 1191-1203.

Squires, K.D., Eaton, J.K., 1990b. Particle response and turbulence modification in isotropic turbulence. Physics of Fluids A: Fluid Dynamics (1989-1993) 2, 1191-1203.

Stübing, S., Sommerfeld, M., 2010. Lagrangian modelling of agglomerate structures in a homogeneous isotropic turbulence, International Conference on Multiphase Flow, ICMF.

Subramaniam, S. and Balachandar, S., 2018. Towards Combined Deterministic and Statistical Approaches to Modeling Dispersed Multiphase Flows. In Droplets and Sprays(pp. 7-42). Springer, Singapore.

Sun, T., Faeth, G., 1986. Structure of turbulent bubbly jets—I. Methods and centerline properties. International journal of multiphase flow 12, 99-114.

Takeda, Y., 1986. Velocity profile measurement by ultrasound Doppler shift method. International journal of heat and fluid flow 7, 313-318.

Takeda, Y., 1987. Measurement of velocity profile of mercury flow by ultrasound Doppler shift method. Nuclear Technology 79, 120-124.

Taylor, A.R., Middleman, S., 1974. Turbulent dispersion in drag-reducing fluids. AIChE Journal 20, 454-461.

Thielmann, F., Naderi, M., Ansari, M.A., Stepanek, F., 2008. The effect of primary particle surface energy on agglomeration rate in fluidised bed wet granulation. Powder Technology 181, 160-168.

Thompson, J.F., Thames, F.C., Mastin, C.W., 1974. Automatic numerical generation of body-fitted curvilinear coordinate system for field containing any number of arbitrary two-dimensional bodies. Journal of Computational Physics 15, 299-319.

Tian, L., Ahmadi, G., 2007. Particle deposition in turbulent duct flows—comparisons of different model predictions. Journal of Aerosol Science 38, 377-397.

Travin, A., Shur, M., Strelets, M., Spalart, P., 2000. Detached-eddy simulations past a circular cylinder. Flow, Turbulence and Combustion 63, 293-313.

Tsuji, Y., Morikawa, Y., 1982. LDV measurements of an air–solid two-phase flow in a horizontal pipe. Journal of Fluid Mechanics 120, 385-409.

Tsuji, Y., Morikawa, Y., Shiomi, H., 1984. LDV measurements of an air-solid two-phase flow in a vertical pipe. Journal of Fluid Mechanics 139, 417-434.

Tanaka, T. and Tsuji, Y., 1991. Numerical simulation of gas-solid two-phase flow in a vertical pipe: on the effect of inter-particle collision. ASME/FED Gas–Solid Flows, 121, pp.123-128.

Tsuji, Y., Tanaka, T., Yonemura, S., 1994. Particle induced turbulence. Applied Mechanics Reviews 47, S75-S79.

Uhlmann, M., Pinelli, A., Kawahara, G., Sekimoto, A., 2007. Marginally turbulent flow in a square duct. Journal of fluid mechanics 588, 153-162.

Van de Wall, R., Soo, S., 1997. Measurement of transport properties of a gas-solid suspension using phase Doppler anemometry. Powder technology 94, 141-151.

van Wachem, B., Zastawny, M., Zhao, F., Mallouppas, G., 2015. Modelling of gas–solid turbulent channel flow with non-spherical particles with large Stokes numbers. International Journal of Multiphase Flow 68, 80-92.

Vassallo, P.F., Kumar, R., 1999. Liquid and gas velocity measurements using LDV in air–water duct flow. Experimental thermal and fluid science 19, 85-92.

Vázquez, M.S., Métais, O., 2002. Large-eddy simulation of the turbulent flow through a heated square duct. Journal of Fluid Mechanics 453, 201-238.

Veenman, M.P.B., 2004. Statistical analysis of turbulent pipe flow: numerical approach. Ph.D. thesis, Eindhoven University of Technology, Faculty of Mechanical Engineering.

Versteeg, H.K., Malalasekera, W., 2007. An introduction to computational fluid dynamics: the finite volume method. Pearson Education.

Viswanathan, A.K., Tafti, D.K., 2006. Detached eddy simulation of turbulent flow and heat transfer in a two-pass internal cooling duct. International Journal of Heat and Fluid Flow 27, 1-20.

Volavy, J., Forman, M., Jicha, M., 2012. Large eddy simulation of turbulent particle-laden channel flow considering turbulence modulation by particles, EPJ Web of Conferences. EDP Sciences, p. 02030.

Vreman, B., Geurts, B., Kuerten, H., 1997. Large-eddy simulation of the turbulent mixing layer. Journal of Fluid Mechanics 339, 357-390.

Wallace, J.M., Eckelmann, H., Brodkey, R.S., 1972. The wall region in turbulent shear flow. Journal of Fluid Mechanics 54, 39-48.

Wang, Q., Squires, K.D., 1996. Large eddy simulation of particle-laden turbulent channel flow. Physics of Fluids 8, 1207-1223.

Wang, J., Shi, Q., Huang, Z., Gu, Y., Musango, L. and Yang, Y., 2015. Experimental investigation of particle size effect on agglomeration behaviors in gas–solid fluidized beds. Industrial & Engineering Chemistry Research, 54(48), pp.12177-12186.

Wei, T., Willmarth, W., 1989. Reynolds-number effects on the structure of a turbulent channel flow. Journal of Fluid Mechanics 204, 57-95.

Wells, A., Chamberlain, A., 1967. Transport of small particles to vertical surfaces. British Journal of Applied Physics 18, 1793.

Wenren, Y., Fan, M., Wang, L., Xiao, M., Steinhoff, J., 2003. Application of Vorticity Confinement to prediction of the Flow over Complex Bodies. AIAA journal 41, 809-816.

Westerweel, J., 1997. Fundamentals of digital particle image velocimetry. Measurement science and technology 8, 1379.

Westerweel, J., Draad, A., Van der Hoeven, J.T., Van Oord, J., 1996. Measurement of fully-developed turbulent pipe flow with digital particle image velocimetry. Experiments in Fluids 20, 165-177.

Wilcox, D., 1988. Reassessment of the scale-determining equation for advanced turbulence models. AIAA journal 26, 1299-1310.

Wu, X., Moin, P., 2008. A direct numerical simulation study on the mean velocity characteristics in turbulent pipe flow. Journal of Fluid Mechanics 608, 81-112.

Xia, Z., Shi, Y. and Chen, S., 2016. Direct numerical simulation of turbulent channel flow with spanwise rotation. Journal of Fluid Mechanics, 788, pp.42-56.

Xie, F., Zheng, X., Triantafyllou, M.S., Constantinides, Y., Zheng, Y. and Karniadakis, G.E., 2017. Direct numerical simulations of two-phase flow in an inclined pipe. Journal of Fluid Mechanics, 825, pp.189-207.

Xiong, Y., Zhang, M., Yuan, Z., 2005. Three-dimensional numerical simulation method for gas–solid injector. Powder technology 160, 180-189.

Xu, H., Pollard, A., 2001. Large eddy simulation of turbulent flow in a square annular duct. Physics of Fluids 13, 3321-3337.

Yamanaka, G., Kikura, H., Takeda, Y., Aritomi, M., 2002. Flow measurement on an oscillating pipe flow near the entrance using the UVP method. Experiments in fluids 32, 212-220.

Yang, W., Kuan, B., 2006. Experimental investigation of dilute turbulent particulate flow inside a curved 90 bend. Chemical Engineering Science 61, 3593-3601.

Yao, J., Fairweather, M., 2010. Inertial particle resuspension in a turbulent, square duct flow. Physics of Fluids 22, 033303.

Yao, J., Fairweather, M., 2012. Particle deposition in turbulent duct flows. Chemical engineering science 84, 781-800.

Yoder, J., Silverman, L., 1967. Influence of turbulence on aerosol agglomeration and deposition in a pipe. Paper No. 67-33, 60th Annual APCA Meeting, Cleveland, Ohio.

Young, J. and Leeming, A., 1997. A theory of particle deposition in turbulent pipe flow. Journal of Fluid Mechanics, 340, pp.129-159.

Zagarola, M.V., Smits, A.J., 1998. Mean-flow scaling of turbulent pipe flow. Journal of Fluid Mechanics 373, 33-79.

Zanoun, E.-S., Nagib, H., Durst, F., 2009. Refined cf relation for turbulent channels and consequences for high-Re experiments. Fluid dynamics research 41, 021405.

Zastawny, M., Mallouppas, G., Zhao, F., Van Wachem, B., 2012. Derivation of drag and lift force and torque coefficients for non-spherical particles in flows. International Journal of Multiphase Flow 39, 227-239.

Zhang, H., Ahmadi, G., 2000. Aerosol particle transport and deposition in vertical and horizontal turbulent duct flows. Journal of Fluid Mechanics 406, 55-80.

Zhang, H., Trias, F.X., Gorobets, A., Oliva, A., Yang, D., Tan, Y., Sheng, Y., 2015. Effect of collisions on the particle behavior in a turbulent square duct flow. Powder Technology 269, 320-336.

Zhang, J., Tao, B., Katz, J., 1997. Turbulent flow measurement in a square duct with hybrid holographic PIV. Experiments in Fluids 23, 373-381.

Zhang, Z., Kleinstreuer, C., 2001. Effect of particle inlet distributions on deposition in a triple bifurcation lung airway model. Journal of Aerosol Medicine 14, 13-29.

Zhou, L.X. and Liu, Y., 2018. Two-fluid LES and RANS modeling of sudden-expansion gas-particle flows. Powder Technology, 323, pp.45-50.